VOLUME 106 – NO. 1/2 – APRIL 1992

ISSN 0025-3227

MARINE GEOLOGY

INTERNATIONAL JOURNAL OF MARINE GEOLOGY, GEOCHEMISTRY AND GEOPHYSICS

ELSEVIER

MARINE GEOLOGY

Scope of the journal
Marine Geology is an international medium for the publication of original studies and comprehensive reviews in the field of Marine Geology, Geochemistry and Geophysics. The editors endeavour to maintain a high scientific level and it is hoped that with its international coverage the journal will contribute to the sound development of this field.
A *letter section* is provided as a publication outlet for short papers which require *rapid* publication.

Publication schedule and subscription information – 1992
Marine Geology (ISSN 0025–3227) is published as six volumes (24 issues) a year. The subscription price for 1992 (Volumes 102–107) is Dfl. 1800 + Dfl. 186 p.h. = Dfl. 1986 (approx. US$983). The Dutch guilder price is definitive. The U.S. dollar price is subject to exchange-rate fluctuations and is given only as a guide. Subscriptions are accepted on a prepaid basis only, unless different terms have previously been agreed upon. Personal subscription rates and conditions are available upon request from the Publisher. Subscription orders can be entered only by calendar year (Jan.–Dec.) and should be sent to Elsevier Science Publishers, Journal Department, P.O. Box 211, 1000 AE Amsterdam, The Netherlands, tel. 31.20.5803642, fax 31.20.5803598, or to your usual subscription agent. Postage & handling (p.h.) charges include surface delivery, except to the following countries where air delivery via S.A.L. (Surface Air Lift) mail is ensured: Argentina, Australia, Brazil, Canada, Hong Kong, India, Israel, Japan*, Malaysia, Mexico, New Zealand, Pakistan, PR China, Singapore, South Africa, South Korea, Taiwan, Thailand and the USA. *For Japan, air delivery (S.A.L.) requires an additional charge of 25% of the normal postage and handling charge. For all other countries, airmail rates are available upon request. Claims for missing issues must be made within three months of publication (mailing) date; otherwise, such claims cannot be honoured free of charge. For further information, or a free sample copy of this or any other Elsevier Science Publishers journal, readers in the USA and Canada can contact the following address: Elsevier Science Publishing Co. Inc., Journal Information Center, 655 Avenue of the Americas, New York, NY 10010, U.S.A., tel. 212.63337502. Back issues can be ordered. For further information regarding prices etc., please contact Elsevier Science Publishers, Journal Department, P.O. Box 211, 1000 AE Amsterdam, The Netherlands, tel. 31.20.5803642, fax 31.20.5803598.

Journal Information Center
For customers in the U.S.A. and Canada wishing additional bibliographic information on this and other Elsevier journals, please contact: Elsevier Science Publishing Co. Inc., Journal Information Center, 655 Avenue of the Americas, New York, NY 10010, U.S.A., Tel: (212) 633-3750.

Publication of abstracts and contents lists
Abstracts and/or contents lists of this journal are published in the following journals: *Geoscience Contents, Geo Abstracts, Current Contents, Bulletin Signalétique, Chemical Abstracts, Marine Science Contents Tables, A.G.I.'s Bibliography and Index of Geology, Aquatic Sciences and Fisheries Abstracts, PASCAL/CNRS and Oceanic Abstracts.*

(continued on inside back cover)

 0025-3227/92/$05.00

This issue is printed on acid-free paper.

PRINTED IN THE NETHERLANDS

MARINE GEOLOGY

VOL. 106 (1992)

MARINE GEOLOGY

International Journal of Marine Geology, Geochemistry and Geophysics

VOL. 106 (1992)

ELSEVIER
AMSTERDAM – LONDON – NEW YORK – TOKYO

0025-3227/92/$05.00

This issue is printed on acid-free paper.

PRINTED IN THE NETHERLANDS

Marine Geology, 106 (1992) 1–24
Elsevier Science Publishers B.V., Amsterdam

Frequency dependent cross-shore suspended sediment transport. 1. A non-barred shoreface

Philip D. Osborne and Brian Greenwood

Scarborough College Coastal Research Group, University of Toronto, Scarborough, Ont. M1C 1A4, Canada

(Received June 14, 1991; revision accepted December 5, 1991)

ABSTRACT

Osborne, P.D. and Greenwood, B., 1992. Frequency dependent cross-shore suspended sediment transport. 1. A non-barred shoreface. *Mar. Geol.*, 106: 1–24.

The local, time-varying and time-averaged suspended sediment transports across a marine, non-barred shoreface were obtained from field measurements of the near-bed velocity and sediment concentration vectors using electromagnetic current meters and optical backscatterance suspended solids sensors. Co-spectral analyses of velocity and sediment concentration revealed the contributions of waves of different frequencies to the total transport; the transport attributable to quasi-steady currents was determined from the product of the time-averaged cross-shore velocity and sediment concentration. Estimates of the local, time-integrated sediment volume flux (total and net) and the associated erosion or accretion were determined using depth-of-activity rods.

Suspended sediment transport was associated with: (1) local wind-forced waves; (2) swell; (3) low frequency waves (group-bound long waves) and (4) offshore-directed mean currents (undertow). These transport components varied spatially and temporally in response to changes in the wave height to water depth ratio. The local net oscillatory sediment transport rate at wind-wave and swell-wave frequencies was directed onshore predominantly, and increased as water depth decreased in association with wave shoaling. The local mean sediment transport rate was predominantly offshore and dominated the net transport rate wherever wave-induced components were weak relative to the mean currents. Under breaking waves the suspended sediment transport contribution associated with wind-waves and swell-waves was reduced as a result of dissipation. The net suspended sediment transport rate exhibited a distinct vertical structure, reflecting the balance at each elevation between the opposing mean and oscillatory components of transport. The local time-averaged total and net sediment volume flux and resulting erosion and accretion patterns support the hypothesis of a near balance in sediment flux for the complete storm event.

Introduction

The sediment transport processes responsible for maintaining equilibrium profiles on both non-barred and barred shorefaces remain poorly defined. Theory, which suggests that sediment transport on non-barred beaches is controlled by a simple balance between some perturbation in the dominant oscillatory velocity field and gravitational constraints is in qualitative agreement with observed sediment behaviour (e.g. Bagnold, 1963, 1966; Bowen, 1980a,b; Bailard, 1981). However, this explanation is complicated by a nearshore velocity field composed of temporally and spatially varying oscillatory and quasi-steady components (e.g. Greenwood and Osborne, 1990a). The frequency distribution of cross-shore velocity vectors at a point, for example, is typically non-Gaussian, characterized by a non-zero mean and a marked skewness (e.g. Guza and Thornton, 1985; Doering and Bowen, 1985; Doering, 1988; Greenwood and Osborne, 1990b). More importantly, sediment concentrations near the bed respond in a rather complex way to changes both in the instantaneous velocity (e.g. Huntley and Hanes, 1987; Doering

Correspondence to: B. Greenwood, University of Toronto, Scarborough College Coastal Res. Gr., Department of Geography, 1265 Military Trail, Scarborough, Ont. M1C 1A4, Canada.

and Bowen, 1989; Greenwood et al., 1990) and the form of the bottom boundary (e.g. Inman and Bowen, 1963; Sleath, 1982; Nielsen et al., 1979, 1982). Peaks in sediment concentration appear to be associated with individual wave cycles, wave groups (Doering and Bowen, 1989; Greenwood et al., 1990, 1991a,b; Osborne et al., 1990) and low frequency waves (Hanes and Huntley, 1986; Beach and Sternberg, 1988; Osborne et al., 1990), but no simple correlation with wave or current motion has emerged. Direct field measurement of sediment transport rates are urgently required to resolve the relative contributions of the various mechanisms proposed to the sediment transport maintaining a shoreface profile in quasi-equilibrium.

The aims of this paper are: (1) to identify cross-shore suspended sediment transport mechanisms; (2) to define their relative importance in controlling the net cross-shore flux of sediment; and (3) to relate the net flux to observed morphological changes in a marine, non-barred shoreface. Rapid response sensors were used during a storm to obtain field measurements of the near-bed, cross-shore velocity and the suspended sediment concentration necessary to calculate local, time-varying fluxes of suspended sediment. Time-integrated sediment volume fluxes and local scour and accretion patterns were also determined for comparison with the measured net sediment transport rates and to document the morphological response to the sediment transport.

Location of study

Data for this study were collected from a non-barred, marine nearshore environment during a field experiment conducted at Queensland Beach, Nova Scotia, Canada (Fig. 1), as part of the C-COAST Programme (see Greenwood et al., 1990, 1991a,b). Situated at the head of St. Margaret's Bay, the beach is exposed to the Atlantic Ocean through a narrow opening that substantially restricts the directional spread of the incident wave field. The shoreface is relatively steep and concave upwards (slope $\approx$0.10 near the shoreline, decreasing to a slope $\approx$0.03 further offshore—Fig. 2). It is composed of fine-to-medium, moderately sorted sand (Table 1) overlying cobbles; grain-size distributions are negatively skewed, a characteristic of wave-winnowed sediments (Greenwood and Davidson-Arnott, 1972). The Bay is meso-tidal (range $\approx$2 m at springs) and experiences periods of moderate, wind-forced waves (H_s = 0.5–2.0 m; T_{pk} = 4–8 s) followed by periods of long-crested swell.

TABLE 1

Grain size characteristics of the shoreface at Queensland Beach. Note: samples were dry sieved at 1/4 Φ intervals and statistics computed by the method of moments

Location (m)	Mean size		Sorting Φ	Skewness Φ
	Φ	mm		
140	2.62	0.16	0.69	−2.03
130	2.72	0.15	0.56	−1.56
120	2.71	0.15	0.57	−1.20
110	2.48	0.18	0.69	−1.57
100	2.55	0.17	0.62	−2.19
90	2.32	0.20	0.53	−0.55
80	2.11	0.23	0.56	−0.28
70	2.03	0.25	0.56	−0.32
60	2.04	0.24	0.63	−0.65
50	1.90	0.27	0.57	−0.22
40	1.77	0.29	0.53	−0.43
30	1.53	0.35	0.58	−0.79
20	1.76	0.30	0.68	−1.57
10	1.86	0.27	0.45	−0.33

Instrumentation and measurements

Wind

Wind speed and direction were measured at the beach face with a Beaufort anemometer and wind vane.

Water surface elevations

Waves and mean water surface elevations were measured using piezo-resistive strain gauge transducers (Hazen et al., 1989); the transducers respond linearly and were calibrated in a 30 m deep tank using a Paroscientific Digi-quartz pressure transducer/computer (see Hazen et al., 1989). Pressure data were not corrected for effects of depth attenuation as these were negligible for the depths incurred in this study.

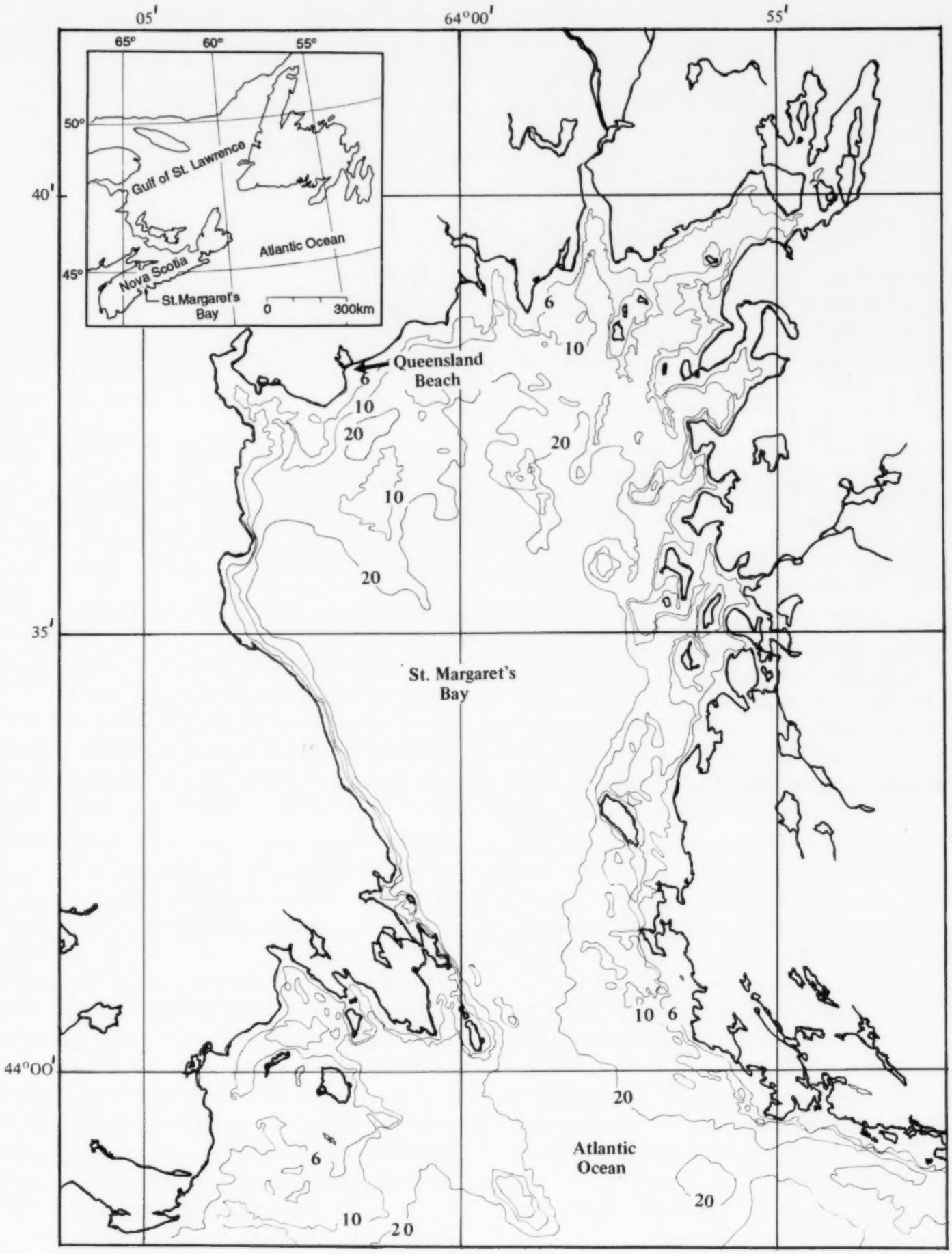

Fig. 1. Field site, Queensland Beach, St. Margaret's Bay, Nova Scotia, Canada. Note: contours in fathoms.

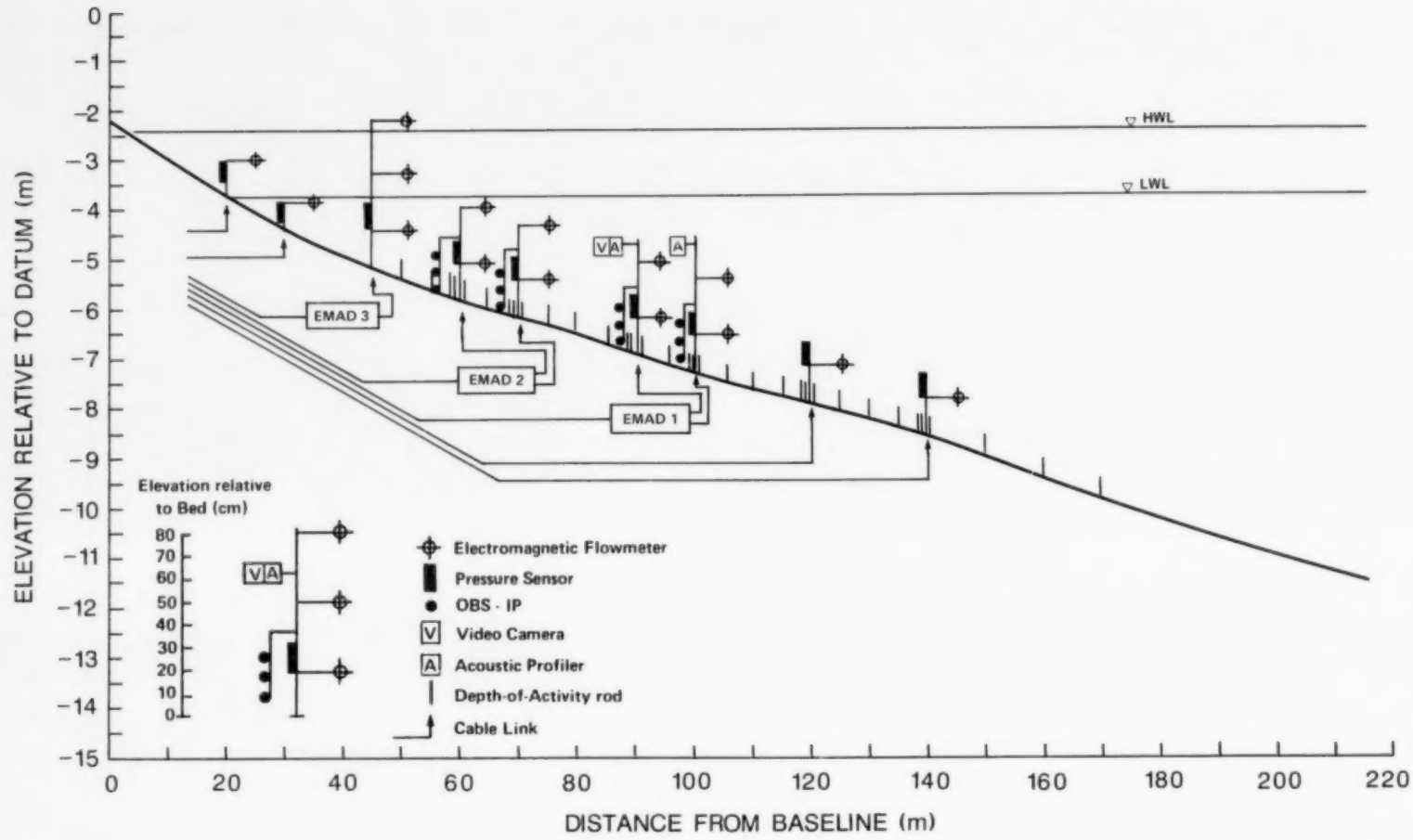

Fig. 2. Shoreface profile and sensor deployment. Note: *EMAD 1–3* are underwater analogue-to-digital converters and digital transmission packages; they also distribute power to the sensors.

Velocity

The horizontal components of the shore-normal and shore-parallel velocity were measured with Marsh-McBirney Inc. biaxial electromagnetic current meters (Model OEM 512). These were calibrated by towing at a number of speeds in both the positive and negative directions; the gain was determined from a first-order, least squares regression of the sensor output. Zero offsets were checked in still water in the field both before and after deployment, as well as during calm conditions while deployed. Current records were also corrected for errors in gain and phase introduced by the output filter characteristics of the standard OEM 512 electronics (see Guza et al., 1988, and Doering, 1988 for discussion).

Suspended sediment concentration

High resolution time-series of suspended sediment concentration were obtained using optical backscatterance suspended solids sensors (OBS-1P; Downing et al., 1981; Downing, 1983; D and A Instruments and Engineering, 1988). Each OBS-1P sensor was calibrated in a sediment recirculating facility using sand from the respective field deployment locations. Linear correlations accounted for upwards of 95% (usually >99%) of the variance in the time-averaged analogue signal output over ranges of sediment concentration from 0.5 to 30 g l^{-1} (Greenwood et al., 1990). Although the relative variance does not increase systematically with concentration for a given sensor, those sensors with higher gains appear to be more responsive to large magnitude short period fluctuations in concentration, even after calibration (Osborne, 1990). This implies a nonlinear response to "concentration fluctuations" even though time-averaged calibrations are linear; care was taken to collocate sensors with similar response characteristics. Preliminary results from laboratory and field cross-calibrations between the OBS-1P and a 2.25 MHZ acoustic backscatter suspended sediment profiler have revealed signal responses that are temporally coherent and highly correlated (Greenwood et al.,

1990). This similarity in response to concentration fluctuations gives credibility to both sensors. The OBS-1P offset is, however, affected by backscatter from both organics and bubbles. Non-stationarity in the field offset prevented direct application of the laboratory offsets and therefore "clear water" offsets were determined from repetitive field measurements under calm conditions. The OBS-1P data were low-pass filtered in the frequency domain to remove high frequency noise (1.5–2.0 Hz) which appeared occasionally in the OBS signals (e.g. at the 60 m station) and to reduce the magnitude of large amplitude, short duration fluctuations (spikes) in some of the data which were uncorrelated with concentrations at other elevations. These "spikes" were often associated with the presence of organics in the water column (confirmed by video and diver observations). However, the filter also reduced the amplitudes of local, high frequency fluctuations in sediment concentration; such fluctuations are observed in calibration time-series.

Morphodynamics and sediment volume flux

Large-scale changes in beach morphology to depths <2 m were measured using either a level and staff or an OMNI Total Station. Survey lines were oriented normal to a baseline and spaced 15 m apart to the north and south of the shore-normal sensor transect. A Raytheon Fathometer (Model DE719) was used to record shore-normal profiles extending offshore to approximately 400 m. The transducer position was fixed by triangulation and water depths were corrected for the transducer depth below water level; all survey points were reduced to a common benchmark at coordinates 0,0 on the survey grid.

Pre- and post-storm measurements from a grid of depth-of-activity rods provided greater resolution of morphological changes. The rods also provided measures of depth-of-activity, time-integrated total (ITVF) and net (INVF) sediment volume flux, and were used to examine the balance of sediment in a shoreface control volume for individual storm events (Greenwood and Hale, 1980, p. 91, fig. 7.2; Greenwood, 1987, pp. 1124–1125, figs. 4 and 5). The control volume was determined by taking the areal extent of the rod grid and multiplying by a arbitrary depth of 0.50 m. The latter is a conservative depth for potential "re-activation". Depth-of-activity rods also indicate limits to the relative displacement of sensors above the bed during the storm (e.g. Greenwood and Sherman, 1988; Greenwood and Osborne, 1988).

Sensor deployment

Four sediment transport stations were located respectively 60, 70, 90, and 100 m offshore from the baseline close to the upper limit of the foreshore. Each transport station (Fig. 2) consisted of: (1) a vertical array of 3 optical sensors (nominal elevations of $z \approx 0.08$, 0.18 and 0.28 m); (2) two current meters (nominal elevations of $z \approx 0.20$ and 0.50 m); and (3) a pressure sensor (nominal elevation of $z \approx 0.20$ m). A vertical array of 3 current meters ($z \approx 0.20$, 0.50 and 0.80 m) and a pressure transducer ($z \approx 0.20$ m) were collocated 45 m offshore, and individual current meters ($z \approx 0.20$ m) and pressure transducers ($z \approx 0.20$ m) were collocated at 20, 30, 120 and 140 m offshore (Fig. 2).

An underwater video camera was deployed at the 90 m station to record bedforms and sediment re-suspension on a semi-continuous basis during daylight hours. Similar observations were made at the remaining stations by SCUBA divers whenever conditions permitted.

Data acquisition and analytical techniques

All electronic sensors were hardwired to analogue-to-digital conversion and transmission packages (EMAD, Fig. 2). During transport events, output signals were recorded at 4 Hz essentially continuously, being interrupted for one minute after every 29 for data control purposes only. Data were stored directly to magnetic tape, allowing monitoring to proceed continuously for up to 8 hours. A complete description of the computer-controlled data acquisition system and underwater digitization and transmission system is given by Hazen et al. (1987). Sensor outputs were converted from voltages to appropriate units using the offset and gain characteristic of each sensor.

Time-series were truncated to approximately seventeen minutes of record to ensure stationarity in this rapidly changing environment, while at the

same time retaining a sufficient number of points (4096) to maintain a high degree of statistical confidence, especially with respect to the fast Fourier transforms. Statistical descriptions of the nearshore velocity and suspended sediment concentration fields and the water-surface elevation (mean, standard deviation and skewness) were computed using the BMDP 2D Statistical Analysis Program (Dixon, 1985). Average and maximum values of both wave height and oscillatory current speed were estimated from the standard deviation of water surface elevation and velocity records respectively using the accepted conventions. Variance spectra, cross-spectra and cross-correlations were computed using the BMDP 1T and 2T Time Series Analysis Programs (Dixon, 1985). The data were demeaned using standard BMDP 1T preprocessing routines and spectral estimates were obtained every 0.01 Hz from 0.0 to 2.0 Hz with a resolution bandwidth of 0.03 Hz and 70 degrees of freedom.

Sediment transport calculations

The product of the instantaneous sediment concentration and velocity measured at a point gives the local instantaneous sediment transport rate, uc. The time-average of the instantaneous products gives the local net sediment transport rate:

$$<uc>_{\text{net}} = \frac{1}{n}\sum uc$$

where n = the sample size. Assuming that the concentration and velocity at any instant in time are composed of a steady component (overbar) and an unsteady or fluctuating (′) component, then:

$$c = \bar{c} + c'$$

$$u = \bar{u} + u'$$

and the local net sediment transport rate, $<uc>$, may also be given by:

$$<uc> = <(\bar{u}+u')(\bar{c}+c')>$$

$$= \bar{u}\bar{c} + <\bar{u}c'> + <\bar{u}'c> + <u'c'>$$

The terms $<\bar{u}c'>$ and $<u'\bar{c}>$ go to zero because by definition the time-average of the fluctuations is zero. Thus:

$$<uc> = \bar{u}\bar{c} + <u'c'>$$

The term $\bar{u}\bar{c}$ is called the local mean sediment transport rate, computed as the time-averaged velocity multiplied by the time-averaged concentration. The term $<u'c'>$ is a measure of the correlation between fluctuations in concentration and velocity (termed "flux coupling" by Jaffe et al., 1985). Low values of this term indicate that fluctuations in concentration relative to fluctuations in velocity are random; large values indicate a large degree of temporal correlation. Jaffe et al. (1985) have already demonstrated that this term is typically non-zero in the surf zone. While this fluctuating component of sediment transport may be computed by taking the product of residuals about the mean for both concentration and velocity, a more convenient way uses cross-spectral analysis (e.g. Huntley and Hanes, 1987). Additionally, the co-spectrum gives the cross-product between concentration and velocity as a function of frequency; this reveals the relative contributions to the rate and direction of sediment transport of oscillations at different frequencies. Integration of the co-spectrum over all frequencies and division by the number of frequency bands gives the local net oscillatory sediment transport rate, which is equivalent to the "flux coupling" term introduced by Jaffe et al. (1985).

It is obvious from the physical size of the current and sediment concentration sensors that they cannot be perfectly collocated in space; furthermore, there are greater limitations on the electromagnetic flowmeter with respect to its proximity to the bed. A number of theories exist which could be used to predict the form of the time-averaged velocity profile (e.g. Grant and Madsen, 1979); however, given the large uncertainties in the bed roughness and the effects of wave, current and suspended sediment interactions under breaking waves, it seems more useful to discuss the results assuming a uniform current profile, and only later to examine their sensitivity to various forms of the velocity profile. In this research a first approximation to the computation of suspended sediment flux rates is made by using cross-products of the concentrations measured at each of the OBS-1P elevations

($z \approx 0.08$, 0.18, and 0.28 m) and local velocities measured at the lowest current sensor elevation ($z \approx 0.20$ m). When a uniform velocity profile is assumed, the vertical structure of the mean sediment transport for example, simply reflects the vertical variation of time-averaged concentrations and the magnitude and direction of the mean flow.

Storm event summary

The storm event described in this paper occurred on October 25/26, 1987 and lasted for approximately 18 h over a complete spring tidal cycle; Figure 3 illustrates the temporal variation in wind, waves, tide and wave-induced currents. Significant wave heights (H_s) increased and decreased coincident with the wind; the peak period (T_{pk}) however, shows a gradual increase throughout the event as energy shifted from wind-forced waves to swell. The peak of the storm coincided with low tide and wave heights exceeded 2 m at breaking with a peak period of 8 s. Maximum orbital speeds (u_s) reached 1.58 m s^{-1} and cross-shore mean currents ($\bar{u}$) reached 0.20 m s^{-1} at the storm peak in the inner surf zone. Maxima in orbital speeds, onshore velocity skewness (u_{sk}) and offshore mean flow (Fig. 3) coincided with both the maximum incident wave and low tide (p-minimum depth) at approximately 1500 h on October 25, when wind speed reached 20 knots (10.3 m s^{-1}). Wind speed peaked for a short time at 35 knots (18.0 m s^{-1}) at approximately 1800 h on the same day during a rising tide; a second (smaller) peak in orbital speeds occurred at this time. During the storm maximum, breaking waves extended 60–70 m offshore, causing damage to both stations at these locations. Owing to the steepness of the nearshore slope, however, the surf zone was confined within 45 m of the shoreline for much of the storm.

Figure 4 illustrates the temporal and spatial variation in both the near-bed ($z \approx 0.20$ m) oscillatory velocities (u_s) and the mean sediment concentrations ($\bar{c}$; $z \approx 0.08$ m) across the shoreface throughout the storm cycle. Orbital speeds followed a coherent pattern increasing and decreasing in phase with the storm waves as they increased in height and then decayed. Speeds were clearly depth dependent, increasing landwards from the 100 m station. The pattern of mean sediment concentrations ($\bar{c}$) was less coherent both spatially and temporally, as might have been expected; however, increases and decreases in concentration did occur as orbital speeds increased and decreased. Unfortunately, with the exception of the 100 m station, the optical sensors at all other stations were contaminated by organics for the period 1500–1800 h inclusive, thus limiting interpretations to the period of the storm buildup and decay. Sediment concentrations recorded at the 100 m station however, indicated mean values increasing to a maximum of 2.6 g l^{-1} between 1500 and 1600 h and then decreasing in phase with the near-bed orbital speeds.

Wave-induced suspended sediment transport

It is evident from previous studies that the magnitude and the direction of suspended sediment transport depends directly upon the form of the surface gravity waves and thus the character of the near-bed velocity field. Changes in surface gravity wave form occur through shoaling; a useful first approach to the examination of sediment transport is therefore to consider it in relation to changes that occur in the wave height-to-water depth ratio at a given location. Furthermore, shifts in the flow regime (Simons and Richardson, 1962, 1966; Sherman and Greenwood, 1984; Greenwood and Sherman, 1986, 1988; Ollerhead and Greenwood, 1990) associated with the bedform response to increases or decreases in bed shear will also affect the direction and magnitude of the sediment transport (Inman and Bowen, 1963; Sleath, 1982). The magnitude of sediment concentration at any elevation, its rate of change and the phase relationships between concentration and fluid velocity have been shown to be strongly influenced by the height and spacing (steepness) of bedforms (Osborne and Greenwood, 1992).

Non-breaking waves ($0.1 < H_s/h < 0.2$)

Figure 5a illustrates cross-shore velocity and sediment concentration spectra and the corresponding co-spectra obtained from the 70 m station under shoaling waves. Wave-induced kinetic

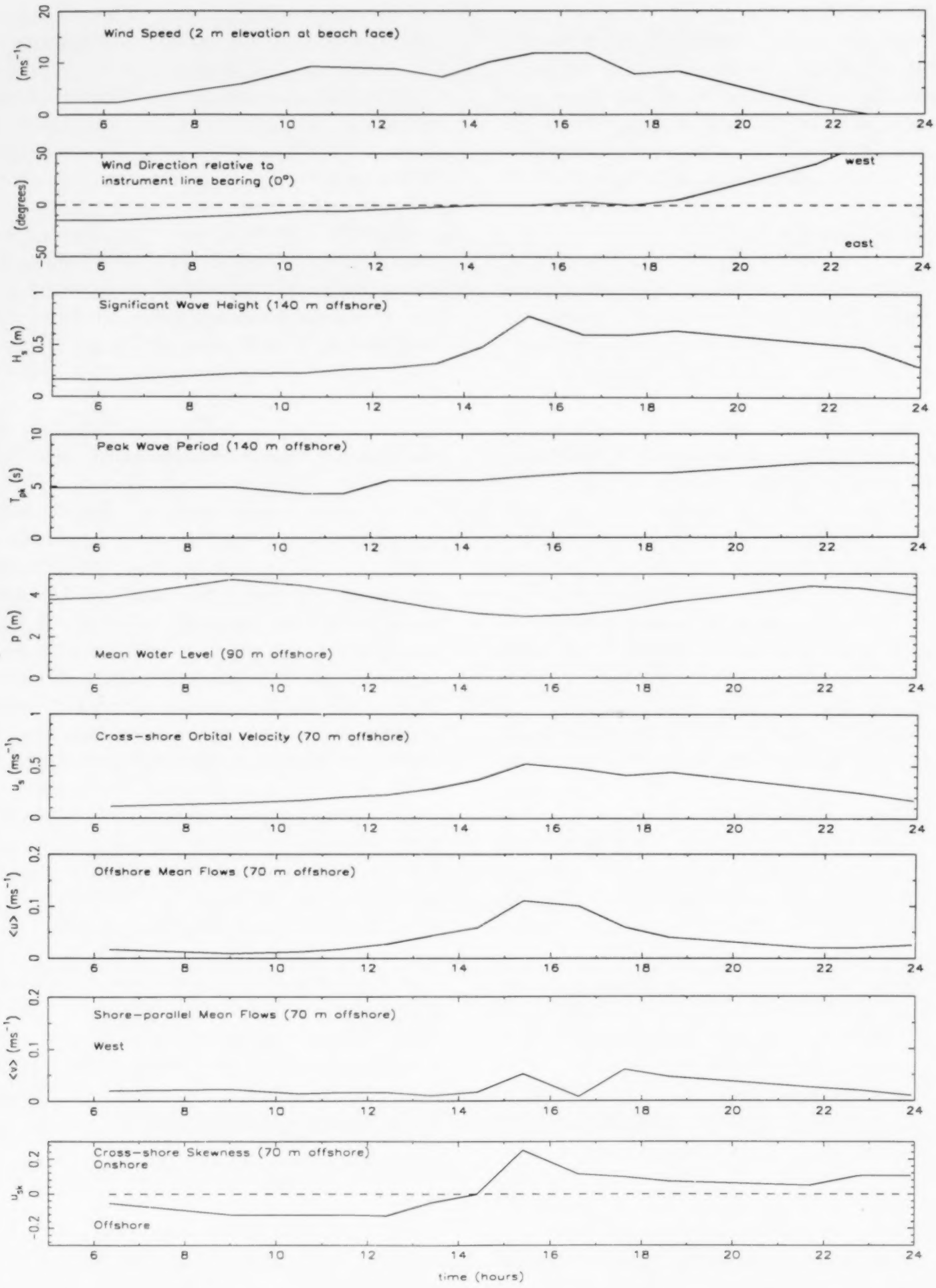
Wind Speed (2 m elevation at beach face)
(ms⁻¹)
Wind Direction relative to instrument line bearing (0°)
(degrees)
west
east
Significant Wave Height (140 m offshore)
H_s (m)
Peak Wave Period (140 m offshore)
T_{pk} (s)
Mean Water Level (90 m offshore)
p (m)
Cross-shore Orbital Velocity (70 m offshore)
u_s (ms⁻¹)
Offshore Mean Flows (70 m offshore)
<u> (ms⁻¹)
Shore-parallel Mean Flows (70 m offshore)
West
<v> (ms⁻¹)
Cross-shore Skewness (70 m offshore)
Onshore
Offshore
u_{sk}
time (hours)

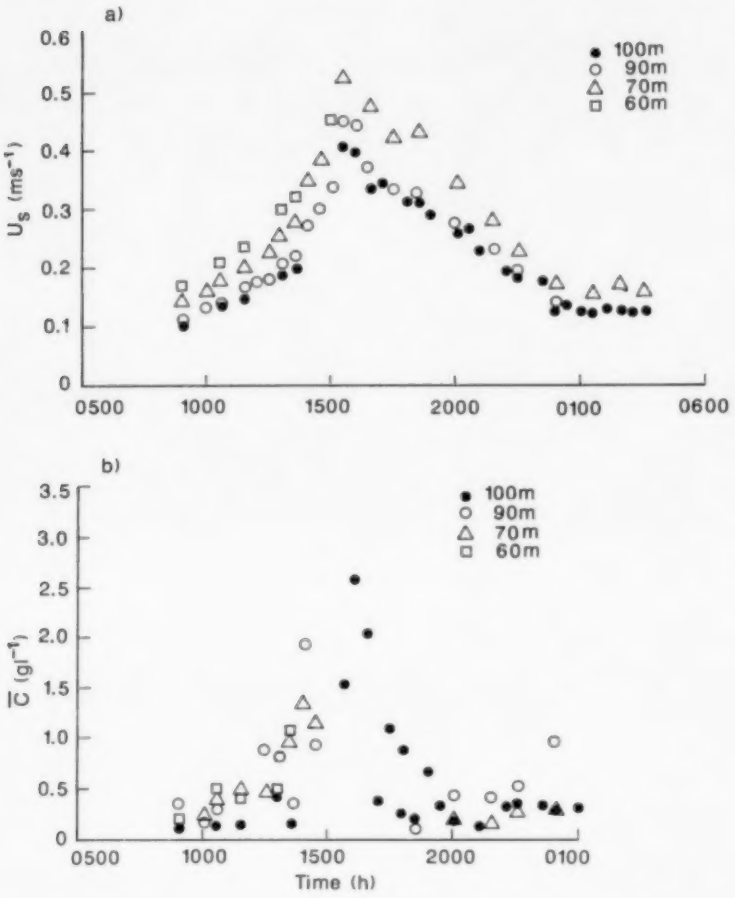

Fig. 4. Temporal and spatial variability of: (a) near-bed orbital speeds ($z \approx 0.20$ m); (b) time-averaged sediment concentrations ($z \approx 0.08$ m). Note: concentrations recorded at the storm peak from the 60, 70 and 90 m stations were contaminated and are not plotted; velocities from the 60 m station were not available after 1500 h.

energy is spread across a wide frequency band, but the peak of the velocity spectrum occurs at 0.33 Hz (3 s) corresponding to the wind-driven incident waves. A minor, but statistically significant, spectral peak occurs at 0.125 Hz (8 s) corresponding to long period swell which was present prior to the wind-wave growth. Another minor peak occurs near the wind-wave harmonic at 0.75 Hz (1.3 s). In contrast, most of the variance in the concentration spectrum occurs at frequencies less than 0.1 Hz (10 s). There are no significant peaks in the concentration spectrum corresponding to either the wind-wave frequency (0.20–0.40 Hz) or the wind-wave harmonic (0.75 Hz) as might have been expected if sediment concentrations were responding to individual incident waves. These do occur under some conditions, however, as shown by Greenwood et al. (1990).

The co-spectrum from the 0.08 m elevation exhibits peaks which correspond to both the wind wave and swell frequencies in the cross-shore velocity spectrum. In this example, the larger positive spectral densities coincident with the wind wave frequencies (0.20–0.40 Hz) indicate a larger onshore transport of sediment by the wind waves than by the swell. The smaller but distinct negative spectral peak at frequencies <0.05 Hz indicates that offshore transport of suspended sediment is associated with low frequency waves. The co-spectrum from each elevation reveals that no significant suspended sediment transport was occurring at frequencies greater than 0.5 Hz (2 s); this reflects the low velocity variance at frequencies greater than 0.5 Hz and the obvious lack of correlation between concentration fluctuations and velocity fluctuations at these frequencies. Furthermore, they reveal the rapid decrease in transport with elevation at all frequencies. Under shoaling waves oscillatory transport of suspended sediment was restricted to within short distances of the bed and dominated by an onshore flux at wind-wave frequencies (0.20 to 0.4 Hz); a distinct, but much smaller offshore transport occurred at low frequencies (<0.05 Hz).

Occasionally spilling breakers ($H_s/h > 0.2$)

As waves increased in size and began to break, the nature of the sediment transport as revealed in the structure of the co-spectra varied considerably. For example, Fig. 5b illustrates the velocity and concentration spectra together with associated co-spectra from the 70 m station when the wave height-to-water depth ratio had increased to approximately 0.2 and waves were spilling occasionally. An order of magnitude increase in sediment concentrations occurred at all frequencies under these conditions, but once again little or no

Fig. 3. Temporal variability of: wind speed and direction at the beach face; significant wave height (H_s) and peak wave period (T_{pk}) at the 140 m station; mean water level (p) at the 90 m station; average orbital current speed (u_s), cross-shore and alongshore mean flows ($<u>$, $<v>$) and cross-shore velocity skewness (u_{sk}) at the 70 m station.

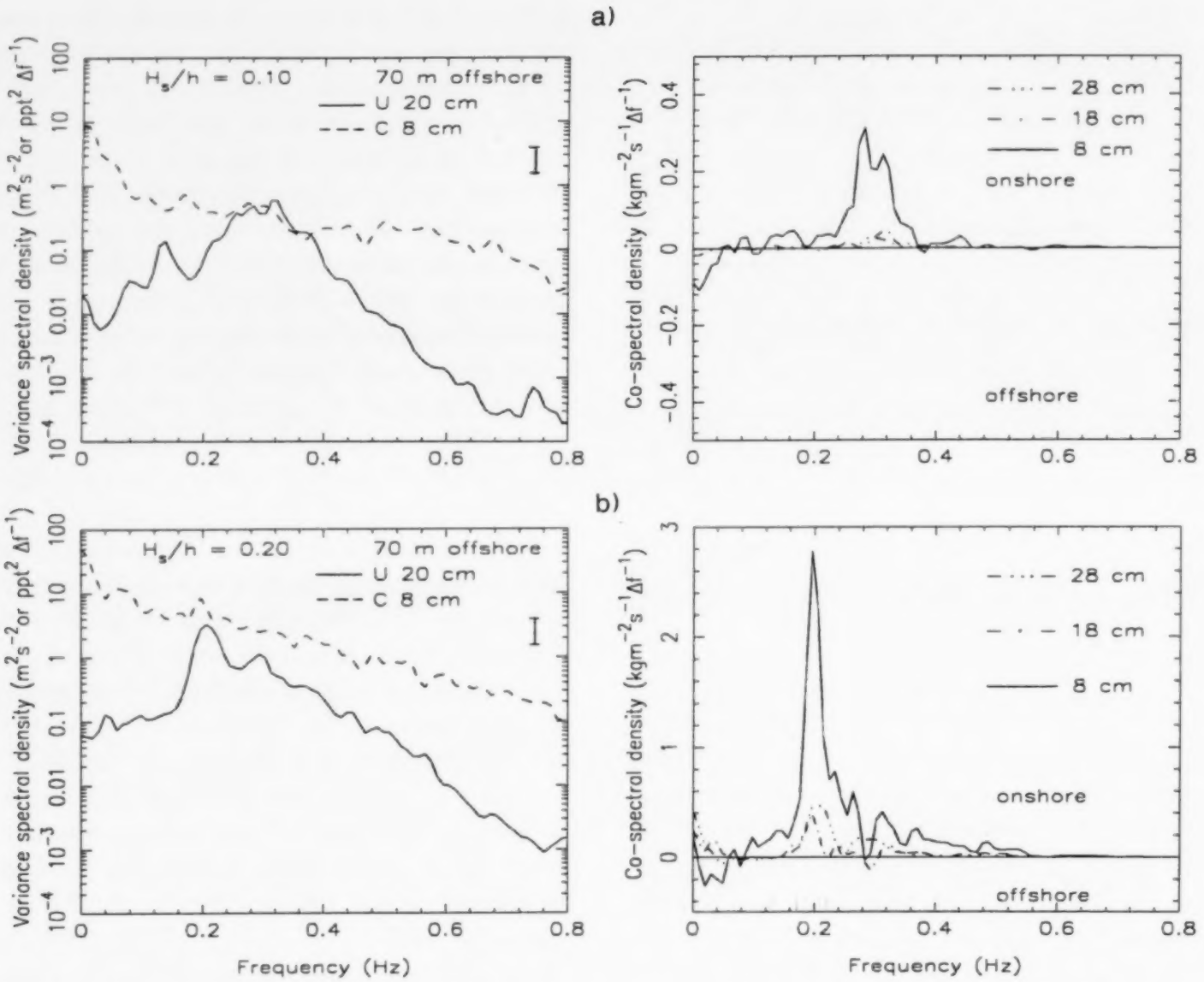

Fig. 5. Cross-shore velocity (u) and concentration (c) spectra and co-spectra (70 m station) typical of storm-wave growth: (a) shoaling waves; (b) breaking waves (spilling breakers). Note: the error bar indicates the 95% confidence limits for the spectral estimates.

structure appeared in the spectrum. It is readily apparent that the relative magnitude of the transport associated with the wind waves had increased significantly from that under non-breaking conditions (cf. Fig. 5b with Fig. 5a). Under these near-breaking conditions, the co-spectra from the 0.18 and 0.28 m elevations indicate onshore transport at wind wave frequencies of a magnitude similar to those from much lower elevations (0.08 m) under non-breaking conditions. The co-spectra in Fig. 5b also indicate that the transport of suspended sediment attributable to low frequencies also increased substantially; this long wave transport was now equal in magnitude to that attributable to wind waves earlier in the storm. However, in contrast to the suspended load under shoaling waves, not all of the transport attributable to low frequencies was directed offshore; positive peaks between 0.05 and 0.10 Hz appear in both co-spectra from higher elevations ($z \approx 0.18$ and 0.28 m) indicating onshore transport at these heights above the bed. This reversal of the transport direction higher in the flow reflects important temporal and spatial interdependencies between the sediment concentration and horizontal velocity. It emphasizes the importance of phase lags introduced by the finite time necessary for sediment re-suspension at the bed and its transfer upwards into the flow (Greenwood et al., 1990, 1991a; Osborne and Greenwood, 1992).

The spectra and co-spectra observed under breaking incident waves indicate an increase in the

effectiveness of both wind waves and low frequency waves to transport sediment in suspension. The increase in onshore transport at wind wave frequencies correlates well with the increase in velocity skewness (Fig. 3) observed under the highly non-linear breaking waves. The increase in offshore transport at low frequencies is restricted close to the bed (0.08 m) and reflects the strong coupling between the offshore phases of long waves and large sediment concentrations in the water column; this is associated with groupiness in the incident waves and the presence of a forced long wave (Fig. 6—see also Greenwood and Osborne, 1992; Osborne and Greenwood, 1992).

Spatial dependency of wave-induced suspended sediment transport

The time-series illustrated in Fig. 7 reveal changes in both the cross-shore velocity and suspended sediment concentration across the shoreface under shoaling waves. The H_s/h ratio associated with these time-series increased from 0.07 at the 100 m station to 0.14 at the 60 m station. It is readily apparent that sediment concentrations respond to both individual waves and, more importantly, to wave groups. Sediment resuspension as a wave group passes involves a cumulative increase and then decrease in concentration at any given elevation, which may last for several tens of seconds; fluctuations associated with individual wave cycles are superimposed. Spatially coherent suspension events can be clearly identified from one location to the next as groups of large waves propagate across the shoreface (Fig. 7). Spatial coherence is confirmed by cross-correlations between both velocity and concentration measurements at each of the stations across shore (Fig. 8; Table 2). The time lags associated

TABLE 2

Time lags between stations

Stations	100–90	100–70	100–60	90–70	90–60	70–60
dx	10.0	30.0	40.0	20.0	30.0	10.0
dh	0.3	0.5	1.2	0.2	0.9	0.7
C	6.6	6.5	6.2	6.4	6.1	6.0
t	1.5	4.6	6.4	3.1	4.9	7.1
R_{max-u}	2.0	5.5	7.5	3.5	5.75	2.3
R_{max-c}	1.8	6.3	7.5	4,3	6.0	2.3

dx = separation distance between stations (m);
dh = change in water depth between stations (m);
c = average phase velocity between stations (m s^{-1})
$= 1/N\sum(gh_i)^{0.5}$, where h_i = local depth (m), N = number of depth increments between stations spaced 1 m apart;
$t = C \cdot dx$ = times of travel between stations (s);
R_{max-u} = lag of maximum correlation for velocity data (s); and
R_{max-c} = lag of maximum correlation for concentration data (s).

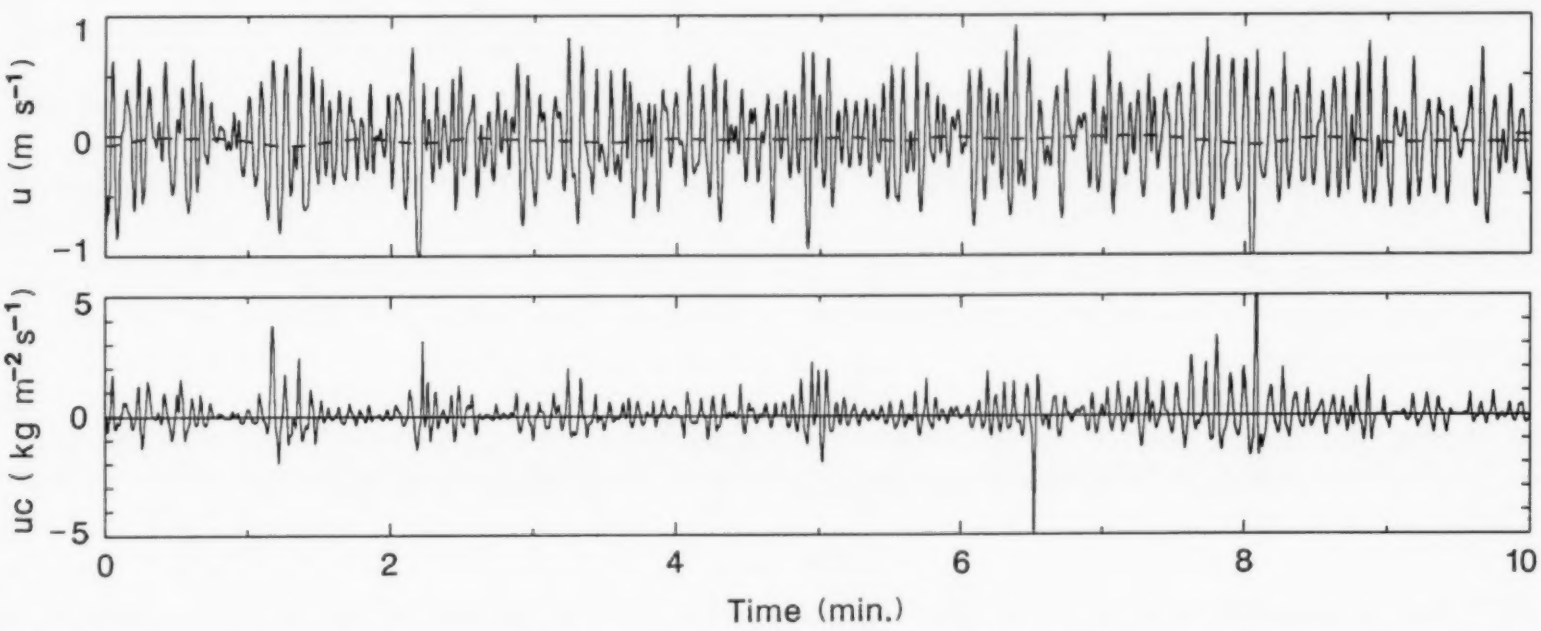

Fig. 6. Time-series of cross-shore velocity (u; $z \approx 0.20$ m) and suspended sediment transport (uc) from the 70 m station during storm-wave growth (1354 h; $H_s/h = 0.2$); concentrations from $z \approx 0.08$ m). Note: instantaneous velocity denoted by a solid line and low-pass filtered series by a dashed line; bandwidth for the low pass filter was 0.1 Hz and the filter bandwidth (−3 db) was 0.025 Hz.

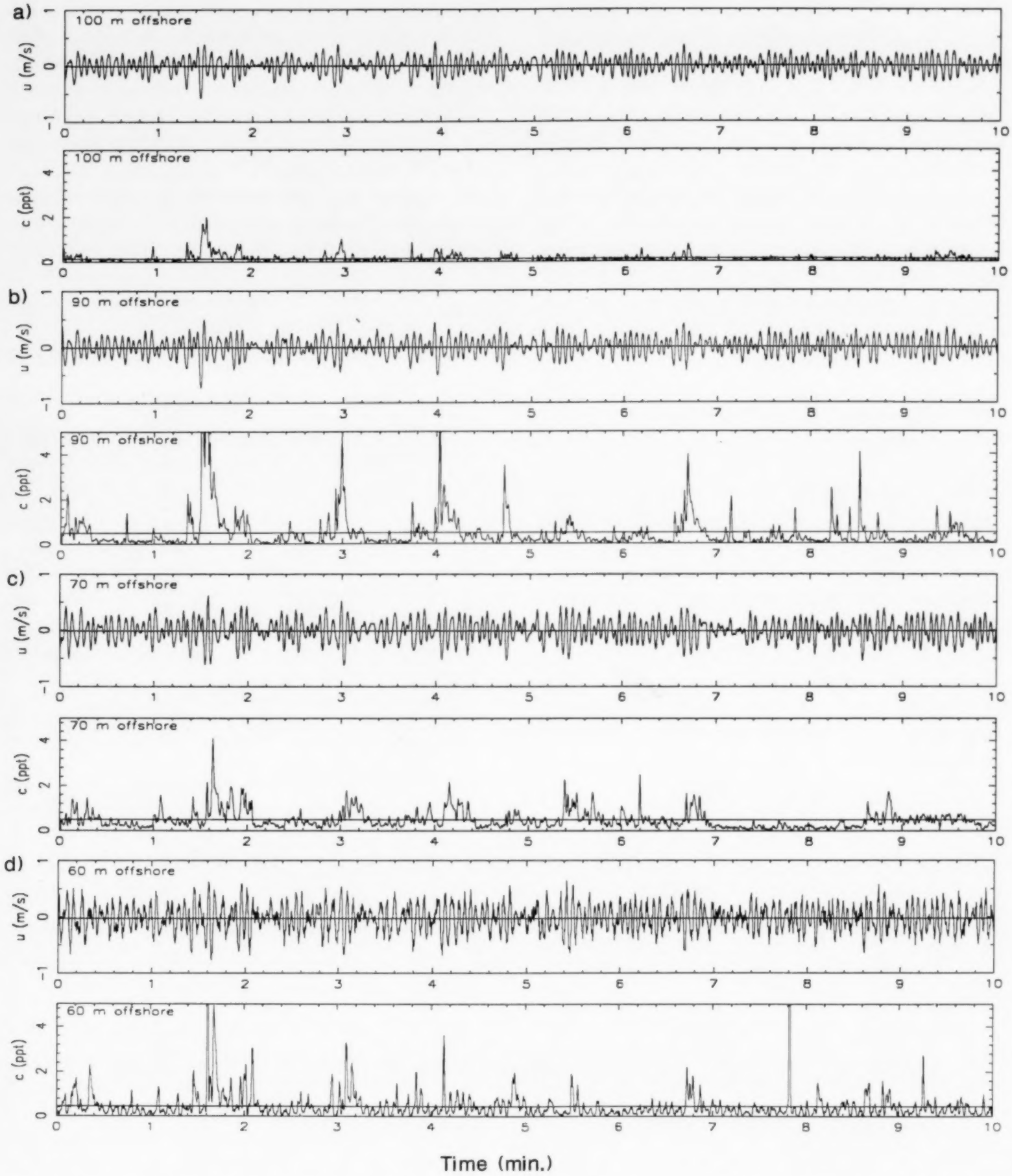

Fig. 7. Time series of cross-shore velocity (u; $z \approx 0.20$ m) and suspended sediment concentration (c; $z \approx 0.08$ m) from Queensland Beach (87:10:25:11:24): (a) 100 m station, $H_s/h = 0.07$; (b) 90 m station, $H_s/h = 0.08$; (c) 70 m station, $H_s/h = 0.09$; (d) 60 m station, $H_s/h = 0.14$.

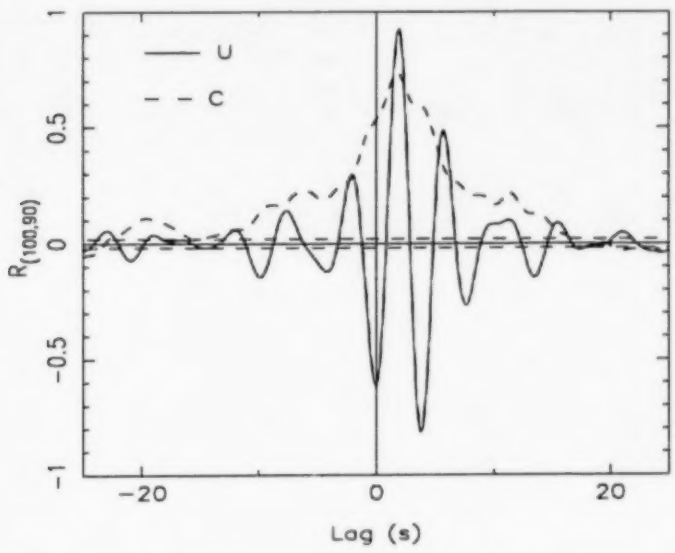

Fig. 8. Cross-correlations between cross-shore velocities (u; $z \approx 0.20$ m) and between suspended sediment concentrations (c; $z \approx 0.08$ m) measured at the 100 m and 90 m stations, respectively, Queensland Beach (87:10:25:11:24). Note: horizontal dashed lines denote 95% confidence intervals.

with the maximum positive correlations compare well with the time lag for wave groups travelling between stations computed using depth-dependent phase velocities based upon shallow water linear wave theory (Table 2).

In general, sediment concentrations tend to increase shoreward, as expected with increasing wave height-to-water depth ratios. The concentrations recorded at 90 m, however, appear somewhat larger than might be expected by the trend. This can be attributed, at least in part, to the increased sensitivity of the sensors deployed at this location to rapid fluctuations in concentration as noted earlier; however, it is not possible to totally eliminate the possibility of shifts in the relative vertical positions of adjacent sensor arrays as a result of local erosion and/or accretion.

The effects of wave shoaling are evident in the increasingly peaked crests and flattened troughs (resulting from wave skewness) and the increasing saw-toothed shape (resulting from wave asymmetry) revealed in the sequence of velocity time-series from the 100 m station to the 60 m station (Fig. 7). These effects are also reflected in the dramatic increase in net onshore transport; compare the co-spectrum from the 60 m station relative to those at the 70, 90 and 100 m stations (Fig. 9). The onshore sediment transport rate at 60 m, for example, is of the order of twice that at 70 and 90 m. Examination of the spatial variability in the cross-shore velocity spectra (Fig. 9) indicates that the relative distribution of energy across frequency space does not change a great deal up to the point of wave breaking on this non-barred beach. There is, however, an overall increase in energy density towards shore as expected, and a slight shift of wind-wave energy towards both higher and lower frequencies. In general, the spatial pattern of sediment flux reflects increasing wave transformation landward, resulting in a shoreward increase in onshore transport at wind-wave frequencies.

Suspended sediment transport by time-averaged cross-shore currents

Visual observations indicated that rip currents (spaced approximately 20 m apart) were present in the inner surf zone by 1230 h on October 25, and these persisted throughout the storm peak. Large rips were clearly visible during a falling tide between 1400 and 1500 h, while somewhat smaller rip currents developed during the next low tide (0200–0600 h on October 26). However, it is unlikely that the rip currents extended any significant distance seaward of the fully saturated surf zone, which was in general restricted to within 45 m of the shoreline at all times. Nevertheless, time-averaged, mean cross-shore currents of relatively large magnitude were recorded well outside this zone (Fig. 10) and therefore could not be attributable to a rip current origin. These time-averaged currents measured close to the bed (0.20 m elevation) at the 45, 70, 90 and 100 m stations were all directed offshore throughout the storm, reaching a maximum of 0.20 m s^{-1} at the shallowest station. In general, these currents decreased in magnitude offshore and were less than 0.10 m s^{-1} seaward of 60 m, except during the storm peak, when speeds reached 0.12 m s^{-1} at both 70 m and 90 m. The largest offshore mean current speeds coincided temporally with the peak in orbital speeds (u_s) and also with the minimum water depths, the latter associated with a low tide at 1500 h, October 25. In general, the mean currents exhibited a small increase in magnitude with elevation between 0.2 and 0.5 m above the bed (Fig. 10); however, at the 45 m station, where a tri-level

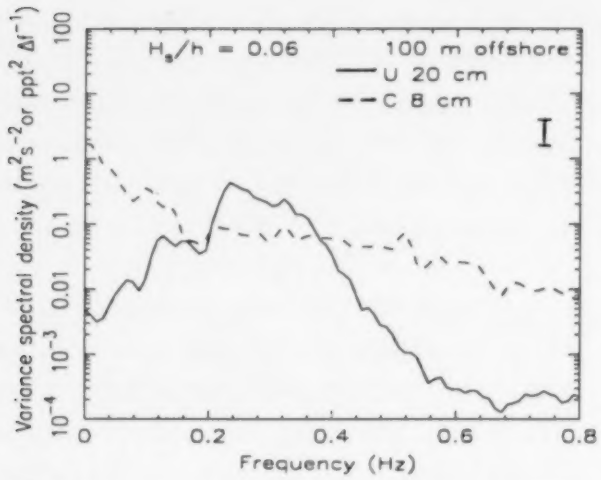
H_s/h = 0.06
100 m offshore
U 20 cm
C 8 cm
Variance spectral density (m^2s^{-2}or ppt^2 Δf^{-1})
Frequency (Hz)

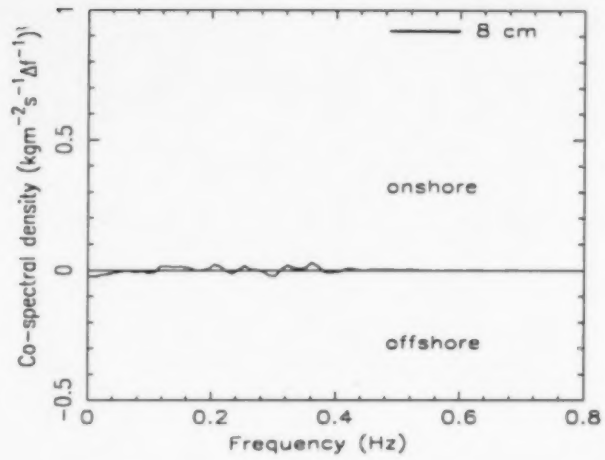
8 cm
onshore
offshore
Co-spectral density ($kgm^{-2}s^{-1}\Delta f^{-1}$)
Frequency (Hz)

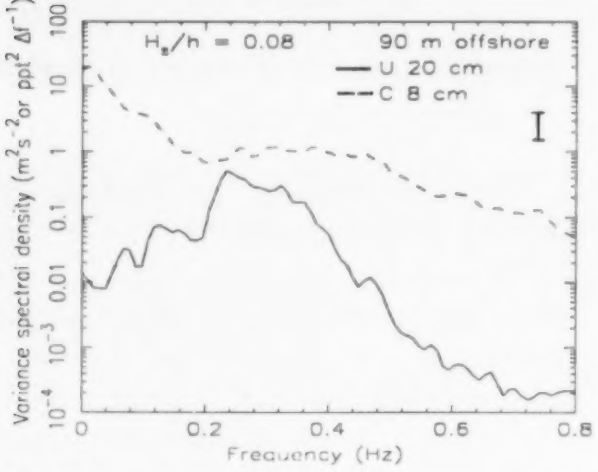
H_s/h = 0.08
90 m offshore
U 20 cm
C 8 cm
Variance spectral density (m^2s^{-2}or ppt^2 Δf^{-1})
Frequency (Hz)

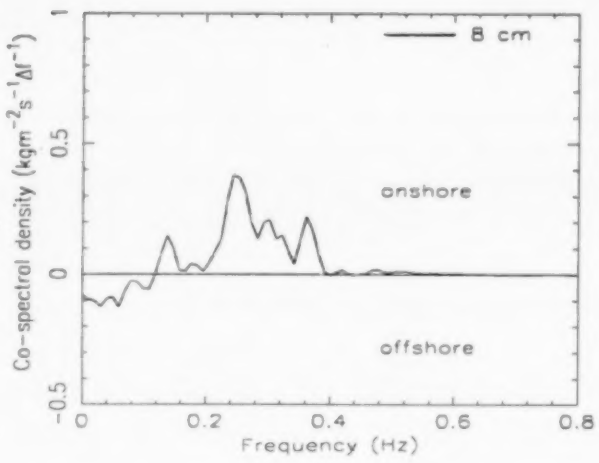
8 cm
onshore
offshore
Co-spectral density ($kgm^{-2}s^{-1}\Delta f^{-1}$)
Frequency (Hz)

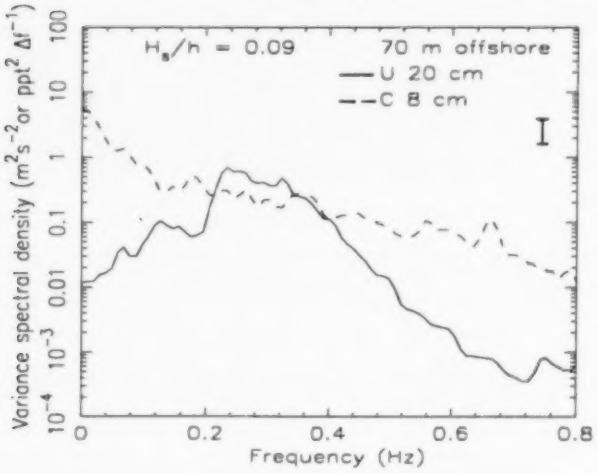
H_s/h = 0.09
70 m offshore
U 20 cm
C 8 cm
Variance spectral density (m^2s^{-2}or ppt^2 Δf^{-1})
Frequency (Hz)

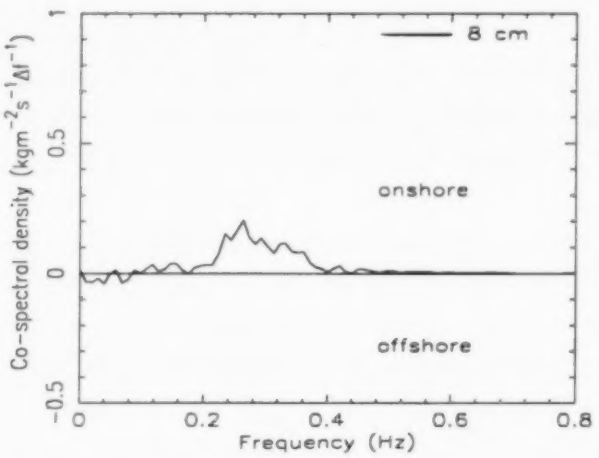
8 cm
onshore
offshore
Co-spectral density ($kgm^{-2}s^{-1}\Delta f^{-1}$)
Frequency (Hz)

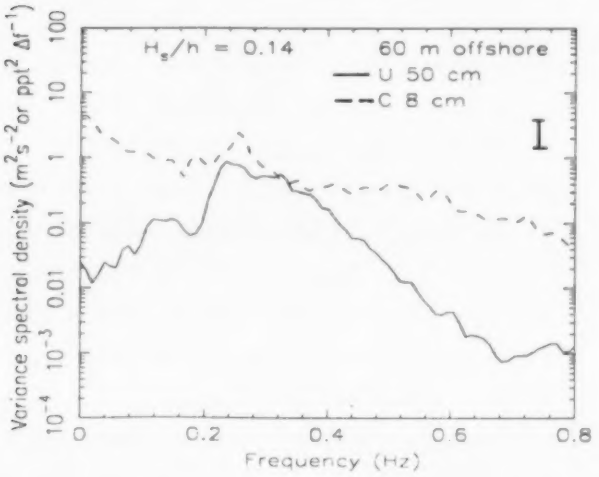
H_s/h = 0.14
60 m offshore
U 50 cm
C 8 cm
Variance spectral density (m^2s^{-2}or ppt^2 Δf^{-1})
Frequency (Hz)

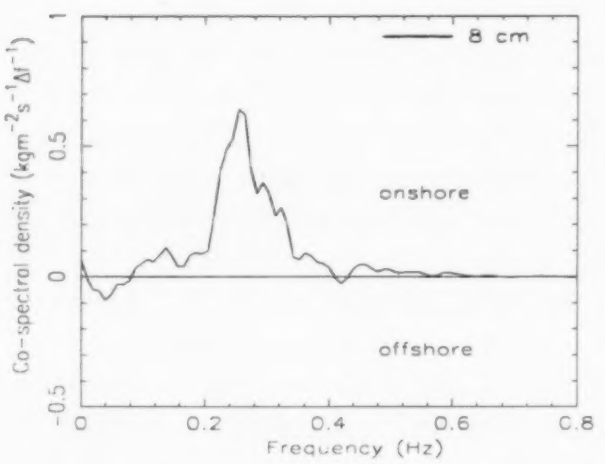
8 cm
onshore
offshore
Co-spectral density ($kgm^{-2}s^{-1}\Delta f^{-1}$)
Frequency (Hz)

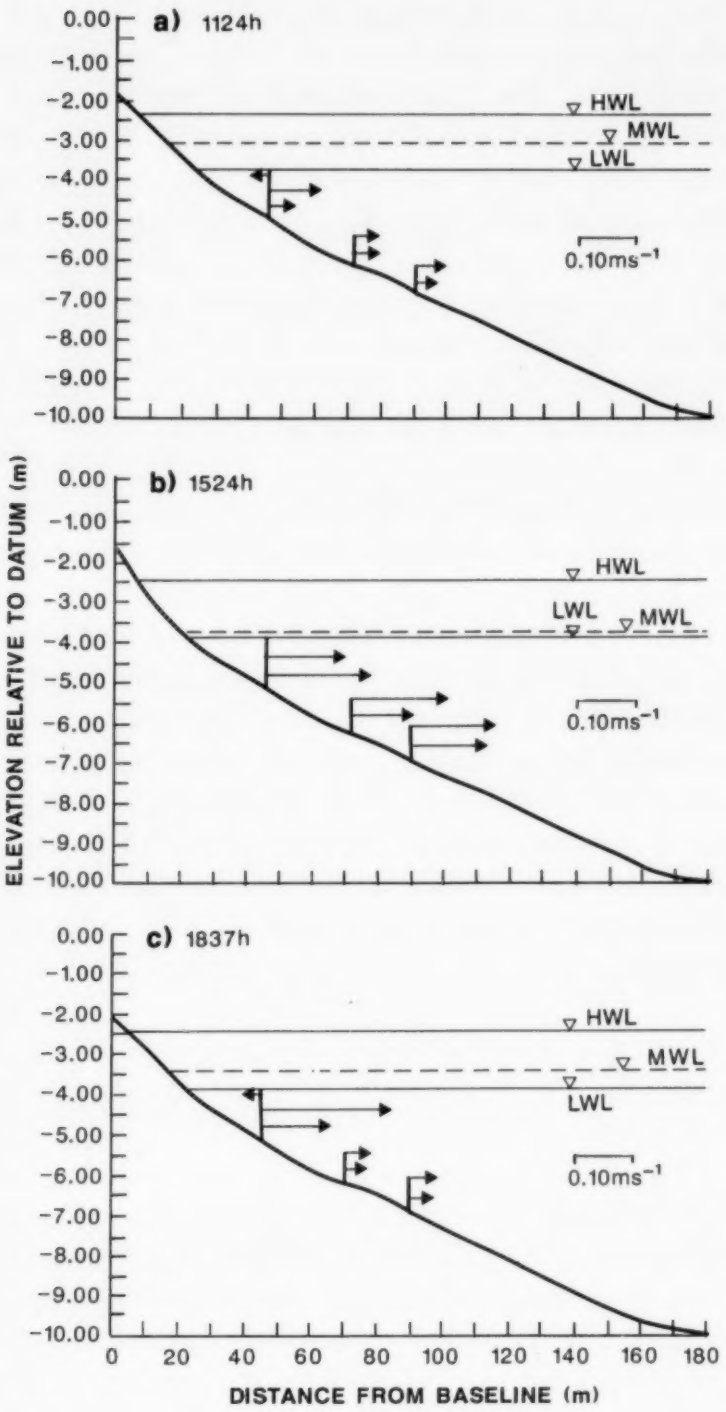

Fig. 10. Temporal and spatial variability in the vertical structure of the time-averaged (mean) cross-shore currents throughout the storm peak at Queensland Beach: (a) 1124 h; (b) 1524 h; (c) 1836 h. Note: arrows are scaled cross-shore current vectors.

array of current meters was deployed, the upper sensor (0.8 m elevation) exhibited onshore mean flows, while mean flows measured by the lower sensors (at 0.5 m and 0.2 m elevation) were directed offshore throughout the storm (Fig. 10a,c). This vertical stratification at 45 m reflects the landward translation of water in the upper water column due to the presence of breaking waves and an offshore current closer to the bed required to balance the shoreward mass and momentum flux at the surface. This mean flow structure is typical of a pressure gradient driven "undertow" resulting from a mean water level set-up in the inner surf zone (e.g. Greenwood and Osborne, 1990a; Osborne and Greenwood, 1991); the details of the set-up driven flow at Queensland Beach are not presented in this paper.

Vertical variations in the magnitude of the time-averaged sediment concentrations are illustrated in Fig. 11, which documents conditions during the storm growth, as both the near-bed orbital velocity and wave height-to-water depth ratios gradually increased. The vertical distribution of the time-averaged sediment concentration follows a non-linear decay with elevation; although only three data points are available, such a pattern supports the large number of earlier laboratory and field observations of an exponential decay function for time-averaged sediment suspensions under waves (e.g. Kennedy and Locher, 1972; Nielsen et al., 1982; Jaffe et al., 1985; Skafel and Krishnappan, 1984; Sternberg et al., 1984, and others). Furthermore, the mean concentrations increased consistently during the storm-wave growth coincident with increases in both the oscillatory and mean currents. Thus the mean suspended sediment transport rate also increased over time up to the storm peak; however, this transport was constrained by local patterns of the vertical distribution of both the mean current and the mean suspended sediment concentration.

Cross-shore orbital speeds near the bed were largest at a water depth of approximately 2.75 m and decreased monotonically with increasing depth throughout the storm peak (Fig. 12). In shallower water (0.5 to 2 m), the orbital speeds were 50 to 75% lower than the maximum, but also exhibited a similar depth dependence. The time-averaged

Fig. 9. Spatial variability of cross-shore velocity (u; $z \approx 0.20$ m) and sediment concentration (c; $z \approx 0.08$ m) spectra and associated co-spectra at Queensland Beach during storm-wave growth (87:10:25:11:24). Note: station locations and wave height-to-water depth ratios (H_s/h) for each are given.

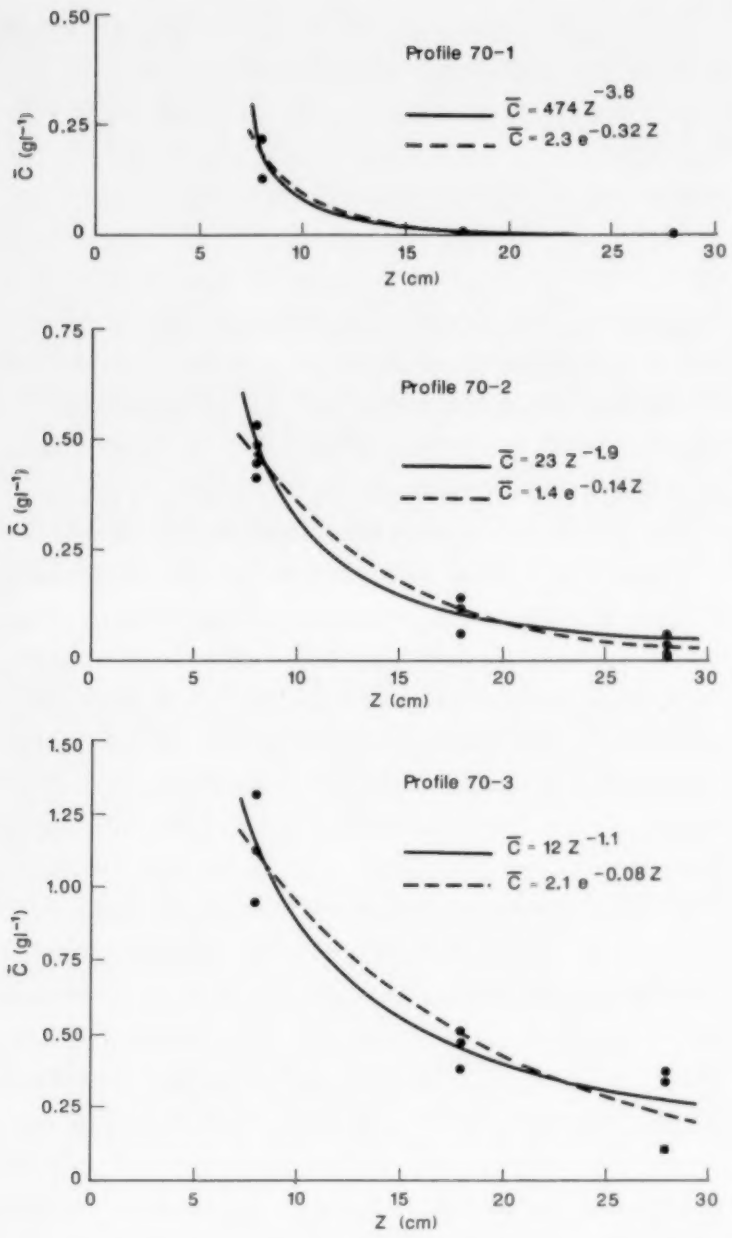

Fig. 11. Vertical profiles of the time-averaged (mean) sediment concentration ($\bar{c}$) determined for the 70 m station during distinct phases of storm-wave growth, Queensland Beach (87:10:25): Profile 70-1 from samples taken at 0906 h and 1006 h; Profile 70-2 from samples taken at 1036 h, 1124 h, 1224 h and 1254 h; Profile 70-3 from samples taken at 1324 h, 1354 h and 1424 h. Average near-bed orbital speeds (u_s) were 0.15, 0.23 and 0.36 m s^{-1}, respectively. Note: least squares exponential and power functions are shown.

mean cross-shore current varied with depth in a similar manner to the orbital speed, with distinct subpopulations in both deeper (> 2.75 m of water) and shallower (< 2.00 m of water); however, in this case the largest mean currents occurred in the shallower water (< 2 m of water). These patterns indicate that both orbital and mean currents are constrained by the spatial pattern of wave shoaling, breaking and reformation across the shoreface, and further imply that most wave breaking took place in water depths between 2 and 2.75 m during this storm. The time-averaged sediment concentration ($<c>$) and the mean sediment transport rate, ($\bar{u}\bar{c}$), also decreased with increasing depth in the wave shoaling region (2.75 to 5.25 m). This is only to be expected if the orbital speeds, which control sediment re-suspension to a large degree, also decrease with depth.

Net suspended sediment transport rates

It is evident from the foregoing analyses, that as incident wave energy increased and decreased so did the magnitudes of the sediment transport contributions attributable to the various frequency components in the energy spectrum, including the mean currents. However, of importance to the sediment mass balance on the shoreface is the relative contribution of these transport components to the local net suspended sediment transport rate; of special significance is the spatial and temporal variation of these discrete transport components.

Vertical structure of sediment transport in time and space

Figure 13 provides a succinct summary of the contributions to the total net suspended sediment transport rate of each of the transport components over both space and time. Conditions of both non-breaking and breaking waves are illustrated. The mean and oscillatory sediment transport rates are plotted, together with the total net sediment transport rates computed using both the instantaneous cross-products and the sum of the mean and net oscillatory components.

Transport profiles under non-breaking waves showed invariably that only a small amount of net sediment transport was occurring, restricted to elevations close to the bed and directed consistently onshore. In Fig. 13a note the near-zero net sediment transport throughout the lower water column at the 100 m and 90 m stations, with significant net transport beginning at the 70 m station and restricted here to within 0.08 m of the bed. This indicates that an onshore transport at

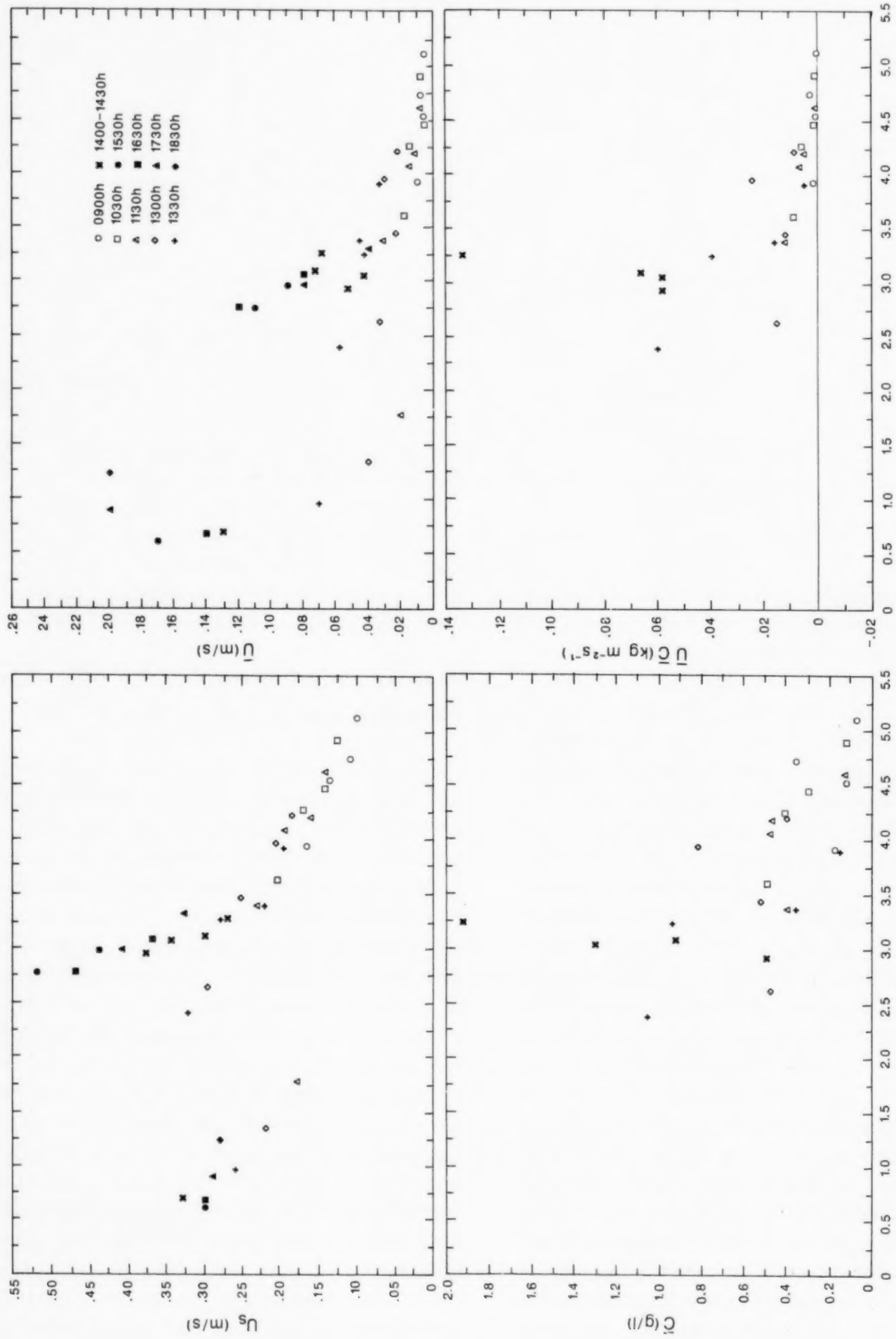

Fig. 12. Depth-dependent patterns of cross-shore orbital speed (u_s; $z \approx 0.20$ m), cross-shore mean current speed ($\bar{u}$; $z \approx 0.20$ m), time-averaged suspended sediment concentration ($\bar{c}$; $z \approx 0.08$ m), and mean suspended sediment transport rate ($\bar{u}\bar{c}$), Queensland Beach (87:10:25).

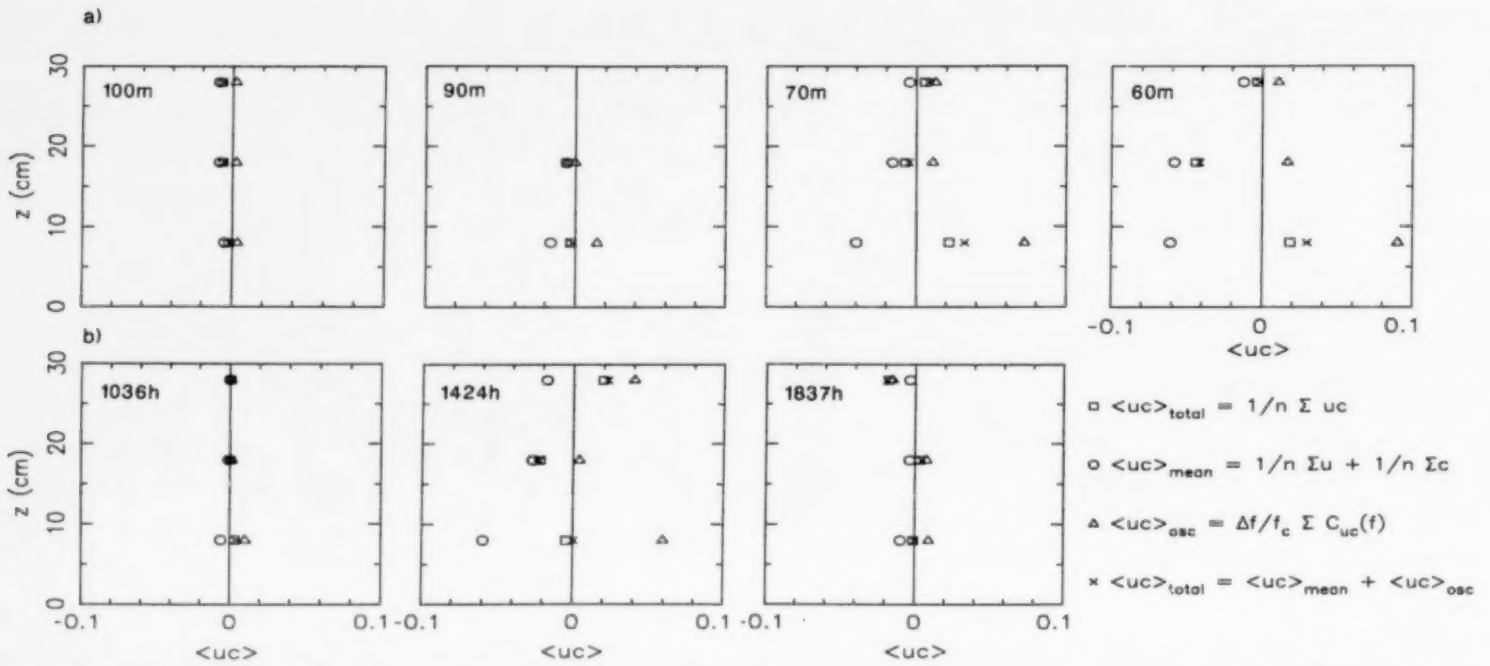

Fig. 13. Vertical structure of the time-averaged suspended sediment transport components, Queensland Beach (87:10:25): (a) spatial variability at 1324 h; (b) temporal variability at the 70 m station through the growth, peak and decay of the storm.

wind-wave frequencies, as observed in the co-spectra, dominates the net suspension transport under these conditions. Transport profiles associated with waves which were breaking occasionally by spilling, show that, while the net oscillatory sediment transport was generally directed onshore, the mean sediment transport was directed offshore at all elevations (Fig. 13a, 60 m station; Fig. 13b, 1424 h). The opposing and near-equal mean and oscillatory transports often result in an approximate balance in the local net sediment transport; the vertical structure at 70 m, for example (Fig. 13a), was characterized by onshore, wave-induced transport at 0.08 and 0.28 m, while at mid-depth (0.18 m) the offshore transport due to mean currents dominates. In contrast, at the 90 m station, the net oscillatory transport at 0.08 m was significantly smaller than at 70 m; this combined with the effects of an offshore mean current, produced an offshore net transport. At the 0.18 m elevation, both the oscillatory and the mean transports are offshore at the 90 m station, resulting also in an offshore net sediment transport. These observations indicate that the total net transport at any elevation depends critically upon the relative magnitudes of both the net oscillatory and mean sediment transport components at that elevation; a balanced transport can therefore be achieved even when individual components are large.

Temporal variability in the net suspended sediment transport

During the early part of the storm, the net sediment transport was directed offshore at 0.18 m above the bed at all locations (Fig. 13a), and appeared to increase in magnitude as the storm progressed (Fig. 13b). This offshore transport was largest at the 90 m station as a result of the strong mean currents occurring at this location coupled with the relatively weak net oscillatory transport in the deeper water. In contrast, the total net sediment transport at 0.08 m was directed onshore throughout the early part of the storm at the 60 m station. In deeper water, where the oscillatory currents were weaker, the onshore and offshore components of transport were nearly in balance; once the mean sediment transport became large enough to offset the net oscillatory transport, then the offshore transport of sediment became dominant.

Unfortunately, during the period of time when wave breaking was most intense and when time-averaged cross-shore currents were at a maximum

(1500–1600 h), the 60 m sediment transport station ceased to function, and the sediment concentration measurements at other locations were contaminated by seaweed. Following the peak of the storm (1837–2355 h), the net oscillatory and mean sediment transports returned to near zero at the 70 m and 90 m stations, even though orbital velocities remained high ($u_s = 0.2$–0.5 m s^{-1}) and sediment concentrations were still large (upto 10 g l^{-1}) during individual wave cycles. This somewhat truncated time-series nevertheless suggests that the greatest potential for onshore suspended sediment transport is restricted to within 0.10 m of the bed; furthermore it is largest just seaward of wave breaking, where the net oscillatory transport is largest and directed onshore as a result of the large skewness and asymmetry in the shoaling waves (cf. Doering, 1988). On the other hand, a net offshore sediment transport dominates at those locations where the time-averaged mean currents are relatively large and where the net oscillatory transport is relatively small; at Queensland Beach this occurred between 70 and 90 m offshore, where wind wave oscillations were large, but still near-symmetrical, and where the mean currents were still relatively large.

Sediment re-activation, volume flux and erosion–accretion patterns

Waves and currents during the storm event of October 25/26, 1987, caused substantial sediment re-activation at least to the seaward limit of the experimental array at Queensland Beach. The maximum depth-of-activity recorded was 0.25 m at the 60 m station (Fig. 14); however, re-activation in the surf zone was so large that all depth-of-activity rods were lost landward of 50 m. Indeed, the sediment transport station at 60 m collapsed during the storm at least in part due to entrainment of sediment. The depth-of-activity appears to have decreased monotonically with distance offshore from approximately 0.20 m near the 70 m station to less than 0.02 m at a distance of 170 m offshore (Fig. 14). Such a strong correlation with offshore distance is to be expected as water depth changes, and has been measured previously across a shoaling slope by Greenwood and Mittler (1984, fig. 8, p. 92).

The time-integrated patterns of erosion and accretion for this event were somewhat more complex than the pattern of depth-of-activity. In general, seaward of the 60 m station (primarily a zone of wave shoaling during this storm) the shoreface was subjected to small amounts of erosion, with not more than 0.10 m of sediment being removed from the pre-storm surface. Bed elevation change landward of 60 m, in contrast, was more substantial. Upto 0.20 m of accretion occurred in the inner part of the surf zone at its maximum extent (between 15 and 50 m offshore) and upto 0.30 m of erosion occurred on the upper foreshore (between the baseline and 15 m offshore). Beach observations during the storm confirmed this pattern: a 5 m wide band of cobbles became progressively exposed by erosion of the upper foreshore at high tide during both the early part of the storm (0900–1100 h) and following the storm peak (2000–2100 h). Furthermore, current meters deployed initially at a nominal elevation of 0.20 m at the 20 and 30 m stations were almost completely buried by sediment when the lower foreshore was exposed during low tide (1500–0200 h on Oct. 26); also the current meter at the 45 m station was approximately 0.10 m closer to the bed following the storm than it was prior to the event, confirming that this amount of accretion had occurred in the area.

The time-integrated net volume flux of sediment (INVF), computed for a unit width of beach between 0 and 170 m offshore using both survey and depth-of-activity data, indicates only a small net gain of sediment of approximately 8 m^3. A net gain of approximately 56 m^3 of sediment in the inner part of the surf zone was almost completely balanced by net sediment losses of approximately 12 m^3 from the upper foreshore and approximately 36 m^3 from the shoaling zone. It is clear that sediment from the upper foreshore was transported downslope and deposited in the inner part of the surf zone; it would appear also that sediment eroded from the shoaling wave zone was transported landward and also deposited in the surf zone (in this case the outer part).

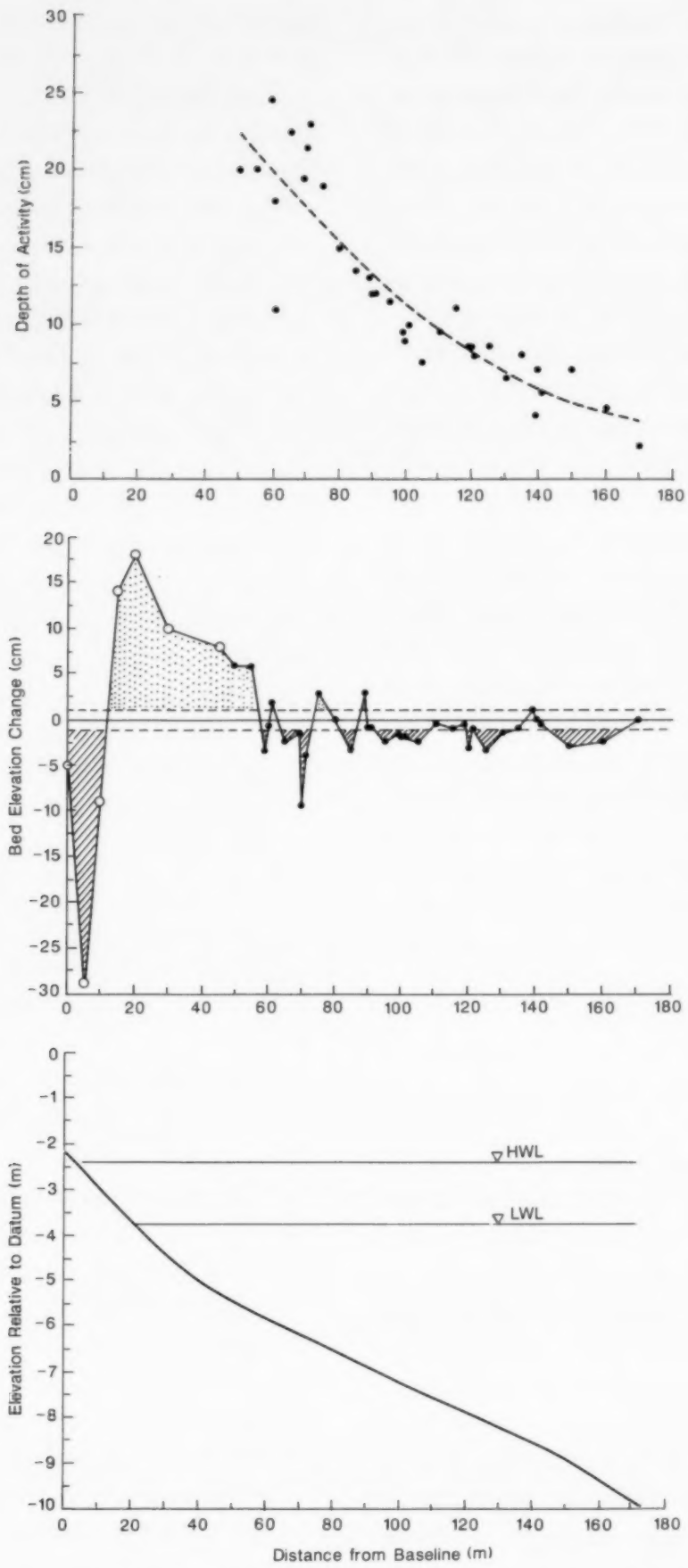

Fig. 14. Variation in elevation, bed-elevation change and depth-of-activity across the shoreface. Note: stippling represents accretion and cross-hatching represents erosion; the horizontal dashed lines on the bed elevation change graph represent the estimated measurement error band of ± 1 cm. Solid circles are rod measurements, open circles are survey measurements; the dashed line through the depth-of-activity data is the best fit (second order) curve.

Discussion

The measurements and analyses documented above provide new insights into both the spatial and temporal patterns of suspended sediment transport under wave-induced currents across a non-barred shoreface during a storm event. In particular, the critical importance of both oscillatory currents of various frequencies and the time-averaged cross-shore currents to the net suspended sediment transport has been demonstrated.

Co-spectral analyses of the near-bed, cross-shore velocity and suspended sediment concentration vectors reveal that shoaling waves produce a relatively strong onshore transport at wind-wave frequencies, which contrasts with a weaker offshore transport of sediment at frequencies lower than those of the wind-wave band. A similar pattern was suggested previously by Huntley and Hanes (1987) from a more restricted dataset. It is now clear that the sedimentary response to wave forcing depends critically upon not only the instantaneous velocity associated with the large amplitude, short period wind waves, but also upon any low frequency modulation associated with wave groups. Larger onshore oscillatory currents associated with the passage of skewed, asymmetric incident waves, lead not only to the mobilization and suspension of sediment, but also to a net onshore transport (Doering and Bowen, 1989; Greenwood et al., 1990, 1991 a,b; Osborne et al., 1990). The smaller offshore net transport associated with low frequency oscillations is due to a "flux coupling" between the offshore flow associated with the bound long wave, forced by the "groupiness" in the incident waves (Longuet-Higgins and Stewart, 1962; Wells, 1967) and the large sediment concentrations associated with re-suspension by the larger waves constituting the wave group. Doering and Bowen (1989) suggested that a large onshore transport observed at wind-wave frequencies reflects the greater ability of the onshore currents to entrain sediment than the weaker offshore currents; they further implied that most of the sediment entrained in each half-wave cycle fell out of suspension before the flow reversed. Measurements from this study, however, suggest that the latter implication is not a requirement for the co-spectral structure observed, since the minimum time required for sediment to settle from 0.08 m, for example, is on average greater than or equal to, half a wave period (assuming a still water settling velocity of approximately 2 cm s^{-1} for a median grain size of 0.18 mm and wave periods of 3–4 s).

Examination of vertical profiles of the components contributing to the net suspended sediment transport rates indicates that it is the "relative magnitudes" of the mean and oscillatory sediment transport, which play a critical role in the local sediment transport balance. Furthermore, suspended sediment flux shows a clear vertical stratification. The net oscillatory sediment transport is most often onshore under wave shoaling and may dominate the total net transport both near the bed and also higher in the water column; in contrast, the mean sediment transport is most frequently offshore and may dominate the sediment flux at mid-depth.

As might have been expected, the greatest potential for net suspended sediment transport coincides with the time of maximum kinetic energy input (i.e. the storm peak), when waves are breaking or near breaking over large sections of the upper shoreface. The data from this non-barred environment indicate that the largest net onshore transport occurs just seaward of the point of wave breaking, where the net oscillatory transport is largest and directed onshore under strongly skewed, asymmetric shoaling waves. On the other hand, net offshore sediment transport occurs in zones of relatively strong mean currents and relatively weak oscillatory currents; these occur both seaward and landward of the initial breaker line.

It is also evident from this study that while substantial amounts of sediment re-activation may occur, changes to the nearshore morphology may be relatively minor (see also Greenwood, 1987). The observed erosion/accretion patterns suggest that the strong rip currents observed in the inner part of the surf zone (within 45 m of the shoreline) may have been responsible for the offshore transport of material eroded from the beach face. Sediment from the upper beach face appears to have been moved downslope and deposited between 15 and 60 m offshore. A relatively strong onshore transport driven by shoaling waves during

the early and late parts of the storm (as observed at 60 m in the early part of the storm) may have balanced the seaward transports from the inner surf zone, resulting in the observed accretion in the surf zone; however, accretion in this zone did not result in the development of a barred profile.

The relative importance of mean and net oscillatory sediment transport to the total net sediment transport in the shoaling zone are uncertain for the storm peak. It is possible that the net oscillatory sediment transport increased as the water depth decreased with the falling tide and as the extent of the surf zone increased. Since no substantial net change in the bed elevation occurred in this area, even though the depth-of-activity was in excess of 0.10 m, it seems possible that sediment may have been carried seaward from this area by the dominant mean currents in the early part of the storm, and later returned by onshore oscillatory transports during the storm peak. It is thus important to note that a local sediment balance over a storm event may also be achieved by temporal changes in local sediment transport rates and directions, as well as spatial changes.

Conclusions

Field measurements reveal that important contributors to the cross-shore transport of suspended sediment under combined waves and currents across a non-barred shoreface are:

(1) "quasi-steady" mean currents, with characteristics typical of a set-up driven undertow;

(2) oscillatory currents at wind-wave frequencies;

(3) oscillatory currents at low frequencies outside the wind-wave band and forced by group bound long waves.

The net sediment transport rate controlling both the local sediment balance and the morphological response is a reflection of the relative magnitudes and directions of transport attributable to these components. A balanced transport state can therefore be achieved even when the individual components are large.

The sediment transport attributable to mean currents is frequently balanced by that attributable to net oscillatory currents. The net oscillatory sediment transport rate is most frequently dominated by the wind-wave component (at least outside the surf zone) and is coincident with the direction of wave propagation; in contrast, the mean sediment transport rate is predominantly downwave or offshore driven frequently by undertows.

A distinct vertical structure in the "total" net sediment transport rate is identifiable in the near-bed water column in the region of shoaling waves; this results from a time-dependency between horizontal velocity (stress) and sediment concentration which varies with elevation. A net onshore sediment transport (attributable to oscillatory currents) occurs both near the bed and higher in the water column, while a net offshore sediment transport (attributable to mean currents) dominates the middle portion of the lower water column. Thus a transport balance can be achieved through vertical integration of the transport rates throughout the lower water column. However, measurements with greater spatial resolution (of both velocity and concentration) are required to confirm these patterns.

The notion of a balanced sediment flux across the full shoreface, resulting from interactions between the discrete components of suspended sediment transport, is supported not only by the local net sediment transport rates but also by the spatial variability in suspended sediment transport and by measured erosion and accretion patterns. The net onshore sediment transport at wind-wave frequencies was greatest just seaward of wave breaking and decreased offshore. A net offshore sediment transport occurred in areas of relatively strong mean currents and relatively weak oscillatory currents, i.e. both in the seaward part of the shoaling wave zone and landward of the point of initial wave breaking.

These conclusions suggest that sediment transport predictors based on the simple cross-products of time-averaged mean flows and mean concentrations (e.g. Dally and Dean, 1984; Deigaard et al., 1986) cannot be successful, at least not for the suspended load. Furthermore, even the best physically-based models for sediment transport (e.g. Bowen, 1980a; Bailard, 1981; Roelvink and Stive, 1989) which include contributions to the velocity field from both wave and current induced flows,

still assume time and depth-integrated terms and therefore, will not be able to achieve more than a qualitative agreement with observed sediment behaviour. The spatial (horizontal and vertical) and temporal variations in suspended sediment transport identified by this research suggest that important fluid–sediment interactions occur close to the boundary which are critical to determining net sediment transport rates. Therefore, accurate field measurements of both the velocity and sediment concentration near the bed (within the wave–current boundary layer) are required to understand the flux of sediment in the near bed region.

Acknowledgements

This is a contribution from the Canadian Coastal Sediment Transport Programme (C-COAST) supported by Strategic Grants from the Natural Sciences and Engineering Research Council of Canada awarded to B. Greenwood and A.J. Bowen. P.D. Osborne acknowledges support in the form of a post-graduate scholarship from the same body. We would like to thank R. Brander, J. Ollerhead, N. Sela, Xu Zhiming and A. Hincenbergs, from the University of Toronto, and D. Hazen, S. McLean, R. Tatavarti, and K. Lewis from Dalhousie University for their assistance in data collection and processing; Dr. David Huntley is to be thanked for fruitful discussion. The support of the Academic Workshops and Graphics Department at the Scarborough Campus of the University of Toronto is also gratefully acknowledged.

References

Bagnold, R.A., 1963. Mechanics of marine sedimentation. In: M.N. Hill (Editor), The Sea. Wiley–Interscience, New York, 3, p. 507–528.

Bagnold, R.A., 1966. An approach to the sediment transport problem from general physics. U.S. Geol. Surv. Prof. Pap., 422-1, 37 pp.

Bailard, J.A., 1981. An energetics total load sediment transport model for a plane sloping beach. J. Geophys. Res., 86: 10938– 10954.

Beach, R.A. and Sternberg, R.W., 1988. Suspended sediment transport in the surf zone: response to infragravity motion. Mar. Geol., 80: 61–79.

Bowen, A.J., 1980a. Simple models of nearshore sedimentation: beach profiles and longshore bars. In: S.B. McCann (Editor), The Coastline of Canada. Geol. Surv. Can. Pap., 80-10: 1–11.

Bowen, A.J., 1980b. Nearshore velocity measurements and beach equilibrium. Proc. Can. Coastal Conf. (Burlington, Ont.). Assoc. Comm. Res. Shoreline Erosion and Sedimentation, Natl. Res. Counc. Can., Ottawa, pp. 21–46.

D and A Instruments and Engineering, 1988. Optical backscatterance turbidity monitor—Instrumentation Manual. 32 pp.

Dally, W.R. and Dean, R.G., 1984. Suspended sediment transport and beach profile evolution. J. Waterway Port Coastal Ocean Eng., 110: 15–33.

Deigaard, R., Fredsoe, J. and Hedegaard, I.B., 1986. Mathematical model for littoral drift. J. Waterway Port Coastal Ocean Eng., 112: 351–369.

Dixon, W.J. (Editor), 1985. BMDP Statistical Software, 1985 Printing. Univ. California Press, Berkeley, 734 pp.

Doering, J.C., 1988. Wave–wave interactions in the nearshore. Ph.D. Thesis, Dalhousie Univ., Halifax, N.S., 140 pp. (Unpubl.)

Doering, J.C. and Bowen, A.J., 1985. Skewness et al., the spatial distribution of some moments of the nearshore velocity field. Proc. Can. Coastal Conf. (St. John's, Nfdld.). Assoc. Comm. Res. Shoreline Erosion and Sedimentation, Natl. Res. Counc. Can., Ottawa, pp. 5–16.

Doering, J.C. and Bowen, A.J., 1989. Wave-induced flow and nearshore suspended sediment. Proc. 21st Coastal Eng. Conf. (Malaga, Spain). Am. Soc. Civ. Eng., New York, pp. 1452–1463.

Downing, J.P., 1983. An optical instrument for monitoring suspended particulates in ocean and laboratory. Proc. Oceans '83, (San Francisco, Calif.). IEEE and MTS, pp. 199–202.

Downing, J.P., Sternberg, R.W. and Lister, C.R.B., 1981. New instrumentation for the investigation of sediment suspension processes in the shallow marine environment. Mar. Geol., 42: 19–34.

Grant, W.D. and Madsen, O.S., 1979. Combined wave and current interaction with a rough bottom. J. Geophys. Res., 84: 1797–1808.

Greenwood, B., 1987. Sediment balance and bar morphodynamics in a multiple bar system: Georgian Bay, Canada. In: V. Gardiner (Editor), International Geomorphology 1986 Part I. Wiley, New York, pp. 1119–1143.

Greenwood, B. and Davidson-Arnott, R.G.D., 1972. Textural variation in the sub-environments of the shallow-water wave zone, Kouchibouguac Bay, New Brunswick. Can. J. Earth Sci., 9: 679–688.

Greenwood, B. and Hale, P.B., 1980. Depth of activity sediment flux and morphological change in a barred nearshore environment. In: S.B. McCann (Editor), The Coastline of Canada. Geol. Survey Can. Pap., 80-10: 89–100.

Greenwood, B. and Mittler, P.R., 1984. Sediment flux and equilibrium slopes in a barred nearshore. Mar. Geol., 60: 79–98.

Greenwood, B. and Osborne, P.D., 1988. Vertical structure in shore-parallel flows and bed roughness. Proc. Workshop on Roughness and Friction (Toronto, Ont.). Assoc. Comm. on Shorelines, Natl. Res. Counc. Canada, Ottawa, pp. 75–91.

Greenwood, B. and Osborne, P.D., 1990a. Vertical and structure in cross-shore flows: an example of undertow and set-up on a barred beach. Coastal Eng., 14: 543–580.

Greenwood, B. and Osborne, P.D., 1990b. Equilibrium slopes and cross-shore velocity asymmetries in a storm-dominated, barred nearshore system. Mar. Geol., 96: 211–235.

Greenwood, B. and Osborne, P.D., 1992. Sediment resuspension and wave groups: a time series approach. Proc. Workshop on Wave Groups. Assoc. Comm. on Shorelines, Natl. Res. Counc. Can., Ottawa, in press.

Greenwood, B. and Sherman, D.J., 1986. Hummocky cross-stratification in the surf zone: flow parameters and bedding genesis. Sedimentology, 33: 33–45.

Greenwood, B. and Sherman, D.J., 1988. Bedforms and roughness in prototype surf zones. Proc. Workshop on Roughness and Friction. Assoc. Comm. on Shorelines, Natl. Res. Counc. Can., Ottawa, pp. 45–59.

Greenwood, B., Osborne, P.D., Bowen, A.J., Hazen, D.G. and Hay, A.E., 1990. C-Coast: The Canadian Coastal Sediment Transport Programme. Proc. Can. Coastal Conf. (Kingston, Ont.). Assoc. Comm. on Shorelines, Natl. Res. Counc. Can., Ottawa, pp. 319–336.

Greenwood, B., Osborne, P.D., Bowen, A.J., Hazen, D.G. and Hay, A.E., 1991a. Nearshore sediment flux and bottom boundary dynamics. In: The Canadian Coastal Sediment Transport Programme (C-Coast). Proc. 22nd Coastal Eng. Conf. (Delft, The Netherlands). Am. Soc. Civ. Eng., New York, pp. 2227–2240.

Greenwood, B., Osborne, P.D., Bowen, A.J., Hazen, D.G. and Hay, A.E., 1991b. Measurements of suspended sediment transport in prototype shorefaces. In: The Canadian Coastal Sediment Transport Programme (C-Coast). Proc. Coastal Sediments '91. (Seattle, Wash.). Am. Soc. Civ. Eng., New York, pp. 284–289.

Guza, R.T. and Thornton, E.B., 1985. Velocity moments in nearshore. J. Waterway Port Coastal Ocean Eng., 111: 235–256.

Guza, R.T., Clifton, M.C. and Rezvani, F., 1988. Field intercomparisons of electromagnetic current meters. J. Geophys. Res., 93: 9302–9314.

Hanes, D.M. and Huntley, D.A., 1986. Continuous measurements of suspended sand concentration in a wave dominated nearshore environment. Cont. Shelf Res., 6: 585–596.

Hazen, D.G., Huntley, D.A., and Bowen, A.J., 1987. UDATS: A system for measuring nearshore processes. Proc. Oceans '87. (Halifax). IEEE, pp. 993–997.

Hazen, D.G., Doering, J.C. and Bowen, A.J., 1989. A note on a low cost pressure sensor for nearshore wave measurement. Cont. Shelf Res., 14: 85–90.

Huntley, D.A. and Hanes, D.M., 1987. Direct measurement of suspended sediment transport. Coastal Sediments '87. (New Orleans). Am. Soc. Civ. Eng., New York, pp. 723–737.

Inman, D.L. and Bowen, A.J., 1963. Flume experiments on sand transport by waves and currents. Proc. 8th Coastal Eng. Conf. Am. Soc. Civ. Eng., New York, pp. 137–150.

Jaffe, B.E., Sternberg, R.W. and Sallenger, A.H., 1985. The role of suspended sediment in shore-normal beach profile changes. Proc. 19th Coastal Eng. Conf. (Houston). Am. Soc. Civ. Eng., New York, pp. 1983–1996.

Kennedy, J.F. and Locher, F.A., 1972. Sediment suspension by water waves. In: R.E. Meyer (Editor), Waves on Beaches and Resulting Sediment Transport. Plenum, New York, pp. 249–295.

Longuet-Higgins, M.S. and Stewart, R.W., 1962. Radiation stress and mass transport in gravity waves, with application to "surf beats". J. Fluid Mech., 13: 481–504.

Nielsen, P., Svendsen, I.A. and Staub, C., 1979. Onshore–offshore sediment movement on a beach. Proc. 16th Coastal Eng. Conf. (Hamburg). Am. Soc. Civ. Eng., New York, pp. 1475–1492.

Nielsen, P., Green, M.O. and Coffey, F.C., 1982. Suspended sediment under waves. Coastal Studies Unit, Dept. of Geography, Univ. Sydney, Australia, Tech. Rep. 82/6, 157 pp.

Ollerhead, J. and Greenwood, B., 1990. Bedform geometry and dynamics in the upper shoreface, Bluewater Beach, Ontario, Canada. Proc. Can. Coastal Conf. (Kingston, Ont.). Assoc. Comm. on Shorelines, Natl. Res. Counc. Can., Ottawa, pp. 337–348.

Osborne, P.D., 1990. Suspended sediment transport on barred and non-barred beaches. Ph.D. Thesis, Univ. Toronto, 196 pp. (Unpubl.)

Osborne, P.D. and Greenwood, B., 1991. Set-up driven undertows on a barred beach. Proc. 22nd Coastal Eng. Conf. (Delft, The Netherlands). Am. Soc. Civ. Eng., New York, pp. 227–240.

Osborne, P.D. and Greenwood, B., 1992a. Sediment suspension under waves and currents: time scales and vertical structure. Sedimentology, (submitted).

Osborne, P.D. and Greenwood, B., 1992b. Sediment resuspension and wave groups: a spectral approach. Proc. Workshop on Wave Groups. Assoc. Comm. on Shorelines, Natl. Res. Counc. Can., Ottawa, in press.

Osborne, P.D., Greenwood, B. and Bowen, A.J., 1990. Cross-shore suspended sediment transport on a non-barred beach: the role of wind waves, infragravity waves and mean flows. Proc. Can. Coastal Conf. (Kingston, Ont.). Assoc. Comm. on Shorelines, Natl. Res. Counc. Can., Ottawa, pp. 349–361.

Roelvink, J.A. and Stive, M.J.F., 1989. Bar generating cross-shore flow mechanisms on a beach. J. Geophys. Res., 94: 4785–4800.

Sherman, D.J. and Greenwood, B., 1984. Boundary roughness and bedforms in the surf zone. Mar. Geol., 60: 199–218.

Simons, D.B. and Richardson, E.V., 1962. Resistance to flow in alluvial channels. Trans. Am. Soc. Civ. Eng., 127: 927–954.

Simons, D.B. and Richardson, E.V., 1966. Resistance to flow in alluvial channels. U.S. Geol. Surv. Prof. Pap., 422-J, 61 pp.

Skafel, M.G. and Krishnappan, B.G., 1984. Suspended sediment transport distribution in a wave field. J. Waterway Port Coastal and Ocean Eng. Div., Am. Soc. Civ. Eng., 110(2): 215–230.

Sleath, J.F.A., 1982. The suspension of sand by waves. J. Hydraul. Res., 20: 439–452.

Sternberg, R.W., Shi, N.C. and Downing, J.P., 1984. Field investigations of suspended sediment transport in the nearshore zone. Proc. 19th Coastal Eng. Conf. (Houston). Am. Soc. Civ. Eng., New York, pp. 1782–1798.

Wells, D.R., 1967. Beach equilibrium and second-order wave theory. J. Geophys. Res., 72: 497–504.

Marine Geology, 106 (1992) 25–51
Elsevier Science Publishers B.V., Amsterdam

Frequency dependent cross-shore suspended sediment transport. 2. A barred shoreface

Philip D. Osborne and Brian Greenwood

Scarborough College Coastal Research Group, University of Toronto, Scarborough, Ont. M1C 1A4, Canada

(Received June 14, 1991; revision accepted December 5, 1991)

ABSTRACT

Osborne, P.D. and Greenwood, B., 1992. Frequency dependent cross-shore suspended sediment transport. 2. A barred shoreface. *Mar. Geol.*, 106: 25–51.

Field measurements of the local time-varying suspended sediment flux across a barred shoreface demonstrate that sediment transport is a response to high frequency wind wave oscillatory currents, low frequency waves and mean flows. The relative importance of the various transport components varies spatially and temporally in association with variability in the incident wave energy. In contrast to the non-barred shoreface, where variations were strongly depth-dependent, sediment transport across the barred shoreface is constrained by position with respect to the bars.

On the lakeward slope of the bar, wind-wave oscillatory currents induce large rates of onshore transport near the bed; low frequency oscillatory currents (<0.05 Hz) in this region are driven by the group-forced, bound long wave and produce an offshore transport, often equal in magnitude to that induced by the wind waves. The sediment transport attributable to mean currents near the bed is always offshore, resulting in a net offshore sediment flux across the slope. On the bar crest, net sediment transport is seen to be close to zero, owing to a balance between the offshore mean transport and the onshore net oscillatory transport (resulting from interaction between both high and low frequency waves).

Landward of the bar crest and in the trough, sediment transport by wind waves decreases owing to dissipation of energy during wave breaking. In contrast, the contribution to suspended sediment transport by low frequency waves increases relatively, and furthermore this transport is now predominantly landward. This transport is probably associated with the release of the group-bound long wave as a free wave and the associated landward sediment flux approximates the offshore transport induced by the mean currents.

Local variability in the frequency dependent transport, both in terms of magnitude and direction is closely related to the bedforms present and their variation in response to increasing and decreasing wave energy. Specifically, the oscillatory transport attributable to wind-wave frequencies is predominantly onshore in the presence of steep vortex ripples, but is directed offshore as the flow regime shifts to lower amplitude post-vortex ripples.

Introduction

Recent field measurements of suspended sediment concentrations and the associated velocity fields under shoaling and breaking waves in the nearshore zone have revealed the strong frequency dependent character of the sediment transport process (Huntley and Hanes, 1987; Beach and Sternberg, 1988; Osborne et al., 1990; Greenwood et al., 1991a,b; etc.). In a previous paper, Osborne and Greenwood (1992c, this issue)—hereafter OG92—demonstrated a direct relationship between the local sediment balance constraining the morphodynamics of a non-barred (planar) shoreface and variations in the frequency-dependent, cross-shore suspended sediment transport both spatially and temporally, over a complete storm cycle. In this paper, field measurements demonstrate the relationships that exist between the local hydrodynamics, the cross-shore suspended sediment transport and the morphodynamics of a barred shoreface. Specific aims of this

Correspondence to: B. Greenwood, University of Toronto, Scarborough College Coastal Res. Gr., Department of Geography, 1265 Military Trail, Scarborough, Ont. M1C 1A4, Canada.

paper are: (1) to identify the important cross-shore suspended sediment transport mechanisms under a variety of shoreface boundary conditions (including shoaling waves, breaking waves, surf bores and various local bed slopes, bedforms, grain sizes etc.); (2) to define the relative importance of these transport mechanisms to the local net cross-shore flux of suspended sediment; (3) to relate the local net cross-shore fluxes of suspended sediment to large scale morphological changes, and hence the maintenance of a barred form; and (4) to document any similarities or differences in sediment transport between barred and non-barred environments.

Location of study

Data were collected from a lacustrine barred shoreface during experiments conducted as part of the C-COAST programme (Greenwood et al., 1990) at Bluewater Beach, Ontario, Canada (Fig. 1). The study site is essentially tideless, with water level shifts restricted in the short-term to

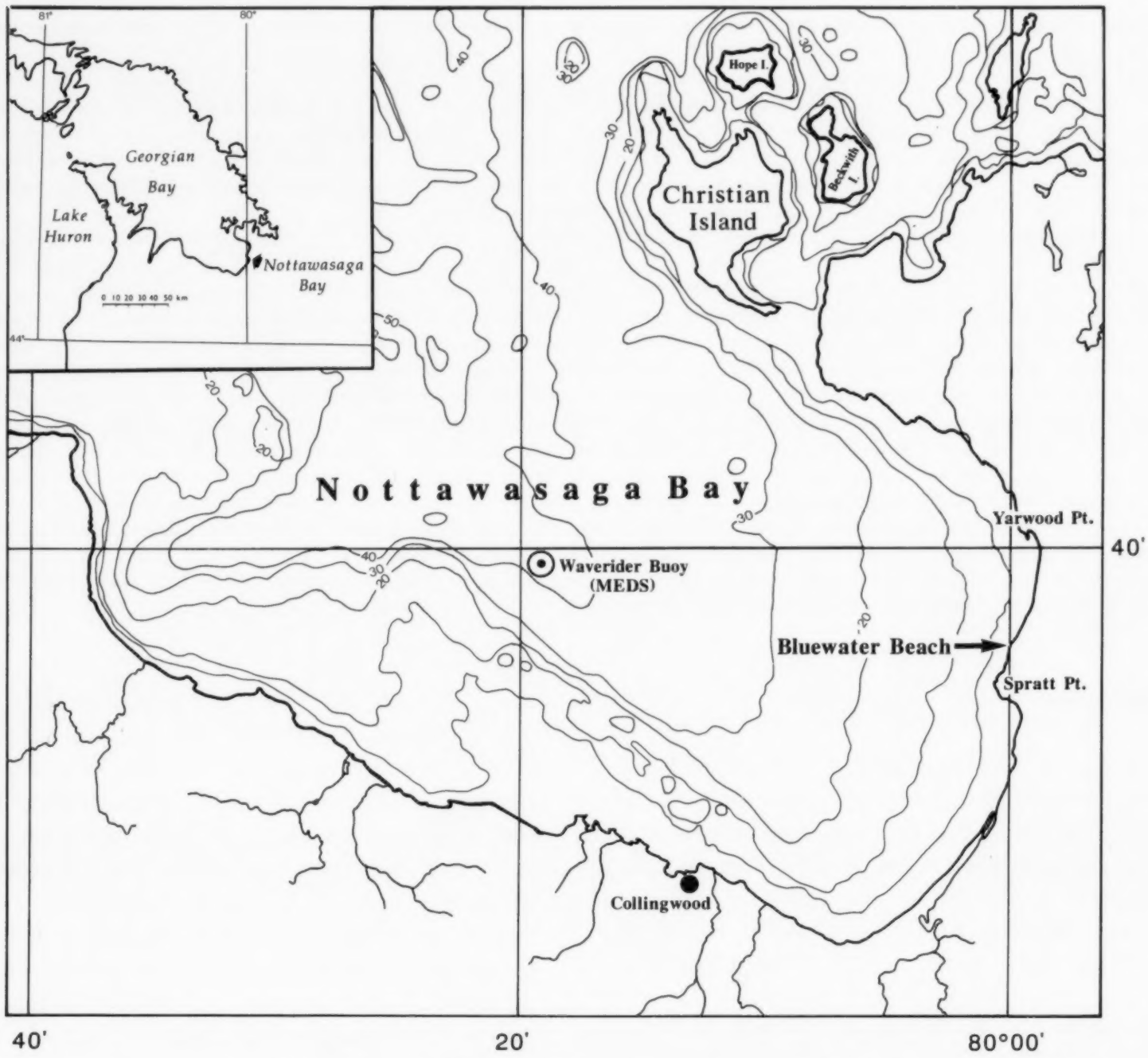

Fig. 1. Field site, Bluewater Beach, Nottawasaga Bay, Ontario, Canada. Note: contours are in fathoms; location of the MEDS Waverider Buoy is indicated.

wind and wave set-up and seiche effects; equally large seasonal and long-term changes are climatically controlled. Low-to-moderate wave energy is generated over discrete time intervals during the passage of meteorological depressions. With a restricted fetch (maximum effective fetch $\approx$84 km from the WNW), wind forcing of short period (<7–8 s) waves is continuous under most wave states and true swell is absent.

Bluewater Beach is typical of the sandy shorefaces in Nottawasaga Bay, exhibiting a well-developed bar-trough system during the ice-free year (Greenwood, 1987). In June 1988, three sinuous-to-crescentic bars were present with crests approximately 35, 63 and 150 m offshore on a mean nearshore slope $\approx$0.015 (Fig. 2) in fine-to-medium, moderately-to-very well-sorted, negatively skewed sands (Table 1). In contrast, a single, sinuous-to-crescentic bar was located approximately 70 m offshore the previous year (Fig. 2).

Instrumentation and measurements

The sensors used to measure waves, currents and suspended sediment concentrations have been described previously, as have the calibration procedures, sampling schemes and data processing techniques (OG92). It is sufficient to note that six sediment transport monitoring stations were deployed along a shore-normal transect at 25, 55,

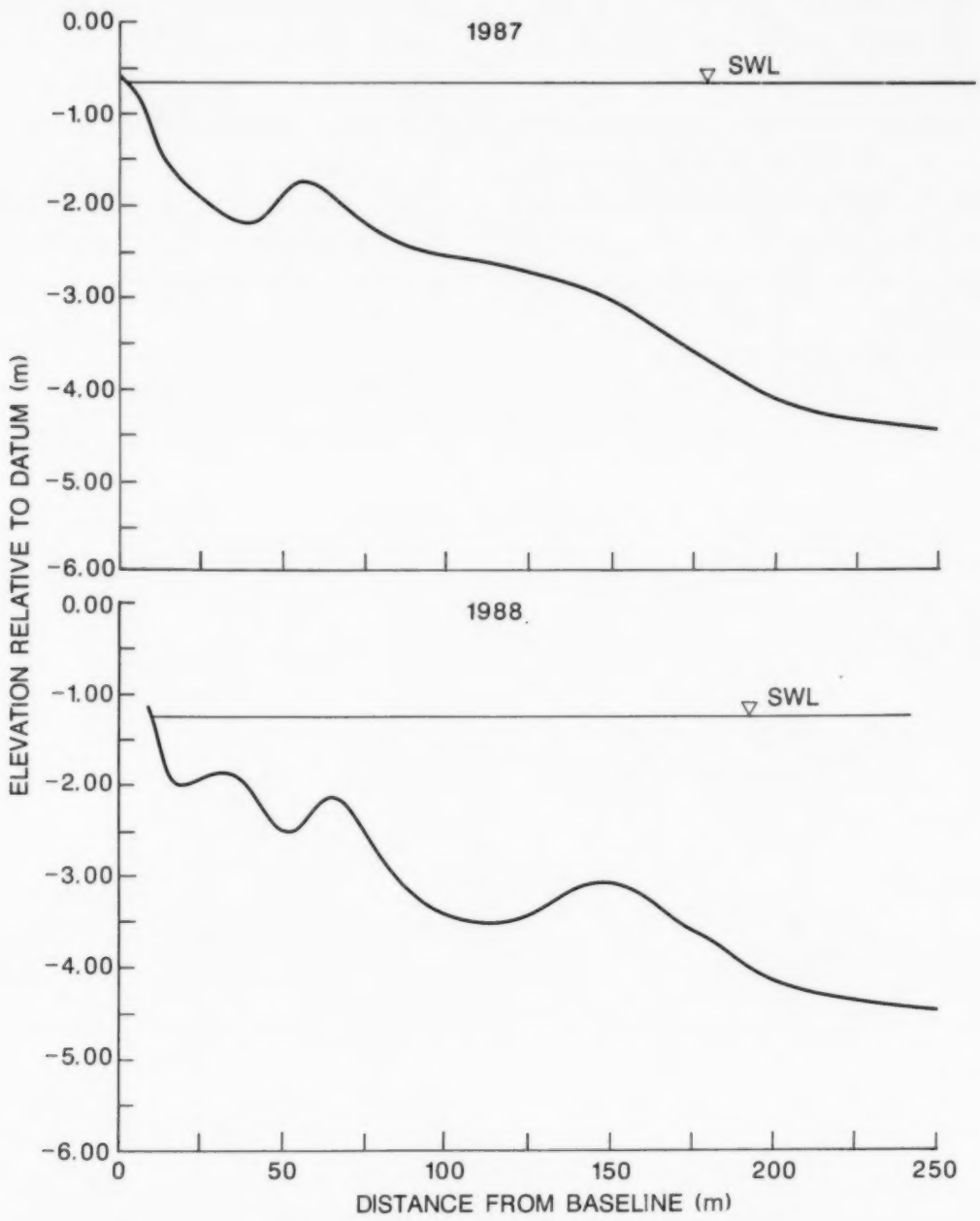

Fig. 2. Shoreface profiles, Bluewater Beach, 1987 and 1988.

TABLE I

Grain size characteristics of the shoreface at Bluewater Beach. Note: samples were dry-sieved at 1/4 Φ intervals and statistics computed by the method of moments

Location (m)	Mean size		Sorting Φ	Skewness Φ
	Φ	mm		
150	2.63	0.16	0.55	−1.34
110	2.11	0.23	0.73	−0.49
85	2.93	0.13	0.33	−0.45
65	2.44	0.18	0.42	−0.49
55	2.07	0.24	0.68	−1.85

63, 85, 110 and 150 m offshore from a fixed baseline (Fig. 3). Each transport station consisted of: (1) a vertical array of two collocated optical backscatterance suspended solids sensors (Model OBS-1P: Downing et al., 1981; D and A Instruments and Engineering, 1988; nominal elevations of $z \approx 0.04$ and 0.10 m; (2) two biaxial electromagnetic current meters (Marsh-McBirney, Model OEM 512; nominal elevations of $z \approx 0.10$ and 0.50 m; and (3) a single pressure transducer (nominal elevation of $z \approx 0.20$ m). A vertical array of 3 electromagnetic current meters (nominal elevations of $z \approx 0.10$, 0.25 and 0.50 m) was located 130 m offshore; single current meters ($z \approx 0.20$ m) and pressure transducers ($z \approx 0.10$ m) were collocated 180 and 230 m offshore respectively (Fig. 3). Local wind speed and direction were recorded continuously using a WindMonitor (Model 05103, R.M. Young Co.) at 10 m elevation at the back of the beach and stored as 10 minute averages.

An underwater video camera was deployed at the 85 m station to record the bedforms and sediment suspension events during daylight hours. Similar observations were made at the remaining stations by SCUBA divers. Large-scale morphological changes were monitored by standard survey procedures (OG92). Pre- and post-storm measurements from two arrays of depth-of-activity rods (5 and 10 m north of the instrument transect—Fig. 3) provided greater morphological resolution and also limits to the displacement of sensors above the bed during the storm. Estimates of the depth-of-activity, the time-integrated total (*ITVF*) and the time-integrated net (*INVF*) sediment vol-

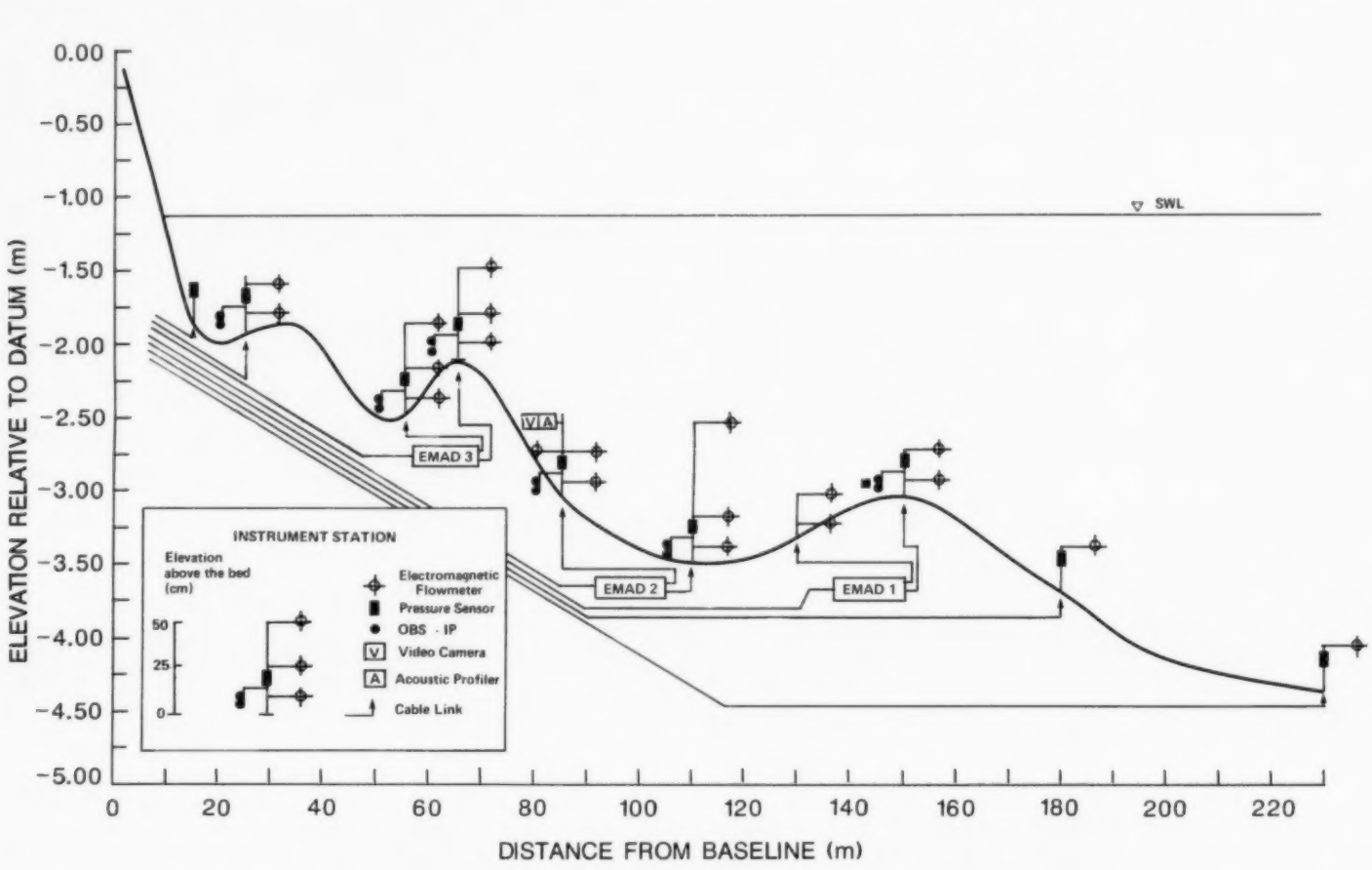

Fig. 3. Shoreface profile and sensor deployment. Note: EMAD 1-3 are underwater analogue-to-digital converters and digital transmission packages; they also distribute power to the sensors.

ume fluxes were also calculated to examine details of the sediment balance as in (OG92).

Sediment transport calculations and analytical procedures

Calculation of the local net, mean and oscillatory transport rates for suspended sediment from the velocity and sediment concentration vectors was identical to that in OG92, namely:

$$<uc>_{net} = \frac{1}{n}\sum uc$$

$$<uc>_{net} = <uc>_{mean} + <uc>_{osc}$$

$$<uc>_{mean} = \frac{1}{n}\sum u \cdot \frac{1}{n}\sum c$$

$$<uc>_{osc} = \frac{\Delta f}{f_c}\sum C_{uc}(f)$$

where u = instantaneous cross-shore velocity (m s^{-1}); c = instantaneous suspended sediment concentration (kg m^{-3}); n = number of observations; C_{uc} = co-spectrum of velocity and concentration; f = frequency (Hz); Δf = bandwidth for spectral estimates; and f_c = frequency range.

Statistics used to describe the waves (e.g. the variance of the water surface elevation), the cross-shore velocities (e.g. the time-averaged mean, standard deviation and skewness) and the suspended sediment concentrations (e.g. the time-averaged mean and variance) were computed using the BMDP 2D Statistical Analysis Program (Dixon, 1985). Standard deviations of the water surface elevation and cross-shore, horizontal velocity records were used to estimate average and maximum values for both the wave heights and oscillatory currents using accepted conventions. Variance spectra, cross-spectra and cross-correlations were computed using the BMDP 1T and 2T Time Series Analysis Programs (Dixon, 1985). All time-series were truncated to approximately 17 minutes prior to analysis to satisfy assumptions of record stationarity in this rapidly changing environment, while at the same time retaining a sufficient number of points (4096) to maintain a high degree of statistical confidence especially in the Fourier transformations. In the latter case data were also demeaned and spectral estimates obtained every 0.01 Hz from 0.0 to 2.0 Hz with a resolution bandwidth of 0.03 Hz and 70 degrees of freedom.

Storm event summary

A single storm on June 16, 1988, provides the focus for this paper, although reference is made to other wave events for specific purposes. During the June 16 storm, deep water (92.4 m) significant wave heights (MEDS buoy—Fig. 1) ranged from 0.14 m with a peak period of 2.25 s (0250 h) to 0.92 m with a peak period of 5.00 s (1620 h). Figure 4 illustrates the wind speed and direction and the significant height (H_s) and peak wave period (T_{pk}) in the nearshore zone; also illustrated are the cross-shore oscillatory velocity (u_s) and velocity skewness (u_{sk}) and the mean cross-shore (u) and mean shore-parallel (v) currents measured within the trough of the second bar. Winds were oriented close to the maximum fetch direction throughout the storm and wave height and period lagged the wind speed by 0.5 to 1 h. Waves reached maxima in shallow water at 0430 h and 1500 h following wind maxima at 0330 h and 1430 h. Wave period increased from 2.5 s early in the storm to a maximum of approximately 4 s at the storm peak when breaking wave heights exceeded 1.00 m. Oscillatory currents of approximately 1.00 m s^{-1} and mean cross-shore currents of approximately 0.10 m s^{-1} were measured under the breaking waves. Shore-parallel currents were directed southwards under the northwesterly wave approach with time-averaged speeds not exceeding 0.40 m s^{-1}. Sediment was re-suspended throughout the June 16 storm across all three bar-trough systems and transport over post-vortex ripples was recorded continuously by the video camera for a period of about six hours at the 85 m station (water depth, $h \approx 1.8$ m). Flat bed with sheet flow was observed on the crest of the second bar (63 m station, $h \approx 0.5$ m) during the peak of the storm.

Wave-induced suspended sediment transport

Bar topography introduces significantly larger and more variable gradients in local shoreface slopes than those associated with non-barred pro-

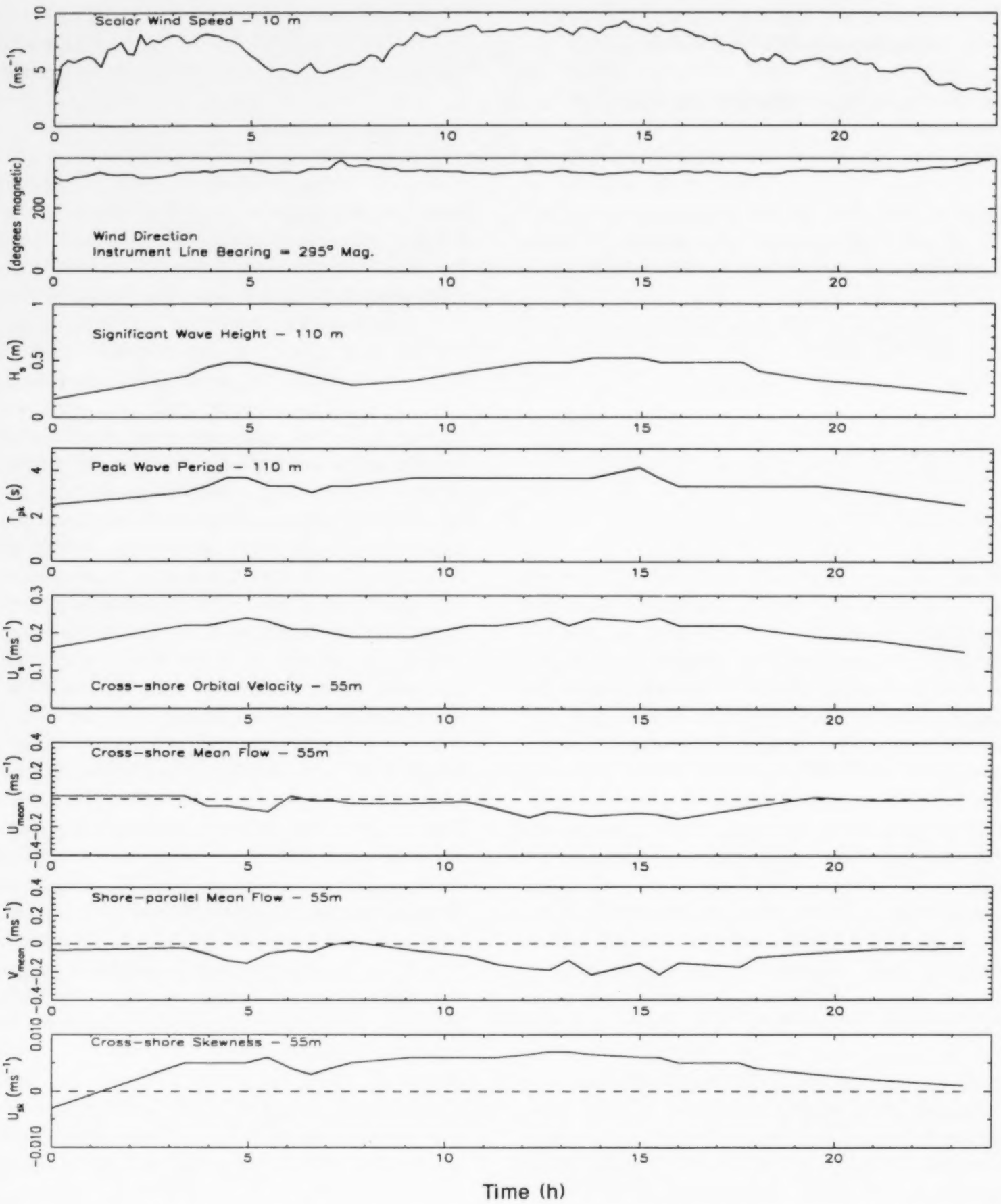

Fig. 4. Temporal variability in local wind speed and direction, significant wave height (H_s) and peak period (T_{pk}) at the 110 m station, average orbital current speed (u_s), mean cross-shore (u_{mean}) and alongshore (v_{mean}) velocity and cross-shore velocity skewness (u_{sk}) at the 55 m station throughout the June 16 storm.

files; this variability results in larger spatial gradients in the fluid dynamics associated with the propagating waves (Greenwood and Sherman, 1984, 1986a; Greenwood and Osborne, 1991a). Furthermore, in fetch-restricted environments temporal gradients in the fluid dynamics are large, since incident wave fields evolve rapidly. Similarly large gradients in sediment dynamics might therefore be expected at Bluewater Beach. A basic understanding of both sediment and bar dynamics will therefore be achieved by examining the suspended sediment transport response to changes in the wave height-to-water depth ratio through space and time (as in OG92). The constraints imposed by bedforms on suspended sediment transport rates will also be considered (as in Osborne and Greenwood, 1992a).

Measurements from the second bar-trough system (85, 63 and 55 m stations—Fig. 3) are emphasized in the following sections to illustrate interactions between the nearshore hydrodynamics, suspended sediment transport and bar morphodynamics over the full range of incident wave conditions. Data from the 85 m station will be used to describe the suspended sediment flux associated with varying waves and bedforms, but where the grain size distribution at the bed remains constant. Sediment flux is computed using the velocity vector at $z \approx 0.10$ m and the sediment concentration vector at $z \approx 0.04$ m.

Non-breaking waves ($H_s/h < 0.2$)

Under non-breaking shoaling waves, kinetic energy is distributed over a wide range of frequencies but with a significant peak corresponding to the incident wind-wave frequency (0.33 Hz, Fig. 5a). This peak is truncated sharply at its lower frequency limit, with spectral variance reduced by more than two orders of magnitude between 0.33 and 0.22 Hz, while a similar reduction in energy is spread over a frequency band of 0.39 Hz at the highest frequencies. A small but statistically significant peak of kinetic energy can be identified in the infragravity band (e.g. centred around 0.05 Hz (20 s) in Fig. 5a). Such a pattern was characteristic throughout the June 16 storm (Fig. 6).

In contrast, most of the variance in the suspended sediment concentration spectra (Figs. 5a and 6) is distributed at frequencies less than 0.10 Hz (10 s). Broad peaks at the wind-wave frequency (0.25–0.40 Hz) and at the frequency of the first harmonic of the primary wave (0.5–0.75 Hz) can occasionally be detected (Figs. 5a and 6a). In these examples, the lack of corresponding peaks at the first harmonic in the velocity spectra indicates that sediment concentrations responded twice during each individual wind-wave cycle (i.e. with both the onshore and offshore components of flow).

Under shoaling waves, the co-spectra of velocity and sediment concentration exhibit peaks corresponding to those at both the incident and infragravity band frequencies in the cross-shore velocity spectrum (Figs. 5b and 6). Relatively large positive peaks (onshore transport) coincide with the incident wave band ($\approx$0.20–0.40 Hz); significantly smaller, negative peaks (offshore transport) were associated with the infragravity band (0.01–0.04 Hz).

In an attempt to identify the low frequency oscillations, the time series of the cross-shore velocities were subjected to a simple band-pass filter (centred at 0.05 Hz, bandwidth 0.05 Hz). The low frequency modulation of the cross-shore velocity (Fig. 5c) has all the characteristics of a group-bound forced long wave (Longuet-Higgins and Stewart, 1962). Grouping of larger amplitude waves increases the local radiation stress gradients and the resultant set-down of the mean water surface, giving rise to the troughs of this long wave. In the time series illustrated (Fig. 5c), eight cycles of the long wave are recognizable, suggesting a frequency of 0.04 Hz which is coincident with the low frequency spectral peak in the cross-shore velocities (Fig. 5a). As a consequence of the group forcing, the troughs of the long wave coincide with the largest sediment concentrations induced by resuspension resulting from the larger bottom shear stresses associated with the larger waves in the group (Fig. 5d). Band pass filtering of the sediment concentration time series revealed a significant concentration cycle with the same frequency (0.04 Hz). The temporal coherence between the troughs of the group bound forced long wave and large sediment concentrations explains, at least in

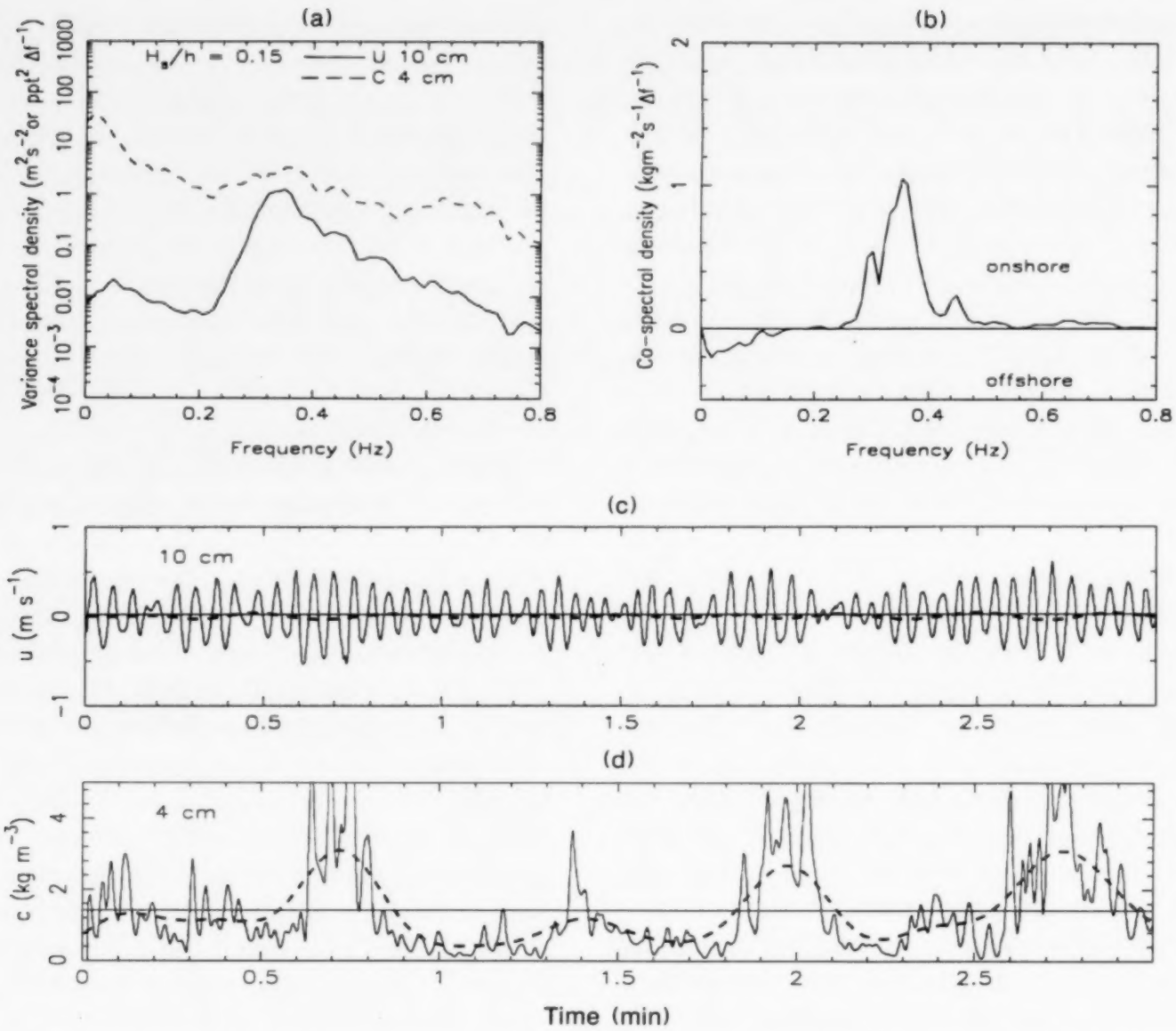

Fig. 5. (a) Cross-shore velocity ($z \approx 0.10$ m; solid line) and suspended sediment concentration ($z \approx 0.04$ m; dashed line) spectra from the 85 m station under shoaling waves ($H_s/h = 0.15$). (b) Co-spectrum of cross-shore velocity and sediment concentration; (c) time series of cross-shore velocity (solid line) and band-pass filtered velocity (dashed line); (d) the cross-product of velocity and suspended sediment concentration (solid line) and the band-pass filtered series (dashed line).

part, the offshore directed net oscillatory transport associated with the low frequencies (Figs. 5b and 6). These observations are consistent with those made previously for shoaling wave groups on a non-barred shoreface (OG92) and with observations under non-breaking waves by other workers (e.g. Huntley and Hanes, 1987; Doering and Bowen, 1989). The important conclusion is that the response of cohesionless sediment to shoaling wave motion in both barred and non-barred environments and the resulting suspended sediment flux, depends critically not only upon the instantaneous velocity (shear) associated with the large amplitude, short period wind waves, but also upon the low frequency modulation associated with the propagation of groups of large waves.

Spilling breakers ($H_s/h > 0.2$)

As the June 16 storm progressed, waves steepened and the larger waves began to spill across the upper lakeward slope and bar crest of the second bar as the significant height-to-water depth ratio exceeded 0.2. At this time (1240 h) the kinetic energy at the incident wave frequency had approximately doubled from its magnitude at 0738 h (cf. Fig. 6a and c). Over the same time period the spectral variance associated with the peak fre-

quency of the infragravity band had increased by more than 400% as had the sediment transport associated with this frequency band (cf. Fig. 6a and c). By 1240 h the magnitude of sediment transport at low frequencies was at least equal to that attributable to the wind-wave band recorded much earlier (cf. Fig. 6a and c).

Under breaking waves the wind-wave component of suspended sediment transport exhibited considerable variability, with sediment fluxes directed both onshore and offshore. At 1240 h, for example, the cospectrum exhibited a complex multimodal distribution indicating both onshore and offshore transport (Fig. 6c); integration of the cospectrum revealed that the net oscillatory suspended sediment transport was, however, approximately zero. With no significant shift in either the magnitude or the distribution of kinetic energy, the cospectrum at 1459 h revealed a simpler bimodal pattern at wind-wave frequencies, but now with an offshore net oscillatory transport (cf. Fig. 6c and d). By 2104 h, as the wave-height-to-water depth ratio decreased, a simple unimodal cospectral structure with an onshore net oscillatory transport was re-established (Fig. 6f).

The transitions from a net onshore oscillatory transport, to a balanced onshore and offshore transport, to a predominantly offshore transport and finally to a net onshore oscillatory transport over the full range of wind-wave frequencies coincided with a shift from wave shoaling to breaking and back to shoaling. These transitions may be explained by changes in the time–velocity relationships under increasingly skewed and asymmetric waves and by the phase lags which exist between velocity and concentration (Osborne and Greenwood, 1992a). Under this hypothesis the lowest frequencies in the wind-wave band would always tend to induce an onshore transport of sediment; during the onshore phase of the motion, the larger speeds would induce larger concentrations, but the length of the onshore half-wave cycle would still be long enough to allow material to rise above the bed ($z \approx 0.04$ m) and be advected shoreward during the same half-wave cycle. At higher frequencies, the onshore phase of wave motion would still induce larger velocities and concentrations than the offshore phase; nevertheless, the time lag inherent in the ejection of sediment from the bed after it has been set in motion, coupled to the shorter length of time of the onshore phase of motion (compared to the offshore phase), would increase the probability of much larger flux couplings between the offshore phase of fluid motion and the larger concentrations induced by the onshore velocities. These transitions in the net oscillatory transport at wind wave frequencies also coincided with changes in the local bottom roughness (bedforms).

Bedform constraints on suspended sediment transport

Under small shoaling waves (e.g. 1035 h) relatively steep (steepness ≈ 0.12), three-dimensional vortex ripples were most commonly observed (Ollerhead and Greenwood, 1990). These bedforms were asymmetric, with steeper landward slopes and separation vortices could be identified by the discrete "clouds" of suspended sediment shed from ripple crests (observed by video imagery and by divers). Particularly large vortices and/or large sediment concentrations were produced at rates of 1 to 3 times per minute during passage of the largest waves in a group (Ollerhead, 1989).

The time-averaged concentrations of suspended sediment associated with half-wave cycles as waves shoaled over a rippled bed have been examined previously (Greenwood et al., 1990). This analysis revealed consistently larger average concentrations associated with the onshore phases of motion, especially at the lowest measurement elevations where phase lags between the current forcing and sediment concentration were small. Table 2 documents differences between the average concentrations of sediment suspended by the onshore and offshore phases of both shoaling and breaking waves for two elevations above the rippled bed. A statistically significant difference occurs under shoaling waves, but only at the lowest elevation (0606 h, $z \approx 0.04$ m); no such difference can be detected at either elevation once waves begin to break (1240 h). Such observations would be consistent with the expected larger kinetic energies (and larger sediment concentrations) associated with the separation vortices induced by the larger onshore

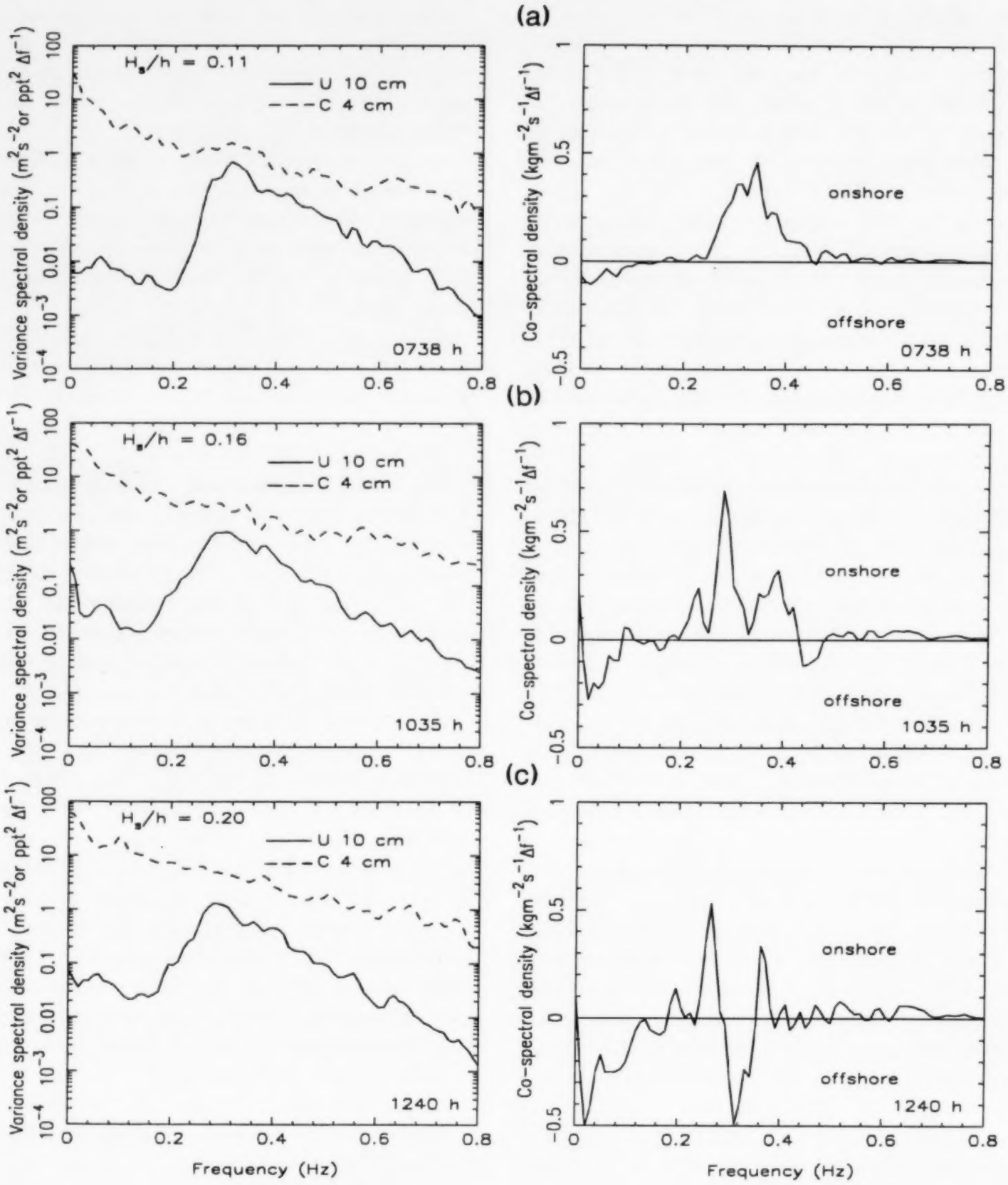

oscillatory velocities. This coupling of large sediment concentrations ($z \approx 0.04$ m) and large onshore velocities confirms the mechanism noted earlier for the dominant onshore net oscillatory transport associated with wind-waves shoaling over a rippled bed (0738 h and 1035 h; Fig. 6).

Under the increasingly skewed, asymmetric waves associated with the onset of breaking, the

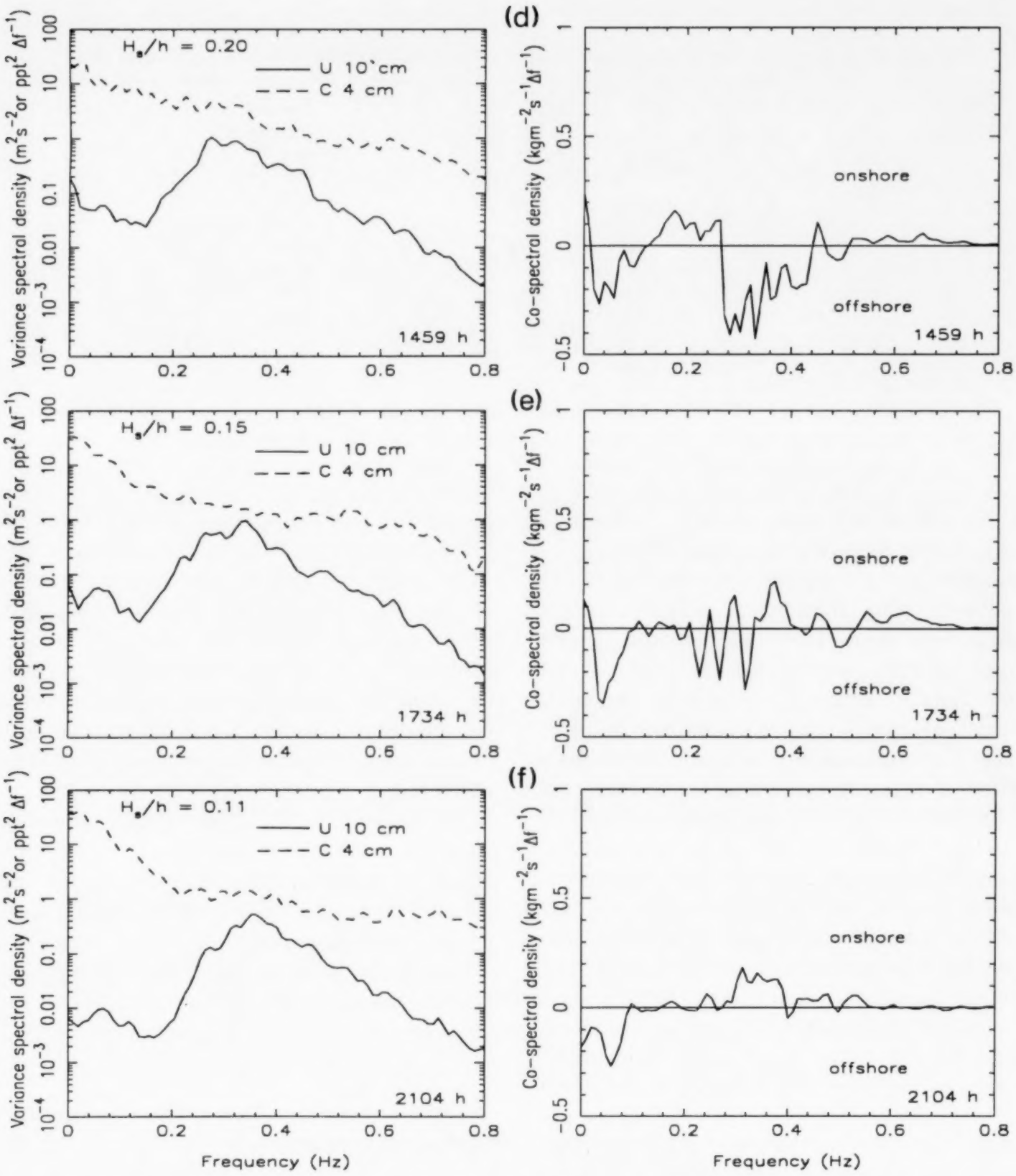

Fig. 6. Temporal variability of the cross-shore velocity ($z \approx 0.10$ m; solid line) and sediment concentration ($z \approx 0.04$ m; dashed line) spectra and the associated co-spectra ($z \approx 0.04$ m, solid line; $z \approx 0.10$ m, dot-dash line) from the 85 m station under a range of wave conditions: (a) 0738 h, $H_s/h = 0.11$; (b) 1035 h, $H_s/h = 0.16$; (c) 1240 h, $H_s/h = 0.20$; (d) 1459 h, $H_s/h = 0.20$; (e) 1734 h, $H_s/h = 0.15$; (f) 2104 h, $H_s/h = 0.11$.

TABLE 2

Difference of means test on suspended sediment concentrations during onshore and offshore phases of flow

Time (h)	z (m)	−95%	C_{on} (n) (g l^{-1})	+95%	−95%	C_{off} (n) (g l^{-1})	+95%	S
0606	0.10	0.32	0.33 (1512)	0.34	0.33	0.34 (2584)	0.35	N
0606	0.04	1.04	1.10 (1512)	1.15	0.94	0.98 (2584)	1.02	*
1240	0.10	0.30	0.31 (1560)	0.33	0.28	0.29 (2536)	0.30	N
1240	0.04	1.22	1.30 (1560)	1.38	1.13	1.18 (2536)	1.24	N

z = elevation above bed; C_{on} = mean sediment concentration during onshore flow; C_{off} = mean sediment concentration during offshore flow; +/−95% = upper/lower confidence limits on mean; (n) = number of samples in mean; S = statistical significance; * = significant at the 5% level; and N = not significant at the 5% level.

steep, three-dimensional, asymmetric, vortex ripples changed to less-steep (steepness ≈ 0.01), two-dimensional post-vortex ripples (Ollerhead and Greenwood, 1990). As a result, coherent vortex shedding from ripple crests was reduced. Time-averaged sediment concentrations increased by 18–20% close to the bed ($z \approx 0.04$ m) as expected, but decreased slightly at higher elevations ($z \approx 0.10$ m). This decrease most probably resulted from a reduction in mixing length, owing to the decreased amplitude of bottom roughness elements (see Nielsen, 1984); however, erosion of the bed and the resulting shift in relative elevation of the concentration sensors cannot be excluded as a cause. Differences in the time-averaged sediment concentrations between each half-wave cycle were now no longer statistically significant (Table 2); with this increased homogeneity of sediment concentration over the wave cycle, cross correlations between concentration and velocity would result in large onshore and offshore flux couplings. Consequently, the observed bidirectionality of transport over the incident wave band (Fig. 6, 1240 h) is not surprising.

As breaking intensified, oscillation ripple steepness decreased further and sediment concentrations became relatively uniform (vertically) over the wave cycle. This increased uniformity coincided with a greater frequency of occurrence of offshore flows (associated with increased skewness and asymmetry of the breaking wave form) which would increase the potential flux coupling between offshore flows and large sediment concentrations. The dominant offshore net oscillatory transport by breaking wind-waves at 1459 h (Fig. 6d) can be accounted for in this way. With the reappearance of three-dimensional, vortex ripples as wave height and cross-shore velocities decreased, a net onshore sediment transport at wind-wave frequencies is observed once more (1734 h and 2104 h, Fig. 6).

A simple sequence of suspended sediment flux appears to be closely linked to both the near-bed fluid dynamics and the bedforms as they change through time at a single location. Such a sequence might also be expected to occur spatially at a single point in time, since wave height-to-water depth ratios are a function of nearshore bathymetry.

Spatial dependency of wave-induced suspended sediment transport

Spatial variation in the cross-shore velocity field reflects both the character of the incident waves and the nearshore bathymetry. Thus the concentrations of suspended sediment and the oscillatory suspended sediment transport rates should exhibit at least as strong a spatial signature across a barred shoreface as that documented previously for a non-barred system (OG92). These signatures

should be strongest when wave transformations are most pronounced.

Time series of the cross-shore velocity and sediment concentration from the lakeward slope, crest and lower landward slope/trough of the second bar recorded close to the storm peak (1600 h) illustrate the extremes for such transformations. Across the lakeward slope a well-defined "groupiness" is evident in the velocity field (Fig. 7a), as waves shoaled but were not yet breaking. Equally well-defined are sediment re-suspension events marked by large concentrations lasting for several wave periods and in-phase with the group-modulated velocities.

At the bar crest the larger waves were spilling. Although group modulation of the velocity field was reduced as a result of the breaking process, discrete re-suspension events can still be recognized (Fig. 7b) and are coherent with those observed at the 85 m station. The time lag recorded is directly proportional to the group propagation speed (Table 3). This confirms the importance of wave groups in re-suspending and transporting sediment even after significant dissipation of wave energy through breaking.

In the trough, most waves were breaking or reforming and group-modulation of the cross-shore velocities is even less well-defined (Fig. 7c). Nevertheless, a distinct low-frequency modulation of the velocity field is superimposed on the high frequency oscillations of the breakers. Sediment re-suspension events in the trough are closely correlated with the local low-frequency oscillation, but are not coherent with re-suspension events on either the bar crest or the lakeward slope. The time lags of maximum correlation for sediment concentration between the 55 m station and those at 85 and 65 m are not compatible with a group-modulated forcing (Table 3) even though the time lag of maximum correlation between cross-shore velocities is consistent with the propagation of the same wave field. It would appear, therefore, that the low frequency modulation of the cross-shore velocity field in the trough is not of the same origin as that on the lakeward slope and bar crest.

As waves shoaled to breaking between the 85 and 63 m stations, the cross-shore velocity spectra revealed significant increases in variance at frequencies $\leqslant 0.2$ Hz (Fig. 8a and b). A further increase in low-frequency energy ($\leqslant 0.05$ Hz) is observed between the 63 and 55 m stations (Fig. 8b and c) as spilling breakers propagate from the bar crest across the trough. The low-frequency oscillation associated with the shoaling wave field reflects clearly the presence of a group-bound forced long wave (see also Greenwood and Osborne, 1992; Osborne and Greenwood, 1992a). In contrast, low-frequency oscillations in the trough most probably represent energy transferred from the forced long wave to long waves constrained by the presence of the bar crest and the time-varying position of the breaker line (e.g. Symonds and Bowen, 1984). Regardless of the actual wave mode, the oscillatory transport rates at low-frequencies landward of wave breaking should be coherent with this new secondary wave; this would explain the observed lack of coherence between the low-frequency oscillatory transport in the trough and that on the lakeward slope and bar crest.

An equally significant increase in high-frequency energy between the bar crest and the trough was observed at the storm peak (Fig. 8b and c). The spectral peak centred around 0.6 Hz represents the first harmonic of the primary wave; harmonics such as this are typical of the spectra of extremely asymmetrical wave forms associated with the highly non-linear waves and surf bores triggered

TABLE 3

Time lags of maximum correlation between stations for cross-shore velocity and sediment concentration

Stations	85–63 m	85–55 m	63–55 m
dx (m)	22	30	8
dh (m)	1.0	0.6	0.4
C (m s^{-1})	3.6 (1.8)	3.8 (1.9)	3.1 (1.6)
t (s)	6.1 (12.2)	7.8 (15.5)	2.6 (5.2)
R_{max-u} (s)	7.0	9.0	2.0
R_{max-c} (s)	12.0	7.3	9.0

dx = separation distance between stations; dh = change in water depth between stations; C = average phase (group) velocity between stations = $1/N\sum (gh_i)^{0.5}$, where h_i = local depth (m), N = number of depth increments between stations; t = wave (group) travel times between stations; R_{max-u} = time lag of maximum correlation for velocity; and R_{max-c} = time lag of maximum correlation for concentration.

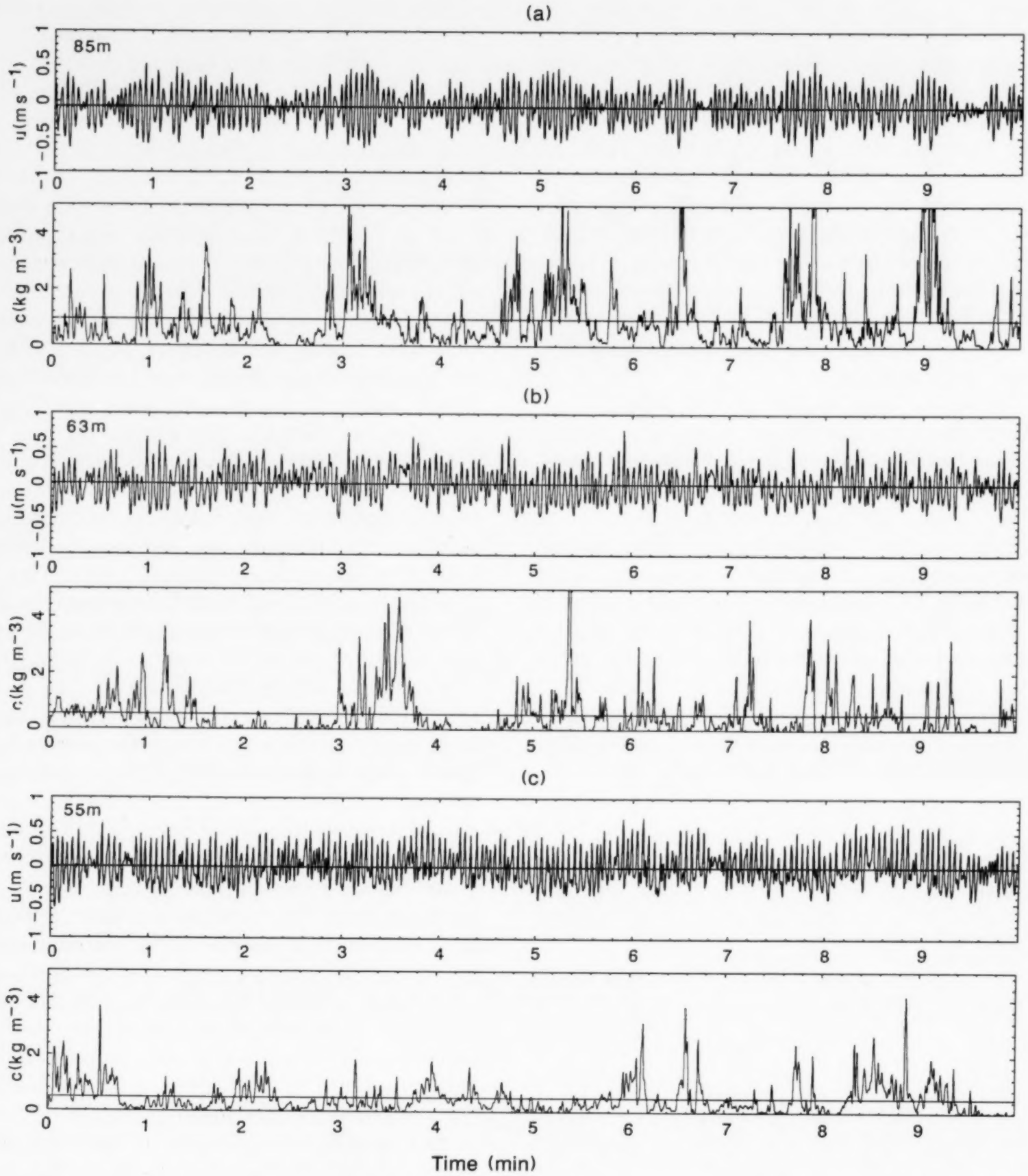

Fig. 7. Time series of the cross-shore velocity (u; $z \approx 0.10$ m) and suspended sediment concentration (c; $z \approx 0.04$ m): (a) 85 m station ($H_s/h = 0.15$); (b) 63 m station ($H_s/h = 0.41$); (c) 55 m station ($H_s/\mathrm{h} = 0.28$).

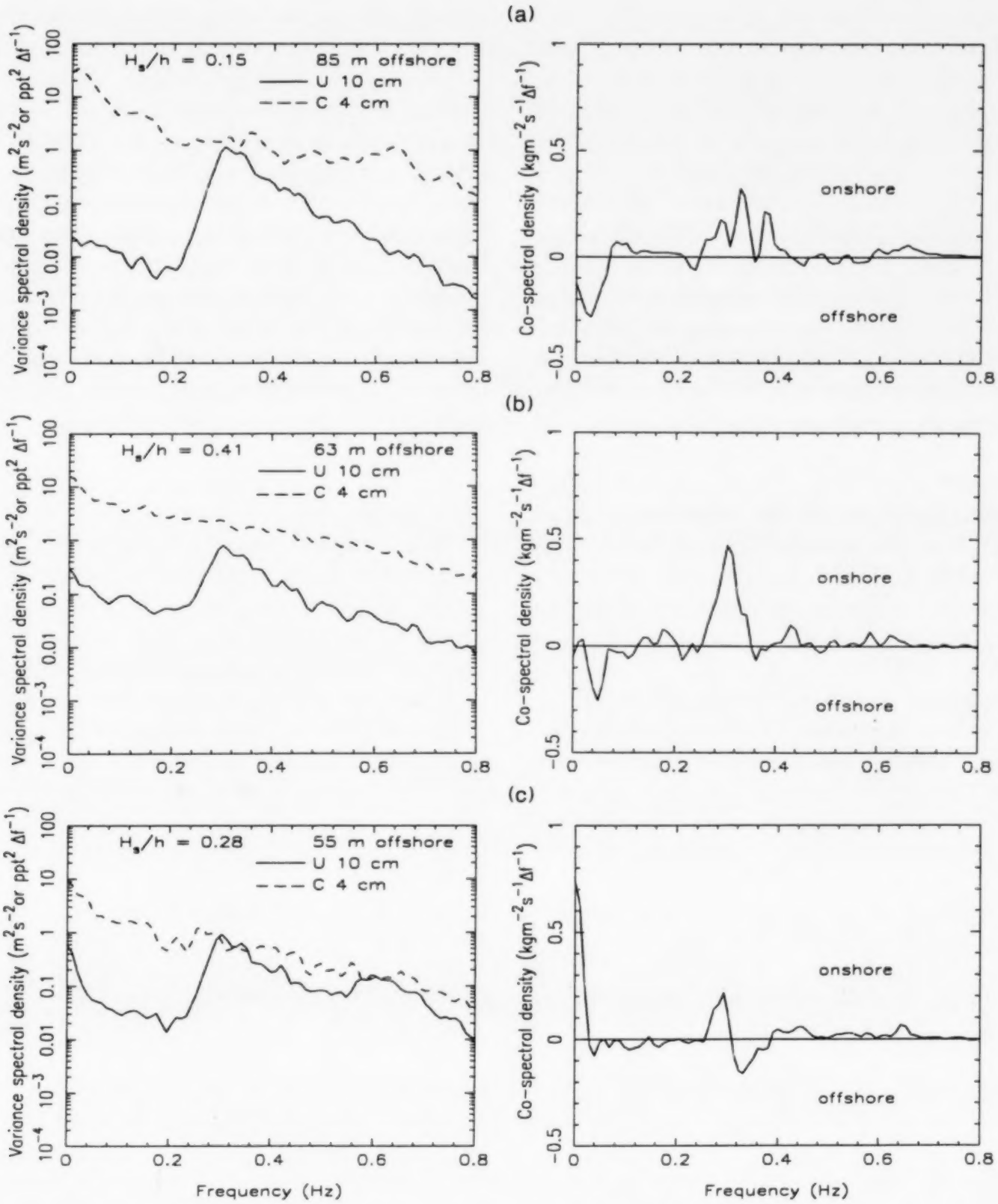

Fig. 8. Spatial variability of cross-shore velocity ($z \approx 0.10$ m; solid line) and sediment concentration ($z \approx 0.04$ m; dashed line) spectra and the associated co-spectra ($z \approx 0.04$ m, solid line) under a range of wave conditions: (a) 85 m station, $H_s/h = 0.15$; (b) 63 m station; $H_s/h = 0.41$; (c) 55 m station, $H_s/h = 0.28$.

by the breaking on the bar crest (Thornton et al., 1977; Greenwood and Osborne, 1991a). The combined effects of redistributing energy towards both lower and higher frequencies during wave shoaling and breaking results in a greater potential for significant transport of suspended sediment at these frequencies. Spatial variation in the co-spectra reinforce many of the earlier conclusions concerning sediment transport drawn from both the time-series and variance spectra. On the lake-

ward slope of the bar (85 m station, Fig. 8a), where waves were shoaling but not breaking, suspended sediment transport at wind-wave frequencies was directed onshore, while that attributable to the low frequencies was directed offshore. The co-spectrum indicates that the total onshore and offshore oscillatory transport rates are nearly equal, with the balance being achieved across frequency space. On the bar crest (63 m station, Fig. 8b), the onshore wind-wave transport rates increased dramatically from those on the lakeward slope (85 m station). This reflects both the increase in sediment re-suspension in shallower water and the increase in velocity skewness and asymmetry as a result of the shoaling transformations across the lakeward slope. The offshore directed oscillatory transport rates in the infragravity band decreased from the lakeward slope to the bar crest (cf. Fig. 8b and a). This is to be expected as the wave group structure is diminished during the breaking process and the forced long wave is released.

In the trough of the second bar (55 m station, Fig. 8c), 8 m landward of the bar crest, the transport rates at wind-wave frequencies are greatly reduced, reflecting the dissipation of energy as a result of both wave breaking and a cascading of energy to lower frequencies. A reduction in energy density also results from the increase in water depth from crest to trough (1.00 m to 1.38 m). At this time the cospectrum was also distinctly bimodal over the wind-wave frequency range, with approximately equal transport rates directed onshore (peak wave frequency and highest frequencies) and offshore (intermediate frequencies). However, the most distinctive feature of the co-spectrum from the trough is the very large onshore suspended sediment transport rates at frequencies <0.05 Hz; this was a characteristic feature of virtually all the spectra from this location for a major portion of the storm event on June 16 (1035 to 1734 h).

The complex bimodal structure of the co-spectrum at the incident wave frequencies, together with the unimodal structure at low frequencies, supports the observation that sediment concentration fluctuations are out of phase with velocity fluctuations at the wind-wave frequencies but in phase with fluctuations associated with relatively large low frequency waves in the inner surf zone.

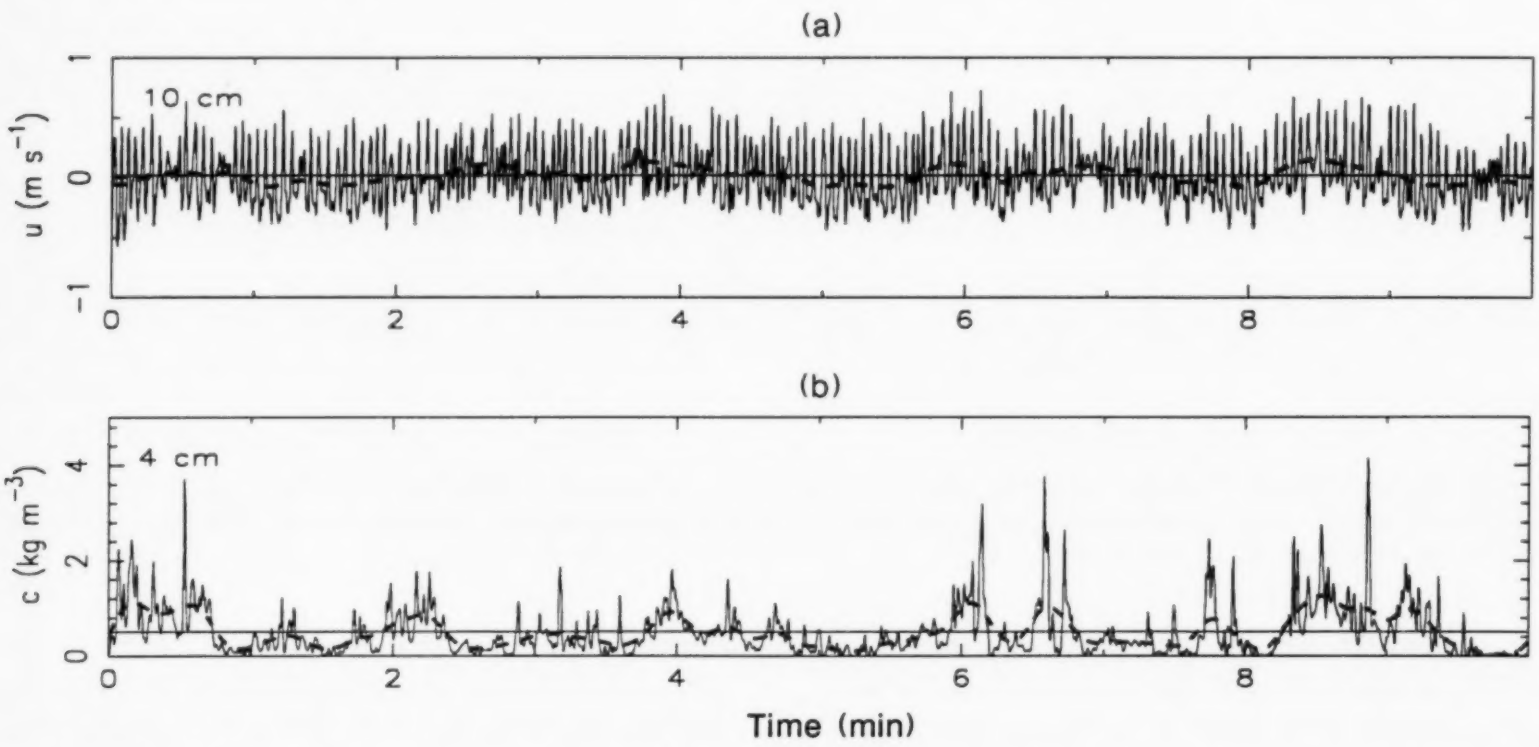

Fig. 9. Observed (solid line) and low pass filtered (dashed line) time series of cross-shore velocity (a) and suspended sediment concentration (b).

To confirm this suggestion, the cross-shore velocities and sediment concentrations (55 m station) were low-pass filtered with a cutoff frequency of 0.1 Hz; excellent coherence was obtained between onshore phases of the low frequency wave and major re-suspension events (Fig. 9a).

Relatively large offshore transport rates were associated with low frequency motions over the bar crest between 1240 h and 1734 h (63 m station, Fig. 8b). However, the co-spectra from 63 m demonstrated substantially larger onshore transport rates at the wind wave frequencies than those at 55 m. This spatial pattern of sediment transport reflects the decreasing importance of incident waves and the relative increase in importance of low-frequency oscillations landward of the bar crest (e.g. Wright et al., 1986).

Suspended sediment transport by time-averaged cross-shore currents

The presence of several bars on a shoreface has been shown previously to be associated with spatially periodic perturbations in the local time-averaged (mean) cross-shore currents during storms (Greenwood and Osborne, 1991). These mean currents were directed offshore, forming classic undertows in response to cross-shore gradients in wave setup superimposed on the wind setup as waves break across each individual bar (Greenwood and Osborne, 1990). Since the time-averaged (mean) concentrations of suspended sediment are a function of the depth-controlled oscillatory velocities, then spatially periodic perturbations in the mean suspended sediment transport rates should be expected.

Prior to the storm the mean cross-shore currents were small and directed onshore, but reversed as the storm waves began to build (0330 h, Fig. 4). Through the subsequent storm a consistent pattern of cross-shore mean currents emerged (Figs. 4 and 10). Such currents were always a minimum across the bar crest (63 m station) dropping to near zero (0.01 m s^{-1}) at the storm peak (1530 h). Maximum mean currents were observed at the storm peak on both the lakeward slope (0.11 m s^{-1}) and in the trough (0.10 m s^{-1}) of the second bar. In contrast, the mean suspended sediment concentrations were at a minimum in the trough and reached a maximum over the bar crest at the storm peak (1530 h, Fig. 10). The significantly lower mean cross-shore currents over the bar crest accounted for the low mean transport, even though mean sediment concentrations peaked at this location (Fig. 10); at 1500 h, for example, the mean transport on the lakeward slope (85 m station) was larger by at least a factor of four.

Wave breaking intensified over the bar crest and upper lakeward slope of the second bar during the storm peak and mean water levels recorded at the 85, 63 and 55 m stations indicated increases of 0.07 to 0.10 m (relative to pre- and post-storm levels) and a maximum increase of 0.20 m even further shoreward (Hazen et al., 1991). The wave setup gradients were small compared to the overall wind-induced lake setup, which accounts for the small mean cross-shore currents. Larger magnitude currents have been observed by previous workers and shown to be spatially extensive across a variety of barred profiles in Southern Georgian Bay (e.g. Greenwood and Sherman, 1984; Davidson-Arnott and McDonald, 1989; Greenwood and Osborne, 1990, 1991; Osborne and Greenwood, 1991). The mean cross-shore currents of June 16 were weak undertows, driven by spatially variable set-up gradients; the offshore mean flow at 55 m being driven by set-up across the innermost bar and that at 85 m by set-up across the second bar (for a more detailed analysis see Hazen et al., 1991).

Net suspended sediment transport rates

As incident wave energy increased during the June 16 storm, so did the magnitudes of both the oscillatory and mean suspended sediment transport rates. Mass balance in the shoreface results, at least in part, from the relative magnitudes and directions of suspended sediment transport attributable to these components as a function of time, cross-shore position and distance above the bed.

Vertical structure of suspended sediment transport

Figure 11 illustrates the local vertical variations in $<uc>_{mean}$ and $<uc>_{osc}$, the sum of which equals the time-averaged, net suspended sediment

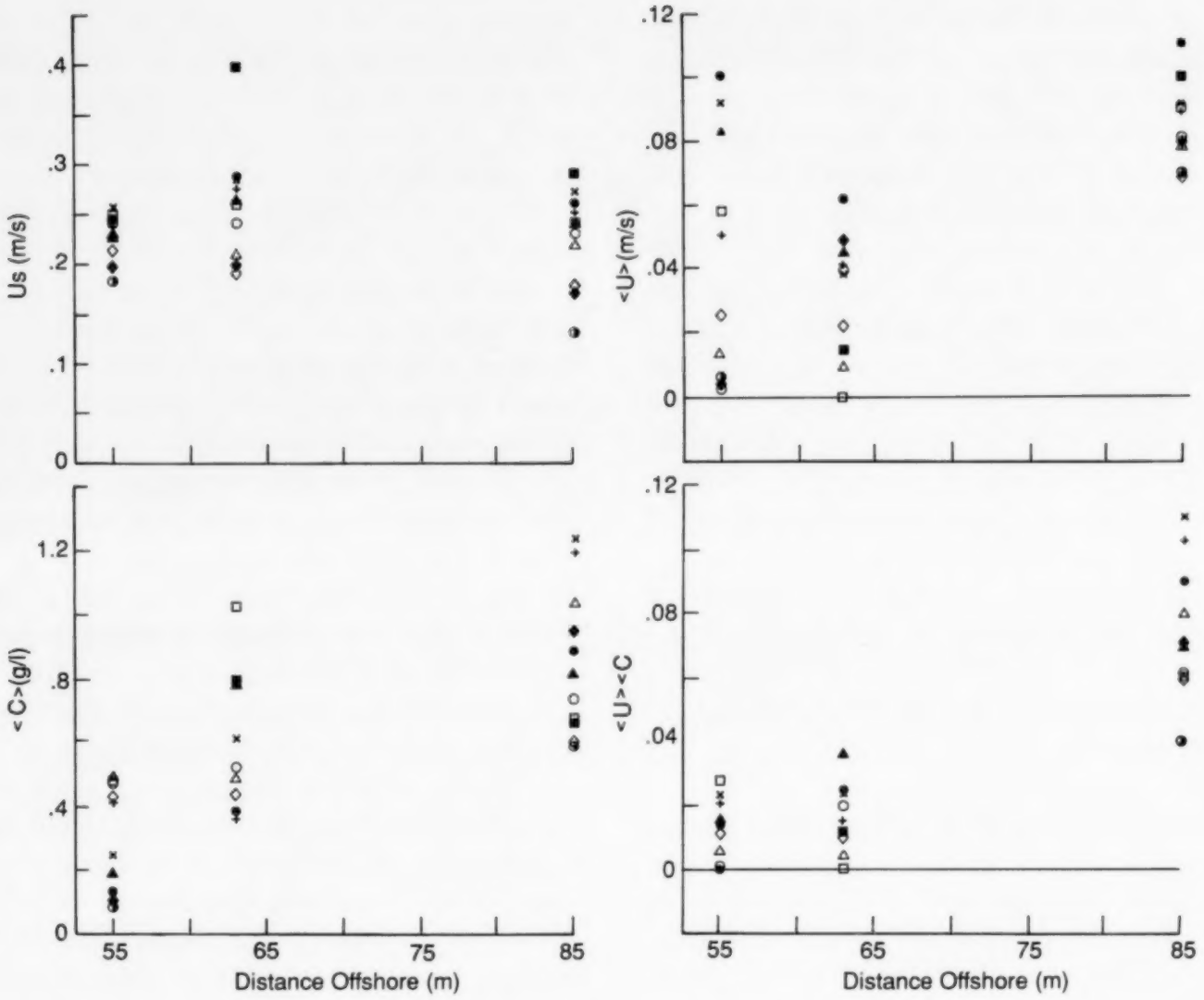

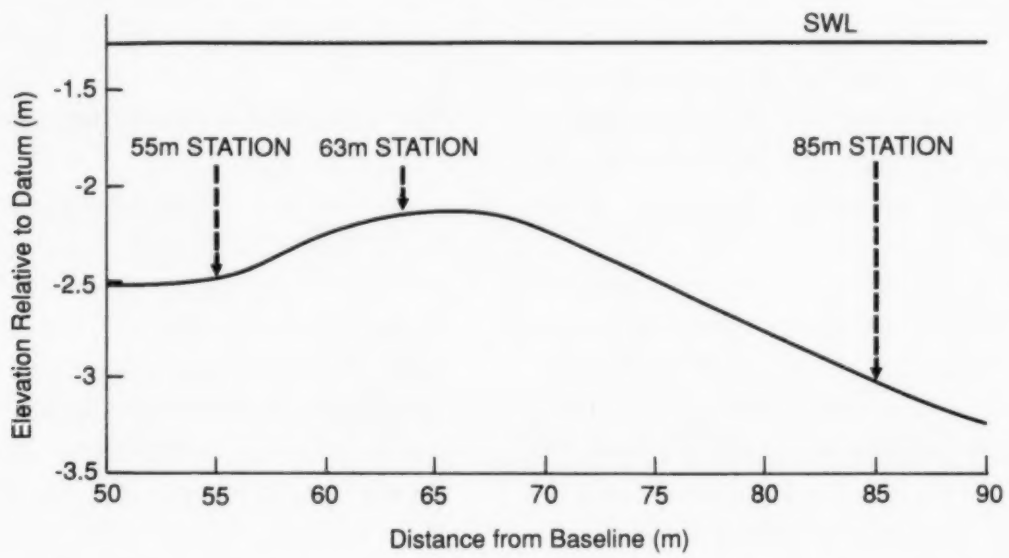

Fig. 10. Depth-dependent patterns in the cross-shore oscillatory velocity (u_s; $z \approx 0.10$ m), cross-shore mean current speed ($\bar{u}$; $z \approx 0.10$ m), time-averaged suspended sediment concentration ($\bar{c}$; $z \approx 0.08$ m), and mean suspended sediment transport rate ($\bar{u}\bar{c}$).

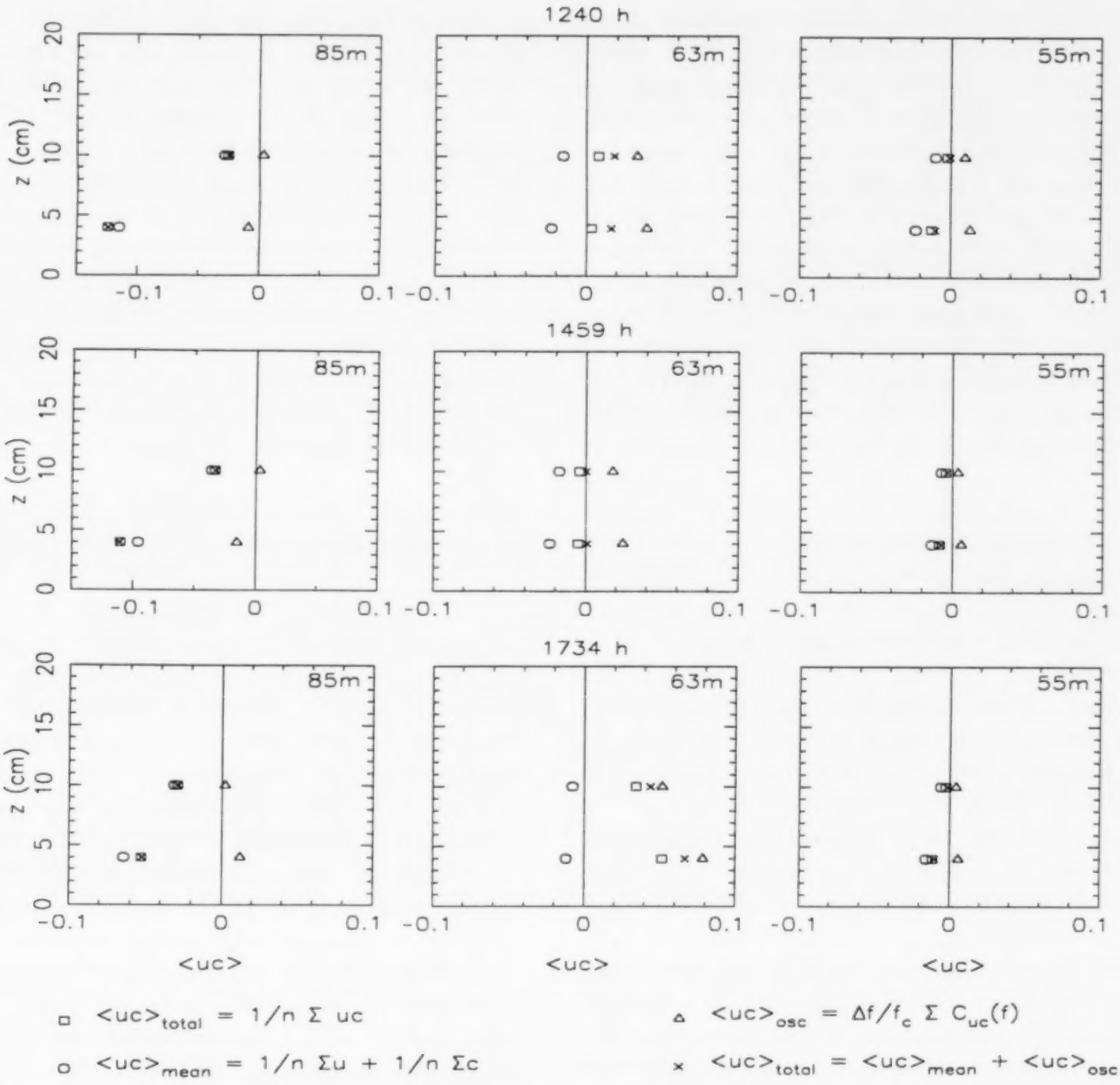

Fig. 11. Time-averaged suspended sediment transport across the bar form ($z \approx 0.04$ and 0.08 m) over the storm peak (1240–1734 h): lakeward slope (85 m station); bar crest (63 m station); landward trough (55 m station). Note: positive values of $<uc>$ signify onshore transport.

transport rate, $<uc>$. On the lakeward slope (85 m station, Fig. 11) the $<uc>_{mean}$ was directed offshore at both the 0.04 and 0.08 m elevations and clearly dominated the net transport rate at this location throughout this period of time. During the buildup and peak of the storm $<uc>_{osc}$ was also directed offshore at the lowermost elevation ($z \approx 0.04$ m) owing to the relatively large component of offshore transport associated with the group-bound, forced long wave. Together with the offshore mean transport rate the result was a large net offshore transport rate near the bed. At $z \approx 0.08$ m, the $<uc>_{osc}$ was directed landwards, but was small compared to the offshore directed $<uc>_{mean}$ resulting in a net offshore transport of sediment in the lower water column.

On the bar crest during the peak of the storm the net suspended sediment transport rate was near zero at both measurement elevations (Fig. 11, 63 m station, 1459 h). This resulted from the nearly equal but opposing offshore directed $<uc>_{mean}$ and onshore directed $<uc>_{osc}$. The

latter was forced by the positive (landward) skewness in the velocity field associated with the nonlinear form of the breaking waves. During the early part of the storm (1240 h) and particularly during the decay phase (1734 h), however, $<uc>_{total}$ was was directed onshore across the bar crest. This resulted from strongly asymmetric oscillatory currents inducing large onshore transport rates, which could not be offset by offshore transport associated with the relatively weak mean currents.

In the trough landward of the bar crest (Fig. 11, 55 m station), transport rates were much smaller overall than on either the bar crest or lakeward slope. The undertow induced $<uc>_{mean}$ was slightly larger than $<uc>_{osc}$, which in this case was dominated by the secondary low frequency waves in the inner part of the surf zone. The result was a small but persistent net offshore sediment flux throughout the lower water column.

During the peak of the storm $<uc>_{total}$ was directed *offshore* across both the lakeward slope and the trough landward of the second bar. On the lakeward slope, the net offshore transport was driven by both the mean cross-shore currents (undertow) and the group-bound, forced long wave. In the trough, the net offshore transport was dominated by the mean cross-shore currents. In contrast, the bar crest was characterized by a near-zero net suspended sediment transport rate. Thus, although the bar crest was an area of considerable sediment re-suspension owing to the large magnitude oscillatory currents and the enhanced turbulence associated with wave breaking, net suspended sediment transport rates were small. The latter would appear to have been achieved by a balance between the transport of sediment offshore by the time-averaged mean currents and the group-forced long wave, and the landward transport of sediment due to the skewed oscillatory velocity field under near-breaking and breaking waves. Oscillatory sediment transport driven by the incident wave frequencies clearly declined away from the bar crest down both the landward and lakeward slopes, and the contributions to the local sediment transport rates from both the low frequency oscillations and the mean currents became dominant.

It is useful to explore the implications of the measured suspended sediment flux rates in terms of the potential for erosion or accretion. With relatively large offshore transport rates on the lakeward slope of the bar and near-zero net transport rates on the bar crest, it might be expected that erosion of the lakeward slope would occur. Accretion would be expected on the upper landward slope or crest of the bar as a result of the net offshore transport rates in the trough and the near-zero net transport across the bar crest. These measured sediment flux rates indicate both a vertical growth and landward migration of the second bar during the storm.

Sediment re-activation, volume flux and erosion–accretion patterns

Sediment volume fluxes estimated from the depth-of-activity rod measurements for all the significant wave events monitored during the 1988 field season are summarized in Table 4. The June 16 storm was obviously not the most significant event in terms of sediment re-activation, ranking fifth in terms of the total amount of sediment re-activated but it did rank first in terms of the net morphological change. Furthermore, it follows a pattern similar to all other storms in that large volumes of sediment were reactivated, while the net sediment volume fluxes through the shoreface sand prism were small. Of the estimated total control volume for the shoreface of 1188 m^3, approximately 8.6% was re-activated by the June 16 storm ($ITVF = 101.8$ m^3). A small net gain of sediment ($INVF = 22.9$ m^3), equivalent to 1.9% of the control volume was also recorded. If the change in sediment volume is taken relative to the volume re-activated, the percentage change is still not large. Over the second bar, with a partial-control volume of 300 m^3, sediment re-activation equalled 10.6% of this control volume ($ITVF = 31.66$ m^3), with a net gain in this case of 3.2% of the partial control volume ($INVF = 9.53$ m^3).

The patterns of depth-of-activity and bed elevation change across the barred shoreface, relative to the pre-storm surface, are documented in Fig. 12. The values plotted represent the averages of measurements from the two lines of rods

TABLE 4

Sediment flux determined from depth-of-activity rods

Date of storm	*ITVF* (m^3)	*INVF* (m^3)	% mobilized	% change
88:06:01	55.9	−11.4	4.7	−1.0 (−20.0)
88:06:02	28.6	2.5	2.4	0.2 (9.0)
88:06:03	33.2	−2.7	2.8	−0.2 (−8.0)
88:06:05	176.2	16.4	14.8	1.4 (9.0)
88:06:08	112.8	6.4	9.5	0.5 (6.0
88:06:09	125.5	22.3	10.6	1.9 (18.0)
88:06:16	101.8	22.9	8.6	1.9 (22.0)
88:06:17–20	106.0	9.4	8.9	0.8 (9.0)
Average	79.2	8.2	7.8	0.7 (6.0)

Note: *ITVF* = time-integrated total volume flux;
INVF = time integrated net volume flux.
The % mobilized and % change are calculated relative to the control volume. The % change relative to the volume reactivated is given in parentheses.

deployed 5 and 10 m north of the instrument line. The maximum depth-of-activity recorded was 0.16 m and was located closest to the shoreline (10 m offshore). In general, the depth-of-activity decreased lakewards to a minimum close to zero 230 m offshore; local re-activation maxima occurred on the bar crests as anticipated (0.10 m over the inner bar and 0.07 and 0.09 m, respectively over the second and outer bars). Local minima were associated with the adjacent troughs.

Up to 0.23 m of accretion was measured on the landward slope of the inner bar (Fig. 12) resulting in a shoreward displacement of the bar form. This shoreward displacement coincided with the lakeward growth of the beach face as a cuspate horn centred on the instrument line (Line 0), such that the inner bar became attached to the shoreline by the end of the storm. This accretion process appears to have occurred relatively late in the storm cycle, as the lowest OBS-1P sensor on the first bar crest was buried between 1734 h and 2104 h.

Up to 0.06 m of accretion was recorded on both the crest and the upper landward slope of the second bar, while approximately 0.05 m of sediment was removed from the trough to landward; the result was a small but measurable vertical growth of the bar and a distinct shoreward displacement of the landward slope. This pattern of erosion and accretion over the second bar crest and trough clearly supports the earlier inferences concerning morphodynamics drawn from the sediment flux measurements. No change in bed elevation could be measured across the lakeward slope of the second bar, even though the depth-of-activity was consistently between 0.06 and 0.08 m. There was no evidence for erosion of the lakeward slope as hypothesized on the basis of the measured sediment flux. The outer bar remained essentially unaltered by the June 16 storm; bed elevation changes were all within the measurement error for the rods of $\pm$ 0.01 m, even though depths of activity over this feature were at least as large as those measured over the second bar.

These measurements of depth-of-activity and bed elevation change, especially over the two inner

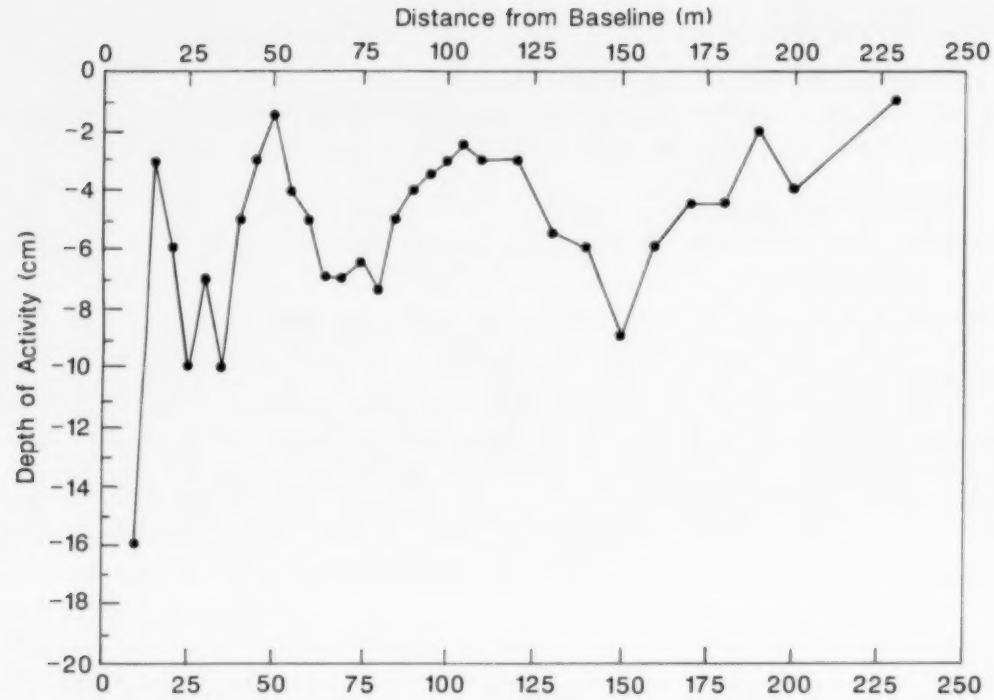
Distance from Baseline (m)
Depth of Activity (cm)
0
-2
-4
-6
-8
-10
-12
-14
-16
-18
-20
0 25 50 75 100 125 150 175 200 225 250

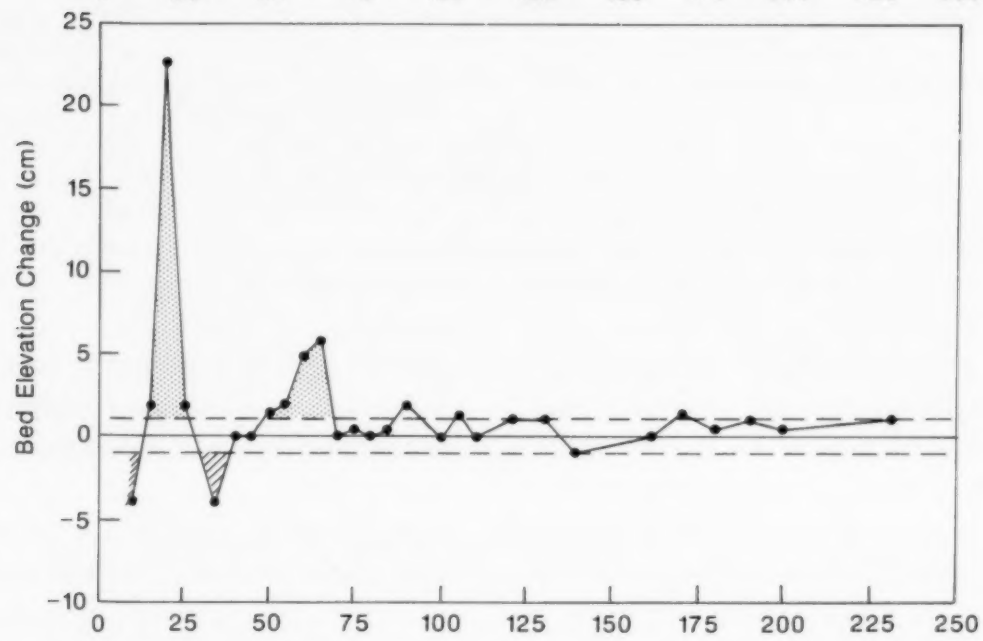
Bed Elevation Change (cm)
25
20
15
10
5
0
-5
-10
0 25 50 75 100 125 150 175 200 225 250

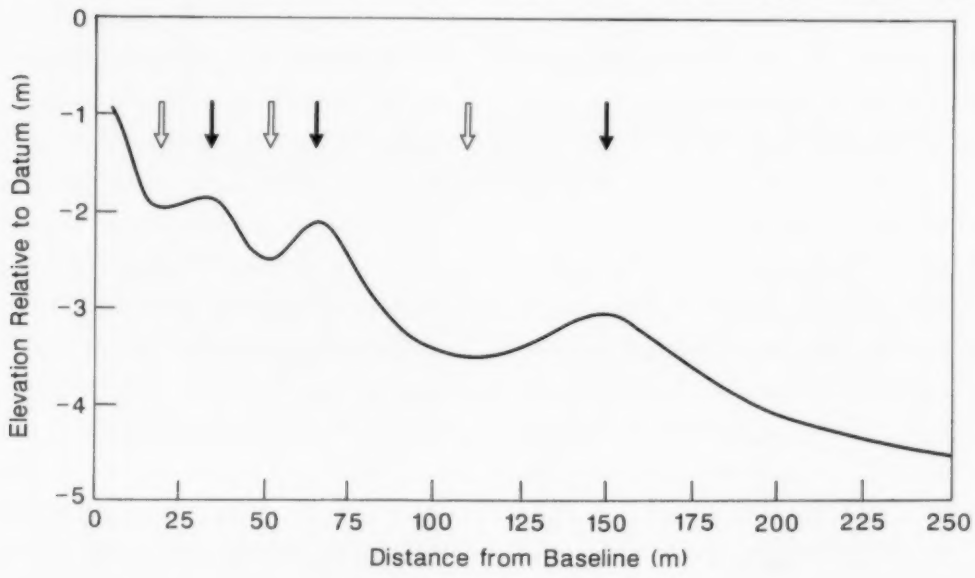
Elevation Relative to Datum (m)
0
-1
-2
-3
-4
-5
0 25 50 75 100 125 150 175 200 225 250
Distance from Baseline (m)

bars, are consistent with previous measurements in this area. For example, Greenwood (1987) reported a simple, inverse linear relationship between depth of re-activation and water depth; local increases and decreases in depth-of-activity were associated, respectively, with the bar crests and troughs. Furthermore, the bar crests experienced sediment accretion while the troughs were eroded; in this way, the bar relief generally increased during storms. Small topographic displacements occurred around average forms such that the bars exhibited a dynamic equilibrium with the prevailing storm-wave climate. The large total time-integrated sediment volume fluxes and the small net volume fluxes measured over several storm events during this study, together with the morphological adjustments recorded during the June 16 storm, would indicate that the Bluewater bars were also in a state of dynamic equilibrium.

Discussion

Field measurements presented in this paper demonstrate that both the time-averaged (mean) cross-shore current and oscillatory currents at various frequencies are critical in determining the local net suspended sediment transport rate across a barred shoreface. Co-spectral analyses of cross-shore velocities and suspended sediment concentrations reveal that grouped, non-linear shoaling waves can induce large onshore sediment transport rates at wind-wave frequencies, while simultaneously producing offshore transport rates at low frequencies. This pattern is essentially similar to that reported earlier for a non-barred shoreface by OG92 (see also Huntley and Hanes, 1987). The propagation of skewed, asymmetric waves in the shoaling zone induces larger onshore velocities within the wave cycle leading to a greater resuspension of sediment and also to a net onshore suspended sediment transport (see also Doering and Bowen, 1989). Outside the surf zone, the resuspension of sediment under groups of large waves is coherent with the offshore phase of a low frequency modulation of the velocity field forced by a group-bound, forced long wave in the manner proposed by Longuet-Higgins and Stewart (1962). The resultant net suspended sediment transport associated with these low frequency oscillations is thus invariably directed offshore, owing to the strong "flux coupling" between the offshore flow associated with the bound long wave (Wells, 1967; Larsen, 1982; Shi and Larsen, 1984) and the large sediment concentrations induced by the larger than average waves constituting the wave group (Greenwood and Osborne, 1992; Osborne and Greenwood, 1992b). Furthermore, under certain conditions the group-bound long waves can dominate the net oscillatory component of suspended sediment transport.

It is evident from the analyses presented in this paper that low frequency waves, other than those associated with wave groups, play an important role in suspended sediment transport across a barred shoreface. Landward of the zone of wave breaking on the bar crests and upper lakeward slope, the wave group structure is diminished; nevertheless, a low frequency modulation of the velocity field is still observed and in fact its magnitude, relative to that of the incident frequency, is larger than its counterpart outside the surf zone. This low frequency wave is not, however, coincident in frequency with that of the group-bound, forced long wave in the shoaling zone and may induce significantly larger absolute and net oscillatory suspended sediment transport than that induced by either the shoaling or breaking wind waves. Another difference with the group-forced wave is that a net onshore transport of suspended sediment may result from the "flux coupling" between large sediment concentrations and the onshore phases of these secondary low frequency oscillations. The waves contributing to this low frequency modulation of the velocity field are not defined in this paper, but may be edge waves and/or reflected long waves (see for example, Bowen

Fig. 12. Elevation, bed-elevation change and depth-of-activity across the upper shoreface. Note: stippling represents accretion and cross-hatching erosion; horizontal dashed lines on the bed elevation change graph represent the measurement error of ± 1 cm. Solid circles are rod measurements; solid and open arrows denote location of pre-storm crest and trough, respectively.

and Huntley, 1984; Kim and Huntley, 1986) in either standing or progressive modes. Previous studies have confirmed the generation of edge waves by storms both in this particular environment (e.g. Bauer and Greenwood, 1990) and elsewhere (e.g. Huntley, 1976; Huntley et al., 1981), but it is clear from other work that leaky long waves are also generated in barred surf zones (e.g. Suhayda, 1974; Katoh, 1984; Wright et al., 1986). Certainly the large magnitudes of suspended sediment transport attributable to the low frequency motions in the surf zone at Bluewater Beach supports the notion that long waves may dominate both the sediment flux and the morphodynamic response under highly energetic conditions (e.g. Holman, 1981; Guza and Thornton, 1982; Bowen and Huntley, 1984).

Under non-linear shoaling and breaking waves the co-spectral signatures were often complex, indicating a constraint upon sediment transport other than the distribution of kinetic energy across frequency space. As waves increased in height to breaking and then subsequently decreased, the oscillatory suspended sediment transport at wind-wave frequencies showed a marked variation associated with changes in bottom roughness (bedforms). Asymmetric vortex ripples were associated consistently with a net onshore oscillatory transport by the wind waves; this transport direction was observed to reverse with increasing wave asymmetry and the onset of post-vortex ripples. Such bedform-sediment transport relationships are consistent with the relatively few laboratory measurements available. Inman and Bowen (1962), for example, indicate that with relatively small asymmetries in the oscillatory velocity field directed in the direction of wave propagation, the net sediment transport was also in this direction. However, as velocity asymmetries favouring the positive phase of wave motion increased, net sediment transport actually decreased and, in one case, reversed. This was a response to the larger sediment concentrations in separation vortices induced by the positive phase of the fluid motion, which, upon ejection from the bed, were in phase with the reversal of the fluid motion. Tanaka and Shuto (1987) demonstrate both theoretically and empirically the existence of an upwave lagrangian fluid motion over steep asymmetric ripples.

More recently, Osborne and Greenwood (1992a) point out that both the regularity with which coherent separation vortices are ejected from the bed and the vertical propagation speed of re-suspended sediment will affect correlations between sediment concentration and horizontal velocity at any given elevation and at any given frequency. For example, as oscillatory speeds increase larger volumes of suspended sediment may be carried to higher elevations in the flow by the associated turbulence; a longer time interval for particle settling will therefore be necessary. As a result, sediment may remain in suspension longer and subsequently correlate more effectively with the lower frequency motions.

Across a non-barred shoreface (OG92, their fig. 12), the mean suspended sediment transport rate exhibited a simple, spatially monotonic dependence upon depth as a result of a similar monotonic dependence of both the mean suspended sediment concentration and the mean current (at least offshore of local rip currents). During the small storm monitored at Bluewater Beach, the relative magnitudes of the mean and the net oscillatory components of suspended sediment transport varied through both space and time. At the storm peak when re-suspension of sediment reached a maximum, the time-averaged cross-shore currents (undertows) were critical in determining the local balance of sediment transport, both in terms of magnitude and direction.

The bar topography exerts an important constraint on both the magnitude and direction of transport by the oscillatory and mean currents. Although the bar crest experienced the largest oscillatory currents and greatest levels of turbulence as a result of wave breaking, the net suspended sediment transport rates were minimal, resulting from a near-balance between the mean transport rate directed offshore by undertows and the net onshore oscillatory transport rate controlled by the skewed, asymmetric waves at or close to breaking. Oscillatory transport rates at wind-wave frequencies decreased with increasing water depth both landward and lakeward of the bar crest; here the net oscillatory transport rates

may be dominated either by long waves or by quasi-steady currents (undertows). Offshore transport across the landward slope will also be constrained by an onshore gravity potential; the converse is true for onshore transport on the lakeward slope, although here the effect should be significantly smaller.

Although only suspended load was monitored in this experiment (and then at only two points in the vertical), the spatial variations in sediment transport do concur with the pattern of accretion, erosion and bar morphodynamics, which resulted from the June 16 storm. Accretion on the crest and upper landward slope of the second bar, coupled with erosion of the trough to landward, caused an increase in topographic relief and a landward migration of the second bar; this pattern of sediment convergence resulted directly from net offshore transport rates in the trough driven by the mean currents (undertows) and near-zero net transport rates across the bar crest. The latter reflect a balance between offshore transport, due to mean currents and group-bound long waves, and onshore transport, induced by the skewed oscillatory velocity field under near-breaking and breaking waves. The large and persistent sediment flux gradient between the near-zero net transport on the bar crest and the net offshore transport on the lower lakeward slope suggested a potential for erosion of the lower lakeward slope. This was not supported by measured bed elevation changes. Since sediment re-activation was significant across the lakeward slope, it is possible that material was indeed removed from the lower lakeward slope during the storm peak and deposited in the outer trough; this could have been balanced by sediment transported across the bar crest by the mean flow and the downslope component of gravity or by a return of sediment late in the storm, when the lakeward slope was once more dominated by shoaling wind waves.

Conclusions

Important contributions to the rates of cross-shore suspended sediment transport on a barred beach are made by:

(1) a mean transport induced by time-averaged ("quasi-steady") currents exhibiting characteristics of set-up driven undertows;

(2) a net oscillatory transport determined by the interaction of oscillatory currents at wind-wave and low frequencies. Outside the surf zone the latter are a response to the presence of group-bound, forced long waves; inside the surf zone the low frequency modulation is no longer driven by the wave groups, but is secondary in origin and at significantly lower frequencies.

The local net suspended sediment transport rate at any point across a barred shoreface is the resultant sum of the transport vectors attributable to "quasi-steady" currents and the various frequencies of oscillatory motion. A zero net suspended sediment transport rate, resulting in a local sediment mass balance, can therefore be achieved even when individual transport rates may be extremely large. Furthermore, both the relative magnitudes and the directions of the individual suspended sediment transport components vary spatially across the barred profile. In contrast with the non-barred shoreface examined in OG92, where variations followed a simple monotonic pattern with increasing depth across shore, spatial variations in the transport components on the barred shoreface were constrained with respect to position relative to the bar crests. Both the absolute magnitude and the net oscillatory transport of suspended sediment at the incident wave frequency increase landward up the lakeward slope of the bar, with the latter being directed landward as a result of the large skewness and asymmetry in the velocity field induced by the non-linear shoaling waves. These components both decrease shoreward of the bar crest as near-bed oscillatory velocities induced by the wind waves are reduced as a result of dissipation during wave breaking near the bar crest and the propagation landward into increasing water depths over the landward slope and trough. The net oscillatory suspended sediment transport rate induced by low frequency waves increases both landward and lakeward of the breaker zone on the bar crest, as does the mean suspended sediment transport rate. However, while the low frequency motion due to group-bound long waves transports sediment offshore over the shoaling slope as in the case of the non-barred shoreface

(OG92), the secondary low frequency modulation induced by wave breaking may transport suspended sediment shoreward. Without more detailed information on the structure of the secondary wave however, it is not possible to be definitive in its role in the maintenance of the bar form.

Acknowledgements

This is a contribution from the Canadian Coastal Sediment Transport Programme (C-COAST) supported by Strategic Grants from the Natural Sciences and Engineering Research Council of Canada to B. Greenwood and A.J. Bowen. P.D. Osborne acknowledges support in the form of a post-graduate scholarship from the same body. We would like to thank R. Brander, J. Ollerhead, N. Sela, and Xu Zhiming from the University of Toronto, and D. Hazen, and S. McLean from Dalhousie University for their assistance in data collection and processing; Dr. David Huntley is to be thanked for fruitful discussion. The support of the Academic Workshops and Graphics Department at the Scarborough Campus of the University of Toronto is also gratefully acknowledged.

References

Bauer, B.O. and Greenwood, B., 1990. Modification of a linear bar-trough system by a standing edge wave. Mar. Geol., 92: 177–204.

Beach, R.A. and Sternberg, R.W., 1988. Suspended sediment transport in the surf zone: response to cross-shore infragravity motion. Mar. Geol., 80: 61–79.

Bowen, A.J. and Huntley, D.A., 1984. Waves, long waves and nearshore morphology. Mar. Geol., 60: 1–14.

D and A Instruments and Engineering, 1988. Optical Backscatterance Turbidity Monitor-Instrumentation Manual. 32 pp.

Davidson-Arnott, R.G.D. and McDonald, R.A., 1989. Nearshore water motion and mean flows in a multiple parallel bar system. Mar. Geol., 86: 321–338.

Dixon, W.J. (Editor), 1985. BMDP Statistical Software, 1985 Printing. Univ. California Press, Berkeley, 734 pp.

Doering, J.C. and Bowen, A.J., 1989. Wave-induced flow and nearshore suspended sediment. Proc. 21st Coastal Eng. Conf. (Malaga, Spain). Am. Soc. Civ. Eng., New York, pp. 1452–1463.

Downing, J.P., Sternberg, R.W. and Lister, C.R.B., 1981. New instrumentation for the investigation of sediment suspension processes in the shallow marine environment. Mar. Geol., 42: 19–34.

Greenwood, B., 1987. Sediment balance and bar morphodynamics in a multiple bar system: Georgian Bay, Canada. In: V. Gardiner (Editor), International Geomorphology 1986, Part I. Wiley, Chichester, pp. 1119–1143.

Greenwood, B. and Osborne, P.D., 1990. Vertical and horizontal structure in cross-shore flows: an example of undertow and wave set-up on a barred beach. Coastal Eng., 14: 543–580.

Greenwood, B. and Osborne, P.D., 1991. Equilibrium slopes and cross-shore velocity asymmetries in a storm-dominated, barred nearshore system. Mar. Geol., 96: 211–235.

Greenwood, B. and Osborne, P.D., 1992. Wave groups and the re-suspension and transport of sand in the nearshore: 1. A time series analysis. In: B. Greenwood and E. Mansard (Editors), Wave Groups: Their Role in Nearshore Dynamics and Engineering Design. Assoc. Comm. Shorelines, Natl. Res. Counc. Can., Ottawa, in press.

Greenwood, B. and Sherman, D.J., 1984. Waves, currents, sediment flux and morphological response in a barred nearshore system. Mar. Geol., 60: 31–61.

Greenwood, B. and Sherman, D.J., 1986a. Longshore current profiles and lateral mixing across the surf zone of a barred nearshore. Coastal Eng., 10: 149–168.

Greenwood, B. and Sherman, D.J., 1986b. Hummocky cross-stratification in the surf zone: flow parameters and bedding genesis. Sedimentology, 33: 33–45.

Greenwood, B. and Sherman, D.J., 1988. Bedforms and roughness in prototype surf zones. Proc. Workshop on Roughness and Friction. Assoc. Comm. Shorelines, Natl. Res. Counc. Can., Ottawa, pp. 45–59.

Greenwood, B., Osborne, P.D., Bowen, A.J., Hazen, D.G. and Hay, A.E., 1990. C-Coast: The Canadian Coastal Sediment Transport Programme. Proc. Can. Coastal Conf. (Kingston, Ont.). Natl. Res. Counc. Can., Ottawa, pp. 319–336.

Greenwood, B., Osborne, P.D., Bowen, A.J., Hazen, D.G. and Hay, A.E., 1991a. Nearshore sediment flux and bottom boundary dynamics: The Canadian Coastal Sediment Transport Programme (C-Coast). Proc. 22nd Coastal Eng. Conf. (Delft, The Netherlands). Am. Soc. Civ. Eng., New York, pp. 2227–2240.

Greenwood, B., Osborne, P.D., Bowen, A.J., Hazen, D.G. and Hay, A.E., 1991b. Measurements of suspended sediment transport in prototype shorefaces: the Canadian Coastal Sediment Transport Programme (C-Coast). Proc. Coastal Sediments '91. (Seattle, Wash.). Am. Soc. Civ. Eng., New York, pp. 284–289.

Guza, R.T. and Thornton, E.B., 1982. Swash oscillations on a natural beach. J. Geophys. Res., 87: 483–491.

Hazen, D.G., Greenwood, B. and Bowen, A.J., 1991. Nearshore current patterns on barred beaches. Proc. 22nd Coastal Eng. Conf. (Delft, The Netherlands). Am. Soc. Civ. Eng., New York, pp. 2061–2072.

Holman, R.A., 1981. Infragravity energy in the surf zone. J. Geophys. Res., 86: 6442–6450.

Huntley, D.A., 1976. Long period wave motion on a natural beach. J. Geophys. Res., 81: 6441–6449.

Huntley, D.A. and Hanes, D.M., 1987. Direct measurement of suspended sediment transport. Coastal Sediments '87. (New Orleans). Am. Soc. Civ. Eng., New York, pp. 723–737.

Huntley, D.A., Guza, R.T. and Thornton, E.B., 1981. Field

observations of surf beat: 1. Progressive edge waves. J. Geophys. Res., 86: 6451–6466.

Inman, D.L. and Bowen, A.J., 1962. Flume experiments on sand transport by waves and currents. Proc. 8th Coastal Eng. Conf. Am. Soc. Civ. Eng., New York, pp. 137–150.

Katoh, K., 1984. Multiple longshore bars formed by long period standing waves. Rep. Port Harbour Res. Inst., 23: 3–46.

Kim, C.S. and Huntley, D.A., 1986. On time delays in the nearshore zone between onshore and longshore currents at incident wave frequencies. J. Geophys Res., 91: 3967–3978.

Larsen, L.H., 1982. A new mechanism for seaward dispersion of mid-shelf sediments. Sedimentology, 29: 279–284.

Longuet-Higgins, M.S. and Stewart, R.W., 1962. Radiation stress and mass transport in gravity waves, with application to "surf beats". J. Fluid Mech., 13: 481–504.

Nielsen, P., 1984. Field measurements of time-averaged suspended sediment concentrations under waves. Coastal Eng., 8: 51–72.

Ollerhead, J., 1989. Bedform geometry and dynamics during storms in a barred nearshore zone, Bluewater Beach, Ontario, Canada. M.Sc. Thesis, Univ. Toronto, 173 pp. (Unpubl.).

Ollerhead, J. and Greenwood, B., 1990. Bedform geometry and dynamics in the upper shoreface, Bluewater Beach, Ontario, Canada. Proc. Can. Coastal Conf. (Kingston, Ont.). Assoc. Comm. Shorelines, Natl. Res. Counc. Can., Ottawa, pp. 337–348.

Osborne, P.D. and Greenwood, B., 1991. Set-up driven undertows on a barred beach. Proc. 22nd Coastal Eng. Conf. (Delft, The Netherlands). Am. Soc. Civ. Eng., New York, pp. 227–240.

Osborne, P.D. and Greenwood, B., 1992a. Sediment suspension under waves and currents: time scales and vertical structure. Sedimentology, (submitted).

Osborne, P.D. and Greenwood, B., 1992b. Wave groups and the re-suspension and transport of sand in the nearshore: 2. A spectral analysis. In: B. Greenwood and E. Mansard (Editors), Wave Groups: Their Role in Nearshore Dynamics and Engineering Design. Assoc. Comm. Shorelines, Natl. Res. Counc. Can., Ottawa, in press.

Osborne, P.D. and Greenwood, B., 1992c. Frequency dependent cross-shore suspended sediment transport. 1. A non-barred shoreface. Mar. Geol., 106: 1–24.

Osborne, P.D., Greenwood, B. and Bowen, A.J., 1990. Cross-shore suspended sediment transport on a non-barred beach: the role of wind waves, infragravity waves and mean flows. Proc. Can. Coastal. Conf. (Kingston). Natl. Res. Counc. Can., Assoc. Comm. Shorelines, pp. 349–361.

Shi, N.C. and Larsen, L.H., 1984. Reverse sediment transport induced by amplitude modulated waves. Mar. Geol., 60: 199–218.

Suhayda, J.N., 1974. Standing waves on beaches. J. Geophys. Res., 79: 3065–3071.

Symonds, G. and Bowen, A.J., 1984. Interactions of nearshore bars with incoming wave groups. J. Geophys. Res., 89: 1953–1959.

Tanaka, H. and Shuto, N., 1987. Velocity measurements of wave-current combined motion over an asymmetric rippled bed. Coastal Sediments '87. (New Orleans). Am. Soc. Civ. Eng., New York, pp. 379–392.

Thornton, E.B., Galvin, J.J., Bub, F.L. and Richardson, D.P., 1977. Kinematics of breaking waves. Proc. 15th Coastal Eng. Conf. (Honolulu). Am. Soc. Civ. Eng., New York, pp. 461–476.

Wells, D.R., 1967. Beach equilibrium and second order wave theory. J. Geophys. Res., 72: 497–504.

Wright, L.D., Nielsen, P., Shi, N.C. and List, J.H., 1986. Morphodynamics of a bar-trough surf zone. Mar. Geol., 70: 251–285.

Marine Geology, 106 (1992) 53–68
Elsevier Science Publishers B.V., Amsterdam

Preliminary interpretation of aeromagnetic data from Spitsbergen, Svalbard Archipelago (76°–79°N): Implications for structure of the basement

Jan Reidar Skilbrei

Norges Geologiske Undersøkelse, P.O. Box 3006 Lade, 7002 Trondheim, Norway

(Received June 7, 1991; revision accepted November 4, 1991)

ABSTRACT

Skilbrei, J.R., 1992. Preliminary interpretation of aeromagnetic data from Spitsbergen, Svalbard Archipelago (76°–79°N): Implications for structure of the basement. *Mar. Geol.*, 106: 53–68.

New Arctic aeromagnetic data from Spitsbergen, Svalbard Archipelago, have been interpreted. The depths to the top of the magnetic source rocks have been interpreted using profile data, and the interpretation shows that the magnetic basement is deeper than 3 km below sea level over large areas. A picture of basement horsts and grabens emerges from this map. A deep N–S trending trough, more than 8 km deep, exists beneath Isfjorden. It has a graben structure and is bordered to the east by a southward extension of the Billefjorden Fault Zone. Model calculations show that steep east-dipping structures in the pre-Devonian Hecla Hoek basement rocks can explain anomalies above the Billefjorden Fault Zone. The Billefjorden Fault Zone is interpreted to extend from the shelf north of Spitsbergen to south of Isfjorden and may extend southwards into the Barents Sea.

A new aeromagnetic map covering Spitsbergen and the adjacent northern Barents Sea has been compiled which shows that structures on Spitsbergen continue far into the Barents Sea.

Some of the anomalies that originate within the crystalline basement occur near the boundaries to younger sedimentary basins and suggest that basement tectonics have influenced basin formation.

Introduction

The Spitsbergen aeromagnetic survey (SPA-88) was conducted in 1988 by *Norges Geologiske Undersøkelse* (NGU) in co-operation with Geco a.s. covering the southern two-thirds of Spitsbergen, the principal island of the Svalbard Archipelago (Fig.1). This new Arctic aeromagnetic data set, in addition to recent surveys in Canada (Nelson et al., 1991), is some of the highest resolution aeromagnetic data obtained this far north. The systematic pattern of flight lines provides data along E–W (4 km spacing) and N–S lines (spacing varies; 12 and 24 km). Data sets and quality are described later.

Correspondence to: J.R. Skilbrei, Geological Survey of Norway, P.O. Box 3006 Lade, Trondheim, N-7002, Norway.

While studies of geology and Landsat images (Ohta, 1982a) from Svalbard have provided information on surface geology and structural geology, geophysical data are needed to interpret and quantify the deep geology in terms of depth to the concealed basement, structure of the basement, and offshore extension of structural elements. In the last few years reflection seismic data have been collected from the fjords, which provide structural information along a few lines (Eiken, 1985; Eiken and Austegaard, 1987; Faleide et al., 1991). Seismic data provide some constraints on the interpretation of aeromagnetic data. Over most of Spitsbergen the new aeromagnetic data reported here provide the only geophysical information on upper crustal structure. Quantitative interpretations of these data (depth to basement) play an important role in understanding the three-dimensional geological structure.

0025-3227/92/$05.00

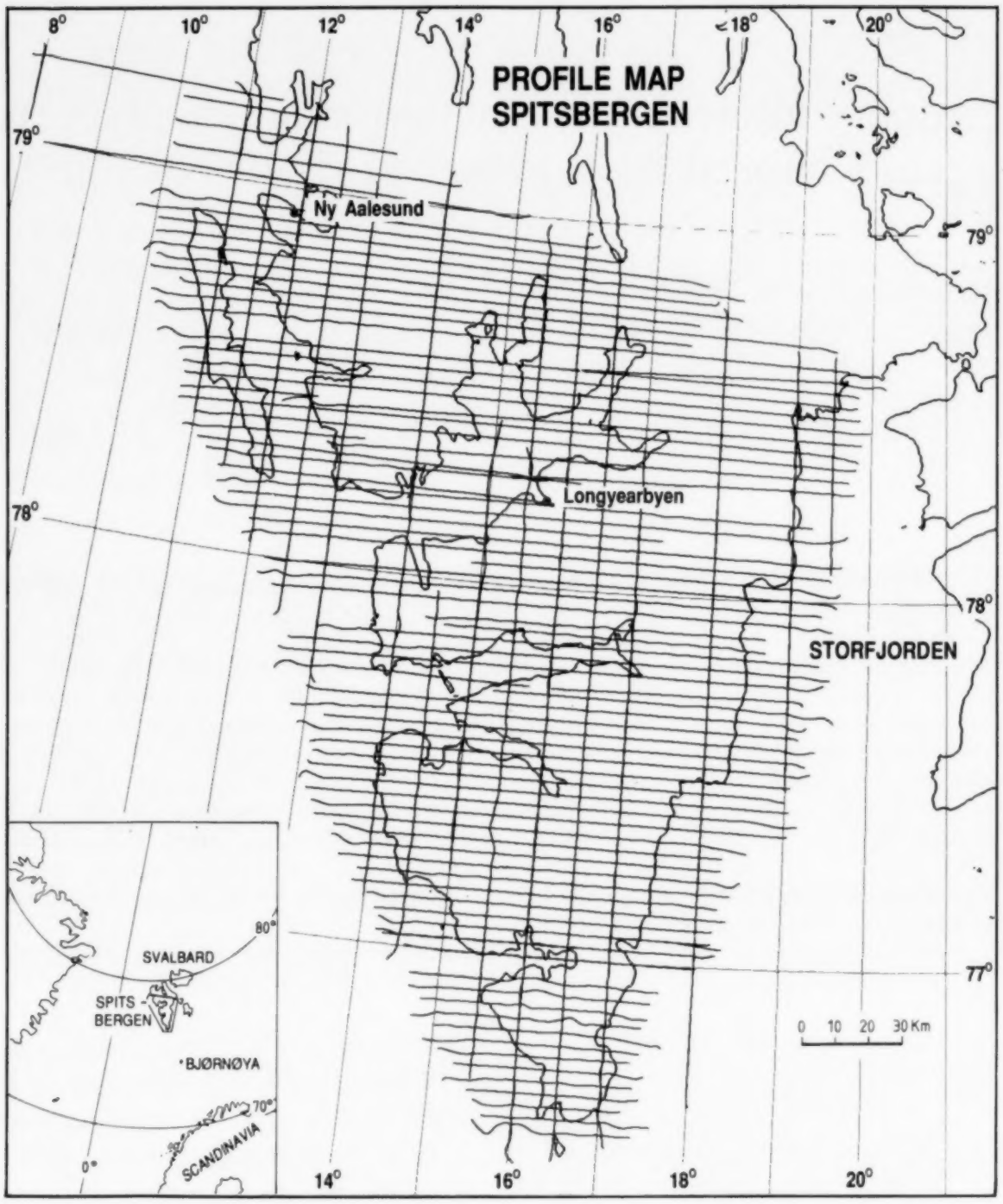

Fig.1. Flight lines used in gridding of aeromagnetic data. The inset shows the location of the survey area on Spitsbergen, the main island within the Svalbard Archipelago.

The author has analyzed each individual profile record displaying the following information: measured anomalies, calculated first vertical derivative of the anomalies, radar altimetry, magnetic base data and surface geology. Thus, it was possible to carefully check measured anomalies for occurrences of diurnal noise, topographic effects in the data and expressions of surface geology.

General geology and tectonic setting

Spitsbergen is the principal island of the Svalbard Archipelago. Svalbard is covered by geological maps at a scale of 1:500,000 (Flood et al., 1971; Winsnes and Worsley, 1981; Hjelle and Lauritzen, 1982; Lauritzen and Ohta, 1984). The Precambrian and Early Palaeozoic basement on Spitsbergen, the so-called Hecla Hoek (HH) rocks, forms the

crystalline basement to the Devonian and younger, unmetamorphosed, sedimentary rocks. HH rocks occur in Ny Friesland (northeast Spitsbergen) and along the West Spitsbergen Tertiary Orogenic Belt (Fig.2). The Orogenic Belt (also called the Tertiary Fold and Thrust Belt) is probably the result of transpression that accompanied dextral strike-slip plate motions between North Greenland and Svalbard during the opening of the North Atlantic Ocean (Harland, 1965, 1966, 1969; Talwani and Eldholm, 1977; Eldholm et al., 1987; Myhre and Eldholm, 1988). The main Tertiary deformation front follows the contact between HH rocks and post-Devonian sediments in West Spitsbergen (Fig. 2). The Old Red Sandstone is mainly preserved in the Devonian graben in central-northern Spitsbergen. The Tertiary Central Basin is elongated along a NNW–SSE trend in central-south Spitsbergen. Mesozoic sedimentary rocks occur as a belt to the west, north and east of the Central Basin/Graben.

Mid-Palaeozoic Caledonian deformation and metamorphism in Svalbard was followed by Late Devonian faulting along a NNW-SSE trend (Harland et al., 1974; Hjelle and Lauritzen, 1982). The Hornsund Fault Zone (HFZ), the Billefjorden Fault Zone (BFZ) and the Lomfjorden Fault (LF) are important basement lineaments (e.g. Harland et al., 1974). The HFZ is close to the continent–ocean boundary offshore west of Svalbard (Sundvor and Eldholm, 1976; Myhre and Eldholm, 1988). The BFZ is the border fault between Devonian rocks (Old Red Sandstone) to the west and a basement horst comprising HH rocks on Ny Friesland (northeast of Isfjorden). South of Isfjorden, the BFZ may border the Palaeogene Central Basin where it is covered by the Tertiary sediments (Mann and Townsend, 1989). The LF is associated with an area of flexure development and differential movements in Palaeozoic, Mesozoic and Cenozoic times (Steel and Worsley, 1984; Andresen et al., 1988), and may represent an important basement fault zone. How far the BFZ and the LF extend to the south cannot be deduced from surface geology.

Data set and data quality

A total of 13,320 profile kilometres were acquired along a network with 4 km spacing between E–W lines and 12, 24 and 36 km between N–S tie lines (Fig.1). The flight altitude was 1000 m above sea level south of 77°N, and 1600 m to the north of this line.

Satellite navigation (GPS) was used in conjunction with a precise radio positioning system operating in the UHF range (SYLEDIS chain). The majority of the profile data were recovered using GPS (88.4%). Comparisons of GPS-SYLEDIS positional fixes revealed that the two positions generally agree to within ± 50 m. Careful checking of the acquired position data revealed a few cases of major departures from pre-plotted survey lines. Errors were corrected by applying linear interpolation assuming that the aircraft had followed a straight line.

Base station magnetometers were recorded in Longyearbyen and at Nordlysobservatoriet in Ny Ålesund (Fig.1). The data from Longyearbyen were used by the author to choose the best periods for acquisition, and to decide which lines to re-fly because of magnetic time variation (diurnal noise).

In preparing the diurnal correction, the following considerations were made, based on the experiences from the northern Barents Sea aeromagnetic survey (Skilbrei, 1988a; Skilbrei et al., 1990). Simple diurnal subtraction of low-pass filtered base magnetic data from the best base station (with respect to location and phase correlation) was superior to applying phase corrections and a weighted use of two base stations. Visual inspections of magnetic data revealed a relatively high degree of correlation between the recorded data and the high-frequency diurnal noise (Skilbrei, 1988b). Even so, to avoid introducing noise, the base data were low-pass filtered prior to diurnal subtraction of the base magnetic data. A 50-km cut-off filter applied to base data was chosen (50 km is approximately equal to the length of the shortest E–W lines).

Conditions were better in Longyearbyen than in Ny Ålesund (Skilbrei, 1988b). This is probably due to the fact that Longyearbyen is near the centre of the survey area, whereas Ny Ålesund is located in the extreme northwest.

The final map was prepared for an elevation of 1600 m. The 1000 m data were upwards continued to fit the 1600 m data. Visual inspection showed

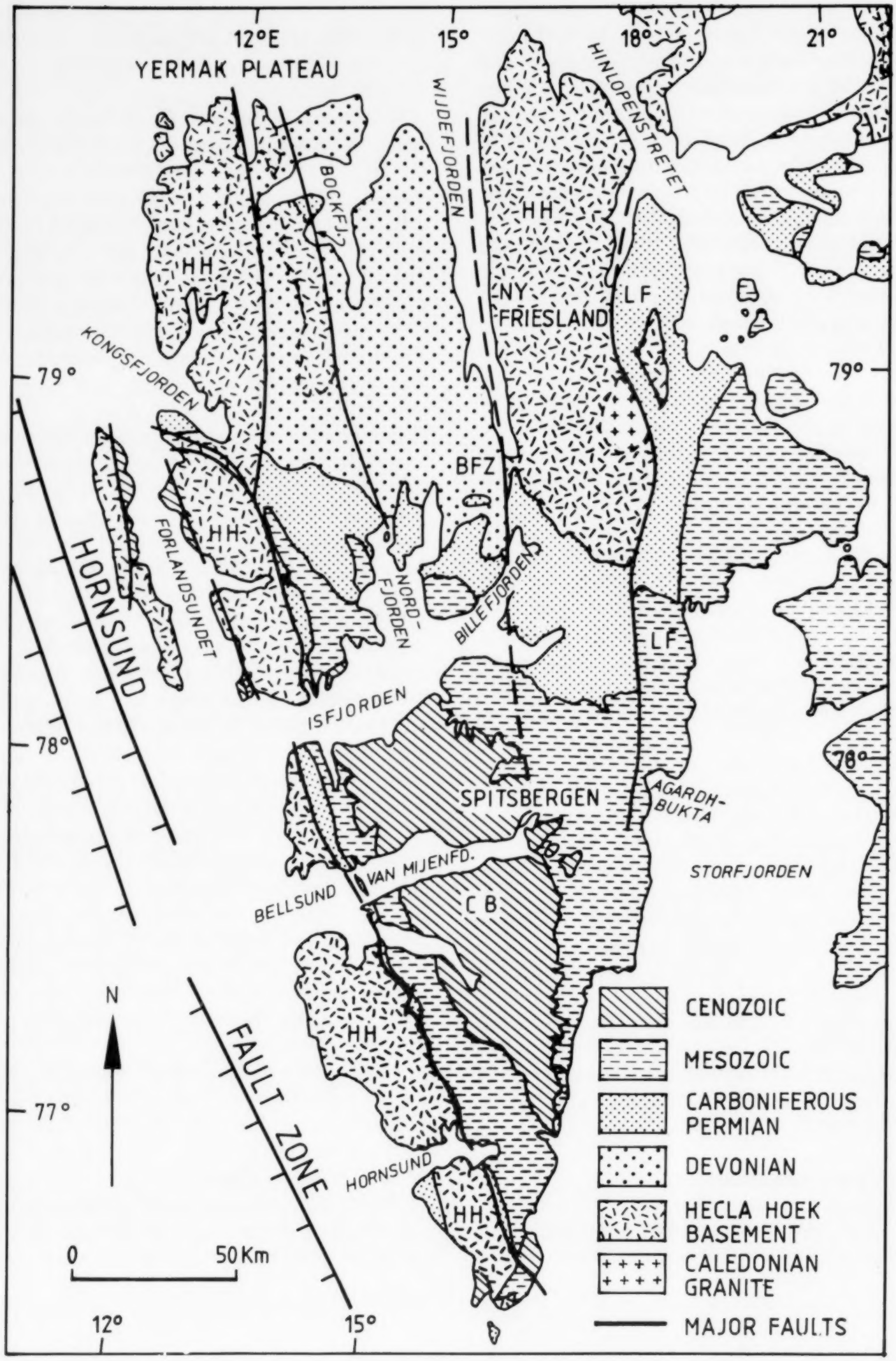
12°E
15°
18°
21°
YERMAK PLATEAU
WIJDEFJORDEN
HINLOPENSTRETET
BOCKFJ.
HH
NY FRIESLAND
LF
KONGSFJORDEN
79°
BFZ
FORLANDSUNDET
NORD-FJORDEN
BILLEFJORDEN
HORNSUND
ISFJORDEN
78°
SPITSBERGEN
AGARDH-BUKTA
VAN MIJENFD.
STORFJORDEN
BELLSUND
C B
N
77°
FAULT ZONE
0
50 Km
CENOZOIC
MESOZOIC
CARBONIFEROUS PERMIAN
DEVONIAN
HECLA HOEK BASEMENT
CALEDONIAN GRANITE
MAJOR FAULTS

that a profile continuation method was superior to grid continuation in the transfer zone between the two data sets; this method was therefore chosen. The final profiles, on which the depth estimates were made, display versions of these lines both at the original acquisition elevation and at the upward continued elevation. Some lines were flown at both elevations in order to enable comparison of the results of the upward continuation method with the measured field at that higher level. The agreement turned out to be good, which means that the 2-D continuation hypothesis (profile continuation method) was a good approximation for the anomalies in question.

After diurnal correction and systematic line level correction, 6.24 nT average deviations remained at line crossings. The anomalies in the survey area are of generally low amplitude (Fig.3). This, combined with the problem of relatively poor tie-line control, caused problems in the map preparation (see later). A manual first-order correction to six of the tie-lines was therefore applied. Seven lines showing diurnal noise were not used in the map preparation. This procedure reduced the average mistie value for the diurnal corrected data (50 km-filtered base data from Longyearbyen) to 4.65 nT. Line effects are visible over the eastern areas where the magnetic field is almost flat. The IGRF-85 model for May 1988 has been subtracted from the recorded data.

Contour maps "filter out" much of the original information content of the data relating to faint features associated with geological structure and trend (Lee et al., 1990). A colour shaded relief map (Fig.4) of the residual total field component is presented which contains information on both anomaly amplitude (colour) and anomaly trend (relief). Illumination is from the east. The shaded relief presentation emphasizes anomalies that strike at a high angle to E–W, and de-emphasize E–W striking anomalies. The map covers both the SPA-88 survey area and the adjacent northern Barents Sea area which was covered by measurements in 1987 (Skilbrei, 1988a; Skilbrei et al., 1990). The map is produced using an Applicon ink-jet plotter which utilizes a programme system developed by Kihle (1985). The Barents Sea data were upward continued to a common level (from 330 m to 1600 m above sea level) to minimize differences between the data sets at their overlap regions. The upward continuation is effectively a smoothing operator and places a lower limit on wavelength of anomaly that may be resolved. Together with the 4 km line spacing, Figs.3 and 4 adequately resolve anomaly wavelengths of about 10 km and greater corresponding to geological features of similar scale. The minimum curvature method of Briggs (1974) was used to grid the data.

Interpretation

General features of the aeromagnetics

Generally, the magnetic trends are NW–SE to NNW–SSE for the whole of the map area, except for the Billefjorden-Wijdefjorden area where the positive magnetic trend is N–S (Figs.3 and 4). It is interesting that the NW–SE to NNW–SSE trend is parallel to the Tertiary Fold and Thrust Belt along western Spitsbergen.

Low- to medium-wavelength anomalies of moderate amplitudes (< 200 nT) occur above the HH basement rocks within the West Spitsbergen Orogenic Belt. During interpretation, the aeromagnetic profiles were placed upon geological maps at the scale 1:500,000. In many areas it was possible to isolate anomalies caused by individual sources within the HH basement. For instance, on the western part of Prins Karls Forland (PKF), short-wavelength magnetic anomalies occur directly above outcropping volcanic formations that are areally significant (Hjelle et al., 1979, detailed geological map in fig.1, p.147). The statement of Kurinin (1965), claiming that HH rocks are practically non-magnetic, is therefore not generally valid.

A belt of low magnetization level trends NNW–

Fig.2. Simplified geological map of Svalbard. *BFZ* = Billefjorden Fault Zone. *LF* = Lomfjorden Fault. *CB* = Central (Tertiary) Basin. The reader may readily observe interesting correlations by photocopying this figure onto a clear base, and overlaying it on Figs. 3 and 4 (the same scale is used in all three illustrations).

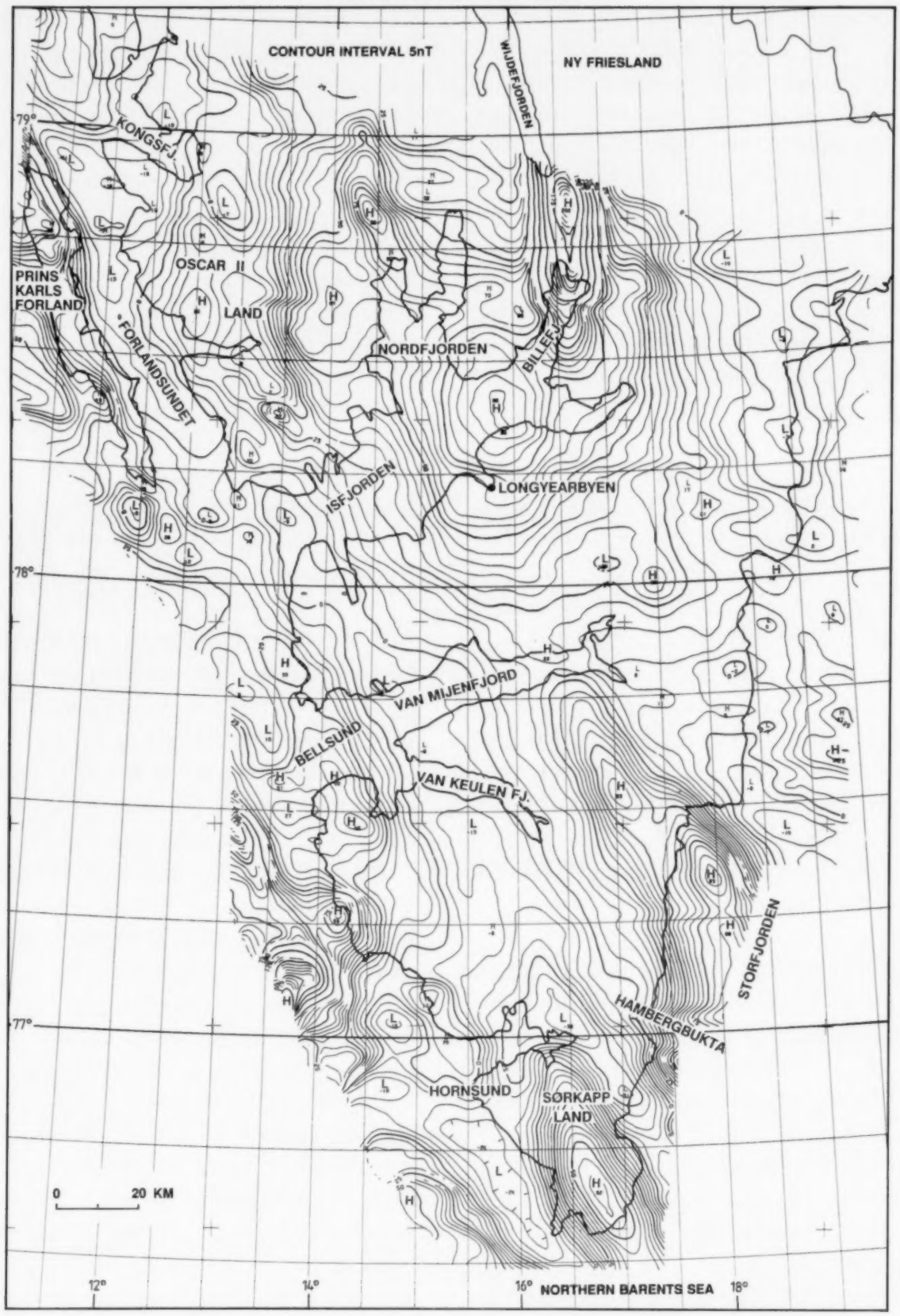

Fig.3. Residual aeromagnetic map of Spitsbergen. The contour interval is 5 nT. *H* denotes high and *L* denotes low. The scale is the same as in Figs. 2 and 4.

SSE from the outer Isfjorden area, along onshore Spitsbergen to the east of the HH rocks, and into the northern Barents Sea. The gradient that separates this low from the positive anomalies that occur farther west, trends from Kongsfjorden to Sørkapp Land, and generally delineates the eastern margin of the basement rocks (Fig.2), which is the Tertiary deformation front (Tdf). Since the sedi-

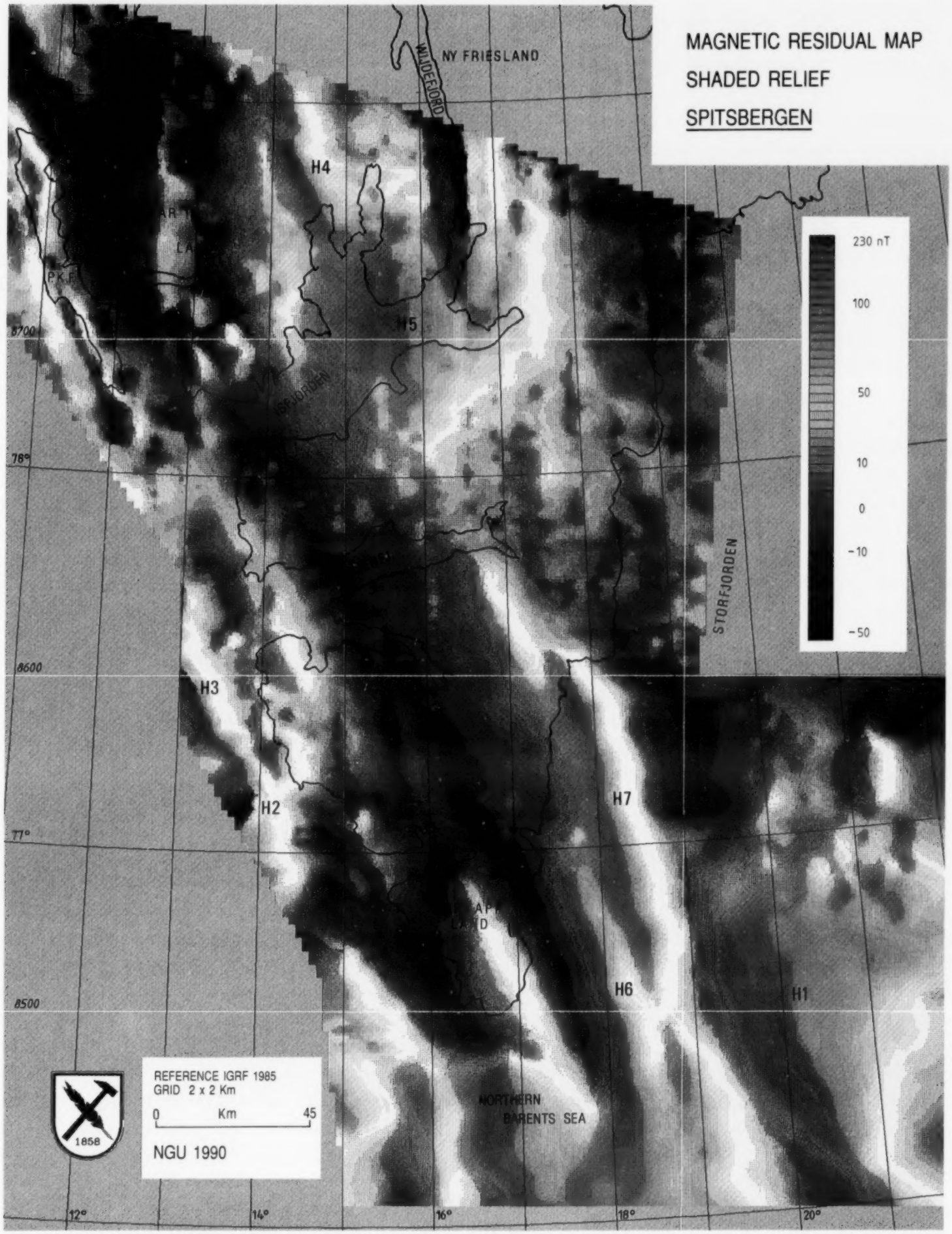

Fig.4. Shaded relief version of the coloured map. Illumination from the east. Data from the Barents Sea that was acquired in 1987 at a height of 300 m above sea level (a.s.l.) has been upward-continued to 1600 m a.s.l., and compiled with the Spitsbergen data. Names of highs (*H1*, *H2*, etc) refer to anomalies discussed in the text. The scale is the same as in Figs.2 and 3.

ments are non-magnetic, the character of the gradient varies along strike due to the variation in magnetization of the HH rocks to the west of the Tdf.

Inspection of profiles across Forlandssundet (Fls) and PKF shows that the magnetic field is flat and low above the sea and the Tertiary rocks on Prins Karl Forland and Oscar II Land to the east of the Fls. (See Fig.3 for geographical names). A steep gradient is associated with the fault-bounded contact between HH rocks and Tertiary rocks (Hjelle et al., 1979; Hjelle and Lauritzen, 1982; Winsnes, 1986). This gradient can be traced along the entire length of the PKF, separating HH rocks from the non-magnetic Tertiary clastic sediments. Also, Tertiary clastic sediments occur in grabens that have been mapped by seismic reflection data (Eiken and Austegaard, 1987), in basins downfaulted within the basement west of Spitsbergen. These grabens are delineated on the magnetic map by magnetic lows to the west of the coastline of Spitsbergen (northwest Bellsund and northwest Hornsund in Fig.3). The low to the south of Hornsund is probably a negative flank effect of the prominent high on Sørkapp Land.

An anomaly in the southeastern corner of Fig.4 (H1) originates from sources at a depth of more than 9 km in the basement, indicating the presence of thick sediments in Storfjorden. Some line effects, that are due to diurnal problems, can be seen in the northeastern part of the map area where the magnetic field is almost flat (Figs.3 and 4). On the profiles, low-amplitude, short-wavelength anomalies are located above known occurrences of dolerites that are widespread on Spitsbergen (Parker, 1966; Flood et al., 1971; Weigand and Testa, 1982).

Tertiary volcanism?

The Hornsund Fault Zone (HFZ) lies to the west of the survey area (Fig.2). High-amplitude anomalies occur (anomalies H2 and H3 in Fig.4) at the western end of profiles between 77°N and 77°30′N. Depth determinations show that they originate from shallow sources. The anomalies trend roughly NNW–SSE; i.e. sub-parallel to the HFZ. Since these anomalies are close to the important HFZ and the initial plate boundary (transform) between Svalbard and Greenland, they may be caused by Tertiary intrusions.

A magnetic anomaly north of Nordfjorden (anomaly H4, Fig.4), gives depth to magnetic source estimates around 2 km below sea level. The anomaly trends NW–SE, and is situated at the southeastern end of one of the main faults which has been mapped in northern Spitsbergen (e.g. Amundsen et al., 1988). On Sverresfjellet (south of Bockfjorden, see Fig.2), close to the mapped fault, there are volcanic rocks which are considered to be of Quaternary age; hot springs are also present (Skjelkvåle et al., 1989). Many xenoliths of granulites and upper mantle peridotites were brought up by the volcanism (Amundsen et al., 1988). Anomaly H4 trends along the fault and may represent volcanites emplaced at subsurface levels along a zone of weakness in Tertiary time. This interpretation is highly speculative, but not impossible, in view of the proximity of northern Spitsbergen to the plate boundary between oceanic and continental crust on the Yermak Plateau just northnorthwest of Svalbard.

Billefjorden Fault Zone (BFZ)

The BFZ extends from the north along Wijdefjorden and to the Isfjorden area (e.g. Harland et al., 1974), and defines the eastern margin of Devonian sediments. To the north of Billefjorden, the BFZ comprises a 2-4 km wide zone of parallel branching faults that dip to the east (Lamar et al., 1986). In Fig. 5, the location of faults interpreted by Harland et al. (1974) is compared with the magnetic anomaly pattern. Outcrops of HH rocks are shown with a dotted pattern. The Mittag–Lefflerbreen glacier covers large areas. The main fault (Balliolbreen Fault, fault B in Fig.5) is an east-dipping reverse fault which has displaced HH metamorphic rocks in the east onto Devonian sediments in the west. The steep western flank of the magnetic anomaly (Fig.5) correlates with fault B, along which there are slices of HH rocks. Another fault (named C in Fig.5) runs along the axis of the main anomaly. The fault itself, with 40 m downthrow to the west (Harland et al., 1974), cannot explain the anomaly.

Measurements on amphibolite samples from the

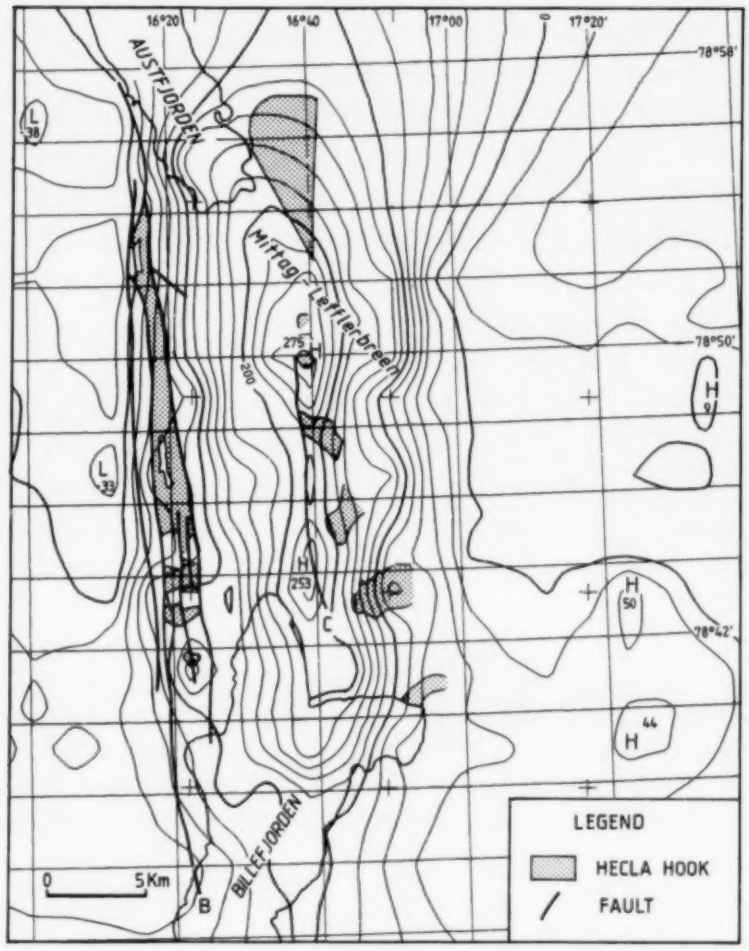

Fig.5. Magnetic contour map of the Billefjorden Fault Zone with the fault interpretation of Harland et al. (1974). The magnetic field has been continued downward to 1000 m a.s.l. Outcrop of HH basement shown by the dotted pattern. Note that the glacier covers large areas (Mittag–Lefflerbreen).

basement in northeast Spitsbergen (Ny Friesland) gave relatively high average magnetic susceptibility values of 0.01600 SI (Kurinin, 1965). Further east five samples of granite were practically non-magnetic (Hjelle, 1966). Also, to the north of Billefjorden, HH basement (the Harkerbreen Formation of Harland et al., 1974) contains many thin concordant and discordant sheet-like dykes of metagabbro-diabase, considered to be pre-Caledonian igneous rocks (Lauritzen and Ohta, 1984; Ohta et al., 1989). Thus, the basement rocks show large contrasts in magnetization.

Depth estimates performed on the profiles range from 1 km to 2 km below the observation plane (1600 m). These depths probably coincide with the depth to the top of the crystalline basement as taken from the geological cross-sections of Harland et al. (1974, fig.9, p.33). This indicates that the anomaly has its source within the basement.

Published geological maps show no volcanic rocks on the surface along the fault zone that could explain the anomaly. Some low-amplitude, short-wavelength anomalies occur 30 km to the east of the BFZ, over outcropping dolerites. These anomalies seem to be unrelated to the anomaly above the BFZ. Also, 10 km to the west of the south end of Wijdefjorden, in the Devonian, a few dykes (alkali lamprophyre) occur subparallel to the BFZ; these are considered to be of Carboniferous age (Gayer et al., 1966). These dykes make up too small a volume to explain anomalies measured at 1600 m flight altitude. From the above considerations, it can be concluded that the anomaly associated with the BFZ is caused by magnetic sources within the crystalline basement, and not by the fault itself.

A geological model of the BFZ has been tested for line SPA-7842 using forward modelling (Fig.6). HH metamorphic rocks are exposed in a sliver within the fault zone. North of Billefjorden the HH consists of feldpathic and amphibolitic gneisses, with a high proportion of basic igneous rocks (Harland et al., 1974; Hjelle and Lauritzen, 1982). The latter may be highly magnetic. The modelling work showed that basement topography alone cannot explain the anomalies, since this required unrealistically high susceptibility values for the basement, or too high basement relief incompatible with the structural geology as reported by Harland et al. (1974) and Lamar et al. (1986), as well as seismic work carried out in Isfjorden (Faleide et al., 1988). In the model we have therefore used a combination of intrabasement susceptibility contrasts and basement topography. The BFZ constitutes the western margin of a basement high (Fig.6). A small Carboniferous basin occurs to the east of the basement high, trending parallel to the BFZ (Harland et al., 1974). A reasonably good fit between observed and calculated anomalies is obtained. The aeromagnetic map shows that a large volume of magnetic HH rocks occurs along, and to the east of, the N–S trending BFZ.

Isfjorden area

The magnetic field over central and inner parts of Isfjorden is characterized by a positive, long-

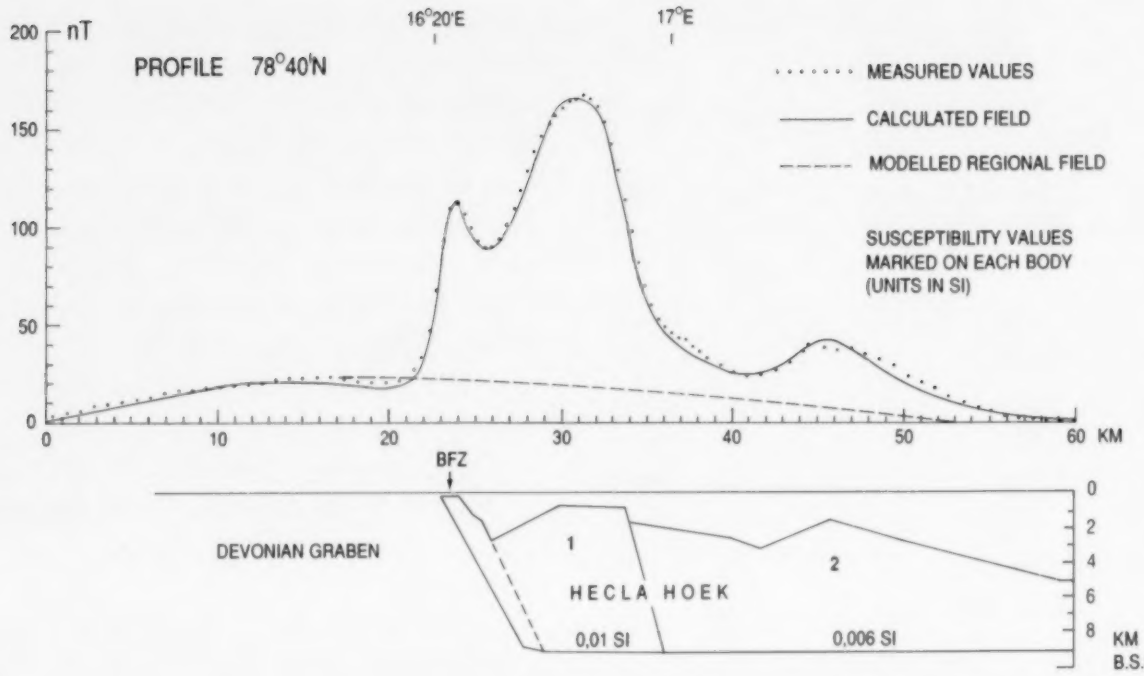

Fig.6. Magnetic model (2 1/2 D.) across the Billefjorden Fault Zone (BFZ) along SPA-7840. Black dots represent the observed value. The solid line is the calculated field. A non-linear regional field was modelled and subtracted (broken line) before the response of the displayed bodies was calculated. Susceptibility in SI-units. Body 1 represents faulted, Precambrian magnetic basement (HH) rocks containing amphibolites. Body 2 is weakly magnetized basement gneisses. The computer program used was developed by Hesselstrøm (1987).

wavelength and low-amplitude anomaly (H5 in Fig.4), with interfering, positive, short-wavelength anomalies of very small amplitudes possibly indicating sources at different depths. The axis along the magnetic maximum correlates with the northern part of the Central (Tertiary) Basin which is underlain by the deeper part of the NNW–SSE trending Devonian graben (Faleide et al., 1988). The western flank of the Devonian graben coincides with the western gradient of the magnetic anomaly. Sills of dolerite in the upper sediments can explain the short-wavelength anomalies. The magnetization of Tertiary sediments and of the Old Red Sandstone is low (Kurinin, 1965). Tertiary intrusions are scattered throughout the Devonian basin to the north of 78°30′N, but apparently make up small volumes (Winsnes, 1986). Extrusive rocks of Devonian age have also been reported further north (Murasov, 1983), but can hardly explain the Isfjorden anomaly.

Magnetic modelling did not contribute much towards an understanding of the anomaly source(s). It merely demonstrated the fundamental problem of ambiguity of potential field anomaly interpretation: It was possible to model the observed anomaly both by applying an intrusion within the lower part of the Devonian, and by assuming an intrabasement magnetic body with its top at the basement surface which is about c.8 km as determined by depth-to-source estimates. The depth estimates were made independently of the modelling using several techniques that utilize only the form of the anomaly (Åm, 1972; Skilbrei, 1991). The depth estimates agree with the depth to the bottom of the Devonian Graben as depicted on a published seismic profile from Isfjorden (Faleide et al., 1988, 1991).

Magnetic basement map

From the form of a magnetic anomaly it is possible to estimate the depth to the top of its causative body (Peters, 1949; Vacquier et al., 1951). An aeromagnetic survey over sedimentary basins is very useful for determining the general picture of the basement surface. However, for mapping small-scale structures in the top basement surface, the fallibility of the method has been demonstrated (e.g. Jacobsen, 1961). Basement depths are generally found to be in reasonably good agreement

with seismic data (e.g. Nettleton, 1971). The magnetic basement map (Fig.7) is based on a careful analysis of the original magnetic profiles. A manual interpretation using characteristic points and distances (straight-slope method and Peters' method) of all suitable anomalies has been performed (see e.g. Åm, 1972, for a review of methods). These methods assume that anomalies originate from intrabasement susceptibility contrasts, and that the top of the vertical causative bodies defines the basement surface. The autocorrelation method (Phillips, 1975) was also applied to find depth estimates automatically, using the Mapran3 program (Thorning, 1982), a modification of the ADEPTH-program (Phillips, 1975, 1979). This method is also described in Olesen et al. (1990) and Skilbrei (1990). For depth estimates that were considered reliable, the average of the estimates resulting from different methods was in most cases used as the "point estimate".

In some parts of the map area, few anomalies exist to provide depth estimates. In these areas the contours are dashed. The estimated depths agree fairly well with published depth converted seismic profiles (Eiken, 1985; Eiken and Austegaard, 1987; Faleide et al., 1988). However, the magnetic basement may not always coincide with the acoustic basement. Seismic data improved the contouring in Isfjorden. Elsewhere, the contouring is based only on the point estimates.

The most pronounced feature of the basement map is the very deep structure beneath inner Isfjorden. Strong gradients in the depth contours suggest it to be fault bounded, at least to the east, perhaps against a southerly continuation of the BFZ. The basement depths beneath central Spitsbergen become shallower (and the basin becomes narrower) to the south-southeast. This probably corresponds to a termination of the Central (Tertiary) Basin off the southeast coast of Spitsbergen. A similar situation occurs to the north of Isfjorden. Depths increase rapidly towards the centre of Storfjorden, where a N–S trending deep basin is suggested.

An eastward directed slope in the basement surface in the west coincides with the Tertiary deformation front (the front/zone is discussed in Dallman et al., 1988). An en echelon arrangement of shallow troughs along the western margin of the survey area corresponds to the grabens on the Spitsbergen shelf, and in the Forlandssundet (see Eiken and Austegaard, 1987).

Although the drawing of isolines of equal depth is subjective in some areas, the basement map suggests that the prevailing trends of the structure of the top of the magnetic basement are NW–SE to NNW–SSE. Figure 8 depicts this pattern more clearly. The trend of the top of the magnetic basement surface is similar to tectonic trends (compare Fig.8 with Fig.2), and to the main aeromagnetic anomalies. Such a congruence of trends, which may indicate that the stongest gradients in the basement surface coincide with basement faults, allows speculation that the basement fault zones have been reactivated several times during basin formation.

Discussions

Basement control of structure along the BFZ?

There is strong directional and spatial correlation between the surface trace of the BFZ and N–S trending aeromagnetic anomalies over exposed Precambrian HH rocks along the BFZ. This suggests that the BFZ existed as an important lineament in the Precambrian, and that the BFZ has been reactivated along this zone which is marked by an aeromagnetic lineament. A few reconnaissance profiles flown by NGU north of the SPA-88 survey area show strong magnetic anomalies above the HH rocks where they meet Wijdefjorden to the west (Åm, 1975), which can be related to the BFZ. The positive magnetic high can be followed from the continental shelf north of Svalbard, along the eastern coast of Wijdefjorden and to the Isfjorden area, where they become unresolvable.

Offshore extension of structures?

(1) There is indirect evidence that the crystalline rocks of the Svalbard Archipelago also constitute the basement rocks to the south of Spitsbergen, in the adjacent Barents Sea. First, the geology of Bjørnøya (see inset in Fig.1 for location south of Spitsbergen) is similar to the geology of Spitsber-

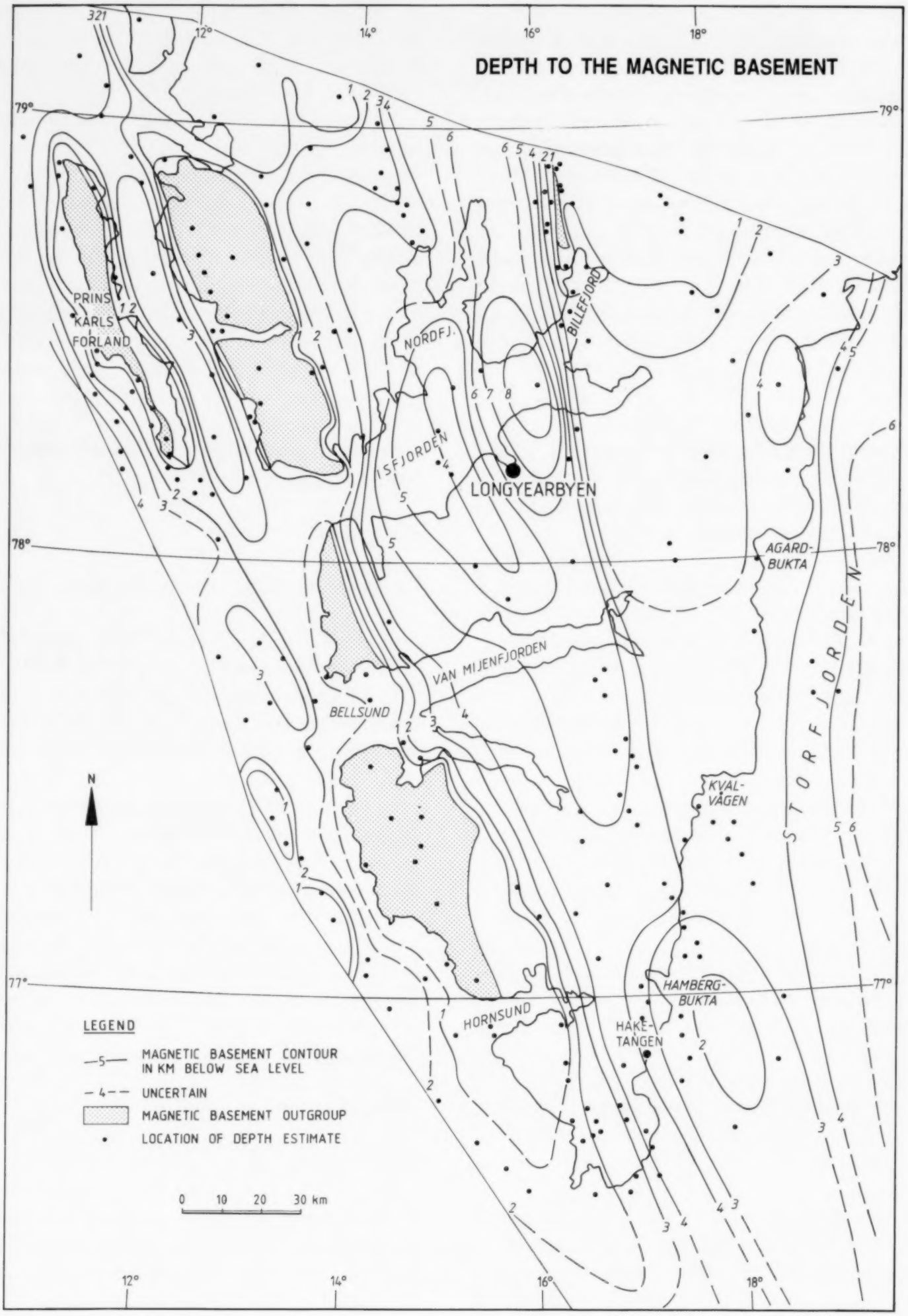
DEPTH TO THE MAGNETIC BASEMENT
12°
14°
16°
18°
79°
78°
77°
PRINS KARLS FORLAND
NORDFJ.
BILLEFJORD
ISFJORDEN
LONGYEARBYEN
AGARD-BUKTA
VAN MIJENFJORDEN
BELLSUND
KVAL-VÅGEN
STORFJ
HORNSUND
HAMBERG-BUKTA
HAKE-TANGEN
N
LEGEND
5 MAGNETIC BASEMENT CONTOUR IN KM BELOW SEA LEVEL
4 UNCERTAIN
MAGNETIC BASEMENT OUTGROUP
LOCATION OF DEPTH ESTIMATE
0 10 20 30 km

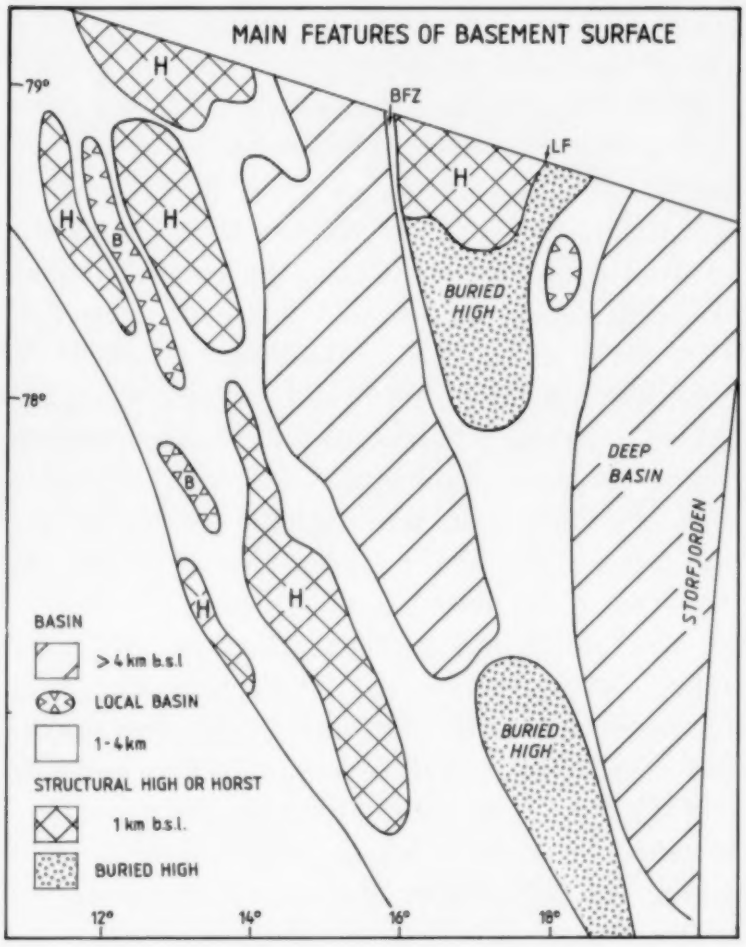

Fig.8. Sketch map of main structural elements inferred for the magnetic basement map. The positions of the Billefjorden Fault Zone (*BFZ*) and Lomfjorden Fault (*LF*) is shown. *H* denote basement high/horst and *B* is a local basin.

gen (e.g. Birkenmajer, 1975). Secondly, the lower crust in the Svalbard area is generally reflective with an abundance of diffractions, similar to that of the northern Barents Sea (Gudlaugsson et al., 1991). Thirdly, the trends of aeromagnetic anomalies on Spitsbergen and the adjacent northern Barents Sea are very similar. If the anomalies reflect intrabasement strike trends, then the character of the basement underlying the adjacent Barents Sea can be assumed to be similar to the HH basement on Spitsbergen.

(2) The BFZ and the LF may continue southwards into the Barents Sea, perhaps as far south as the pair of positive magnetic anomalies striking NNW–SSE (H6 and H7 in Fig.4) in Storfjorden. This suggestion is speculative, because there is no direct continuation between the magnetic anomaly over the BFZ and either of the two magnetic anomalies trending from the Barents Sea onto Spitsbergen. However, thicker sediment cover south of Isfjorden (Fig.8), and/or a non-magnetic basement here, would suppress the magnetic response of the basement rocks along the fault. Additionally, it must be mentioned that the magnetic response of the LF is very weak to non-detectable in the northeastern part of the map area where, unfortunately, evidence of diurnal noise is found. However, small steps on some of the original profiles (2–5 nT in magnitude) are observed above the surface trace of the LF, which could tentatively be associated with the fault. In Fig.9, the most likely traces of the southern extensions of the BFZ and the LF are shown. The westernmost (stippled) line follows the present erosional level of the eastern limit of Tertiary rock in Svalbard (Mann and Townsend, 1989). The interpretation favoured here merges the two fault zones with the pair of positive anomalies (H6 and H7 in Fig.4) that occur over the northern Barents Sea. Ohta's (1982b) interpretation, which was based only on bathymetry, is shown for comparison.

(3) The BFZ and the LF may define the margins of a basement horst on Ny Friesland (Figs.7 and 8). The Basement horst is buried south of Isfjorden where a sub-basin is probably present, but basement depths again become shallower further to the south (around 2 km). To the east of the southern extension of the LF, the basement is very deep (in Storfjorden).

Conclusions

(1) The map of estimated depth to the magnetic basement suggests a series of basement horsts and grabens/basins which trend N–S and NNW–SSE on Spitsbergen. The N–S trending Devonian graben is at least 8 km deep beneath central to inner parts of Isfjorden. This interpretation agrees with the seismic interpretation of Faleide et al. (1988). The deep basin is bordered to the east by a southerly extension of the Billefjorden Fault Zone

Fig.7. Magnetic basement map. Seismic data improved the contouring in Isfjorden. Elsewhere, the contouring is based only on the point estimates.

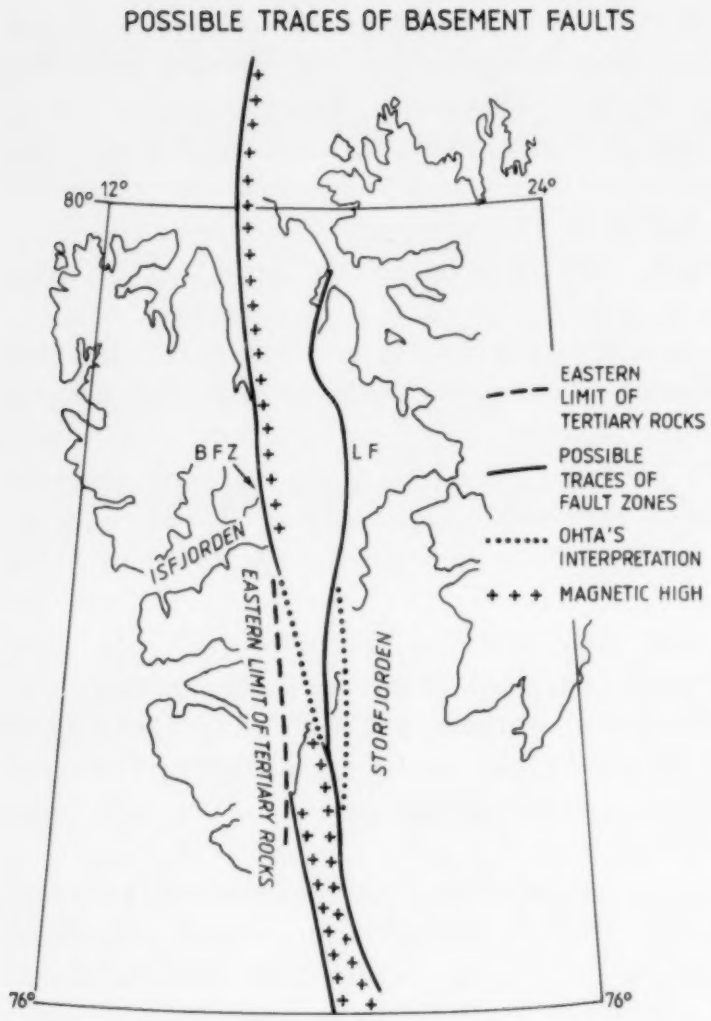

Fig.9. Possible traces of the Billefjorden Fault Zone (*BFZ*) and the Lomfjorden Fault (*LF*) on Spitsbergen. Crosses mark the axes of magnetic highs. The stippled line is along the eastern limit of the present outcrop of Tertiary rocks. Possible traces of faults as interpreted from magnetics are shown by solid lines. On the north shelf, the aeromagnetic interpretation and extension of the BFZ was made using NGU data (Åm, 1975), and data provided by Mr. A.A. Krasilscikov who works for *Sevmorgeologija* (pers. commun., 1990).

(BFZ), which is the border fault to the Devonian graben in the north.

(2) The BFZ and the Lomfjorden Fault form the borders to a basement horst on Ny Friesland which trends N–S to NNW–SSE from northern to central Spitsbergen. The estimated depths suggest this horst to be locally subdued to the southeast of Isfjorden (towards Storfjorden). The structure reappears as a buried basement horst further south and continues southwards to approximately 76°N. At the southern end the horst is bordered to the west by a seaward continuation of the Tertiary Central Basin, and to the east by a deep basin in Storfjorden (see Fig.7).

(3) From structural geology it has been concluded that the BFZ is a long-lived structural feature with movements spanning the time from at least pre-Devonian to Tertiary (Harland et al., 1974). The aeromagnetic data illustrate the trend of the BFZ and suggest that this feature extends from north of Svalbard to the Barents Sea.

(4) The aeromagnetic lineaments are probably a direct expression of basement lithologies beneath a non-magnetic sedimentary cover of variable thickness. The main aeromagnetic lineament system trends NW–SE to NNW–SSE which is also the trend of the main basement fracture direction. In general, geological field data, satellite data (Ohta, 1982a), seismic data (Faleide et al., 1988) and aeromagnetic data indicate a close directional, and sometimes spatial, correlation. This suggests that the main fault zones present in the crystalline basement have imposed a great deal of control during the subsequent tectonic evolution of the Svalbard area and the adjacent Barents Sea.

(5) Positive magnetic anomalies to the west of Spitsbergen *may* reflect Tertiary volcanic intrusions along the Hornsund Fault Complex.

Acknowledgements

I thank the participating oil companies, Norsk Hydro, Statoil, Elf Aquitaine Norge and Esso Norge, for allowing me to publish the data. Ola Kihle, Henrik Håbrekke (both at the NGU), Reidun Myklebust and Trond Christoffersen (formerly Geco, now at Amarok a.s.) are thanked for stimulating discussions on the acquistion, processing and interpretation of the data. Dr. O. Olesen (NGU) and Dr. Y. Ohta (*Norsk Polarinstitutt*) are thanked for comments on an early version of the manuscript. The manuscript was improved significantly by comments and suggestions made by one of the referees, Dr. Dave Forsyth. Dr. D. Roberts improved the English text. Dr. A. Krasilschikov at *Sevmorgeologija* St. Petersburg (formerly Leningrad) is thanked for letting me see a Russian aeromagnetic map.

References

Åm, K., 1972. The arbitrarily magnetized dyke: interpretation by characteristics. Geoexploration, 10: 63–90.

Åm, K., 1975. Magnetic profiling over Svalbard and surrounding shelf areas. Nor. Polarinst. Årbok 1973: 87–99.

Amundsen, H.E.F., Griffin, W.L., and O'Reilly, S.Y., 1988. The nature of the lithosphere beneath northwestern Spitsbergen: xenolith evidence. In: Y. Kristoffersen (Editor), Progress in Studies of the Lithosphere in Norway. Nor. Geol. Unders. Spec. Publ., 3: 58–65.

Andresen, A., Haremo, P. and Bergh, S.G., 1988. The southern termination of the Lomfjorden Fault Zone; evidence for Tertiary compression on east Spitsbergen. Nor. Polarinst. Rapp., 46: 75–78.

Birkenmajer, K., 1975: Caledonides of Svalbard and plate tectonics. Bull. Geol. Soc. Den., 24: 1–19.

Briggs, I.C. 1974. Machine contouring using minimum curvature. Geophysics, 39: 39–48.

Dallmann, W.K., Ohta, Y. and Andresen, A., (Editors), 1988. Tertiary Tectonics of Svalbard. Extended Abstracts from Symp. (Oslo, 26 and 27 April 1988). Nor. Polarinst. Rapportser., 46: 1–110.

Eiken, O., 1985. Seismic mapping of the post-Caledonian strata in Svalbard. Polar Res., 3: 167–176.

Eiken, O. and Austegaard, A., 1987. The Tertiary orogenic belt of West-Spitsbergen: Seismic expression of the offshore sedimentary basins. Nor. Geol. Tidsskr., 67 (4): 383–394

Eldholm, O., Faleide, J.I. and Myhre, A.M., 1987. Continent–ocean transition at the western Barents Sea/Svalbard continental margin. Geology, 15: 1118–1122.

Faleide, J.I., Gudlaugsson, S.T., Eiken, O and Hanken, N.M., 1988. Seismic structures of Spitsbergen: Implications for Tertiary deformation. Nor. Polarinst. Rapp., 46: 47–50.

Faleide, J.I., Gudlaugsson, S.T., Eldholm, O., Myhre, A.M. and Jackson, H.R., 1991. Deep seismic transects across the western Barents Sea—Svalbard continental margin. Tectonophysics, 189: 73–89.

Flood B., Nagy, J. and Winsnes, T.S., 1971. Geological map of Svalbard 1:500,000. Sheet 1G, Spitsbergen, Southern Part. Nor. Polarinst. Skr., 154 A, Map and Explanatory Notes.

Gayer, R.A., Gee, D.G., Harland, W.B., Miller, J.A., Spall, H.R., Wallis, R.H. and Winsnes, T.S., 1966. Radiometric age determinations from Spitsbergen. Nor. Polarinst. Skr., 137: 1–39.

Gudlaugsson, S.T., Fanavoll, J., Røssland, K. and Johansen, B., 1992. Structure and tectonics of the Barents Shelf-results from deep seismic reflection profiles. (in prep.).

Harland, W.B., 1965. The tectonic evolution of the Arctic-north Atlantic region. Philos. Trans. R. Soc. London, 258: 59–75.

Harland, W.B., 1966. A hypothesis of continental drift tested against the history of Greenland and Spitsbergen. Cambridge Res., 2: 18–22.

Harland, W.B., 1969. Contribution of Spitsbergen to understanding of tectonic evolution of the North Atlantic Region. In: M. Kay (Editor), North Atlantic Geology and Continental Drift. Am. Assoc. Pet. Geol. Mem., 12: 817–851.

Harland, W.B., Cutbill, J.L., Friend, P.F., Gobbett, D.J., Holliday, D.W., Maton, P.I., Parker, J.R. and Wallis, R.H., 1974. The Billefjorden Fault Zone, Spitsbergen — the long history of a major tectonic lineament. Nor. Polarinst. Skr., 161: 1–72.

Hesselstrøm, B., 1987. GAMMA86 user's manual. Swedish Geological Company, Uppsala, 17 p.

Hjelle, A., 1966. The composition of some granitic rocks from Svalbard. Nor. Polarinst. Årbok, 1965: 7–13.

Hjelle, A. and Lauritzen, O., 1982. Geological map of Svalbard 1:500,000. Sheet 3G. Spitsbergen Northern Part. Nor. Polarinst. Skr., 154 E, Map and Explanatory Notes, pp.1–15.

Hjelle, A., Ohta, Y., and Winsnes, T.S., 1979. Hecla Hoek rocks of Oscar II Land and Prins Karl Forland, Svalbard. Nor. Polarinst. Skr., 167: 145–169.

Jacobsen, P., 1961. An evaluation of basement depth determinations from airborne magnetometer data. Geophysics, 24: 309–319.

Kihle, O., 1985. Produksjonssystem for fargerasterkart, versjon 85-X, forløpig brukerbeskrivelse. Inter. NGU-Rep. (in Norwegian), 25 p.

Kurinin, R.G., 1965. Density and magnetic susceptibility of Spitsbergen rocks. In: V.N. Sokolov (Editor), Materiala po Geologii Spitsbergena. Inst. for Geology of the Arctic, Leningrad, pp.276–284. (Translated into English 1970. Nat. Lending Libr. Yorkshire, UK.)

Lamar, D.L., Reed, W.E. and Douglass, D.N., 1986. Billefjorden Fault Zone, Spitsbergen: Is it part of a major Late Devonian Transform? Geol. Soc. Am. Bull., 97: 1083–1088.

Lauritzen, O., and Ohta, Y., 1984. Geological map of Svalbard, 1:500,000, Sheet 4G Nordaustlandet. Nor. Polarinst. Skr. 154D, Map and Explanatory Notes.

Lee, M.K., Pharaoh, T.C. and Soper, N.J., 1990. Structural trends in central Britain from images of gravity and aeromagnetic fields. J. Geol. Soc., London, 147: 241–258.

Mann, A. and Townsend, C., 1989. The post-Devonian tectonic evolution of southern Spitsbergen illustrated by structural cross-sections through Bellsund and Hornsund. Geol. Mag., 126 (5): 549–566.

Murasov, L.G., 1983. New data on evidence of volcanism in the lower Devonian and upper Triassic formations of West Spitsbergen (in Russian). Geologica Spitsbergena, Sevmorgeologija, Leningrad, pp.109–135.

Myhre, A.M. and Eldholm, O., 1988. The western Svalbard margin (74°–78°N). Mar. Pet. Geol., 5: 135–156.

Nelson, B., Hardwick, D., Forsyth, D., Bower, M., Marcotte, D., MacPherson, M., Macnab, R. and Teskey, D., 1991. Preliminary analysis of data from the Lincoln Sea aeromagnetic surveys 1989–1990. In: Curr. Res., Part B, Geol. Surv. Can. Pap., 91-1B: 15–21.

Nettleton, L.L., 1971. Elementary gravity for geologists and seismologists. Soc. Explor. Geophys. Monogr., 1, 121 pp.

Ohta, Y., 1982a. Caledonian Fractures on Svalbard. In: R.H. Gabrielsen, I.B. Ramberg, D. Roberts, O.A. Steinlein, (Editors), Proc. Fourth Int. Conf. Basement Tectonics. Int. Basem. Tect. Assoc. Publ., Salt Lake City, Utah, 4: 339–350.

Ohta, Y., 1982b. Morpho-tectonic studies around Svalbard and the northern-most Atlantic. In: A.F. Embry and H.R. Balkwill (Editors), Arctic Geology and Geophysics. Can. Soc. Pet. Geol. Mem., 8: 415–431.

Ohta, Y., Dallmeyer, R.D. and Peucat, J.J., 1989. Caledonian

terranes in Svalbard. In: R.D. Dallmeyer (Editor), Terranes in the circum-Atlantic Palaeozoic Orogens. Geol. Soc. Am. Spec. Pap., 230: 1–16.

Olesen, O., Roberts, D., Henkel, H., Lile, O.B. and Torsvik, T.H., 1990. Aeromagnetic and gravimetric interpretation of regional structural features in the Caledonides of West Finnmark and North Troms, Northern Norway. Nor. Geol. Unders. Bull., 419: 1–24.

Parker, J.R., 1966. Folding, faulting and dolorite intrusions in the Mesozoic rocks of the fault zone of central Spitsbergen. Nor. Polarinst. Årbok, 1964: 47–55.

Peters, J.L., 1949. The direct approach to magnetic interpretation and its practical application. Geophysics, 14: 290–320.

Phillips, J.D., 1975. Statistical analysis of magnetic profiles and geomagnetic reversal sequences. Ph.D. Thesis, Stanford Univ., 134 pp.

Phillips, J.D., 1979. ADEPT: A program to estimate depth to magnetic basement from sampled magnetic profiles. U.S. Geol. Surv. Open-File Rep., pp.79–367.

Skilbrei, J.R., 1988a. Flymagnetiske målinger over nordlige Barentshavet (BSA-87). Nor. Geol. Unders. Inter. Tech. NGU-Rep., 88.037 (in Norwegian), 72 pp.

Skilbrei, J.R., 1988b. Spitsbergen Aeromagnetic Survey 1988 (SPA-88). Inter. Tech. NGU-Rep., 88.038 (in Norwegian), 33 pp.

Skilbrei, J.R., 1990. Interpretation of Depth to the Magnetic Basement in the northern Barents Sea. NGU-Rep., 90.046, 42 pp.

Skilbrei, J.R., 1991. Short note: The straight-slope method for basement depth determination revisited. (in prep.).

Skilbrei, J.R., Håbrekke, H., Christoffersen, T. and Myklebust, R., 1990. Aeromagnetic surveying at high latitudes, a case history from the northern Barents Sea. First Break, 8 (2): 46–50.

Skjelkvåle, B.-L., Amundsen, H.E.F., O'Reilly, S. Y., Griffin, W.L. and Gjelsvik, T., 1989. A primitive alkali basaltic stratovolcano and associated eruptive centres, northwestern Spitsbergen:volcanology and tectonic significance. J. Volcanol. Geotherm. Res., 37: 1–19.

Steel, R.L. and Worsley, D., 1984. Svalbard's post-Caledonian strata — an atlas of sedimentational patterns and palaeogeographic evolution. In: A.M. Spencer (Editor), Petroleum Geology of the North European Margin. Graham and Trotman, London, pp.109–135.

Sundvor, E. and Eldholm, O., 1976. Marine geophysical survey on the continental margin from Bear Island to Hornsund, Spitsbergen. Univ. Bergen, Seismological Obs., Rep. 3, 28 pp.

Talwani, M. and Eldholm, O., 1977. Evolution of the Norwegian–Greenland Sea. Geol. Soc. Am. Bull., 88: 969–999.

Thorning, L., 1982. Processing and interpretation of aeromagnetic data in The Geological Survey of Greenland. Geol. Surv. Greenland Rep., 114: 31–34.

Vacquier, V., Steenland, N.C., Henderson, R.G. and Ziets, I., 1951. Interpretation of aeromagnetic maps. Geol. Soc. Am. Mem., 47, 151 pp.

Weigand, P. W. and Testa, S. M., 1982. Petrology and geochemistry of Mesozoic dolerites from the Hinlopstretet area, Svalbard. Polar Res., 1: 35–52.

Winsnes, T.S., 1986. Bedrock map of Svalbard and Jan Mayen 1:1 Mill. Nasjonalatlas for Norge. Kartblad 2.2.2. Norwegian Mapping Authority, Hønefoss, Norway.

Winsnes, T.S. and Worsley, D., 1981. Geological Map of Svalbard 1:500,000 Map Sheet 2G Edgeøya. Nor. Polarinst. Skr., 154 B, Map and Explanatory Notes.

Marine Geology, 106 (1992) 69–87
Elsevier Science Publishers B.V., Amsterdam

Reflector "Pc" a prominent feature in the Maud Rise sediment sequence (eastern Weddell Sea): Occurrence, regional distribution and implications to silica diagenesis

Gerhard Bohrmann[a], Volkhard Spieß[b], Heinrich Hinze[a] and Gerhard Kuhn[a]

[a]*Alfred-Wegener-Institut für Polar- und Meeresforschung, Columbusstraße, W-2850 Bremerhaven, Germany*
[b]*Universität Bremen, Fachbereich Geowissenschaften, Bibliothekstraße, W-2800 Bremen, Germany*

(Received March 21, 1991; revision accepted November 14, 1991)

ABSTRACT

Bohrmann, G., Spieß, V., Hinze, H. and Kuhn, G., 1992. Reflector "Pc" a prominent feature in the Maud Rise sediment sequence (eastern Weddell Sea): Occurrence, regional distribution and implications to silica diagenesis. *Mar. Geol.*, 106: 69–87.

Condensed pelagic deposits characterize the uppermost sediment sequence of the Maud Rise in the eastern Weddell Sea. The comparison of subbottom profiling data with the sediments drilled at two ODP sites shows that Lithologic Unit Ib deposited during late Miocene to late Pliocene times is generally characterized by acoustic transparency. A prominent reflector with strongly increased amplitude (called Reflector "Pc") occurs within this mainly homogeneous diatom ooze unit and is correlated with the porcellanite horizon found at ODP Site 689. As evidenced by sediment findings, Reflector "Pc" marks a distinct stratigraphic layer of early Pliocene age. The development of the Reflector "Pc" and its amplitude of reflection in the echosounding records is most likely caused by the silica cementation of porcellanite within this layer. The analyses of the sediment echosounder profiles from five R.V. *Polarstern* cruises make it possible to map the regional distribution of Reflector "Pc". In large areas of the central Maud Rise, a patchy but also continuous distribution of Reflector "Pc" was found. The reflector does not occur in sediments below 3000 meters of water. On average Reflector "Pc" is detected around 11 and 12 meters below seafloor, but depth occurrence is highly variable within the range of 8 m to more than 18 m. The apparent amplitude of Reflector "Pc" is higher in those areas where the diatom ooze Unit Ib reaches greater thicknesses, which may be causedby local enhanced tectonic subsidence. In general a good correlation of Reflector "Pc" amplitude and thickness of lithologic Unit Ib is observed. This may imply that the diatom ooze Unit Ib serves as a silica source, since the extent of silica cementation of the porcellanite layer is controlled by the amount of dissolved silica supply. Other possible interpretationsfor silica sources include silica-rich interstitial water ascending from deeper sediment levels using tectonic structures for migration.

Introduction

Maud Rise is an isolated submarine plateau in the eastern part of the Weddell Sea Abyssal Plain about 700 km north of the East Antarctic continent (Fig. 1). As an aseismic ridge the Maud Rise is elevated more than 2000 m above its surroundings. This topographic high off the Antarctic continent separates the Weddell Sea Abyssal Plain from the Enderby Abyssal Plain in the East. Since December 1985 R.V. *Polarstern* has conducted five expeditions (ANT-IV/3, ANT-IV/4, ANT-VI/3, ANT-VIII/6, and ANT-IX/3) with mainly marine geologic investigations to the Maud Rise area (Fütterer, 1987, 1988; Fütterer and Schrems, 1991; Kuhn et al., in press). During these cruises bathymetric surveys of the seafloor were carried out continuously by swath sonar systems *Seabeam* and *Hydrosweep*. Based on a compilation of the data sets, the seafloor topography of the entire Maud Rise as well as selected features can be presented. A comprehensive program of piston, gravity and box coring during the expeditions of R.V. *Polarstern* has given the oppor-

Correspondence to: G. Bohrmann, Forschungszentrum für marine Geowissenschaften, Wischhofstraße 1–3, W-2300 Kiel 14, Germany.

0025-3227/92/$05.00

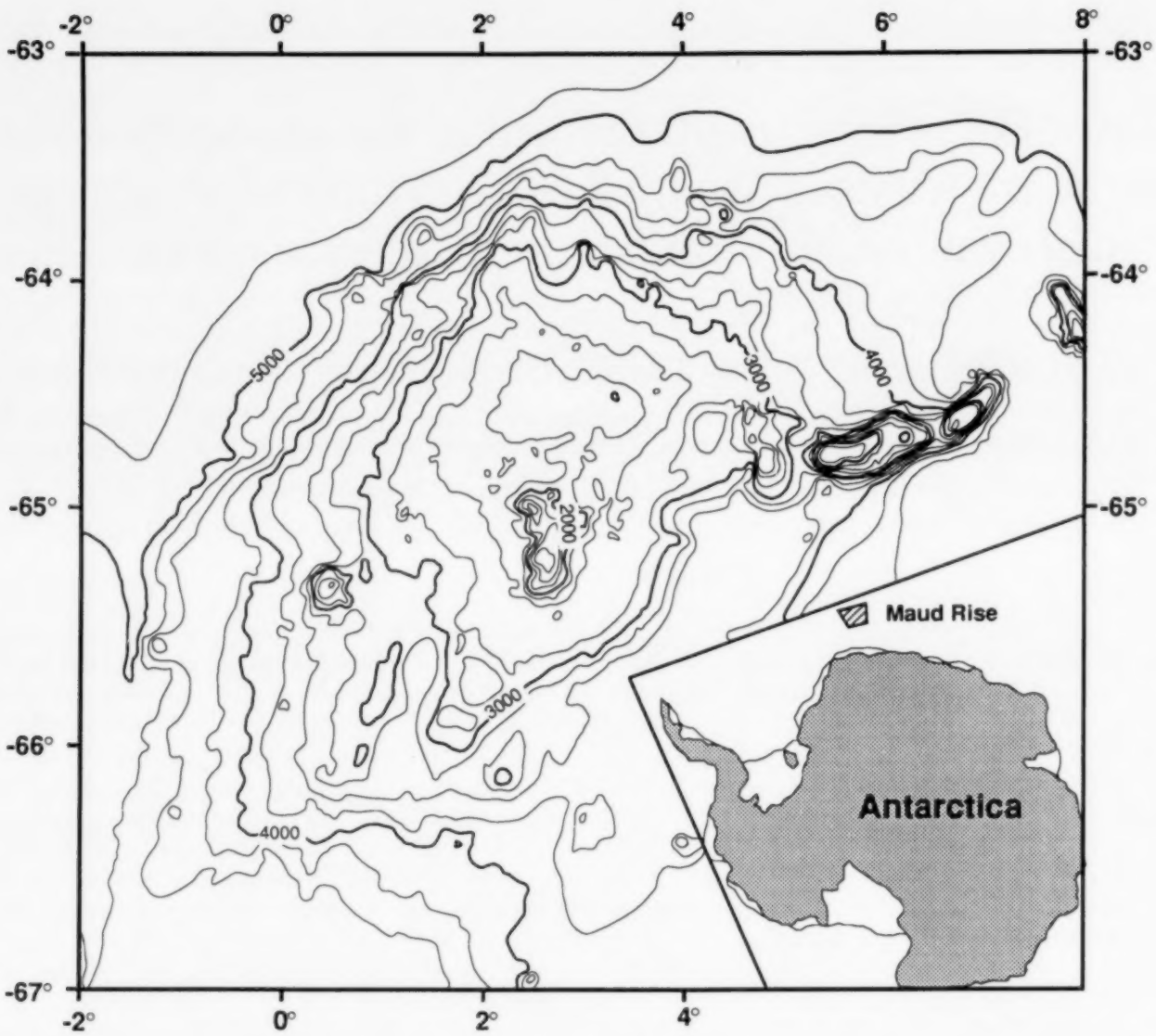

Fig. 1. Bathymetric map of the Maud Rise area, compiled after *Seabeam* and *Hydrosweep* data from *Polarstern* expeditions (ANT-IV/3, ANT-IV/4, ANT-VI/3, ANT-VIII/6, ANT-IX/2 and ANT-IX/3) and additional depth information (see text). Bathymetric contours are given in intervals of 250 m below sea level.

tunity for micropaleontological, stratigraphic and sedimentological investigations in this area (Cordes, 1990; Abelmann et al., 1990).

During the marine geologic cruises on Maud Rise, extensive subbottom profiling surveys were also carried out with a 3.5 kHz system (ANT-IV/3, ANT-IV/4, ANT-VI/3) and *Parasound* (ANT-VIII/6, ANT-IX/3). A compilation of numerous sediment records now allows a spatial consideration of the sediment distribution and sediment types to be traced and mapped over large distances. In addition, specific sediment horizons, which where recovered by the Ocean Drilling Program during Leg 113 (Barker et al., 1988) at Sites 689 and 690, can be correlated with the sediment echosounding records. Due to the high penetration depth of the sedimentechographic systems the upper 50–150 m below seafloor can be investigated. Since the pelagic sediment sequence is condensed in this area, detailed interpretations of deposition history since at least Oligocene times are possible. Our presentation in this paper is focussed on a prominent acoustic reflector which we call Reflector "Pc". This reflector occurs in the uppermost sediment sequence of Maud Rise and is the most remarkable feature in the records. The analysis of the deeper records will be published elsewhere.

Database

Seafloor mapping

In the bathymetric maps of the Maud Rise area depth data were compiled from different sources.

Single beam soundings of the NGDC data base (National Geophysical Data Center, USA), digitized soundings from UK Nautical Charts (NC 3170, 4075) and R.V. *Polarstern* measurements of several cruises were selected. About 2,700,000 data points were used for mapping. The *Polarstern* data were taken from the single beam sensor (NBS) as well as from the multibeam systems *Seabeam* and *Hydrosweep*. The swath data for the Maud Rise study area represent more than 98% of the complete data set. Most of the swath data were collected during *Polarstern* cruises ANT-IV/3, IV/4, VI/3, VIII/6, IX/2 and IX/2. Details on the *Seabeam* survey system aboard *Polarstern* are given by Schenke and Ulrich (1987). The multibeam system *Hydrosweep* (=*hydro*graphic multibeam *sweep*ing survey echosounder) was installed on R.V. *Polarstern* in summer 1989. The system is introduced by Gutberlet and Schenke (1989) for its technical aspects and by Schreiber and Schenke (1990) for its scientific efforts on polar marine research. Since data quality and precision vary significantly, reliability and amount of information were critically reviewed before developing a digital terrain model for the whole Maud Rise area. All maps and views shown in this paper are based on gridded digital terrain models.

Subbottom echosounding

The echosounder data set used in this study derive from two different sources and systems. The conventional 3.5 kHz echosounder (ORE 140) was used during *Polarstern* cruises ANT-IV and ANT-VI whereas the *Parasound* System was run during ANT-VIII/6 expedition. The data of the first system are characterized by a wide beam angle acoustic source of 3.5 kHz, transmitting 95% of the total energy over more than 20° opening angle. The repetition rate was constant in time with a few seconds, but the horizontal scale and resolution varies with the ship's speed (5–12 knots) accordingly. Because of an acoustic footprint diameter of more than 35% of the water depth, which ranges between 700 and 1500 meters for the profiles in the Maud Rise area, diffraction patterns and reduced spatial resolution are common features in 3.5 kHz analogue records.

In contrast, the *Parasound* Echosounder System (Krupp Atlas Elektronik GmbH, Bremen; Grant and Schreiber, 1990; Rostek et al., 1991) used during *Polarstern* cruise ANT-VIII/6 is based on a parametric source transmitting at a beam angle of less than 4°. Increased spatial resolution of 7% of the water depth for the footprint diameter significantly reduces diffractions and sharpens the reflection pattern in the seismic sections. In addition a different analogue output scheme is used, which is not based on the 16 grey scales of the EPC recorder as was used for the 3.5 kHz instrument. The analogue unit uses the envelope function as well as the differentiated analogue signal instead, and plots all intervals above an operator controlled threshold amplitude in grey. Black lines are added for maxima in the differentiated signal, which coincide with steep flanks and reflectors. This reduces the dynamics and also allows weak reflections to be identified by a coherent line in the echogram. Amplitudes can not be read from this type of analogue record, but are available from the digital recording.

Physiographic and structural settings

Maud Rise is a marginal plateau in the eastern Weddell Sea. Its geological structure is related to the complex tectonic history of the separation of East Antarctica, Africa, India and Madagascar. In contrast to the Astrid Ridge and Gunnerus Ridge, which are pronounced elongated structures connected to the Antarctic continent, Maud Rise is more separated from Antarctica.

In general Maud Rise can be characterized as a block-shaped feature having an extent of about 400 by 280 km lying between 63°30'S and 66°0'S and 1°E and 5°E (Figs. 1 and 2). Its longer side strikes NE–SW and measures about 340 km in diagonal length as defined by the 3000 m isobath. To the southeast Maud Rise shows partly a steep scarp (Fig. 3), which is a distinct NE–SW striking feature on the bathymetric map of Fig. 1. The other slopes of this aseismic ridge are characterized by minor steep scarps (Figs. 3 and 4). However, as documented in the profile sections (Figs. 3 and 4) slopes and scarps are not uniform and not

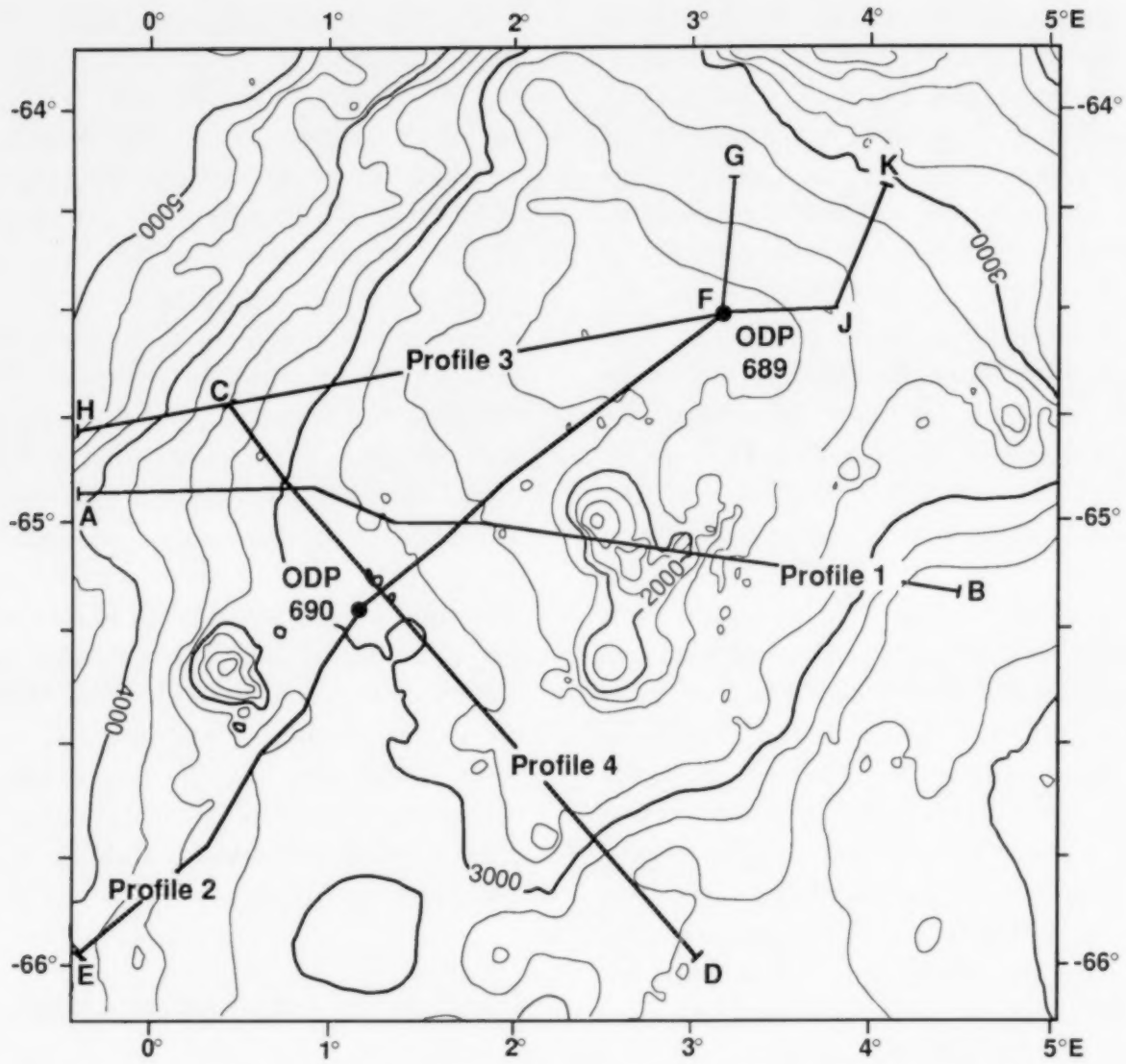

Fig. 2. Index map from the central part of Maud Rise showing locations of the bathymetric profiles *1–4* and ODP drill Sites 689 and 690. The profiles are selected subbottom profiler track lines from *Polarstern* cruises. Isolines of seabottom topography are in 250 m contour intervals.

generally smooth. They are interspersed by sections of minor slopes or associated with little seamounts.

The topographic elevation rises in its western and northern part from the base of the 5000 m deep Weddell Sea Abyssal Plain to the plateau-like area approximately at 2000–3000 m of water. At its eastern side the topographic high rises from the 4400–4600 m deep Lazarev Sea which separates Maud Rise from Astrid Ridge.

Although several details of Maud Rise given in the GEBCO charts (Sheets 5.16 and 5.18) vary from the compiled bathymetric map presented in Fig. 1, the general structure of the rise was confirmed. Especially the central flat area previously charted in the northern part between 64°50'S and 64°20'S could be confirmed by *Polarstern* multibeam measurements. This plateau-like area ranges up to 2080 m below sea level (mbsl). It seems to be the highest area of Maud Rise with a layered undulating sediment cover.

At 65°11'S and 2°40'E the highest elevation of 1100 mbsl was measured by *Polarstern* surveys crossing Maud Rise in a N–S transect. This profiling revealed a large area above 2000 mbsl of highly variable morphology south of the central Maud Rise Plateau (Figs. 1 and 3). Several narrow conical features often between 100 and 400 m high with typical circular isobaths were mapped by multibeam depth measurements. Although very little is known about the nature of these structures, it is thought they represent volcanic features. Similar bathymetric structures at greater water depths occur at the western slope at 65°20'S, 0°30'E. Isolated morphologic cones or peaks (Figs. 11 and

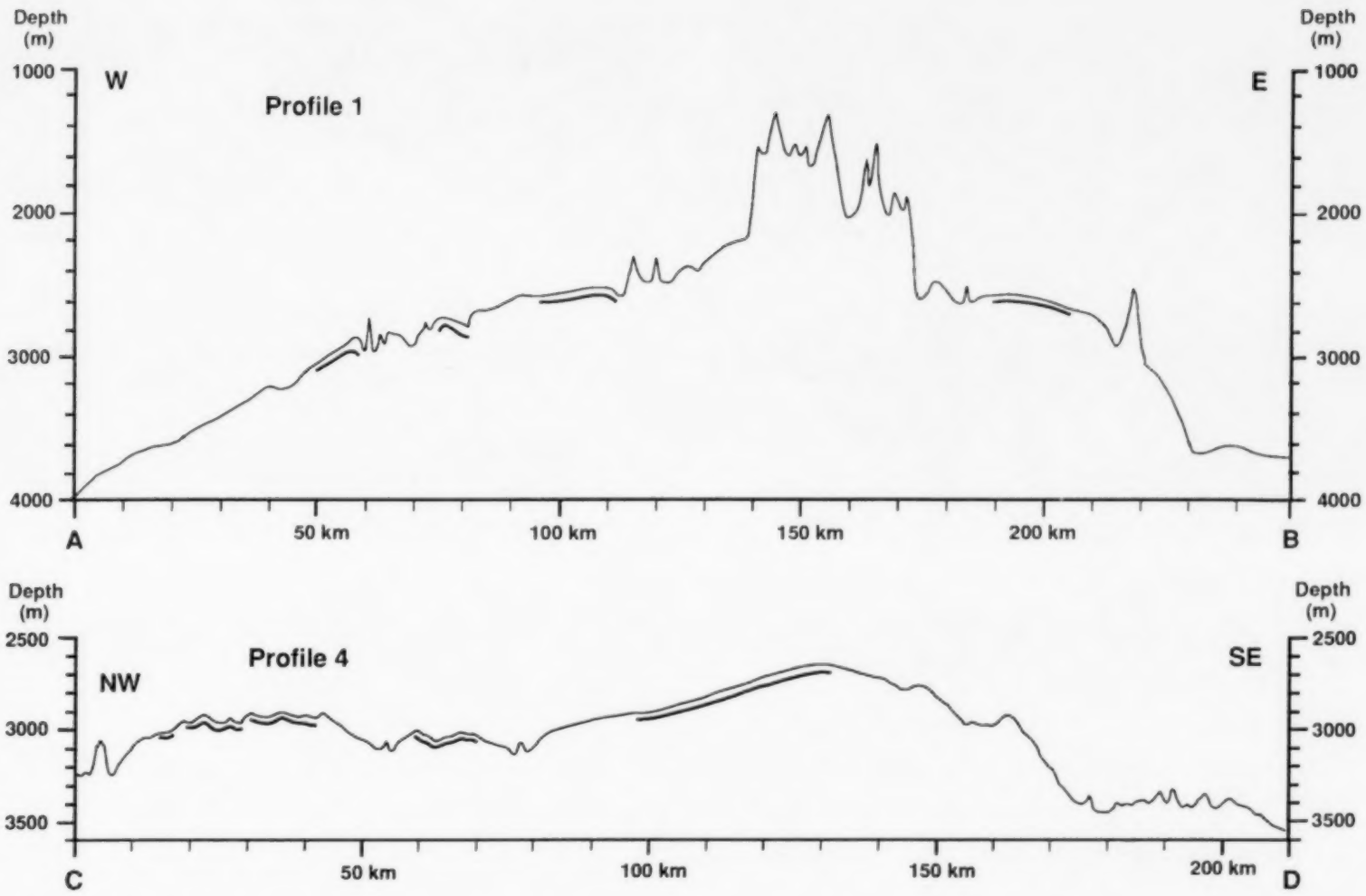

Fig. 3. Sediment surface profiles 1 and 4 from Maud Rise (lines are shown in the index map; Fig. 2). Vertical occurrence of Reflector "Pc" as it was found in 3.5 kHz and *Parasound* records on the track lines is sketched without scale for elucidation.

12) are common features found on the gentle smooth seafloor of Maud Rise. Such cone-shaped elevations are characterized by very steep flanks showing high slope angles between 10° and 30° and are typical for single volcanic outcrops. A volcanic nature is also supported by sediment echosounding records showing typically strong basement reflections yielding no internal layered structure. Bathymetric data and several detailed morphological features discussed here suggest that volcanism played an important role in the buildup of Maud Rise. Basaltic rocks were recovered during ODP Leg 113 in ODP Hole 690C at 317 mbsf (Barker et al., 1988). Such drilled basement rocks seem to be of Cretaceous age since they are overlain by Upper Campanian sediments (Schandl et al., 1990). Based on our bathymetric and sediment profiling observations numerous features of volcanic nature seem to be more recent than the drilled basalts. Recently a highly altered basalt was recovered during *Polarstern* cruise ANT-IX/3 by a piston core at Site PS2069 on the top of Maud Rise (Kuhn et al., in press).

Correlation of sediments with subbottom profiling records

The sediment sequence of Maud Rise was drilled by the Ocean Drilling Program during Leg 113 at Sites 689 and 690 (Barker et al., 1988). Site 689 lies at 64°31'S, 3°6'E in 2080 m of water at the northern crest of Maud Rise (Figs. 2 and 4). Site 690, on its southeastern flank (Figs. 2 and 4) is located at 65°9.6'S, 1°12.3'E in 2914 m below sea level (Barker et al., 1988). The upper sedimentary sequence drilled at both sites is of purely pelagic origin. Changes in the amount of calcareous and siliceous microfossils with increasing depth cause a typical succession of sediment types within the Lithologic Units II and Unit I (Barker et al., 1988). The early Miocene to recent sediment sequences were more completly represented at ODP Site 690

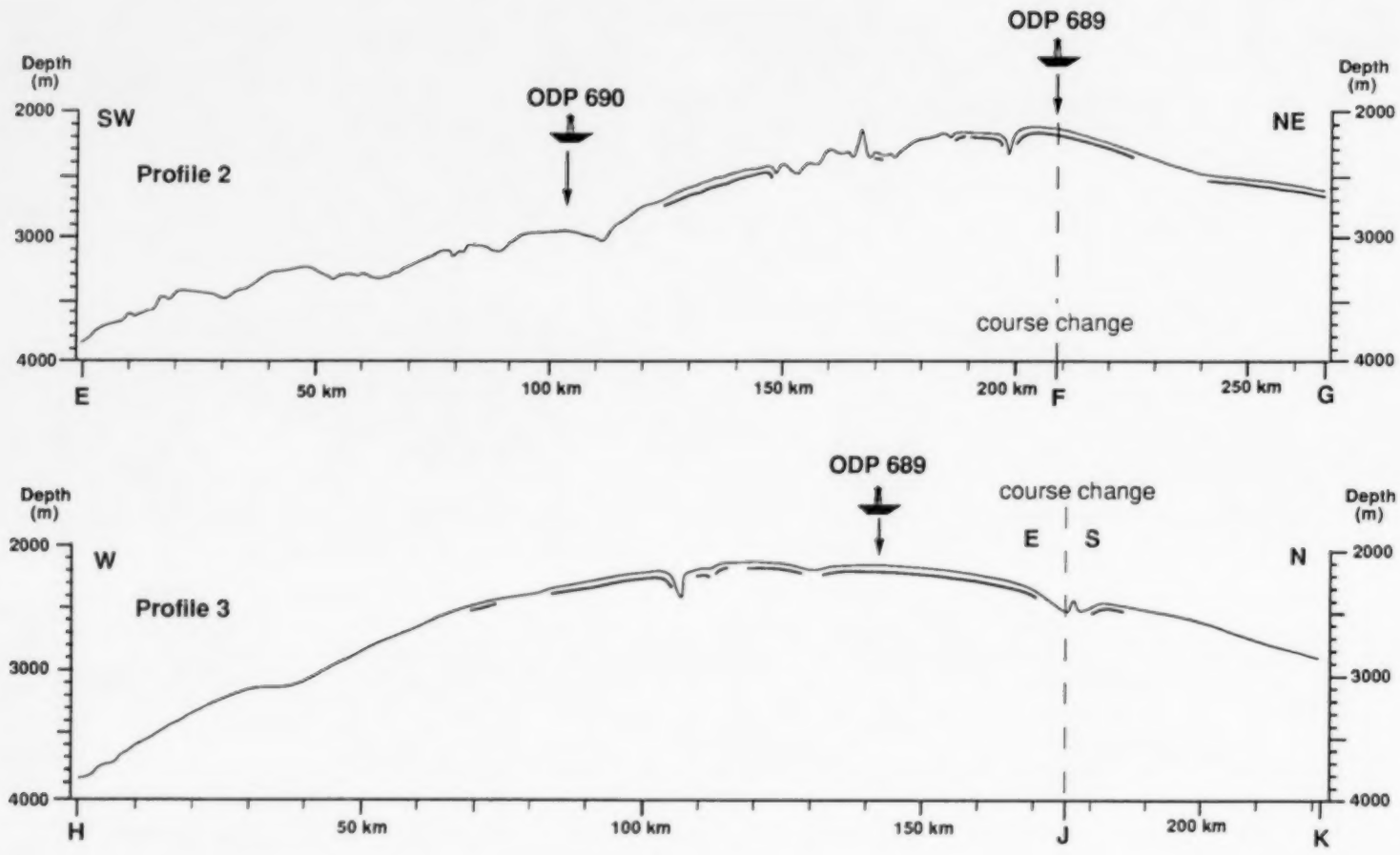

Fig. 4. Sediment surface profiles 2 and 3 (for explanation see Fig. 3).

(Fig. 5) than at Site 689 (Fig. 6). At ODP Site 689 in none of the three holes the mud line was recovered (Fig. 6) and the topmost sediments were disturbed.

In Hole 690 the uppermost foraminiferal ooze and diatom-bearing foraminiferal ooze of Quaternary to late Pliocene age (Lithologic Subunit Ia) is characterized by carbonate contents of more than 80% (Fig. 5). This subunit of variable thickness is well known from *Polarstern* cores of the entire Maud Rise area (Fütterer, 1988). It was not recovered by drilling at Site 689 (Fig. 6) due to disturbance, but at Site 690 it occurs down to 3.1 m subbottom depth (Fig. 5). In the *Parasound* records, some reflections of variable amplitude appear just below the bottom echo and may be correlated with small-scale changes in impedance within the carbonate-rich layer and just below (Fig. 5).

Subunit Ib is composed of diatom ooze and partly radiolarian-bearing diatom ooze of variable color. This lithologic subunit ranges at ODP Site 690 from 3.1 to 24.4 m below seafloor (mbsf) and is well defined by extremely low contents of biogenic carbonate (<1%; Fig. 5). Some carbonate excursions are observed within this subunit at ODP Site 689B (Fig. 6). Subunit Ib is of late Miocene to Pliocene age revealing numerous hiatuses of short duration, where at least 3 Ma are missing (Gersonde et al., 1990).

As indicated at ODP Site 690 by the correlation of the core data with the *Parasound* profile (Fig. 5), the relatively homogeneous sediments of Subunit Ib form an acoustically transparent layer. In contrast, distinct reflection patterns were observed above and below. A weak reflection of low amplitude is visible at about 10 mbsf (Fig. 5), whereas at ODP Site 689 a very strong reflector is detected at about 13 mbsf within the same stratigraphic interval. Besides the seafloor reflection the strongest amplitudes within the entire sediment sequence were found at this depth range. At ODP Site 689 porcellanite fragments were recovered at the top of the first two cores (Barker et al., 1988). The porcellanite pieces were broken and partly displaced due to the drilling process. This rock is highly cemented, reveals very high density values and causes the most obvious contrast in acoustic

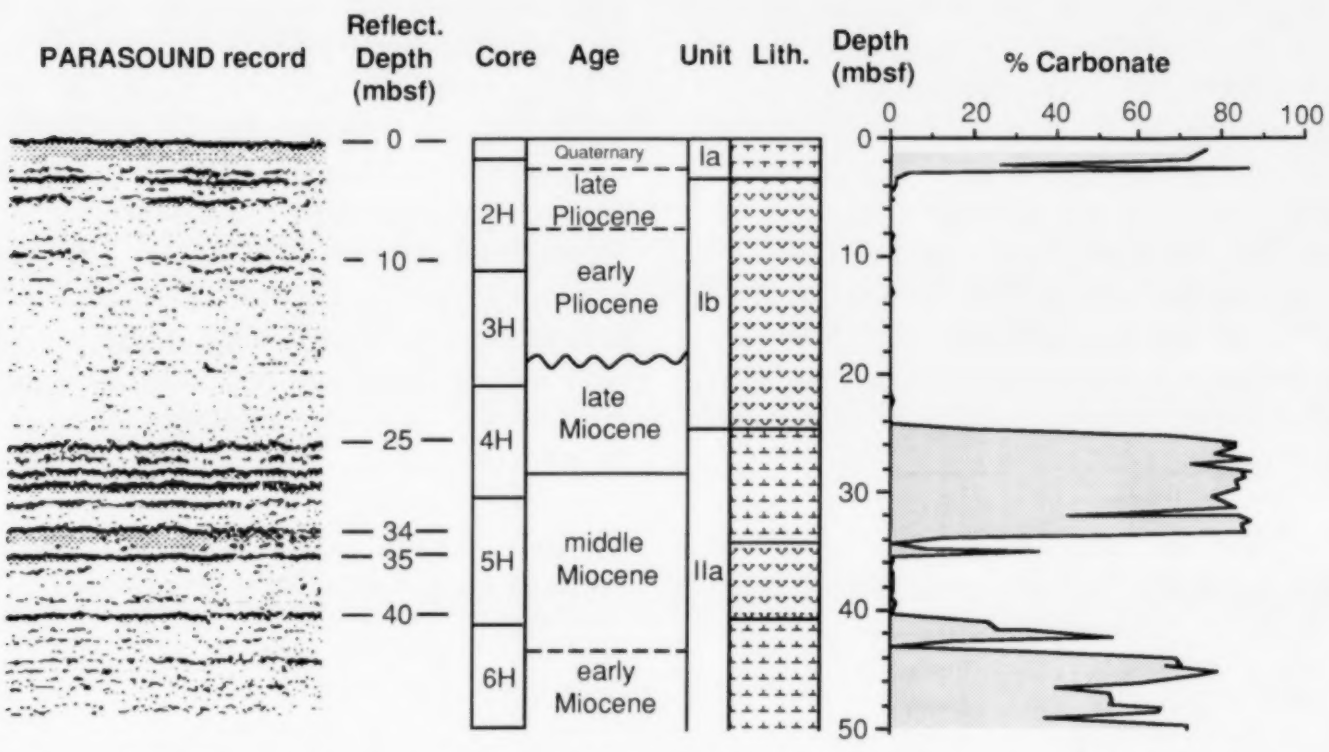

Fig. 5. Correlation of the *Parasound* reflection pattern with lithologic units, age and carbonate curve at ODP Site 690.

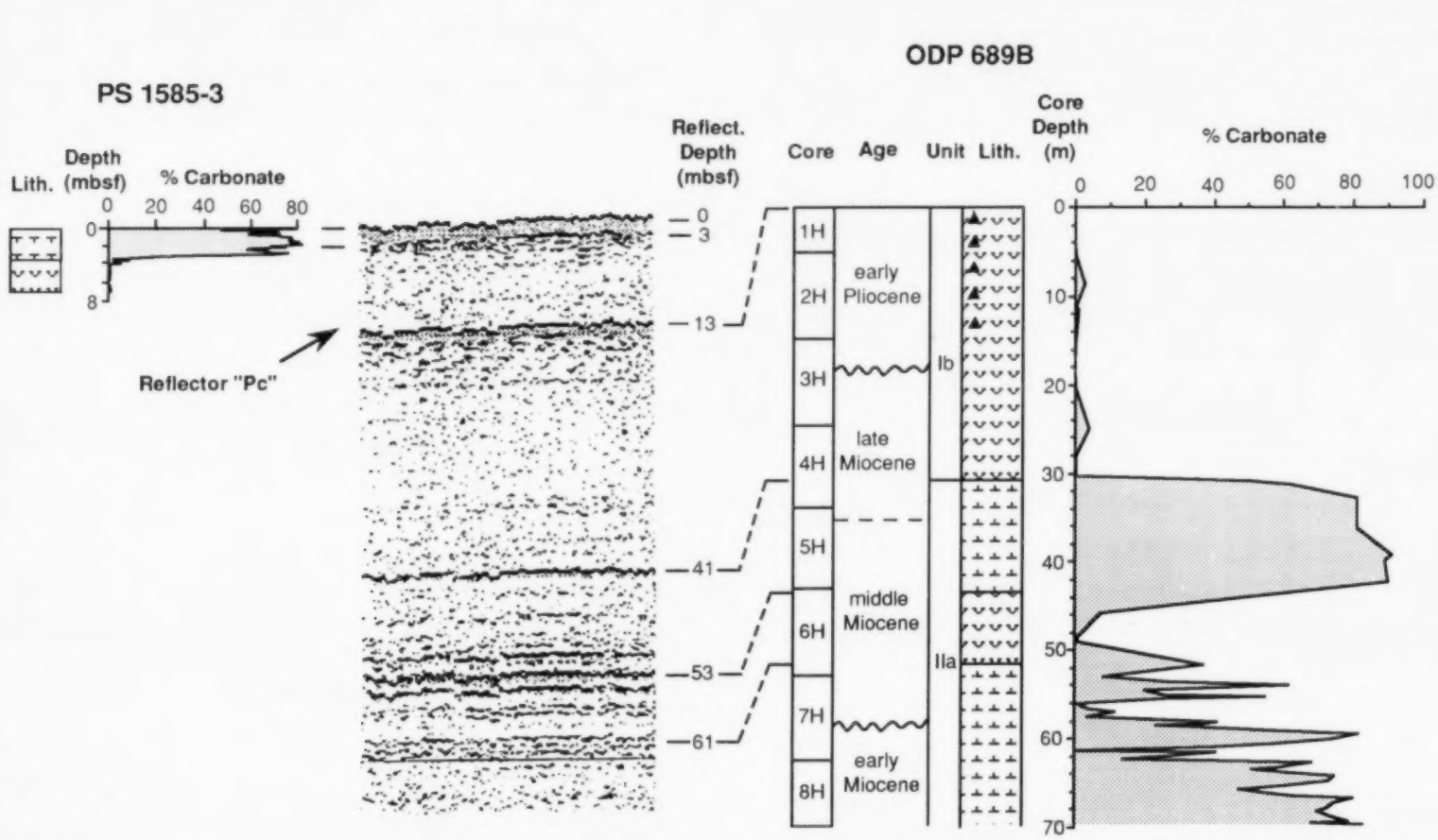

Fig. 6. Correlation of the *Parasound* reflection pattern with lithologic units, age and carbonate curve at ODP Site 689. The uppermost sediment sequence which is missing in the cores drilled at Site 689 is shown by the *Polarstern* Core PS1585-3 record.

properties and lithologies within the overall homogeneous Unit Ib. We, therefore, assign the porcellanite occurrence at ODP Site 689 to the strong reflector at 13 mbsf (Fig. 7) and call this acoustic feature Reflector "Pc". The uppermost sediment sequence missing in the cores of Site 689 was recovered by *Polarstern* core PS1585-3 (Fütterer, 1988), which contains late Pliocene to Quaternary sediments (Fig. 6). This piston core was taken by R.V. *Polarstern* during Leg ANT-VI/3 at the same location on Maud Rise (Fütterer, 1988). A similar porcellanite was not encountered at ODP Site 690, thus Reflector "Pc" is not present in the subbottom profiles (Figs. 5 and 8).

Lithologic Unit IIa is characterized by a wide variety of pure and mixed biogenic siliceous and calcareous sediments. Such changes as documented e.g. in the carbonate curve find their expression in the pattern of acoustic records (Figs. 5 and 6). The uppermost sediment of Unit II is a diatom-bearing nannofossil ooze with carbonate contents >80%, which cover the boundary between the middle and late Miocene. The top of this nannofossil ooze layer at 25 mbsf at ODP Site 690 (41 mbsf at Site 689) correlates well with the top of a sequence of reflectors, which marks the boundary between Lithologic Units I and II. At Site 690 the base of the nannofossil ooze can also be correlated with a high amplitude reflection at 34 mbsf (53 mbsf at Site 689). Deeper in the sequence within Lithologic Unit IIa, a diatom ooze layer of low carbonate content (between 35 and 40 mbsf at Site 690 and between 53 and 61 mbsf at Site 689) is followed by diatom-bearing nannofossil ooze with

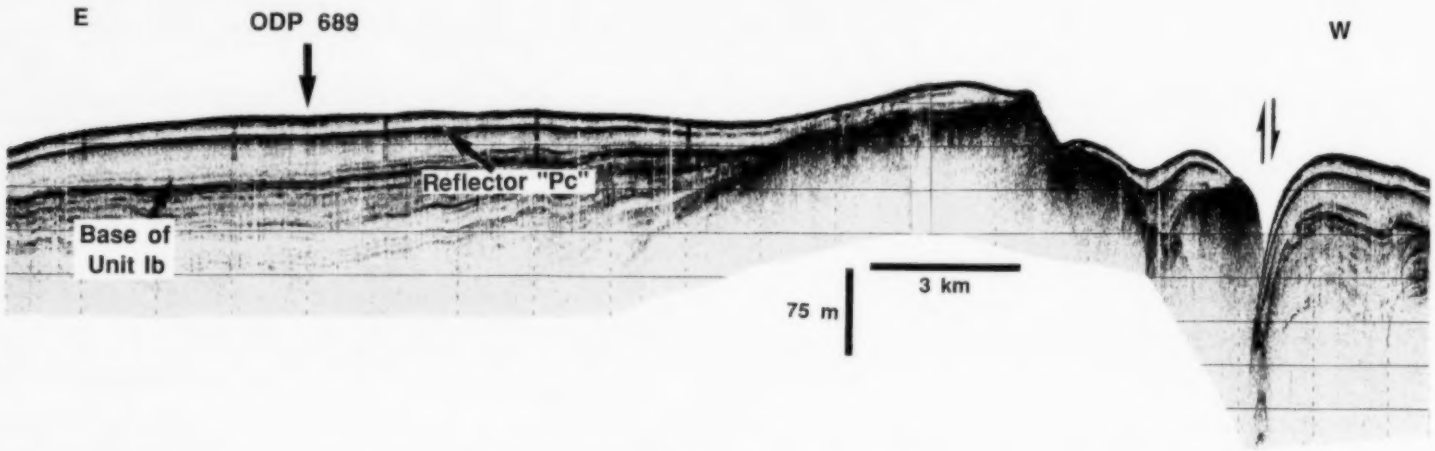

Fig. 7. Analogue record of 3.5 kHz profiling passing over ODP Site 689 obtained by *Polarstern* during Leg ANT-VI/3.

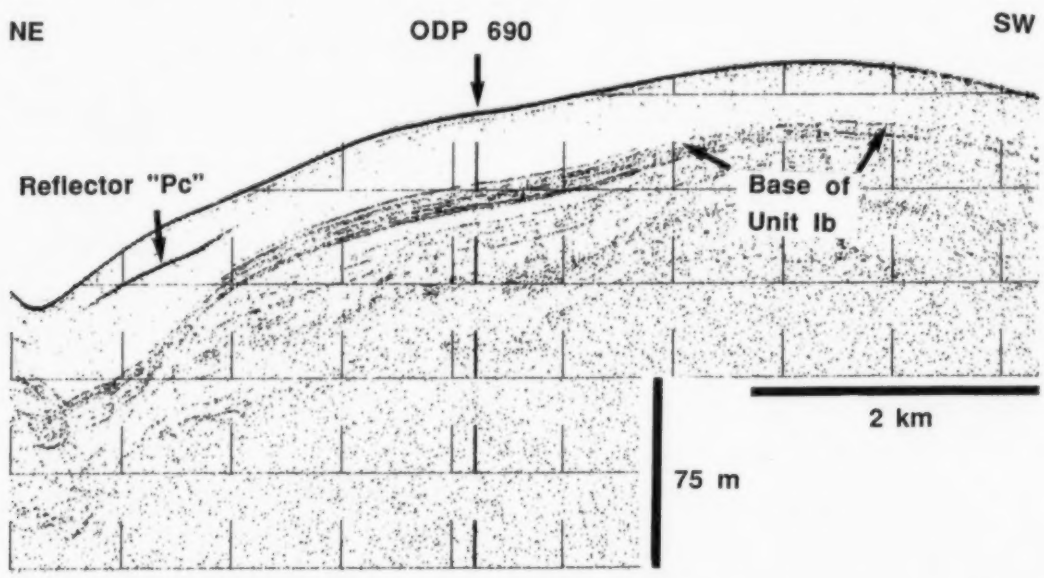

Fig. 8. The 3.5 kHz profile crossing over ODP Site 690 obtained onboard *JOIDES Resolution* (modified from Barker et al., 1988).

highly fluctuating carbonate contents between 0 to 80% below (Figs. 5 and 6).

Occurrence and regional distribution of Reflector "Pc"

The reflection pattern of Reflector "Pc" shows slight differences between the 3.5 kHz and *Parasound* echosounding system. Figure 9 shows a comparison of the analogue records of both systems from two different locations. In the case of the distinct occurrence of Reflector "Pc" both analogue systems show a high amplitude reflection (e.g. in Fig. 9A and B at ca. 13 mbsf). At the location where the 3.5 kHz record reveals no reflection (Fig. 9D) a slight reflection is partly visible in the *Parasound* pattern at 10 mbsf (Fig. 9C), which is most likely originated by the better lateral resolution of the *Parasound* system. For mapping of Reflector "Pc" we have not used similar reflections of low amplitude.

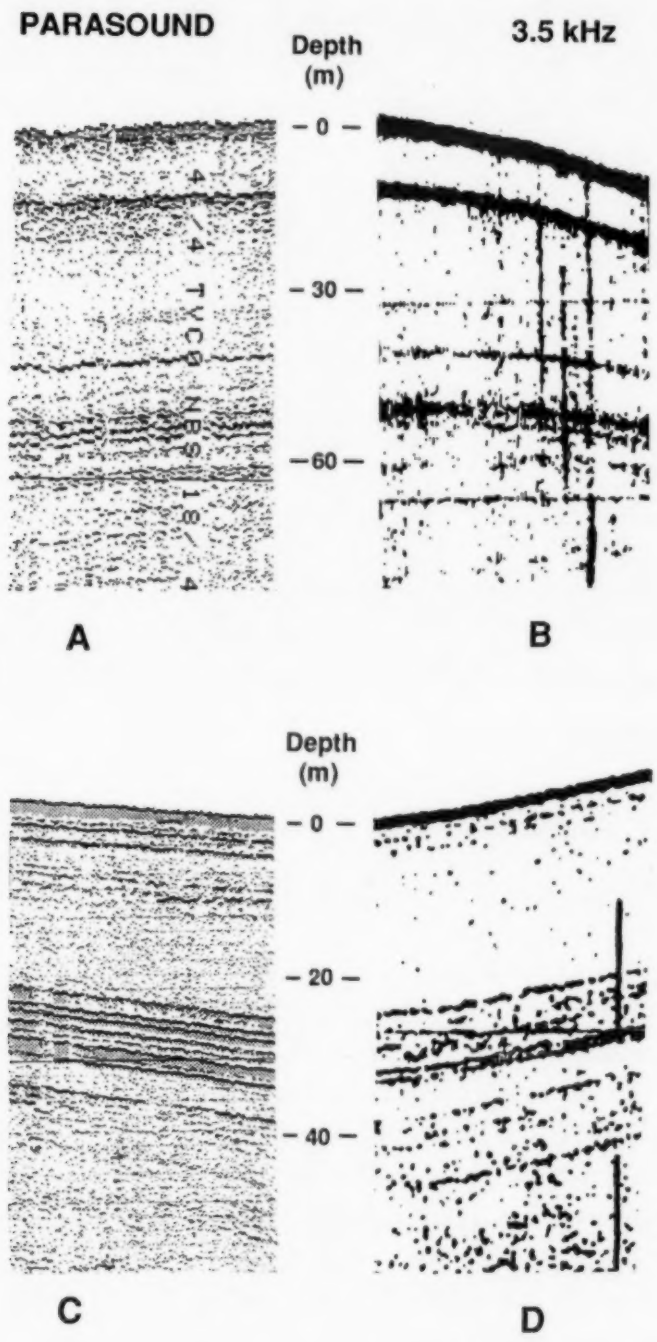

Fig. 9. Comparison of *Parasound* and 3.5 kHz echosounding profiles at two different locations on Maud Rise. Figure 9A and B shows records where Reflector "Pc" occurs at 13 mbsf. In Fig. 9C and D a slight reflection at ca. 10 mbsf is only seen in the *Parasound* record and not in the 3.5 kHz profile.

All echosounding records made during four *Polarstern* cruises to Maud Rise were analysed in order to elucidate the distribution of Reflector "Pc". The regional occurrence is shown along the ships track (Fig. 10) as well as in the compiled profile sections (Figs. 3 and 4). Since the occurrence of Reflector "Pc" is highly variable and the spacing of survey profiles is irregular and widely spaced, we have not interpolated between the lines to define provinces. Nevertheless Fig. 10 already gives a good impression of the regional distribution of Reflector "Pc". With the exception of a small area in the southwestern part of the survey area, the reflector was not found below the 3000 m isobath. It was mainly detected in the northern part of the central shallow Maud Rise as well as on its western side. In some areas Reflector "Pc" is found continuously, e.g. in the surroundings of ODP Site 689 and between 64°45'S and 65°S and 1°E and 2°E (Fig. 10), indicated on profiles 2 and 3 (Fig. 4). In other areas the occurrence seems to be more patchy.

In general, Reflector "Pc" occurs around 12 mbsf with a depth range from 8 to 18 mbsf. A minimum depth of 5–6 mbsf and maximum values between 18 and 23 m are rarely observed. At ODP Site 689, Reflector "Pc" appears at 13 mbsf and can be traced over long distances. To the east Reflector "Pc" disappears where slopes become steeper and the thickness of Lithologic Unit Ib is diminished. To the west of ODP Site 689 the 3.5 kHz record shows a shallow buried basement high, with onlap structures of the deeper reflectors of Lithologic Unit II (Fig. 7). Lithologic Unit Ib of reduced thickness seems to cover the basement high over a long distance and Reflector "Pc" can be traced close to the summit of the basement high

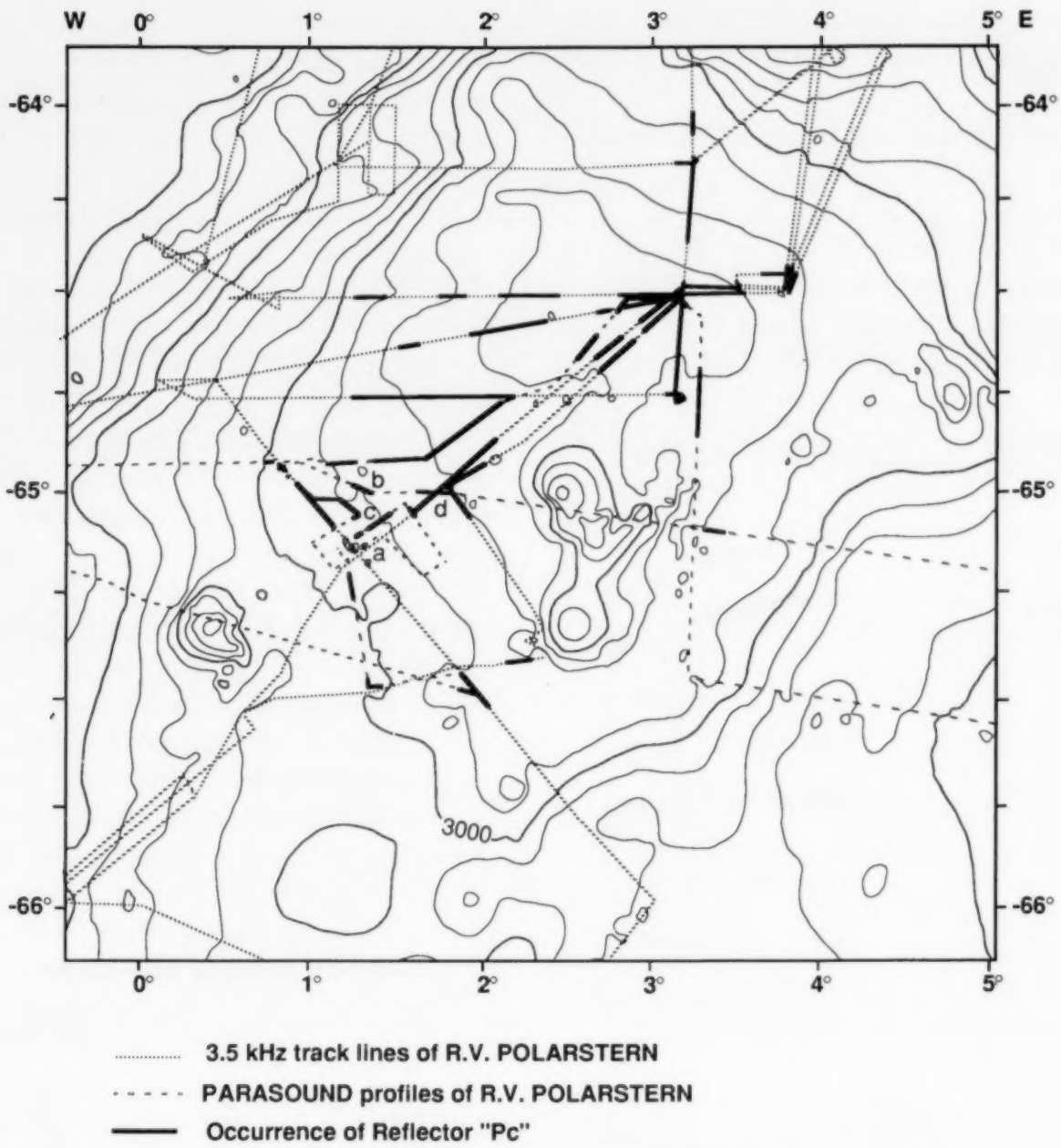

Fig. 10. Track lines of R.V. *Polarstern* on Maud Rise and geographic distribution of Reflector "Pc". Locations of *Parasound* records given in Figs. 13a–13d are marked (*a–d*).

with varying amplitudes. The western end of the basement feature is formed by a fault (Fig. 7).

In contrast to ODP Site 689, Reflector "Pc" was not found at Site 690 (Fig. 8). However, 3.5 kHz profiling during ODP Leg 113 site survey onboard *JOIDES Resolution* shows Reflector "Pc" in a small area in the vicinity of Site 690 (Fig. 8). It occurs to the northeast where the Neogene sediment cover is tectonically complicated by a volcanic structure. During *Polarstern* cruise ANT-VIII/6 the bathymetry and subsurface sediments were studied in detail (Fig. 11). In the relatively flat area northeast of ODP Site 690 a distinct cone was found rising ca. 350 m above its base at 3025 m of water. Due to the cone-shaped morphology and the average slope angle of 15° we interpret the feature as a volcanic edifice (Fig. 12). A second volcanic structure is found farther to the east (Figs. 11 and 12). The submarine volcanic cone is associated with a circular morphologic depression around the volcano. Such moats are typical morphological features and often observed around cones or pinnacles on the entire Maud Rise. In the northeastern part of the Rise at Profile 3 east of ODP Site 689 (Fig. 4 at the course change) a volcanic mount occurs with extensive erosion structures in the sediments around the cone (Gersonde and Abelmann, 1987). Bottom currents

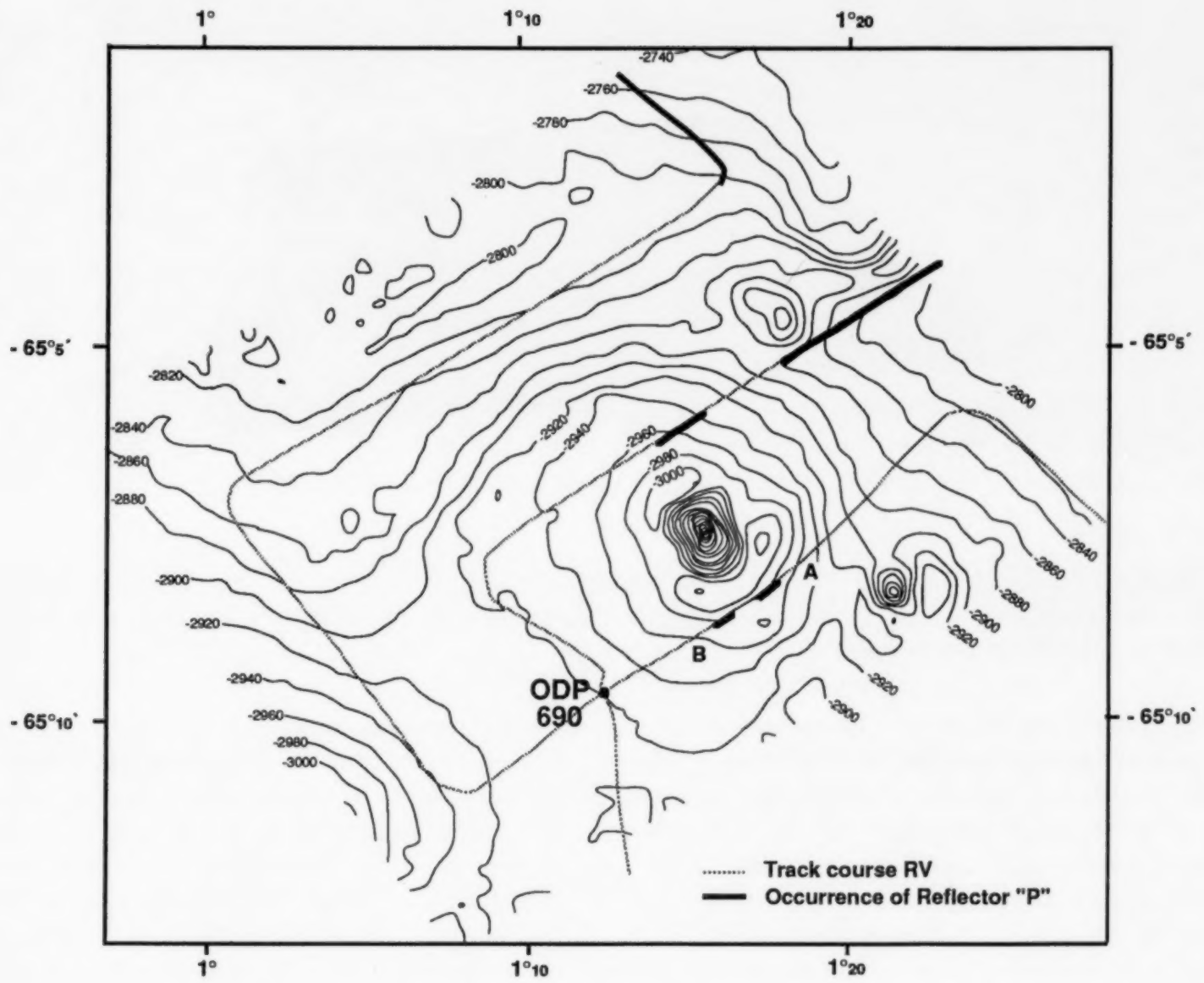

Fig. 11. Bathymetric detail from the western central part of Maud Rise at ODP Site 690 and its vicinity. Isolines of seabottom topography are from *Hydrosweep* measurements conducted during *Polarstern* cruise ANT-VIII/6. Track lines and vertical occurrence of Reflector "Pc" are indicated.

could have eroded the sediments around the volcanic cone producing large hiatuses in their sediment record. Based on the *Parasound* records the sediments around the volcanic feature near ODP Site 690 do not show erosion within Lithologic Unit I. In contrast sediments in the depression around the volcanic feature reveal enhanced thickness (Fig. 13a). Greatest thicknesses of Lithologic Unit Ib are reached at the surface depression shown between the marks A and B on the NE–SW striking *Parasound* profile (Fig. 11). This is most probably caused by subsidence at the flanks of the volcano. Details of Neogene tectonic movements and subsidence are not known. However, beneath the volcanic feature, subsidence could be caused by cooling of the magmatic body leading to shrinkage in the basement.

In general, occurrence and amplitude of Reflector "Pc" seems to be related to the thickness of Lithologic Unit Ib. Figure 13b gives an example from the western Maud Rise where the Neogene sediment cover shows irregular sediment layers in a large area. Sediment beds of Units I and II are faulted and form a half-graben structure. Closer to the fault, sediment thickness increases and documents synsedimentary tectonic movements. Within the half-graben the base of Lithologic Unit Ib lies at 55–50 mbsf (Fig. 13b), which is much deeper than the average value of 30 mbsf. There, Reflector "Pc" shows higher amplitudes than farther to the

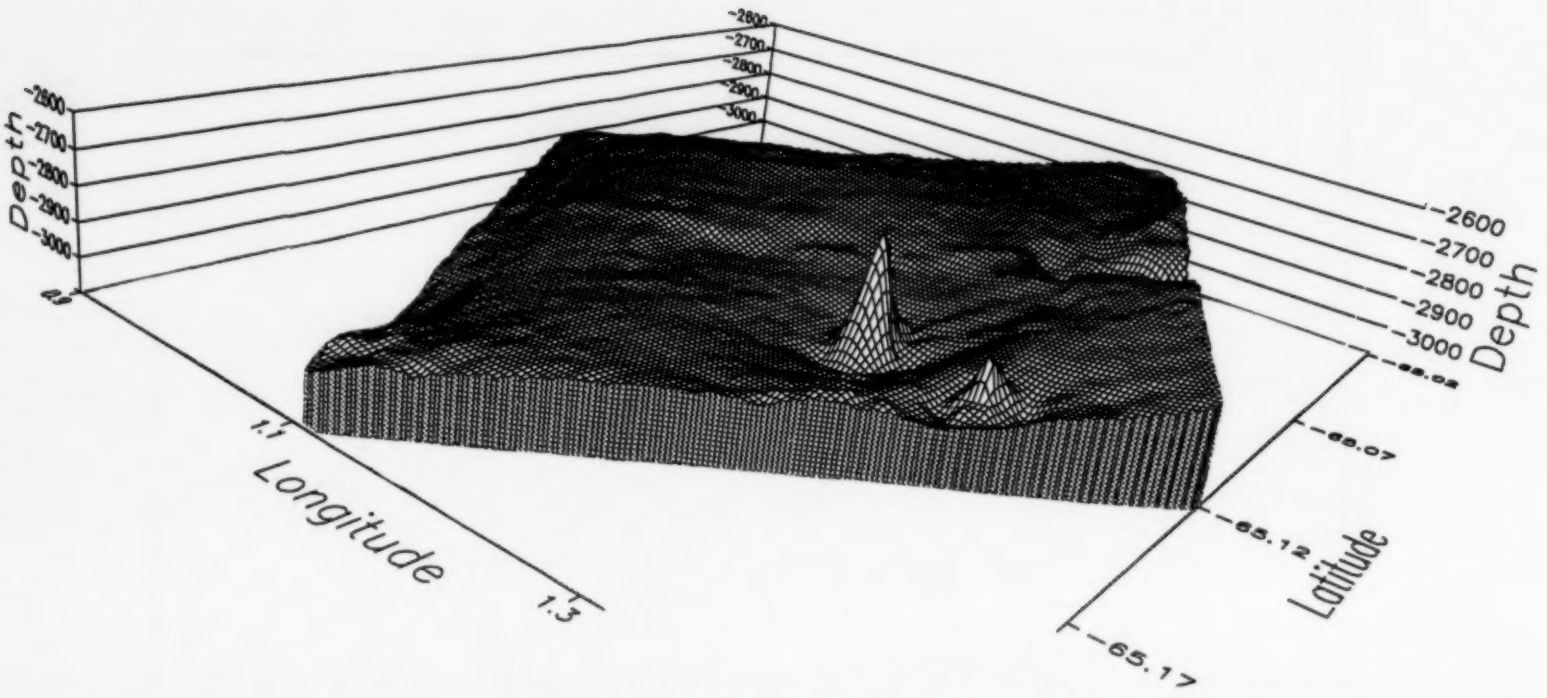

Fig. 12. Perspective view of the seabottom topography at ODP Site 690 from the map of Fig. 11. The view is from southeast to northwest, vertical exaggeration is 8 times.

west, where thickness of Lithologic Unit I decreases. Highest amplitudes of Reflector "Pc" were recorded in an area of maximum thickness for Unit Ib, with more than 100 m (Fig. 13c). There greatest subbottom depth of Reflector "Pc" is detected at around 23 mbsf.

In the other case, the disappearance of Reflector "Pc" is associated with a reduced thickness of Unit Ib. The E–W section of Fig. 13d documents Reflector "Pc" in the eastern part in a subbottom depth of 10 m, where the base of Lithologic Unit Ib reaches greater depth than 20 mbsf. Although Reflector "Pc" does not crop out, the reflector itselfs disappears to the west, which is associated with decreasing thickness of Lithologic Unit Ib to less than 20 m. The examination of all profiler records has shown that Reflector "Pc" cannot be detected if the thickness of Unit Ib is less than 15–20 m.

Reflector "Pc" and porcellanite formation

High seismogram amplitudes indicate that Reflector "Pc" is caused by a major change in acoustic properties of the sediments. Although porcellanite samples have not yet been directly analysed, the unusual highly cemented rock, observed at ODP Site 689 exhibits physical properties that differ significantly from the values of the diatom ooze Unit Ib (Barker et al., 1988). The dissolution of the highly porous diatom ooze and the reprecipitation of opal-CT leads to a distinct loss of porosity. The sediment wet-bulk density, which next to *p*-wave velocity is the most important parameter of acoustic impedance, is thus enhanced. In sediments from the southern Bering Sea an increase of wet-bulk density values from 1.4 g cm^{-3} to > 1.8 g cm^{-3} were reported from diatom oozes that have been changed to opal-CT cemented deposits (Creager et al., 1973). The abrupt change in bulk density is associated with a major acoustic reflector. In the northern Pacific belt of diatomaceous ooze this regional acoustic reflector was generally produced by the conversion of unconsolidated diatom oozes to opal-CT cemented porcellanites at around 600 m below the seafloor (Hein et al., 1978). The reflector mirrors seafloor topography and was therefore described as a bottom simulating reflector (BSR) by Creager et al. (1973). Hein et al. (1978) interpreted the BSR as an isothermal surface at around 35°C and concluded that its topography depends on the depth of burial and the geothermal gradient. Silica transformation occurs at the isothermal surface. It moves upwards with continued sedimentation as a diagenetic front (Hein et al., 1978).

In the North Atlantic the relation of silica diagenesis to the development of a seismic reflector was also reported by Thein and Von Rad (1987). At several drill sites, they observed a sharp transition from opal-A to opal-CT in Eocene sediments. This front of silica diagenesis causes the seismic reflector A^c, which has been described in large areas of the western North Atlantic (Tucholke and Mountain, 1979). The seismic reflector A^c is missing in the area of DSDP Site 603, where the conversion of opal-A to opal-CT is inhibited and the diagenetic front is not developed (Thein and Von Rad, 1987).

The conversion of opal-A to opal-CT, representing porcellanite formation, occurs in the marine environment during later diagenesis when sediments reach higher temperatures (Calvert, 1974; Keene, 1975; Hein et al., 1978; Riech and Von Rad, 1979; Williams and Crerar, 1985). In contrast, the porcellanite found at ODP Site 689 is young and occurs at low burial depth. It belongs to only a few unusual young porcellanite occurrences known from the Kerguelen Plateau, Maud Rise and from the Southwest Indian Ridge (Weaver and Wise, 1973; Barker et al., 1988; Schlich et al., 1989; Bohrmann et al., 1990). These porcellanites in 5.5 to 14 m sediment depth are intercalated in very pure diatom oozes and their occurrence seems to be restricted to submarine plateaus and rises of the Southern Ocean (Bohrmann et al., 1990). Since several authors favor temperature as a major factor for the opal-A to opal-CT conversion, the porcellanite precipitation in near-surface sediments on the Kerguelen Plateau has often been explained by the influence of higher temperature due to magmatic processes (e.g. Hesse, 1988). Based on oxygen isotopic analyses of the opal-CT samples Botz and Bohrmann (1991) calculated porcellanite formation temperatures of only 0° to 4°C. Such evidence for low temperature opal-CT precipitation seems to be important especially for the Maud Rise porcellanite since volcanic features discussed in this paper are found on Maud Rise. Although the porcellanite is younger than 4 Ma (Barker et al., 1988) and there is no evidence of volcanic activity during that time, volcanism can not totally be excluded. Based on the isotopic data a distinct higher temperature did not occur in the near-surface sediments during the formation of porcellanite (Botz and Bohrmann, 1991).

In general, the opal-CT cemented porcellanite recovered at ODP Site 689 is intercalated into the sedimentary sequence of unconsolidated diatom ooze. Such a silica precipitation could either occur as one or more well-bedded precipitation layers or as concretion nodules that are arranged in a horizontal layer. Similar silica concretions, known as nodular and bedded cherts, are common in hemipelagic and pelagic sequences of various ages and are found in onshore outcrops. In most cases the silica concretions occur in well-defined layers. Since the porcellanite recovered at ODP Site 689 is highly fragmented and displaced by coring, the shipboard scientific party was not able to determine the primary texture and shape of the porcellanite (Barker et al., 1988).

Since we attribute the origin of the Reflector "Pc" to a layer of silica precipitation, the highly variable amplitude of the acoustic reflector may be attributed to a variable occurrence of the silica precipitation horizon. If our interpretation is correct the extent of silica precipitation could be roughly correlated to the amplitudes of Reflector "Pc", although interference phenomena in thin beds have still to be taken into account. Transitions may occur between small silica nodules where Reflector "Pc" shows low amplitudes to a thick porcellanite bed, where high amplitudes of the acoustic reflector are recorded. However, this interpretation remains speculative since the porcellanite was sampled only once in the region and there is no more information available from direct sampling.

Up to now, there are no reasonable explanations for porcellanite formation during early diagenesis. In general, silica precipitation occurs from dissolved silica of pore water. Such silica can be derived by dissolution of opal-A from diatom frustules which are the major components in the sediment. However, the skeletons show variable resistance to dissolution, which is not clearly understood in all its specific aspects (Schinck et al., 1975). Since only small portions of the diatoms are easy to dissolve, a continuous silica supply causing precipitation by oversaturation could be limited. In that case the extent of silica precipita-

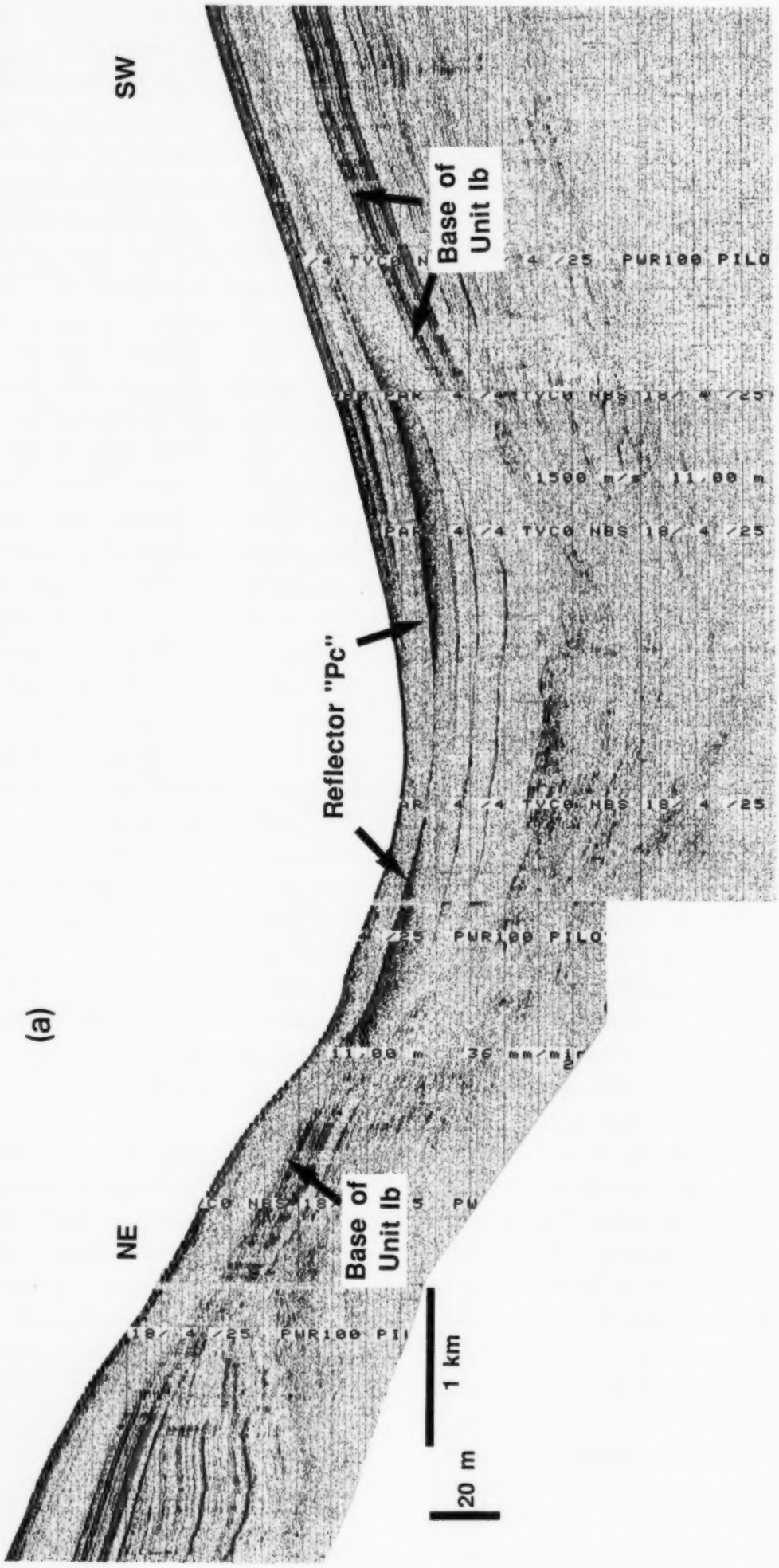
SW
Base of Unit Ib
Reflector "Pc"
Base of Unit Ib
NE
(a)
1 km
20 m

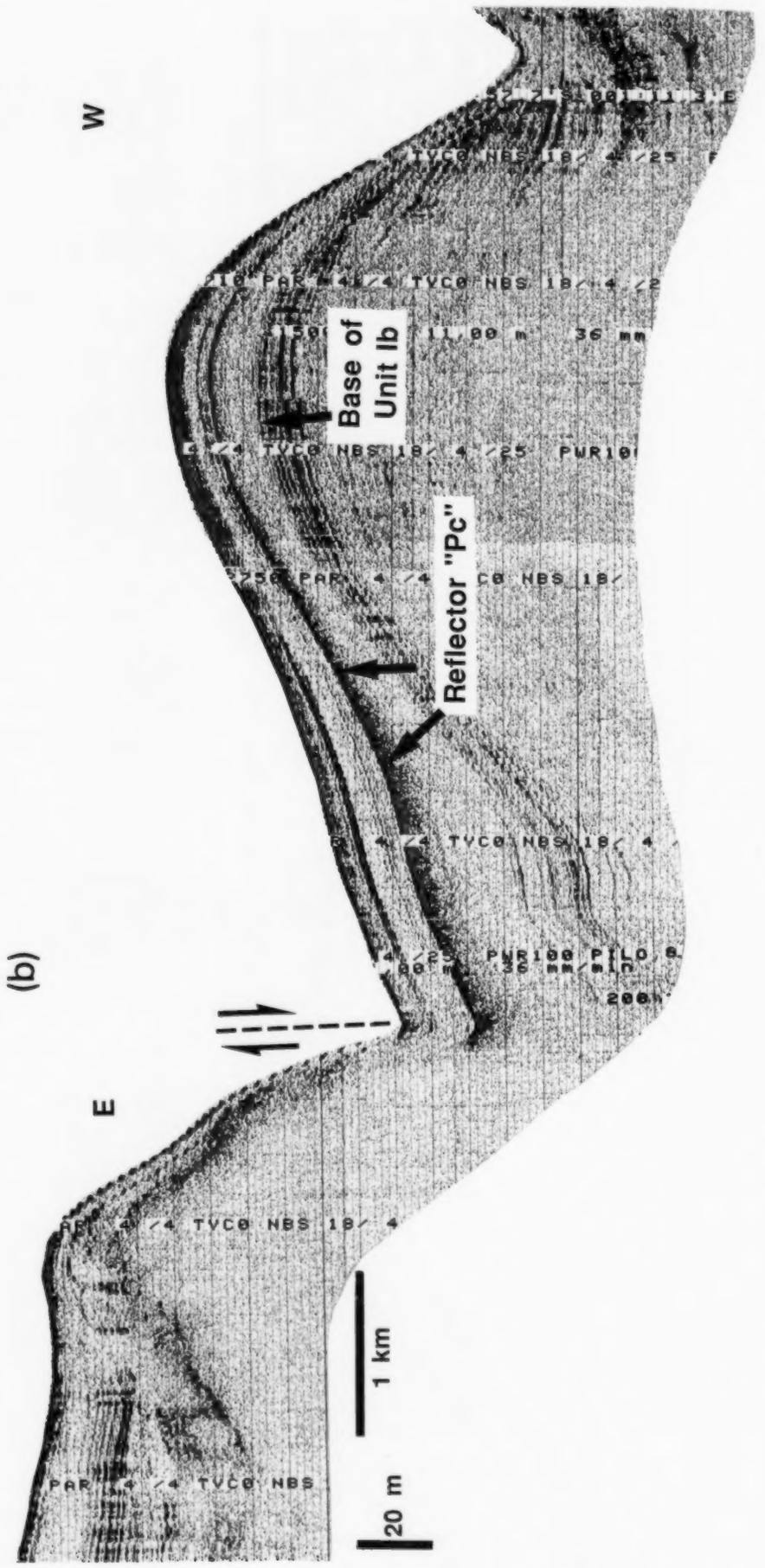
W
Base of Unit Ib
Reflector "Pc"
E
(b)
1 km
20 m

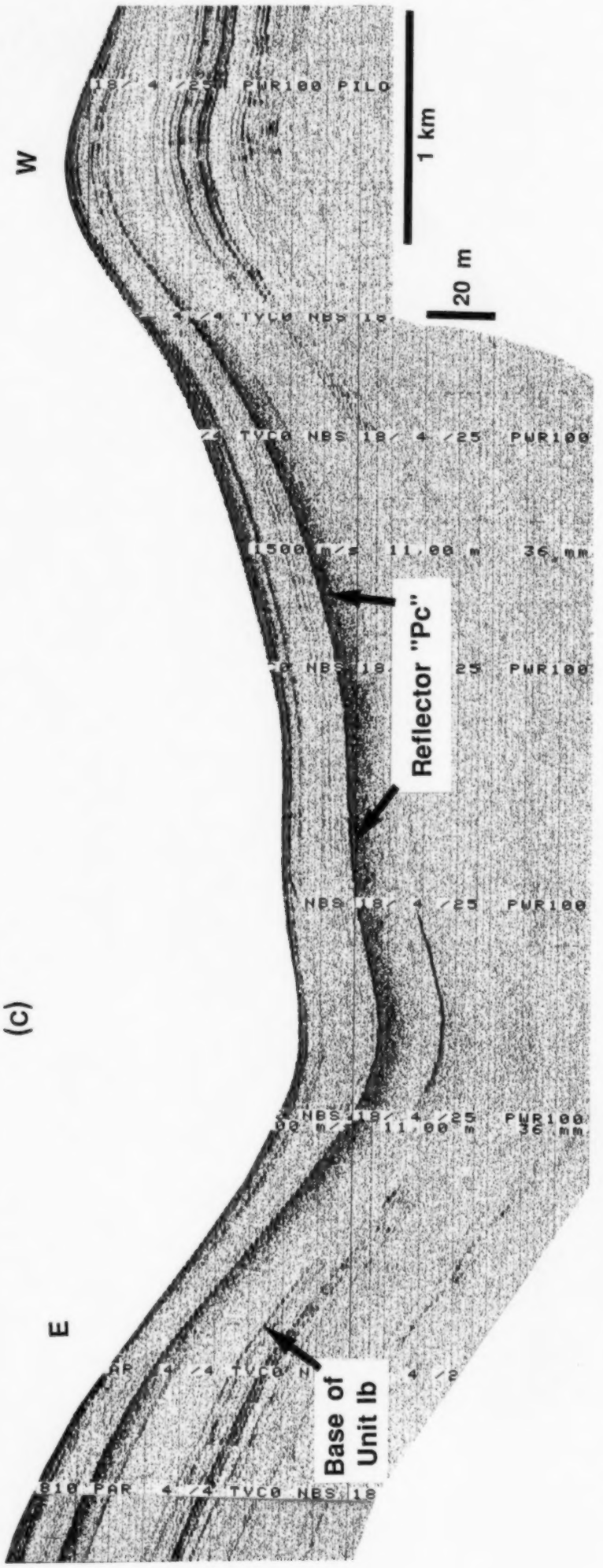
W
E
(c)
1 km
20 m
Reflector "Pc"
Base of Unit Ib

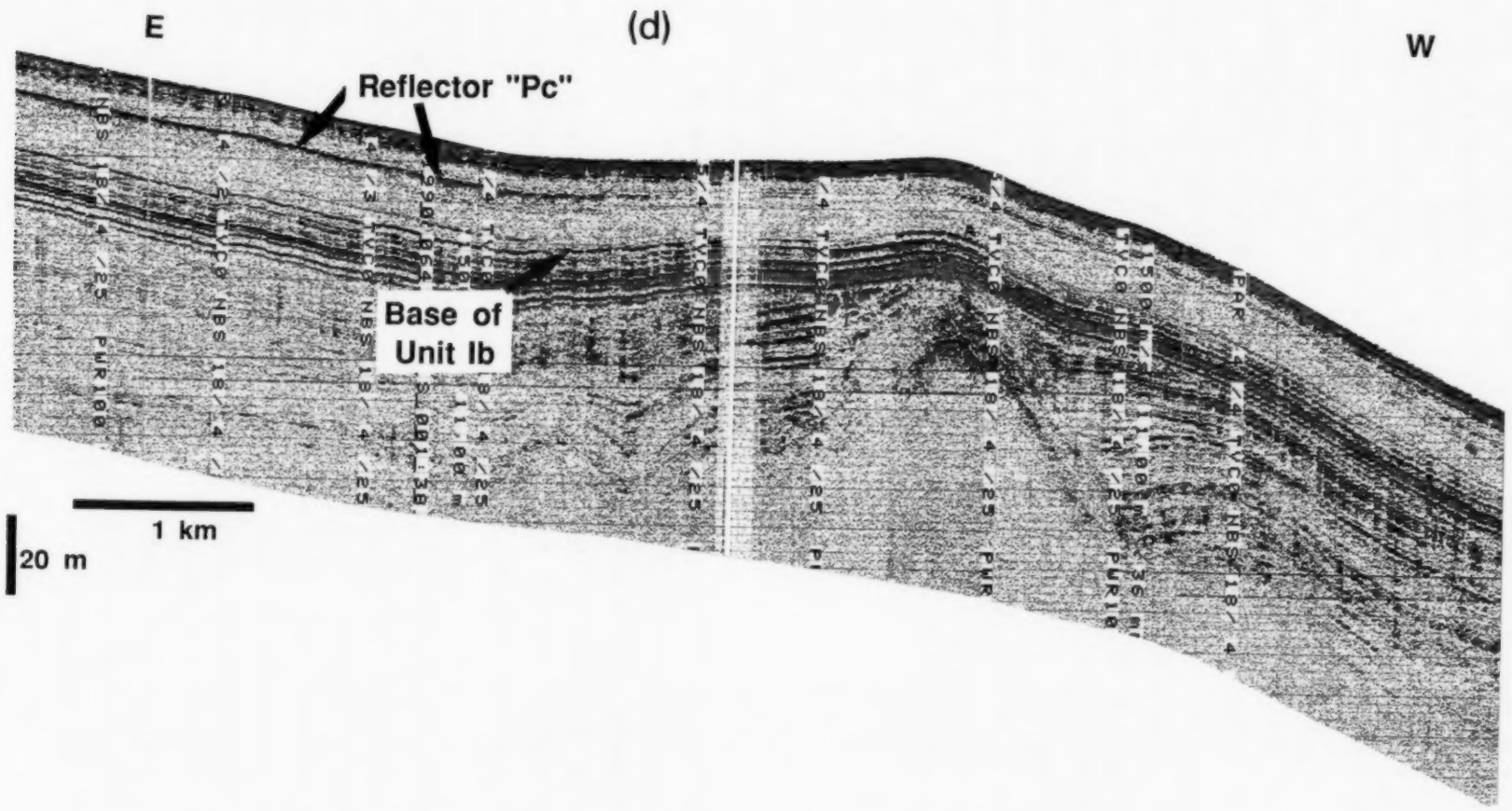

Fig. 13. (a) *Parasound* record south of the volcanic feature in the vicinity of ODP Site 690 (beginning and end of the profile are marked with *A* and *B* in Fig. 11).
(b) *Parasound* record of a half-graben structure indicating variable thicknesses of Unit Ib and variable buried depths of Reflector "Pc".
(c) *Parasound* record showing strong signal of Reflector "Pc" in an area of deep subsidence.
(d) *Parasound* record showing disappearence of Reflector "Pc" to its western direction.

tion may be controlled by the thickness of the diatom ooze layer (Lithologic Unit Ib), which is the potential source sediment for dissolved silica. This agrees well with the observation that the occurrence and the amplitudes of Reflector "Pc" are generally related to the thickness of Lithologic Unit Ib. Based on the examination of all subbottom profiler records, Reflector "Pc" is not detected where thickness of Unit Ib becomes less than 15–20 m (Fig. 13d). This could imply that a minimum thickness of siliceous sediments is necessary for silica dissolution and precipitation. A greater extent of silica cementation is reached in areas where Unit Ib shows greater thicknesses (Figs. 13a–c). This is found mostly in areas of higher subsidence due to tectonic activity. In the other cases the areas of local tectonic movements favour the ascent of pore fluids. Such ascending interstitial water could probably provide enough silica supply for the porcellanite formation, if it is silica-enriched.

Conclusions

Detailed surveys of subbottom profiling and bathymetric investigations, supplemented with sediment drilling data of ODP in the Maud Rise area have elucidated some questions about the nature of Reflector "Pc" in the post-upper Miocene sediment sequence. Major results can be summarized as follows:

(1) The uppermost lithologic units drilled by ODP can be assigned to characteristic reflection patterns in the subbottom profiler records. With the exception of the highly reflective calcareous Subunit Ia the otherwise homogenous diatom ooze of Unit I is dominated by transparent reflection character. The underlaying Unit IIb is well defined by numerous reflectors associated with large changes in carbonate content. Both characteristic reflection units can be traced over long distances on top of Maud Rise.

(2) Except for some small occurrences on its eastern part, Reflector "Pc" was only found in sediments of the northern and western flat area of Maud Rise between 3000 and 2000 mbsl. Reflector "Pc" occurs mainly between 8 and 18 mbsf with average depth occurrence around 12 mbsf.

(3) The pattern of the regional distribution of Reflector "Pc" and its amplitude is often related to the thickness of lithologic Unit Ib, which seems to be highly influenced by the deeper geological structures. Reflection amplitude of Reflector "Pc" is enhanced where local tectonic synsedimentary subsidence causes greater thicknesses of lithologic Unit I (e.g. in half-graben regions and in the surroundings of postulated volcanic cones).

(4) The depth level of Reflector "Pc" represents a specific stratigraphic horizon, in the diatom ooze of lower Pliocene age. We suggest that the existence of Reflector "Pc" strongly depends on the formation of the porcellanite horizon, e.g. at ODP Site 689. The acoustic Reflector "Pc" does not develop where silica was not precipitated, as shown at ODP Site 690. Since silica cementation increases the acoustic impedance of the sediment the amplitude of reflection may be directly correlated with the extent of porcellanite formation. The relation of Reflector "Pc" occurrence and thickness of Unit Ib implies a possible influence of diatom ooze as a source material for silica precipitation.

Acknowledgements

The authors gratefully acknowledge critical reading and enlightening discussion of the manuscript by Dieter Fütterer, Peter Hempel, Gabi Uenzelmann and Heiner Villinger. The help of the technical staff, especially Rita Fröhlking, Helga Rhodes, Imke Engelbrecht, Norbert Lensch and the crew of R.V. *Polarstern* is acknowledged. We gratefully acknowledge data processing made by Fred Niederjasper and Clemens Heidland. This paper represents contribution 486 of the Alfred Wegener Institute for Polar and Marine Reasearch and publication 43 of Special Research Project SFB 261. Financial support was kindly provided by the *Deutsche Forschungsgemeinschaft* (Ku 683/1 and Sp 296/2).

References

Abelmann, A., Gersonde, R. and Spieß, V., 1990. Pliocene–Pleistocene paleoceanography in the Weddell Sea—Siliceous microfossil evidence. In: U. Bleil and J. Thiede (Editors),

Geological History of the Polar Oceans: Arctic Versus Antarctic. (NATO ASI Ser. C) Kluwer, Dordrecht, 308: 729–759.
Barker, P.F., Kennett, J.P. et al., 1988. Proc. Init. Rep. ODP, 113.
Bohrmann, G., Kuhn, G., Abelmann, A., Gersonde, R. and Fütterer, D., 1990. A young porcellanite occurrence from the Southwest Indian Ridge. Mar. Geol., 92: 155–163.
Botz, R. and Bohrmann, G., 1991. Low-temperature opal-CT precipitation in Antarctic deep sea sediments: evidence from oxygen isotopes. Earth Planet. Sci. Lett., 107: 612-617.
Calvert, S.E., 1974. Deposition and diagenesis of silica in marine sediments. In: K.J. Hsü and H. Jenkyns (Editors), Pelagic Sediments on Land and under the Sea. Spec. Publ. Int. Assoc. Sedimentol., 1: 273–299.
Cordes, D., 1990. Sedimentologie und Paläomagnetik an Sedimenten der Maudkuppe (Nördliches Weddellmeer). Ber. Polarforsch., 71, 158 pp.
Creager, J.S. et al., 1973. Init. Rep. DSDP, 19: 897–913.
Fütterer, D., 1987. Die Expedition Antarktis-IV mit FS "Polarstern" 1985/86; Bericht von den Fahrtabschnitten ANT-IV/3–4. Ber. Polarforsch., 33, 204 pp.
Fütterer, D., 1988. Die Expedition Antarktis-VI mit FS "Polarstern" 1987/88. Ber. Polarforsch., 58, 267 pp.
Fütterer, D. and Schrems, O., 1991. Die Expedition Antarktis-VIII mit FS "Polarstern" 1990. Bericht von den Fahrtabschnitten ANT-VIII/6–7. Ber. Polarforsch., 90, 231 pp.
Gersonde, R. and Abelmann, A., 1987. Erste Ergebnisse zur Biostratigraphie am Maud Rise. In: D. Fütterer (Editor), Die Expedition Antarktis-IV mit FS "Polarstern" 1985/86; Bericht von den Fahrtabschnitten ANT-IV/3–4. Ber. Polarforsch. 33: 184–187.
Gersonde, R., Abelmann, A., Burckle, L.H., Hamilton, N., Lazarus, D., McCartney, K., O'Brian, P., Spieß, V. and Wise, S.W., Jr., 1990. Biostratigraphic synthesis of Neogene siliceous microfossils from the Antartic Ocean, ODP Leg 113 (Weddell Sea). In: P.F. Barker, J.P. Kennett et al. Proc. ODP, Sci. Results, 113: 915–936.
Grant, J.A. and Schreiber, R., 1990. Modern swaths sounding and sub-bottom profiling technology for research apllications: The Atlas Hydrosweep and Parasound systems. Mar. Geophys. Res., 12: 9–19.
Gutberlet, M. and Schenke, H.W., 1989. Hydrosweep: New era in high precision bathymetric surveying in deep and shallow water. Mar. Geod., 13: 1–23.
Hein, J.R., Scholl, D.W., Barron, J.A., Jones, M.G. and Miller, J., 1978. Diagenesis of Late Cenozoic diatomaceous deposits and formation of the bottom simulating reflector in the southern Bering Sea. Sedimentology, 25: 155–181.
Hesse, R., 1988. Origin of chert, I. Diagenesis of biogenic siliceous sediments. Geosci. Can., 15: 171–192.
Keene, J.B., 1975. Cherts and porcellanites from the North Pacific DSDP, Leg 32. In: R.L. Larson, R. Moberly et al. Init. Rep. DSDP, 32: 429–507.
Kuhn, G., Ehrmann, W., Hambrey, M., Melles, M. and Schmiedl, G., 1992. Glaciomarine sedimentary processes in the Weddell Sea and Lazarev Sea. In: U. Bathmann et al., Die Expedition Antarktis IX 1–4 des Forschungsschiffes "Polarstern" 1990/91. Ber. Polarforsch., 100 (in press).
Riech, V. and Von Rad, U., 1979. Silica diagenesis in the Atlantic Ocean: Diagenetic potential and transformations. In: M. Talwani, H.W. Hay and W.B. Ryan (Editors), Deep Drilling Results in the Atlantic Ocean: Continental Margins and Paleonvironment. Am. Geophys. Union, M. Ewing Ser., 3: 315–340.
Rostek, F., Spieß, V. and Bleil, U., 1991. *Parasound* echosounding; comparison of analogue and digital echosounder records and physical properties of sediments from the Equatorial South Atlantic. Mar. Geol., 99: 1–18.
Schandl, E.S., Gorton, M.P. and Wicks, F.J., 1990. Mineralogy and geochemistry of alkali basalts from Maud Rise Weddell Sea, Antarctica. In: P.F. Barker, J.P. Kennett et al. Proc. ODP, Sci. Results, 113: 5–14.
Schenke, H.W. and Ulrich, J., 1987. Mapping the seafloor. Appl. Geogr. Dev., 30: 110–126.
Schink, D.R., Guinasso, N.L. and Fanning, K.A., 1975. Processes affecting the concentration of silica at the sediment–water interface of the Atlantic Ocean. J. Geophys. Res., 80: 3013–3031.
Schlich, R., Wise, S.W. et al., 1989. Proc. Init. Rep. ODP, 120.
Schreiber, R. and Schenke, H.W., 1990. Atlas Hydrosweep: Efficient hydrographic surveying of EEZ with new multibeam echosounder technology for shallow and deep water. In: D.A. Ardus and M.A. Champ (Editors), Ocean Resources. Kluwer, Dordrecht, I: 73–87.
Thein, J. and Von Rad, U., 1987. Silica diagenesis in continental rise and slope sediments off Eastern North America (Sites 603 and 605, Leg 93; Sites 612 and 613, Leg 95). In: C.W. Poag, A.B. Watts et al. Init. Rep. DSDP, 95: 501–525.
Tucholke, B.E. and Mountain, G.S., 1979. Seismic stratigraphy, lithostratigraphy and paleosedimentation patterns in the North American Basin. 3: 58–86.
Weaver, F.M. and Wise, S.W., 1973. Early diagenesis of deep sea bedded chert. Antarctic J., (September–October): 298–230.
Williams, L.A. and Crerar, D.A., 1985. Silica diagenesis, II, General mechanisms. J. Sediment. Petrol., 55: 312–321.

Marine Geology, 106 (1992) 89–105
Elsevier Science Publishers B.V., Amsterdam

Hypsometry of divergent and translational continental margins of southern Africa

K.O. Emery[a], J.M. Bremner[b] and J. Rogers[c]

[a]*Woods Hole Oceanographic Institution, Woods Hole, MA 02543, USA*
[b]*Marine Geoscience Section of the Geological Survey, University of Cape Town, Rondebosch 7700, South Africa*
[c]*Marine Geoscience Unit, Department of Geology, University of Cape Town, Rondebosch 7700, South Africa*

(Received August 10, 1991; revision accepted November 6, 1991)

ABSTRACT

Emery, K.O., Bremner, J.M. and Rogers, J., 1992. Hypsometry of divergent and translational continental margins of southern Africa. *Mar. Geol.*, 106: 89–105.

Flattenings that may be shelves formed by marine erosion/deposition or by slump masses are present on continental margins of southern Africa that border both the Atlantic and Indian oceans. Breaks in slope, indicated along sounding lines, suggest that a shallow terrace of the Atlantic margin has been warped downward from depths of about 130 m southward to about 200 m, and a deeper terrace lies between depths of about 150 m to about 440 m. Examination of contours and hypsometry (areas measured between depth contours) show widespread flattenings at about −65 and −95 m on the Indian Ocean margin and −125, −155, and −190 m along the Atlantic margin. Seismic profiles indicate that some of these and other more local flattenings are on slump blocks and thus are not correlatable for long distances. An additional complication is that sediment introduced by rivers is transported alongshore by wave-induced and oceanic bottom currents, and that their deltas are ephemeral.

Introduction

The eastern and western continental margins of southern Africa occupy similar latitudes, and both originated at about the same time: during the Early to mid-Mesozoic Era. Yet, they have different profiles, with a wide continental shelf on the Atlantic Ocean side and a narrow shelf on the Indian Ocean side. Moreover, the Atlantic margin may have several submerged shelves, one near the usual depth and the other much deeper (at several hundred meters). One cause of difference between the margins may be their different origin by plate movements: divergence for the Atlantic margin and translation for the Indian Ocean one. As shown by Fig. 1A, both margins of southern Africa were near the southern middle of Gondwana before this megacontinent became disrupted by rifting, beginning about 160 m.y. ago followed by drifting and emplacement of oceanic crust about 130 m.y. ago.

Divergent separation of South America from Africa (Fig. 1B) was associated with widening of the South Atlantic Ocean and development of its mid-Atlantic Ridge, where new oceanic crust still is being formed within the median valley. Just as for other divergent continental margins, the one along the Atlantic coast of southern Africa became bordered by listric faults (down toward the ocean floor), especially during the early stages of divergence when stretching of continental crust led to later actual rifting and emplacement of new oceanic crust (Austin and Uchupi, 1982; Gerrard and Smith, 1982; Emery and Uchupi, 1984; Uchupi and Emery, 1991, and references therein; Fig. 1B). In contrast, the translational margin along the Indian Ocean coast sheared Gondwana in such a way that Madagascar moved southward with

Correspondence to: K.O. Emery, Woods Hole Oceanographic Institution, Woods Hole, MA 02543, USA.

0025-3227/92/$05.00

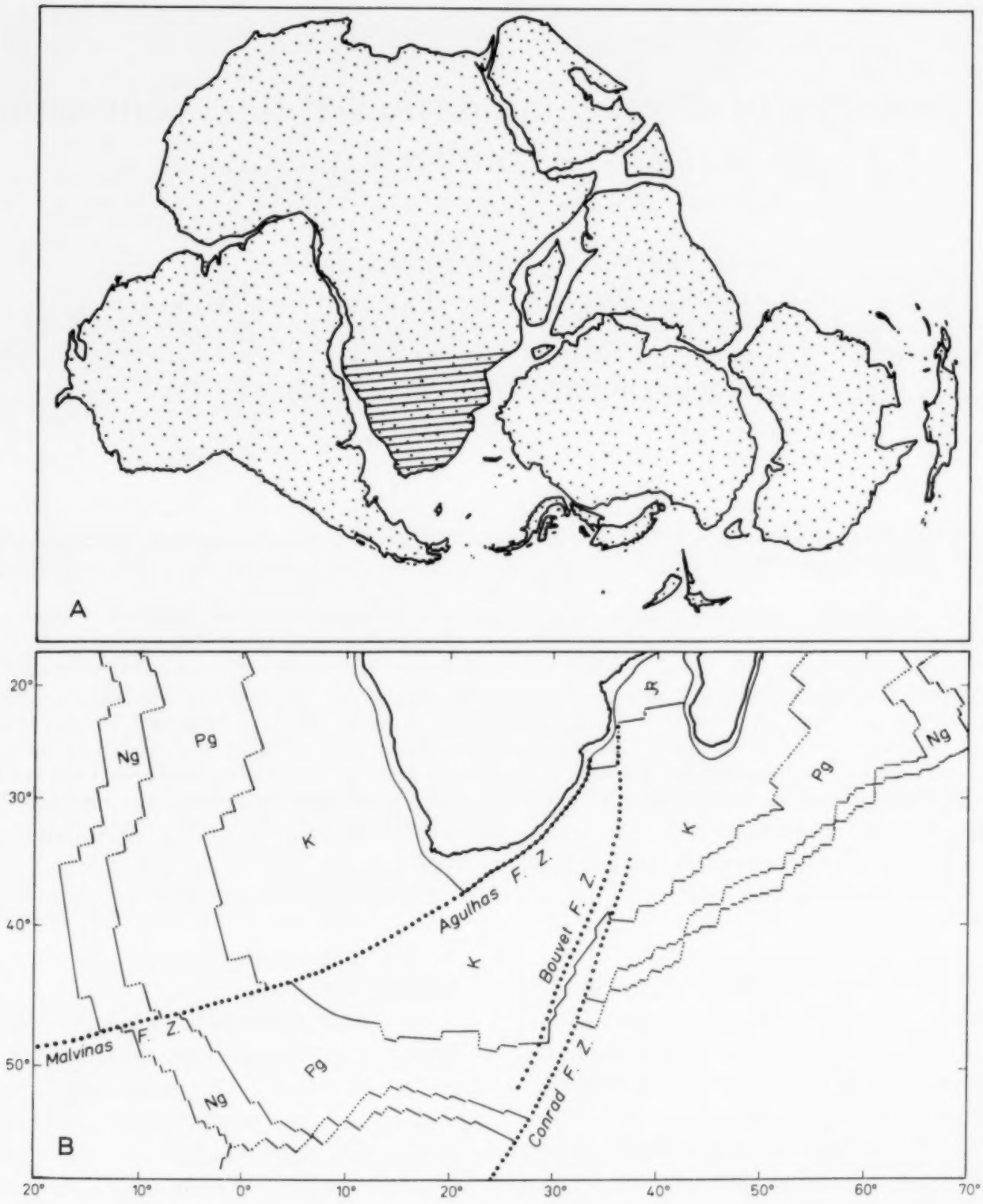

Fig. 1. Southern Africa's place in Gondwana and relationship to plate tectonics. (A) Reconstruction of Gondwana according to De Wit et al. (1988). Outlines of individual continents and microcontinents shown as at present but adjusted for their latitudes at about 150 m.y. B.P. Lined area is southern Africa as in panel B. (B) Region of southern Africa at present (from Larson et al., 1985), with ages of oceanic crust (between continuous lines for age boundaries), fracture zones (lines of small dots that connect age boundaries), and major fracture zones that separate divergent from translation continental margins (lines of large dots). Oceanward limit of these units is the median valley in the mid-ocean ridge, where the oceanic crustal age is zero. Greater ages of oceanic crust (to Early Cretaceous along the Atlantic margin and Jurassic along part of the Indian Ocean margin) indicate the age progression as oceanic crust was emplaced starting at the continental margins. In contrast, most of the land area of southern Africa and part of that of Madagascar consists of Proterozoic Precambrian intrusives and other igneous and metamorphic rocks that constitute shields bordered and partly covered by later volcanic and sedimentary rocks.

respect to Africa, and a lunate section of Gondwana southwest of Madagascar moved farther southwestward to form the Malvinas (Falkland) Plateau and Maurice Ewing Bank, which now are near the eastern tip of South America (Dingle et al., 1983, figs. 2, 65; Emery and Uchupi, 1984, fig. 366; Uchupi and Emery, 1991). As lateral crustal stretching is not involved in plate translation, listric faulting prior to emplacement of oceanic crust probably was unimportant along the Indian Ocean side of southern Africa. Somewhat similar effects on bathymetry may have been produced by later large slumps or mass movements on continental slopes; these have been mapped around most of southern Africa by Dingle (1977, 1980), Summerhayes et al. (1979), Dingle et al. (1983, figs. 157, 169, 172, 173, 179, 187), Dingle and Robson (1985), and Robson and Dingle (1986).

The question arises whether and why multiple and deeper shelves are present on the Atlantic margin and only relatively shallow ones on the Indian Ocean margin. The origins and geological histories of these margins may be investigated by bathymetry (sounding profiles, contours, and hypsometry), by deep structure (boreholes and both seismic refraction and reflection surveys), by shallow structure (medium-frequency seismic profiles), by distribution of outcrops of bedrock (dredging), and by the nature and distribution of surface sediments.

Bathymetry

Sounding lines

Sounding lines across the continental shelves and upper slopes at an average spacing of 17 km were made aboard the University of Cape Town's R/V *Thomas B. Davie*. Additional sounding profiles were derived from medium-frequency seismic profiles made from the same ship and from others. Many of the profiles reveal the presence of flattenings (shelf-like features) bordered on their seaward side by steeper slopes that suggest the presence of either wave-cut or marine depositional terraces that subsequently were submerged by rising sea level or falling land levels. Plots for the depths and distances from shore of shelf breaks, especially for double shelves off the Atlantic coast were reported by Dingle et al. (1971) and Bremner (1981). The depths of these shelf breaks were taken from sharp changes in slope shown on individual sounding profiles. While this method yields precise depths along a given profile, it may be too much influenced by local faults and mass movements to yield reliable regional information about present depths of shelves originally formed by widespread marine erosion or deposition.

Contour charts

Previous publications on bathymetry provided the information needed for our analysis of hypsometry of the region in this article. A large-scale bathymetric chart was compiled by Dingle et al. (1975) mainly on the basis of the many echo-sounding profiles made aboard R/V Thomas B. Davie. These soundings were supplemented by others from ships of the Marine Diamond Corporation and from files of the South African Directorate of Hydrography, and especially in deep water from published charts of the South African Navy and the British Admiralty. This manuscript chart served as the basis for a smaller-scale chart by Dingle et al. (1987) to illustrate general bathymetry and topographic forms of sedimentary origin. Slightly smaller-scale charts were published by Bremner et al. (1986) and Birch et al. (1986) as parts of a study of the texture and composition of ocean-floor sediments around southern Africa. In addition, many local investigations that included bathymetry from this 1975 compilation and from some earlier soundings have been published for short segments of the continental margin. These studies are listed from the Kunene River southeasterly around Cape Agulhas and thence northeasterly to Maputo. They are by Bremner (1981) on sediments of the Kunene and Walvis shelves (Fig. 2), Dingle (1973a) on the shallow geological structure of the Orange and Olifants shelves, Dingle et al. (1971) on the shallow geological structure of the Canyon shelf, Simpson and Forder (1968) on the submarine-canyon region of the Canyon shelf, Dingle (1973b) on the shallow geological structure of the Banks and South shelves, Dingle

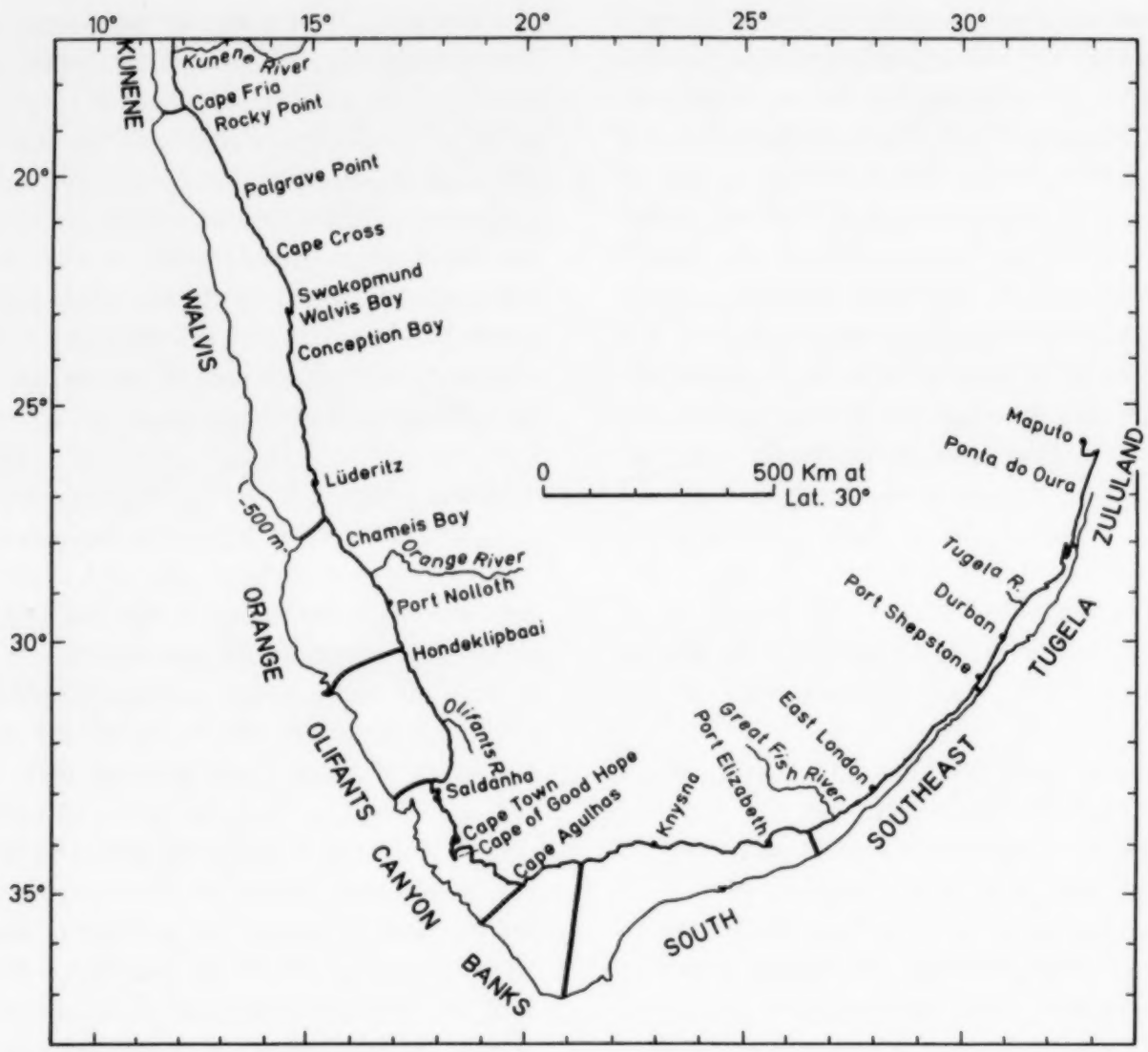

Fig. 2. Continental shelf and slope of Southern Africa between shore and 500 m depth contour. Prominent coastal towns, capes, and rivers are named. Ten segments of the shelf and slope are designated and named. Coastal features and their positions are from Birch et al. (1986) and Bremner et al. (1986).

and Robson (1985) on the shallow structure and slumps off the Southeast shelf, and Dingle et al. (1978) on the shallow geological structure and sedimentary features of the Tugela and Zululand shelves.

Hypsometry

Method

Another method of estimating the shelf-break depths is through hypsometry that measures the areas of topographic surfaces between contours; thus hypsometry is a means of averaging data and thus of avoiding the local effects of small irregularities. The simplest method for determining the areas between contours in each sector of the upper continental margin was to cut out with scissors (Emery, 1979) and to weigh the areas between the contours printed on an ozalid copy of the large-scale chart of Dingle et al. (1975). Wider sectors of the margins (Fig. 2) have more detail than narrower ones. Contours at ten meters intervals extend to depths of -200 m within most sectors; they reach -300 m in the Olifants sector, but only -120 m in the southeast sector, and -100 m in the Southeast, Tugela, and Zululand sectors. In the nearshore parts of most sectors the bottom is so steep that some contours are absent or nearly superimposed, thus their spacing could not be measured directly. Deeper parts of all sectors are shown at 100 m contour intervals. Thus each sector contains 5 to 24 measurements of weight, an average of 17. Conversion of weight to area was

based upon the ratio of the weight of 1° quadrangles of the Mercator-projection chart to the number of square km within the quadrangles at an average latitude for each sector (from tables in U.S. Coast and Geodetic Survey, 1930, p. 6, 7). The hypsometric (cumulative area versus depth) curves of Fig. 3 contain dots to indicate all actual measurements, and the associated histograms are for only the 10 m interval measurements. Compilations of the data into composites for the entire Atlantic (Kunene through Banks sectors) and Indian Ocean (South through Zululand sectors) margins (Fig. 4) were based upon the weight measurements plus interpolations from hypsometric curves of Fig. 3 as an approximation for minor areas of missing 10 m measurements (note that these approximations are for steep slopes, where the areas between contours are relatively small or where contours are missing). Added to the histograms and cumulative curves (Fig. 3) are inferred depths of shelf breaks (or seaward edge of flattenings) for each sector. Many of the measurements also are expressed in Table 1 to permit further manipulation by workers interested in correlations beyond those in this study.

The same graphs that express area versus depth of the sectors of upper continental margin can serve as a first approximation for the average slopes of the sectors (distance from shore versus depth). The total area of each sector divided by the coastal length of the sector yields the average width between shore and the 500 m depth contour. This width, in km, was plotted along the bottom margin of the panel containing the hypsometric curve for each sector and subdivided into a convenient scale, 50 or 25 km units for most sectors (Fig. 3), but 10 km units for the composite Atlantic and Indian Ocean margins (Fig. 4). To provide further information, a small plot of steepness was computed for each sector. High vertical exaggeration of the bottom profiles limited the space so that only angles of steepness 0.1°, 0.2°, 0.5°, and

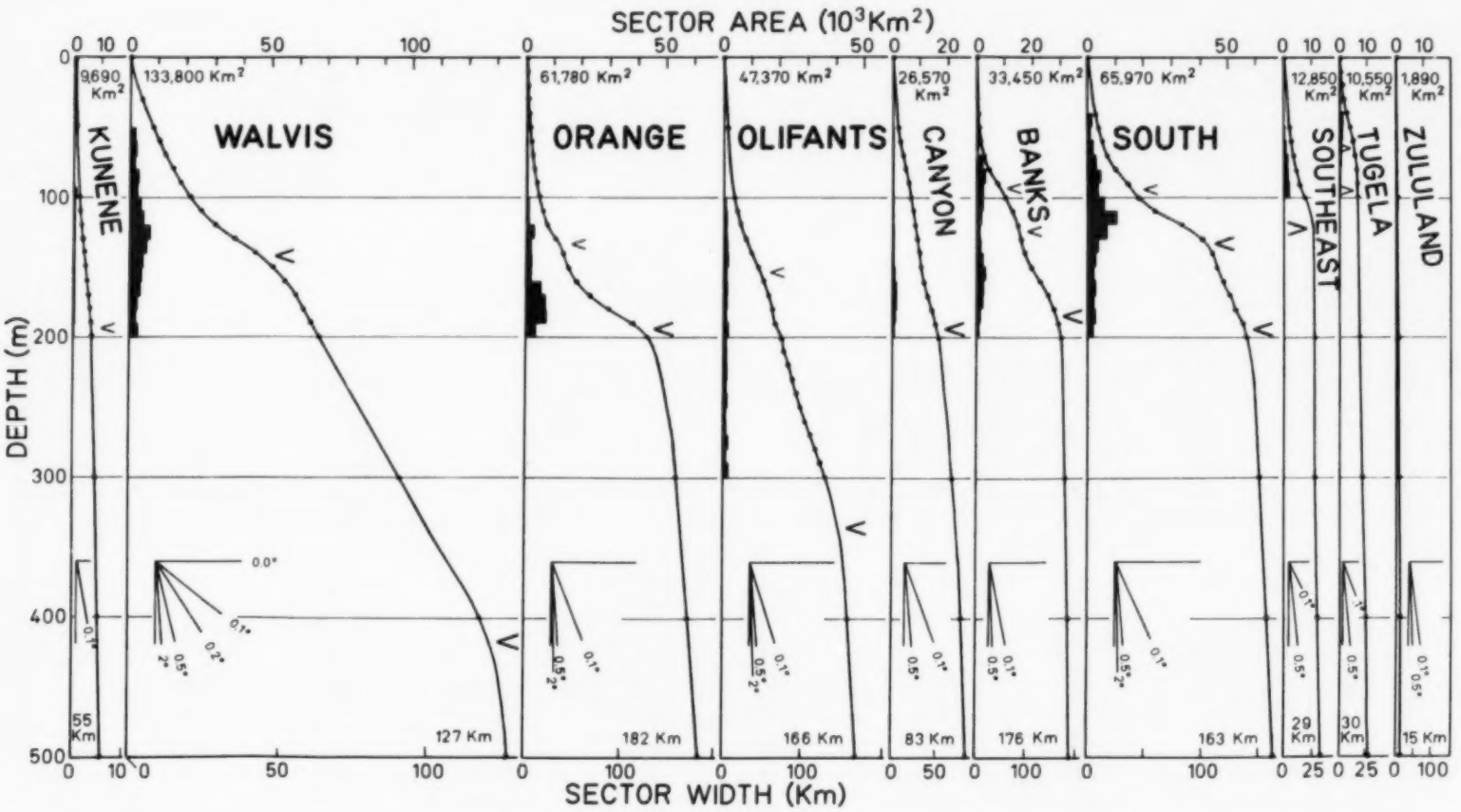

Fig. 3. Depth distributions of areas between the shore and the 500 m contour for each sector of the continental margin around southern Africa (Fig. 2). A uniform scale for area is given at the top of the graph along with the slightly rounded total area between shore and the 500 m contour; similarly, the scale for distance from shore is given at the bottom of the graph along with the total distance from shore to the 500 m contour. Cumulative curves and histograms are the basis for derivation of the depths for shelf breaks that are indicated by chevrons (larger chevrons for better-defined shelf breaks).

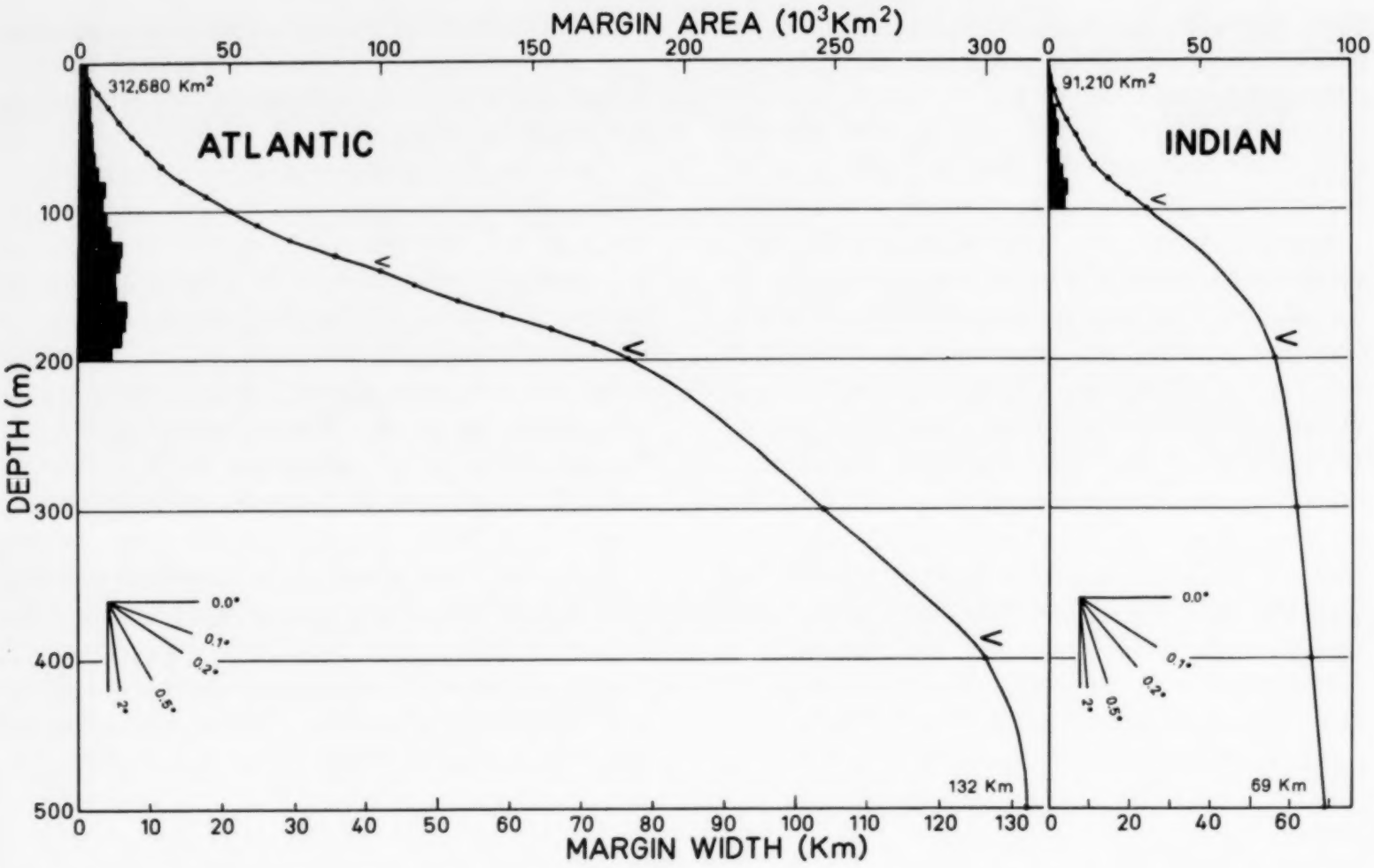

Fig. 4. Depth distribution of areas for Atlantic and Indian Ocean continental margins composited from data for the ten sectors of Fig. 3. Symbols as for Fig. 3.

TABLE 1

Some statistics of area measurements

Sector	Area (km²) per depth increment (m)					Length (km)	Width (km)
	0–100	0–200	0–300	0–400	0–500		
Kunene	2,270	6,505	8,190	9,023	9,693	176	55
Walvis	22,073	66,771	94,770	123,707	133,820	1,056	127
Orange	4,929	42,790	53,774	57,750	61,784	340	182
Olifants	3,988	20,568	36,043	44,048	47,368	286	166
Canyon	6,606	16,195	21,234	24,351	26,570	321	83
Banks	10,323	29,061	31,394	32,769	33,448	190	176
South	17,660	56,193	61,069	63,497	65,973	405	163
Southeast	7,685	10,510	11,144	11,915	12,849	445	29
Tugela	6,566	7,367	8,085	9,156	10,499	355	30
Zululand	485	677	907	1,547	1,890	125	15
Atlantic	50,189	181,890	245,405	291,648	312,683	2,369	132
Indian	32,396	74,747	81,205	86,115	91,211	1,330	69

2.0° could be indicated. Such low angles are typical of continental shelves and upper continental slopes of the world.

Results

Immediately obvious from Fig. 3 is a gradation of hypsometric profiles from gentle to steep for different coastal sectors: Walvis, South, Orange, Banks, Olifants, Canyon, Southeast, Tugela, Kunene, and Zululand, respectively. The gentlest profiles contain most of the evident flattenings (shelves and/or tops of slumps). The steepest profiles may contain flattenings, but such flattenings are too narrow to permit recognition. Depths of shelf breaks are expressed in the text as three-digit numbers in order to identify the most likely 10 m depth intervals that contain the seaward edge of the flattening, although the uncertainty in its identification may be as large as 20 m.

The shallowest general flattening or inflection point is at 95 m in the Banks, South, and Tugela sectors (mostly along the Indian Ocean margin). These are moderate to small sectors, and identification is a bit uncertain. The Tugela sector appears to contain another break at 65 m. The outer edge of the most frequent flattening lies at depths between 125 and 155 m. It occurs in six (Walvis, Orange, Olifants, Banks, South, and Southeast) of the ten coastal sectors, but these sectors include the largest (widest and longest) ones. A shelf break in many of the same sectors (Kunene, Orange, Canyon, Banks, and South) is at depths between 185 and 195 m. For the Orange, Canyon, and Banks sectors it is the most prominent flattening. Very deep flattenings are terminated at 335 and 415 m in the Olifants and Walvis sectors. The profiles for most other sectors are too steep in depth ranges below 200 m for flattenings to be recognized. Altogether, the seaward edge of the identified flattenings may be at 65, 95, 125–155, 185–195, 335, and 415 m. Most widespread and in sectors that include most of the length of the continental margins are the flattenings that are limited between depths of 125–155 and 185–195 m. Less well defined is the shelf break at 95 m and least certain are flattenings at 65, 315, and 415 m.

When viewed on composite profiles for the entire Atlantic and Indian Ocean margins (Fig. 4), only the flattenings at depths of 95 m (Indian), 135 m (Atlantic), 185-195 m (Atlantic and Indian), and an average at 385 m (Atlantic) remain.

Shallow Structure (medium-frequency seismic profiles)

At least 76 seismic-reflection profiles cross large parts of the Atlantic and the southern part of the Indian Ocean continental margins of southern Africa (Dingle; 1971, 1973a,b, 1980; Dingle and Robson, 1985, in press; Dingle et al., 1971; Du Plessis et al., 1972; Emery et al., 1975a,b). They reveal the presence of many buried acoustic reflecting horizons beneath the continental shelf and slope that denote changes in sediment acoustic properties, some related to hiatuses and others to distinct erosional unconformities. Some profiles also show seaward dipping faults and other discontinuities that denote large slump features (Dingle, 1977, 1980; Summerhayes et al., 1979; Dingle et al., 1983, figs. 157, 172, 173, 187; Dingle and Robson, 1985, in press). The scale of these presentations was designed for much broader features, and the steeply sloping bathymetry commonly present at depths of a few hundred meters is difficult to investigate accurately by seismic profiling. For proper investigation of the features one must use slow ship speeds and modern digital processing of acoustic-reflection data.

Deep Structure

Geological structure beneath continental margins is a potential source of information on the origin of topography of the continental margins. Both margins of southern Africa contain many basins separated by transverse ridges. At least some of the basin-ridge boundaries appear to be landward continuations of fracture zones (Dingle, 1981; Emery and Uchupi, 1984, p. 115, 777–783), although the reason for their continuations is not clear. A concentration of basins near the Atlantic coast may be due to local penetration of continental crust by oceanic fracture zones or presence of crustal weaknesses of the continental type described by Burke and Wells (1989) enhanced by

fracture-zone extensions. They also may be related to rejuvenated coast-parallel listric faults along divergent margins (Atlantic side) or by fault systems sub-parallel to translation margins (Indian Ocean side). The basins along the Atlantic coast appear to be more numerous, smaller, and somewhat shallower than those along the Indian Ocean coast, according to Dingle's (1981) study of borehole samples and their lateral extension through use of seismic data. These studies involve basins that border southern Africa (Figs. 1B and 2), but they include ones farther north along the Gulf of Guinea (another translation margin) and nearly to the Gulf of Aden. Outlines of many of these basins are shown by Dingle et al. (1983, figs. 65, 66, 68, 69, 70, 95, 104, 112, 114, 154).

Especially significant for determining origin of flattenings is the presence of similar sediments in most of the basins. These sediments began with thick continental (fluviatile and lacustrine) and volcanic sequences atop block-faulted basement. Their ages start with Upper Jurassic in the Atlantic basins and Permian to Early Jurassic in the Indian Ocean ones: the same general ages of the first new oceanic crust and the first sediments formed off these coasts (Fig. 1B). During the Aptian/Albian of Early Cretaceous a sequence of black shales, evaporites, and carbonates was laid down in basins of both coasts but perhaps more uniformly in the Atlantic basins, where they appear to be lateral extensions of deposits known from the floor of the open Atlantic Ocean (Emery and Uchupi, 1984, p. 795). Subsequently and until basins became filled, the sediments were marine sands, clays, and limestones that were interrupted by hiatuses mostly during the Maestrichtian, Oligocene, and Pliocene. These also were times of widespread hiatuses in sediments of the open Atlantic Ocean (Emery and Uchupi, 1984, p. 785) associated with low sea levels caused by rapid seafloor spreading (Late Cretaceous) and glacial climates (Oligocene and Pliocene).

According to Dingle (1981), Dingle and Hendey (1984), and Dingle et al. (1983, figs. 74, 75, 158), total thicknesses of coastal-basin sediments, and thus the depths of basin-floor sinking, are 11 to 13 km in the southern African Atlantic basins and 14 to 17 km in Indian Ocean ones (including the Zambezi Basin, just north of Maputo; Martin, 1984). Such basin depths are comparable with those of continental-margin basins off northern Africa, eastern South America, eastern North America, and western Europe, so they can be considered typical of the world. As these depths are greater than those of most oceanic crust, they must indicate local subsidence caused by early faulting, crustal sagging associated with continental rifting, and/or sediment loading. Deposition of Mesozoic and Cenozoic sediments in the basins and atop the ridges that separate the basins was followed by additional faulting and formation of many slump structures, as shown by seismic profiles (Dingle, 1980). These rocks crop out at many places on the continental shelf (Dingle et al., 1983, figs. 126, 157, 162, 169), and elsewhere they are covered by thin younger sediments. Interruptions of deposition through faults and large slumps must have been recorded by relict topographic surfaces retained on partly subsided ridges between the basins and on continental crustal slopes landward of the basins. However, the current knowledge of bathymetry and geological structure is too general and inadequate for one to place much confidence upon reliable correlations of depths of structural terraces with geological events within individual basins. Even hypsometry of the continental shelves and upper slopes can indicate only broad average shelf topography along the continental margins of southern Africa.

Coastal winds, ocean currents, swells, and longshore drift

Land and sea breezes are common within 20 km of the coast, and coastal surface winds have a strong tendency to blow parallel to the shore (Anonymous, 1942; Schulze, 1965). Off the west coast, the South East Trade Winds blow steadily between the mainland and a subtropical high-pressure cell in the South Atlantic chiefly from the southeast (Fig. 5A) with an average Beaufort Wind Force of 4 (about 28 km/h). Along the east coast, particularly south of the Mozambique Channel, winds exhibit much greater seasonal variation. In summer, they have variable strength and a wide range of vectors between north and southeast; in

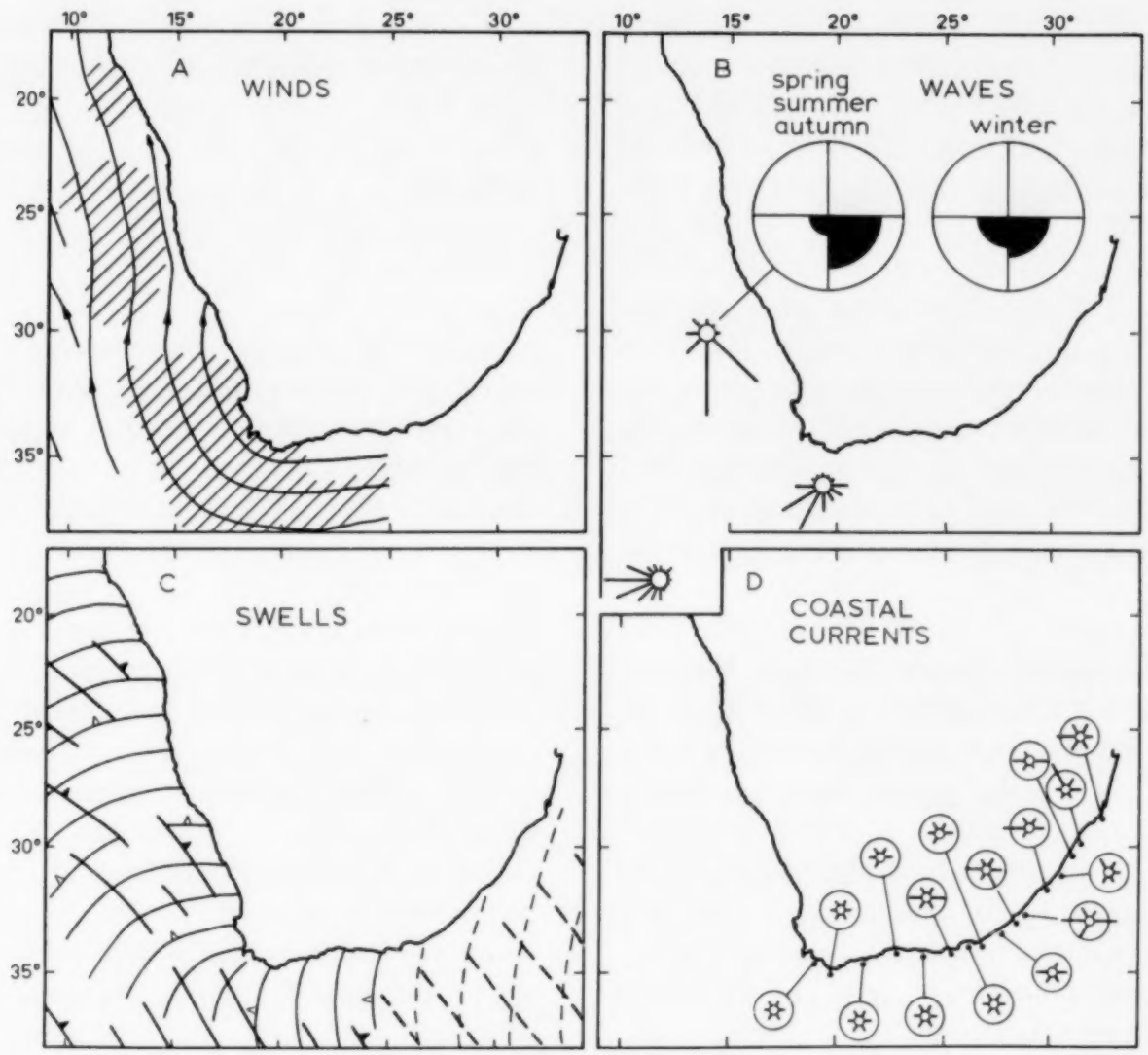

Fig. 5. Water and wind off southern Africa. (A) Wind-flow lines measured aboard R/V *Atlantis II* during February through June 1972. Lined areas had wind speeds exceeding 28 km/h. Redrawn from Emery et al. (1973, fig. 2). (B) Rose diagrams showing direction from which waves arrive at three offshore locations; redrawn from De Decker (1988, fig. 5A). The two plots on land denote the seasonal variation of wave direction at the northernmost location; large circles represent 100%; redrawn from data of De Decker (1988, table 2). (C) Direction of swells measured aboard R/V *Atlantis II* during February through June 1972. Crest lines that move westerly and northwesterly were produced by the winds of panel A. Wider lines denoting crests that move northeasterly are swells from the much stronger winds farther south, near Antarctica. Redrawn from Emery et al. (1973, fig. 3) with inferred pattern in Indian Ocean added by dash lines. (D) Rose diagrams showing direction toward which coastal currents flow along Indian Ocean side of southern Africa. Speed is indicated by length of bars relative to circles where small circle is 0 and large one is 0.5 m/s. From tables by Harris (1978).

winter, however, the wind directions continue to be variable but the passage of cyclones induce much greater wind strengths. Gales (Beaufort Wind Force >7, or >70 km/h) increase in frequency poleward off both the west and east coasts (McDonald, 1938; Anonymous, 1942), although their frequency is always greater off the east than the west coast. This simple picture is complicated at Lüderitz on the west coast, however, where exceptionally strong southerly gales are commonplace during the summer (Rogers, 1977; Corbett, 1989).

Ocean currents off the west and east coasts (Fig. 5B) are markedly different in that the northward flowing Benguela Current, with a mean velocity of only 24 cm/s (Harris and Shannon, 1979) and a maximum of 50 cm/s (Stander, 1964) contrasts strongly with the southward flowing Agulhas Current that has a velocity usually of 110 to 140 cm/s (Tripp, 1975; Pearce et al., 1978; Schumann, 1986) and peak velocity at times exceeding 250 cm/s. The Benguela Current is noted for coastal upwelling of nutrient-rich water, and the seafloor sediments provide ample evidence of the

productivity of the west coast shelf environment (Bremner, 1983a). The Agulhas Current is known not only for its strength but also for its association with freak waves that reach 20 m in height and always are preceded by a deep trough (Tripp, 1975; Mallory, 1977).

Swell is one of the few oceanic parameters that has similar attributes off both the west and east coasts (Fig. 5C). It is generated in the Southern Ocean and comes predominantly from the southwest and south (Anonymous, 1942), reaching far beyond the winds that produce it. Off the west coast, therefore, the swell runs in tandem with the coastal winds, but sometimes off the east coast the direction of swell propagation is countered by northeasterly gales. Likewise, the southerly swell tends to reinforce the sluggish Benguela Current, but it opposes the powerful Agulhas Current, thereby spawning short wave-length freak waves.

A direct result of the ground swell emanating from the southerly quadrant is that littoral drift along both coasts generally is equatorward. The west coast is indented by anti-clockwise logarithmic spiral bays, such as Table Bay, and by spectacular northward pointing sand spits like the one of Walvis Bay known as Pelican Point (Emery et al., 1973; Bremner, 1985). Along the south coast, between Cape Agulhas and Algoa Bay, numerous clockwise logarithmic spiral beaches provide dramatic evidence of the eastbound littoral drift (Bremner, 1983b), and submerged spit bars extend eastward from some of the headlands, e.g., Cape Infanta and Cape Seal (De Decker, 1983; Flemming and Martin, 1985; Martin and Flemming, 1986).

A few semi-quantitative estimates of littoral drift, mostly linked to coastal engineering studies, are as follows: (1) West Coast: just north of the Orange River mouth, where diamond mining along the shore is pursued, about 1.4×10^6 m^3 of sediment moves northward annually (Swart, 1984); (2) South Coast: near Mossel Bay an estimated $> 0.5 \times 10^6$ m^3 moves eastward annually (Nicholson and Serdyn, 1985); (3) at Algoa Bay, 0.4×10^6 m^3 per annum is calculated to bypass the Alexandria Dunefield reservoir toward the east (Bremner and Day, 1987); (4) East Coast: at Durban 0.65×10^6 m^3 of sediment moves northward each year, the volume increasing to 0.8×10^6 m^3 at Richards Bay, 150 km northeast of Durban (Swart, 1983, 1987).

Sediments

Distribution

Sediments contain considerable information about the present and past wave and current environments of the continental margin off southern Africa (Siesser et al., 1974; Rogers and Bremner, 1991). Where sediments are deposited slowly or are absent, former shelves can remain unburied, but where sediments are deposited rapidly these former shelves can become deeply buried and concealed. Information about rates of sediment deposition can be inferred from knowledge about kinds and sources of sediments. Maps of the surface sediments based upon 2536 well distributed samples in an area of 380 700 km^2 (Birch et al., 1986; Bremner et al., 1986) are the basic source of information about kinds and sources. These maps show distribution patterns of grain size, general composition, and percentages of gravel, sand, silt, clay, total mud, fecal pellets, terrigenic detritus, glauconite, phosphorite, calcium carbonate, opal, organic matter, foraminifers, shells, and diatoms. For simplicity and brevity this information was selectively presented in a single chart (Fig. 6) showing sediment components reduced to three groups: (1) authigenic, (2) terrigenic and (3) biogenic.

(1) The authigenic mineral glauconite is sand size and occurs in variable concentrations within terrigenic sand, muddy sand, gravelly sand, and elsewhere in calcareous foraminiferal sands and mollusk-shell sands. Locally, glauconite exceeds 50% of total sediment in about 7% of the area, as shown on Fig. 6. Phosphorite in sand to gravel sizes occurs almost exclusively on the northwesterly two thirds of the Atlantic continental margin in association with molluskan-foraminiferal and terrigenic sands (Bremner and Rogers, 1990) and with gravel in diatomaceous ooze (Bremner, 1980a). It exceeds 20% concentation in only two patches totalling about 2% of the area of sediments outlined in Fig. 2. Both glauconite and phosphorite

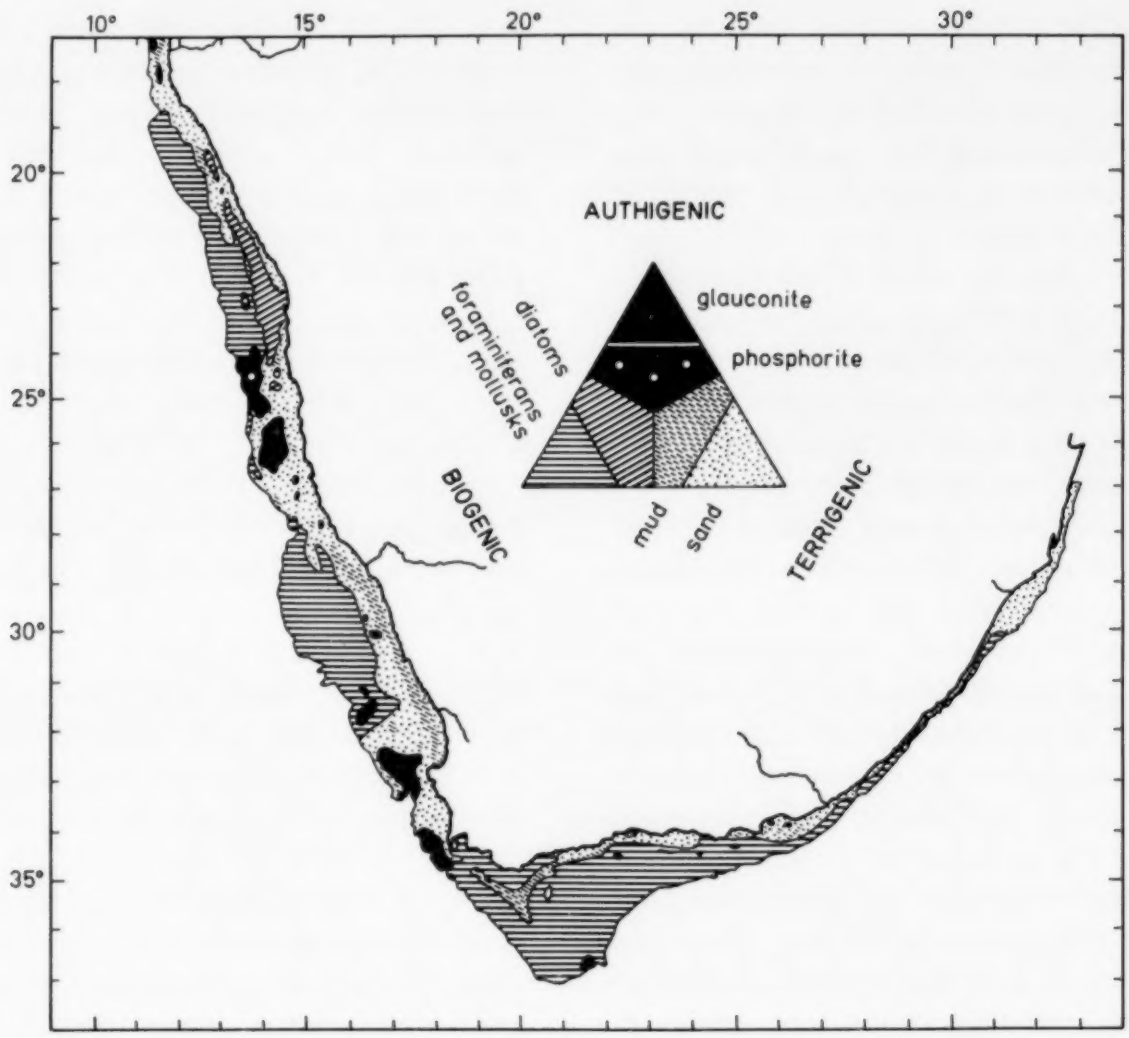

Fig. 6. Nature of surface sediments between the shore and the 500 m contour. Derived from detailed charts by Birch et al. (1986) and Bremner et al. (1986).

are deposited as authigenic and/or diagenetic minerals in shallow to moderate depth areas of slow detrital and biogenic deposition. The sandy and gravelly phosphorites are believed to have formed authigenically during Miocene and Holocene times, respectively, whereas rock phosphorites (replaced calcareous strata) are diagenetic and diagnostic of Miocene–Pliocene age (Baturin, 1970, 1982; Baturin and Bezrukhov, 1979; Birch, 1979, 1980a; Emery and Uchupi, 1984, p. 744–753; Birch et al., 1986; Bremner et al., 1986; Bremner and Rogers, 1990). The latter were formed by replacement of Cretaceous/Tertiary limestone outcrops now exposed on the ocean floor.

(2) The same geological processes that eroded Cretaceous, Tertiary, and Quaternary strata and redeposited some of the originally authigenic glauconite and phosphorite also released detrital gravels, sands, silts, and clays. Probably most of the finer grained detrital sediment came from erosion by streams on land, and even the coarser sands and gravels that were eroded and deposited by marine processes probably came from very shallow water in a nearshore belt. Thus these detrital sediments are grouped as terrigenic in Fig. 6. They constitute about 31% of the total sediment area on the map. Gravels dominate nowhere in the surface of the continental margin except in a very nearshore belt that generally was not reached by shipboard sampling, and locally it occurs in depths of about 80 m around the Alphard Banks (just south of Cape Agulhas). Small percentages of gravel occur in surface sands at water depths mostly between ca. 140 and 200 m and between 50 and 200 km from the present shore; these gravels may be relict from Pleistocene or earlier times of lower than present sea level or of locally higher land levels. A blanket of sand extends seaward from shore to distances as far as 160 km and to depths as great as 500 m, covering sediments

of other kinds. As elsewhere in the world, the terrigenic sand grades into silt and then clay (grouped as mud) on the shelf break and upper slope. Off southern Africa this deeper water mud dominates only at water depths below about 500 m. There is, nevertheless, a discontinuous nearshore belt of terrigenous mud (Fig. 6) in surface sediments at 80 to 140 m depth around much of the coast but especially off the mouths of rivers, the presumed sources. In the Walvis sector of the margin (Fig. 2) the overlying anaerobic waters allow preservation of large concentrations of muddy organic matter and opal from settled diatom frustules (Bremner, 1980b). The implication is that the deeper belt of terrigenic sand and mud is relict from times of low relative sea levels of Pleistocene glacial epochs or earlier. The shallower belt of sand and its fringing belts of mud are deposits that continue to be formed. Support for belief in greater age of sediments in deeper water is provided by the presence of several species of fossil cold-water Pleistocene? molluskan shells and other remains in offshore sediments. They have been identified by John Pether of the South African Museum in Cape Town (J. Pether, pers. commun., 1989) from drill samples obtained by De Beers Marine Corporation during shipboard exploration for diamonds, but they have not yet been radiocarbon dated. Shells of similar cold-water mollusks deep on the continental shelf off the Atlantic coast of North America were dated at 15 000 to 11 000 yrs. B.P. (near the end of glacial times of low sea level); these species now live only in colder waters farther poleward (Emery et al., 1988).

(3) The last sediment group is biogenic, a group that covers about 60% of the continental margin area of Fig. 6. The diatomaceous oozes in the shallow belt of the Walvis sector were discussed above. Far more widespread are calcareous sediments: the skeletal debris of foraminifers, molluskan shells, and a few other animals. The foraminiferal sediment dominates on the Atlantic margin (Bremner, 1983a) and the molluskan sediment on the Indian Ocean margin. On both margins the bulk by far of the biogenic sediment lies seaward of terrigenic sediments. Both foraminiferal and molluskan biogenic sediments grade seaward from coarse to fine through both comminution and sorting. They may represent a contemporary facies of the terrigenic sediments, a later blanketing deposit, or even both types, so far as can be inferred from surface distribution patterns. Bremner et al. (1986) considered the shell debris to be largely relict and the foraminiferal sediment to be Recent, but well distributed drill-hole information would be helpful for establishing relative ages of both biogenic and terrigenic sediments.

Discussion

The general pattern is of modern sediment on the upper slope, palimpsest (modern and relict) sediment on the outer and middle shelves, and belts of modern sediment on the inner shelf (Emery, 1968; Swift et al., 1971). Our approach here is to sketch the extent to which Holocene sediments have modified the continental margin morphology, and an attempt will be made to relate this knowledge to features of the hypsometric curves in Figs. 3 and 4. We proceed anticlockwise from the Kunene to the Zululand sectors, grouping them as follows: (1) West Coast: Kunene to Canyon; (2) South coast: Banks and South; and (3) east coast: Southeast to Zululand (Fig. 2).

(1) Starting in the northwest, the Kunene sector is narrow, steep, subject to massive slumping, and (aside from the shelf break that shoals northward from about −250 to −150 m; Bremner, 1981), muddy sediment on the inner shelf has obscured identification of terraces. The Walvis sector has a double shelf break over most of its length (Van Andel and Calvert, 1971; Bremner, 1981): the inner one at a depth of −150 to −200 m and the outer one between −300 and −450 m. Both breaks are broad ill-defined features, yet both are revealed by hypsometry (Fig. 3). The inner shelf in this sector is subject to the highest biogenic sedimentation rate anywhere on the southern African continental margin (estimates of between 3 and 10 mm/yr; Bremner, 1980b; DeMaster, 1981). As a result, the bedrock morphology on the inner shelf is buried beneath as much as 15 m of modern diatomaceous ooze. In the Orange sector is an unusual phenomenon: a large portion of the outer shelf, known as the Orange Banks, is shallower than the middle shelf because of an extensive bank floored by

middle Miocene rocks. The outer edge of this bank, at about 200 m depth is the shelf break (Fig. 3). Also shown by the hypsometry is a weakly defined inner shelf break between −120 and −160 m that is due to a drowned sandy Pleistocene delta of the Orange River. Terrigenous mud from the Orange River (Bremner et al., 1990) is carried southward beyond Cape Town (in the Canyon sector) by a 30 to 40 m thick subsurface current (Shannon et al., 1990; Shillington et al., 1990), from which the mud settles onto the inner/middle-shelf terrace. Landward of this mud belt, in both the Orange and Olifants sectors, alluvial diamonds are being exploited actively along the shore and inner shelf from atop several terraces that are too narrow to be identified on the scale of this hypsometric study. A wide terrace in the Olifants sector, with an inner shelf break at 160 m depth resulted from upbuilding of Quaternary sediments, according to Dingle (1973a). The northern half of the Canyon sector is distinctive in that both the inner and outer shelves exhibit rugged morphology related to the Cape Canyon, which diverts modern and older sediment southwestward down the slope to the continental rise. A portion of the Orange River mud mentioned above does bypass the head of the canyon and builds a narrow wedge on the middle shelf. The southern half of the Canyon sector has a similar rocky inner shelf but both its middle and outer shelves are masked by a wide seaward thinning wedge of relict sediment that varies from terrigenic to authigenic in composition. A well-defined shelf break shallows southward from about −300 m in the northern half to −200 m in the southern half of the sector.

(2) Along the south coast, in the Banks and South Sectors, a simple distribution pattern of modern terrigenic sediment on the inner shelf and exposed Tertiary bedrock on the middle and outer shelves exists (Birch, 1980b). Both sectors possess two inner shelf breaks, at −95 m and ca. 130 m. In the Banks Sector these shelf breaks are caused by Paleocene intrusives along what is known as the Alphard Rise (that includes Alphard Banks), whereas in the South Sector the breaks reflect changes in gradient of the middle and outer shelves (Fig. 3). The outer shelf break in both sectors lies at about −195 m.

(3) At the east coast, the Southeast Sector is narrow and shallow with the shelf break varying in depth between −100 and −140 m, thus agreeing well with the hypsometric break at −120 m (Fig. 3). The outer shelf is swept by massive Agulhas Current driven sand dunes as high as 17 m (Flemming, 1978, 1980, 1981; Flemming and Hay, 1988), but their transient nature allows them to have little effect on the hypsometry of the continental shelf. All of this calcareous/terrigenic sediment is eventually diverted down the slope along numerous submarine canyons that breach the shelf break (Birch, 1982; Dingle and Robson, 1985). The Tugela Sector has a wider shelf than either the Southeast Sector or the Zululand Sector because of sediment influx from the Tugela River since the Miocene (Dingle et al., 1978). The hypsometry reveals two breaks at −65 m and −95 m, the latter possibly reflecting sediment accumulation from the Tugela River during the Quaternary. The Zululand Sector is the narrowest (2 km) and shallowest (−70 m) of any sector on the southern African margin, and the well-defined shelf break is not disclosed by hypsometry. However, the shelf is unique in that it supports extensive coralgal reefs (Ramsay and Mason, 1990).

Conclusions

Two origins for the flattenings are worthy of consideration: marine erosion and slumps. Most widespread and consistent should be those for marine erosion, whereas smaller and more erratic and variable in depth should be flattenings produced by slumps and local faults. A clean separation of the two causes cannot result from hypsometry alone, but the frequency of occurrence and general consistency of depth suggests that marine erosion may be responsible for flattenings terminated at depths of about 65, 95, 125–155, and 185–190 m; slumps may be the more likely cause for terminations deeper than 300 m shown on the curves of Figs. 3 and 4.

Comparison of the flattenings inferred from hypsometry can be made with the visual impression of the contours shown on the bathymetric charts that accompany the sediment studies of Birch et al. (1986) and Bremner et al. (1986). Hypsometry

and contours correspond well for the 65 m flattening at Tugela and the 95 m flattenings at the Banks, South, and Tugela sectors. For the flattening at 125–155 m the hypsometry and contours correspond at the Banks, South, Southeast, and Walvis and less well at the Orange and Olifants sectors. The 185–195 m flattenings correspond with visual interpretation of the contours at the Kunene, Orange, Banks, and South sectors, but less well at the Canyon sector. The 335 and 415 m flattenings are not evident in the contours. Thus only the flattenings at depths of 65, 95, 125–155, and 185–195 m may represent submerged continental shelf levels produced by marine processes. The poor absence of the 185–195 m level in the Walvis sector may indicate its burial under later thick mainly biogenic sediments supplemented by coastal sediments released by wave erosion and brought by the Orange River; sediments from both sources have been carried northward by wave-induced coastal currents during the past and present. In addition, there is some possibility that deposition of sediments in submerged former deltas may have been significant for the 65 m flattening at Tugela and for some of the variations in the 125–155 m depths elsewhere, as well as at the mouth of the present Orange River (De Decker, 1988). Locally, however, the scattered presence of gravel in detrital surface sands between ca. 140 and 200 m water depth may indicate the relict origin of the gravel and much of the sand from a former time of deposition in a nearshore environment.

Further useful comparisons can be made between hypsometry and the breaks in slope observed along individual sounding lines and reflection profiles across the continental shelf and upper slope. Beginning at the northwest, the Kunene sector is reported by Bremner (1981) to contain nine sounding lines that show shelf breaks at depths of 140 to 215 m (averaging 136 m). These shelf breaks may be related to the 195 m flattening shown in Fig. 3 for Kunene or to the 125–155 m flattening elsewhere that was not recognized by hypsometry in the Kunene sector. In the adjoining Walvis sector this shelf break was shown by Bremner (1981, fig. 2, table 1) to deepen from 265 to 445 m (averaging 350 m for 28 sounding lines). The depth range suggests that these measurements may belong to the 125–155, the 185–195, and the possible 415 m flattenings of Fig. 3, and that they may represent, at least in part, large slump structures (Summerhayes et al., 1979). Supporting the concept of warping is a shallower shelf break at 130 to 180 m depth (averaging 150 m for 33 sounding lines), according to Bremner (1981, fig. 2, table 1). Farther south, in the Canyon sector, Dingle et al. (1971) noted a shelf break at depths between 200 and 380 m (averaging 300 m for 12 sounding lines). Again, this shelf break may correspond with the 195 m flattening noted by hypsometry for the Canyon sector and/or a southward extension of the 335 m flattening in the hypsometry of the adjacent Olifants sector. If the measurements by Dingle et al. (1971) are for a single warped terrace, the southerly upwarping may be a distant continuation of that reported by Bremner (1981) in the southern part of the Walvis sector. According to Dingle (1970) and Dingle et al. (1971), the upwarping of the terrace continues into the next sectors to the east (Banks and South sectors) where the shelf break is only 110–160 m deep.

The advantage in using the depth of seaward increase in slope obtained from sounding lines is that warping of a given terrace level can be traced if sounding lines are closely spaced. Thus much may be gained by detailed study of sounding lines and especially of seismic-reflection profiles in all coastal sectors of southern Africa. This approach could clarify the question of whether there are several erosional (or marine depositional) terraces or whether there are only one or two terraces that are warped and subject to misidentification as multiple terraces within different sectors. Such study also could clarify identification of terraces formed by widespread marine processes versus those that represent the tops of local slump masses.

Presently available information shows that the divergent Atlantic continental margin off southern Africa is both wider and gentler in slope than the adjacent translational Indian Ocean margin. During the Cretaceous and Paleogene the divergent margin received a larger supply of sediment from rivers, and during the Neogene biogenic sediments became dominant as Benguela upwelling developed (Rogers and Bremner, 1991). In contrast, during

the Neogene the Agulhas Current increased in strength and eroded older strata on the translational margin (Dingle et al., 1978). Recognition of deeper flattenings on the divergent than on the translational margin may be the result of less stable, thicker sediments there or to enhanced ability of its gentler slopes to retain evidence of displaced former shelf breaks (through being backed by wider flattenings than permitted along the steeper translational margin). The original down to the ocean listric faulting could not have been a major factor in promoting subsidence of the flattenings into deeper water unless the faulting continued long after that margin was formed by plate divergence. In summary, we must submit that presently available knowledge is unable to provide definite answers to questions regarding the precise depth distribution of flattenings along opposite coasts of southern Africa to allow us to determine the relative roles of the original plate movements and of slumps. Acquisition of additional continuous seismic-reflection profiles, coupled with vibrocoring of formational 'featheredges' may in the future allow the relative roles of plate movements, slumping, erosion, and deposition to be better assessed.

Acknowledgements

This article forms Contribution No. 7805 of the Woods Hole Oceanographic Institution. Bremner thanks Dr. Nok Frick, Director of the South African Geological Survey, for granting permission for involvement with this study.

References

Anonymous, 1942. Climatic Charts of the Adjoining Oceans. Supplement to Volume II of Weather on the Coasts of Southern Africa. Meteorol. Serv. R. Navy S. Afr. Air Force, 16 pp., 33 charts.

Austin, J.A., Jr. and Uchupi, E., 1982. Continental–oceanic crustal transition off Southwest Africa. Bull. Am. Assoc. Pet. Geol., 66: 1328–1347.

Baturin, G.N., 1970. Recent authigenic phosphorite formation on the South West African shelf. In: F.M. Delany (Editor), The Geology of the East African Continental Margin. Inst. Geol. Sci. London, Rep. 70(13): 87–97.

Baturin, G.N., 1982. Phosphorites on the Sea Floor: Origin, Composition and Distribution. (Dev. Sedimentol., 33.) Elsevier, Amsterdam, 343 pp.

Baturin, G.N. and Bezrukov, P.L., 1979. Phosphorites on the sea floor and their origin. Mar. Geol., 31: 317–332.

Birch, G.F., 1979. The nature and origin of mixed apatite/glauconite pellets from the continental shelf off South Africa. Mar. Geol., 29: 313–334.

Birch, G.F., 1980a. A model of penecontemporaneous phosphatization by diagenetic and authigenic mechanisms from the western margin of southern Africa. In: Y.K. Bentor (Editor), Marine Phosphorites: Geochemistry, Occurrence, Genesis. Soc. Econ. Paleontol. Mineral., Spec. Publ., 29: 79–100.

Birch, G.F., 1980b. Nearshore Quaternary sedimentation off the south coast of South Africa (Cape Town to Port Elizabeth). Bull. Geol. Surv. S. Afr., 67: 1–20.

Birch, G. F., 1982. Sedimentological and geophysical investigations of a major sediment exit point on the south-east African continental margin (vicinity of Port St. Johns). Trans. Geol. Soc. S. Afr., 85: 91–103.

Birch, G.F., Rogers, J. and Bremner, J.M., 1986. Surficial sediments of the continental margin of South Africa, Transkei and Ciskei, scale 1:3 646 000 at Lat. 30°. Geol. Sur. S. Afr., Pretoria. Mar. Geosci. Ser. 3: 4 sheets.

Bremner, J.M., 1980a. Concretionary phosphorite from South West Africa. J. Geol. Soc. London, 137: 773–786.

Bremner, J.M., 1980b. Physical parameters of the diatomaceous mud belt off South West Africa. Mar. Geol., 34: 67–76.

Bremner, J.M., 1981. Shelf morphology and surficial sediment off central and northern South West Africa (Namibia). Geo-Mar. Lett., 1: 91–96.

Bremner, J.M., 1983a. Biogenic sediments on the South West African (Namibian) continental margin. In: J. Thiede and E. Suess (Editors), Coastal Upwelling: Its Sedimentary Record. Part B, Sedimentary Records of Ancient Upwelling. Plenum, New York, pp. 73–103.

Bremner, J.M., 1983b. Properties of logarithmic spiral beaches with particular reference to Algoa Bay. In: A. McLachian and T. Erasmus (Editors), Sandy Beaches as Ecosystems. W. Junk, The Hague, 97–113.

Bremner, J.M., 1985. Southwest Africa/Namibia. In: E.C.F. Bird and M.L. Schwartz (Editors), The World's Coastline. Van Nostrand Reinhold, New York, pp. 645–653.

Bremner, J.M. and Day, R.W., 1987. Acoustic stratigraphy and Late Cenozoic sediments in Algoa Bay. Joint Geol. Surv./Univ. Cape Town Mar. Geoscience Unit, Tech. Rep. 17: 74–89

Bremner, J.M. and Rogers, J., 1990. Phosphorite deposits on the Namibian continental shelf. In: W.C. Burnett and S.R. Riggs (Editors), Phosphate Deposits of the World. Univ. Press, Cambridge, 3: 143–152.

Bremner, J.M., Rogers, J. and Birch, G.F., 1986. Surficial sediments of the continental margin of South West Africa (Namibia), scale 1:3 646 000 at Lat. 30°. Geol. Surv. S. W. Afr., Windhoek, Mar. Geosci. Ser., 16 maps on 4 sheets.

Bremner, J.M., Rogers, J. and Willis, J.P., 1990. Sedimentological aspects of the 1988 Orange River floods. Trans. R. Soc. S. Afr., 47: 247–294.

Burke, K. and Wells, G.L., 1989. Trans-African drainage system of the Sahara: Was it the Nile? Geol., 17: 743–747.

Corbett, I.B., 1989. The Sedimentology of Diamondiferous Deflation Deposits within the Sperrgebiet, Namibia. Thesis Geol. Dept., Univ. Cape Town, 430 pp. (Unpubl.).

De Decker, R.H., 1983. The sediments of Plettenberg Bay and the submerged Robberg spit. Joint Geol. Surv./Univ. Cape Town, Mar. Geol. Program, Tech. Rep. 14: 255–265.

De Decker, R.H., 1988. The wave regime on the inner shelf south of the Orange River and its implications for sediment transport. S. Afr. J. Geol., 91: 358–371.

DeMaster, D.J., 1981. The supply and accumulation of silica in the marine environment. Geochim. Cosmochim. Acta, 45: 1715–1732.

De Wit, M., Jeffery, M., Bergh, H. and Nicolaysen, L., 1988. Geological map of sectors of Gondwana reconstructed to their disposition ca. 150 Ma., scale 1 : 10 000 000. Am. Assoc. Pet. Geol. and Univ. Witwatersrand, 2 sheets.

Dingle, R.V., 1970. Preliminary geological map of part of the eastern Agulhas Bank, South African continental margin. Proc. Geol. Soc. London, 1663: 137–142.

Dingle, R.V., 1971. Tertiary sedimenary history of the continental shelf off southern Cape Province, South Africa. Trans. Geol. Soc. S. Afr., 74: 173–186.

Dingle, R.V., 1973a. The geology of the continental shelf between Luderitz and Cape Town (Southwest Africa), with special reference to Tertiary strata. J. Geol. Soc. London, 129: 337–363.

Dingle, R.V., 1973b. Post-Palaeozoic stratigraphy of the eastern Agulhas Bank, South African continental margin. Mar. Geol., 15: 1–23.

Dingle, R.V., 1977. The anatomy of a large submarine slump on a sheared continental margin (South East Africa). J. Geol. Soc. London, 134: 293–310.

Dingle, R.V., 1980. Large allochthonous sediment masses and their role in the construction of the continental slope and rise off southwestern Africa. Mar. Geol., 37: 333–354.

Dingle, R.V., 1981. Continental margin subsidence: A comparison between the east and west coasts of Africa. In: R.A. Scrutton (Editor), Dynamics of Passive Margins. (Geodyn. Ser.), Am. Geophys. Union, 6: 59–71.

Dingle, R.V. and Hendey, Q.B., 1984. Late Mesozoic and Tertiary sediment supply to the eastern Cape Basin (SE Atlantic) and palaeo-drainage systems in southwestern Africa. Mar. Geol., 56: 13–26.

Dingle, R.V. and Robson, S., 1985. Slumps, canyons and related features on the continental margin off East London, SE Africa (SW Indian Ocean). Mar. Geol., 67: 37–54.

Dingle, R.V. and Robson, S., in press. Development of the continental rise off south western Africa. In: C.W. Poag (Editor), The Evolution of the Atlantic Continental Rise. Wiley, New York.

Dingle, R.V., Gerrard, I., Gentle, R.I. and Simpson, E.S.W., 1971. The continental shelf between Cape Town and Cape Agulhas. In: F. M. Delany (Editor), The Geology of the East Atlantic Continental Margin. ICSU/SCOR Working Party 31 Symposium, Cambridge 1971, Inst. Geol. Sci., London, Rep. 70(16): 199–209.

Dingle, R.V., Moir, G.J., Bremner, J.M. and Rogers, J., 1975. Bathymetry of the continental shelf off South Africa and South West Africa, scale 1 : 125000 at Lat. 30°. Geol. Surv. S. Afr., Mar. Geosci. Ser. 1, 2 sheets.

Dingle, R.V., Goodlad, S.W. and Martin, A.K., 1978. Bathymetry and stratigraphy of the northern Natal Valley (SW Indian Ocean): A preliminary account. Mar. Geol., 28: 89–106.

Dingle, R.V., Siesser, W.G. and Newton, A.R., 1983. Mesozoic and Tertiary Geology of Southern Africa. Balkema, Rotterdam, 375 pp.

Dingle, R.V., Birch, G.F., Bremner, J.M., De Decker, R.H., Du Plessis, A., Engelbrecht, J.C., Fincham, M.J., Fitton, T., Flemming, B.W., Gentle, R.I., Goodlad, S.W., Martin, A.K., Mills, E.G., Moir, G.J., Parker, R.J., Robson, S.H., Rogers, J., Salmon, D.A., Siesser, W.G., Simpson, E.S.W., Summerhayes, C.P., Westall, F., Winter, A. and Woodborne, M.W., 1987. Bathymetry around southern Africa (SE Atlantic and SW Indian Oceans), scale 1 : 3 475 000 at Lat. 30°. Ann. S. Afr. Museum, Cape Town, 98: 1–271, 1 sheet.

Du Plessis, A., Scrutton, R.A., Barnaby, A.M. and Simpson, E.S.W., 1972. Shallow structure of the continental margin of southwestern Africa. Mar. Geol., 13: 77–89.

Emery, K.O., 1968. Relict sediments on continental shelves of the world. Bull. Am. Assoc. Pet. Geol., 52: 445–464.

Emery, K.O., 1979. Hypsometry of the continental shelf off eastern North America. Estuarine, Coastal Mar. Sci., 9: 653–658.

Emery, K.O. and Uchupi, E., 1984. The Geology of the Atlantic Ocean. Springer, New York, 1050 pp.

Emery, K.O., Milliman, J.D. and Uchupi, E., 1973. Physical properties and suspended matter of surface waters in the southeastern Atlantic Ocean. J. Sediment. Petrol., 43: 822–837.

Emery, K.O., Uchupi, E., Bowin, C.O., Phillips, J. and Simpson, E.S.W., 1975a. Continental margin off western Africa: Cape St. Francis (South Africa) to Walvis Ridge (S.-W. Africa). Bull. Am. Assoc. Pet. Geol., 59: 3–59.

Emery, K.O., Uchupi, E., Phillips, J., Bowin, C. and Mascle, J., 1975b. Continental margin off western Africa: Angola to Sierrra Leone. Bull. Am. Assoc. Pet. Geol., 59: 2209–2265.

Emery, K.O., Merrill, A.S. and Druffel, E.R.M., 1988. Changed Late Quaternary marine environments on Atlantic continental shelf and upper slope. Quat. Res., 30: 251–269.

Flemming, B.W., 1978. Underwater sand dunes along the southern African continental margin: observations and implications. Mar. Geol., 26: 177–198.

Flemming, B.W., 1980. Sand transport and bedform patterns on the continental shelf between Durban and Port Elizabeth (southeast African continental margin). Sed. Geol., 26: 179–205.

Flemming, B.W., 1981. Factors controlling shelf sediment dispersal along the southeast African continental margin. Mar. Geol., 42: 259–277.

Flemming, B.W. and Hay, R., 1988. Sediment distribution and dynamics on the Natal continental shelf. In: E.H. Schumann (Editor), Coastal Ocean Studies off Natal, South Africa. Lect. Notes Coastal Estuarine Stud., Springer, Berlin, 26: 47–80.

Flemming, B.W. and Martin, A.K., 1985. Nearshore submerged spit bars: A facies model. Terra Cognita, 5: 60.

Gerrard, I., and Smith, G.C., 1982. Post-Paleozoic succession and structures of the southwestern African continental margin. In: J.S. Watkins and C.L. Drake (Editors), Studies in Continental Margin Geology. Mem. Am. Assoc. Pet. Geol., 34: 49–74.

Harris, T.F.W., 1978. Review of coastal currents in southern African waters. S. Afr. Natl. Sci. Program., Rep., 30: 1–103.

Harris, T.F.W. and Shannon, L.V., 1979. Satellite-tracked drifter in the Benguela Current System. S. Afr. J. Sci., 52: 316–317.

Larson, R.L., Pitman, W.C. III, Golovchenko, X., Cande, S.C., Dewey, J.F., Haxby, W.F. and LaBrecque, J.L., 1985. The Bedrock Geology of the World, scale 1 : 20 180 000 at Lat 30°. Freeman, New York, 1 sheet.

Mallory, J.K., 1977. Abnormal waves on the south-east coast of South Africa. Inst. Oceanog., Univ. Cape Town, Occ. Rep., 77(1): 1–18.

Martin, A.K., 1984. Plate tectonic status and sedimentary basin in-fill of the Natal Valley (SW Indian Ocean). Joint Geol. Surv./Univ. Cape Town Mar. Geol. Program, Bull. 14: 1–209.

Martin, A.K. and Flemming, B. W., 1986. The Holocene shelf sediment wedge off the south and east coast of South Africa. In: R.J. Knight and J.R. McLean (Editors), Shelf Sands and Sandstones. Mem. Can. Soc. Pet. Geol., II: 24–44.

McDonald, W.F., 1938, Atlas of Climatic Charts of the Oceans. U.S. Department of Agriculture, Weather Bureau, 1247, 130 charts.

Nicholson, J. and Serdyn, J.D., 1985. The determination of an operating policy for the Hartbeeskuil Dam. Natl. Res. Inst. Oceanology (Counc. Sci. Ind. Res.), Stellenbosch, Rep. C/SEA/8538: 1–22.

Pearce, A.F., Schumann, E.H. and Lundie, G.S.H., 1978. Features of the shelf circulation off the Natal coast. S. Afr. J. Sci., 74: 328–331.

Ramsay, P.J. and Mason, T.R., 1990. Development of a type zoning model for Zululand coral reefs, Sodwana Bay, S. Afr. J. Coastal Res., 6: 829–852.

Robson, S. and Dingle, R., 1986. A GLORIA traverse over the marginal fracture zone and continental margin of SE Africa. Mar. Pet. Geol., 3: 31–36.

Rogers, J., 1977. Sedimentation on the continental margin off the Orange River and the Namib Desert. Thesis Geol. Dept., Univ. Cape Town, 212 pp. (Unpubl.)

Rogers, J. and Bremner, J. M., 1991. The Benguela ecosystem. Part VII. Marine-geological aspects. Ann. Rev. Oceanogr. Mar. Biol., 29: 1–85.

Schulze, B.R., 1965. Climate of South Africa. Part 8. General Survey. Weather Bur., Dept. Transport, S. Afr., WB 28: 1–330.

Schumann, E.H., 1986. Bottom boundary layer inshore of the Agulhas Current off Natal in August, 1975. S. Afr. J. Mar. Sci., 4: 93–102.

Shannon, L.V., Lütjeharms, J.R.E. and Nelson, G., 1990. Causative mechanisms for intra-annual and interannual variability in the marine environment around Southern Africa. S. Afr. J. Sci., 86: 356–373.

Shillington, F.A., Brundrit, G.B., Lutjeharms, J.R.E. Boyd, A.J., Agenbag, J.J. and Shannon, L.V., 1990. The coastal current circulation during the Orange River flood 1988. Trans. R. Soc. S. Afr., 47 (3): 307–330.

Siesser, W.G., Scrutton, R.A. and Simpson, E.S.W., 1974. Atlantic and Indian Ocean margins of southern Africa. In: C.A. Burke and C. L. Drake (Editors), The Geology of Continental Margins. Springer, New York, 641–654.

Simpson, E.S.W. and Forder, E., 1968. The Cape Submarine Canyon, Part I. Bathymetry. Fish. Bull. S. Afr., 5: 35–38.

Stander, G.HJ., 1964. The Benguela Current off South West Africa. Mar. Res. Lab. S. W. Afr., Invest. Rep., 12: 1–122.

Summerhayes, C.P., Bornhold, B.D. and Embley, R.W., 1979. Surficial slides and slumps on the continental slope and rise of South West Africa: A reconnaissance study. Mar. Geol., 31: 265–277.

Swart, D.H., 1983. Physical aspects of sandy beaches: a review. In: A. McLaachlan and T. Erasmus (Editors), Sandy Beaches as Ecosystems. W. Junk, The Hague, 5–44.

Swart, D.H., 1984. Inshore sediment movement along the west coast of South Africa. In: C.G.C. Martin (Editor), Proc. Symp. Surveying Off-shore Mining Concessions S. African Waters. Univ. Cape Town, Survey Dept. Publ., 8 pp.

Swart, D.H., 1987. Erosion of manmade dune in the Beachwood mangrove nature reserve. Counc. Sci. Ind. Res., Stellenbosch, Rep. T/Sen/8713, 28 pp.

Swift, D.J.P., Stanley, D.J. and Curray, J.R., 1971. Relict sediments on continental shelves: A reconsideration. J. Geol., 79: 322–346.

Tripp, R.T., 1975, South African Sailing Directions. General Information. Dir. Hydrogr., S. Afr. Navy, Kenwyn, 1: 1–223.

Uchupi, E. and Emery, K.O., 1991. Genetic global geomorphology. In: R.H. Osborne (Editor), From Shoreline to Abyss: Contributions in Marine Geology Honoring Francis Parker Shepard. Soc. Explor. Paleontol. Mineral., Spec. Publ., 46: 273–290.

U.S. Coast and Geodetic Survey, 1930. Tables for a Polyconic Projection of Maps and Lengths of Terrestrial Arcs of Meridian and Parallels, 5th ed. U.S. Gov. Print. Off., Washington, D. C., 189 pp.

Van Andel, T.H. and Calvert, S.E., 1971. Evolution of sediment wedge, Walvis Shelf, Southwest Africa. J. Geol., 79: 385–602.

Marine Geology, 106 (1992) 107–129
Elsevier Science Publishers B.V., Amsterdam

Middle to late Quaternary sediment flux and post-depositional processes between the continental slope off Gabon and the Mid-Guinean margin

Denis Bonifay and Pierre Giresse

Laboratoire de Recherches de Sédimentologie Marine, Université de Perpignan, 52, Avenue de Villeneuve, 66860 Perpignan, France

(Received January 24, 1991; revision accepted October 30, 1991)

ABSTRACT

Bonifay, D. and Giresse, P., 1992. Middle to late Quaternary sediment flux and post-depositional processes between the continental slope off Gabon and the Mid-Guinean margin. *Mar. Geol.*, 106: 107–129.

Two cores from the continental slope off Gabon (2330 m of water) and one core from the Mid-Guinean margin (4000 m of water) were studied in order to examine climatic and paleoceanographic fluctuations during the middle and late Quaternary. Oxygen isotope variations in one shallow core were correlated with global isotope stages, and extended to the two other cores on the basis of microfaunal and mineralogic contents. Interglacial stages have been characterized by high carbonate content, low carbonate dissolution effect and moderate flux of organic matter derived from primary oceanic production. Glacial stages have included dissolution processes on carbonate tests, related to increased CO_2 content near the seabed due to the sink of organic matter from both planktonic and benthic fauna; at a depth of 4000 m of water, this phenomenon has controlled the vertical carbonate distribution through time. Many interglacial intervals record high terrigenous inputs (increased quartz and kaolinite content), while some glacial intervals contain peaks of both well-crystallized smectites (probably reworked from Mesozoic–Cenozoic outcroppings on the adjacent continental shelf) and poorly crystallized smectites (land derived). At a depth of 4000 m of water, quartz-rich layers deposited during some glacial intervals include surface textures indicative of an aeolian origin. A long-term climatic change is recognized, consisting of a progressive cooling of sea-surface waters and of climatic conditions since 400,000–350,000 yrs B.P.

Introduction

During the *Walda* cruise of the R.V. *Charcot* three cores were collected, two on the Gabon continental slope (2330 m of water) and one close to the volcanogenic Annobon Island (3994 m of water) which rises from the southwest end of the Mid-Guinean ridge (Fig. 1). Mineralogy, lithology and micropaleontology were studied and placed in a chronostratigraphic framework based on oxygen isotope variations in one core, in order to investigate middle to late Quaternary oceanic and terrigenous fluxes in the northern part of the Angola Basin. The location and depths of the analyzed cores allow us to compare the sediment accumulation rates as well as the carbonate dissolution processes prevailing across the continental slope, far from the main fluvial discharges of the Niger and Congo rivers.

The climatic history of the area can be related to fluctuations in the main oceanographic parameters during the Quaternary and to variations in sediment supply from adjacent land areas. The factors controlling these fluctuations are compared with those recently proposed from studies of the Congo–Zaïre deep-sea fan (Giresse et al., 1982; Jansen et al., 1984; Van der Gast and Jansen, 1984; Zachariasse et al., 1984; Bongo-Passi, 1984) and the Niger delta (Pastouret et al., 1978). We also attempt to correlate the major climatic trends

Correspondence to: P. Giresse, Université de Perpignan, Laboratoire de Recherches de Sédimentologie Marine, Avenue de Villeneuve, 66860 Perpignan, France.

0025-3227/92/$05.00

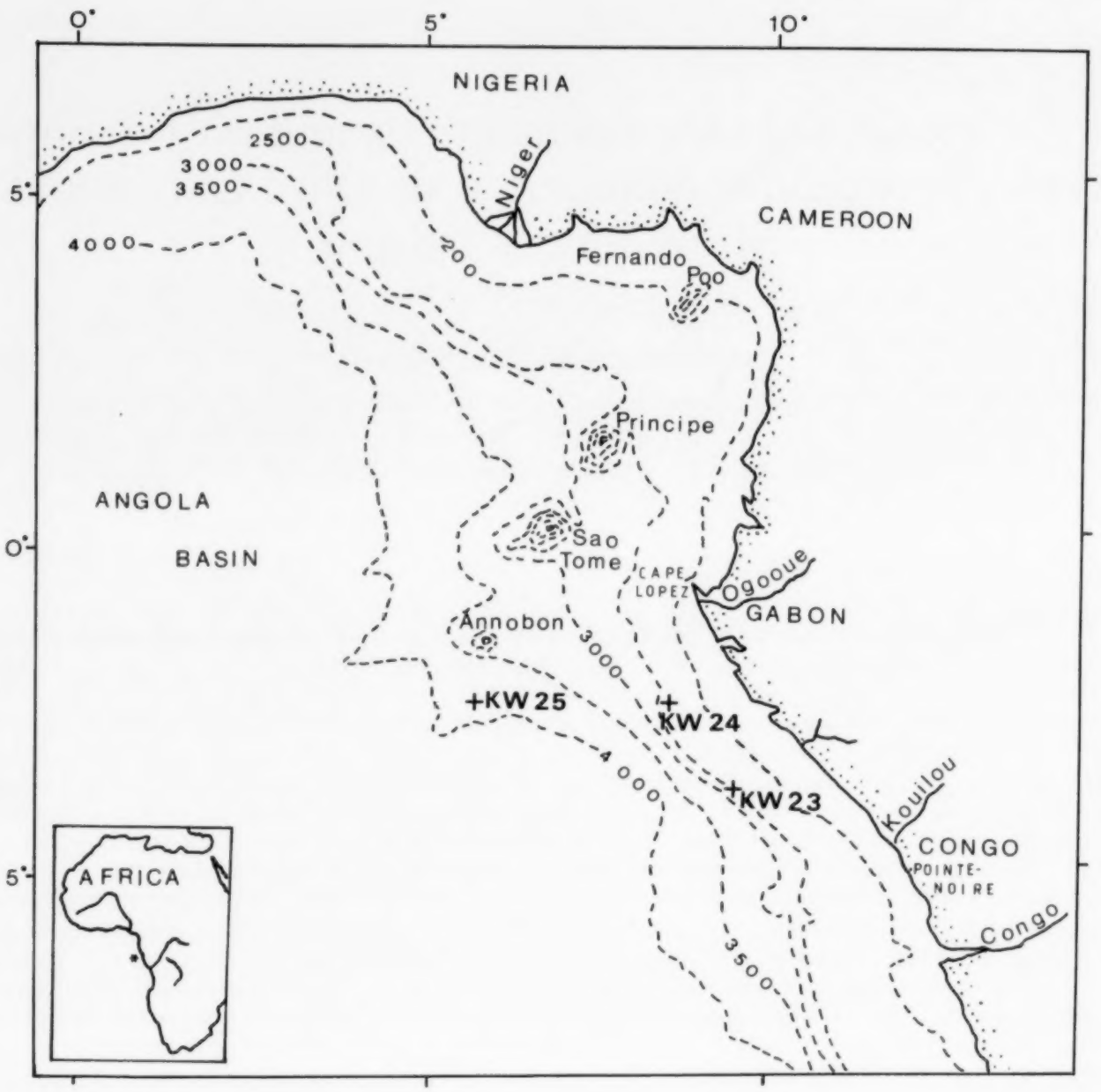

Fig. 1. Location of the core sites in the Angola Basin.

recognized in our study with periodic climatic fluctuations observed off northwest Africa (Sarnthein et al., 1981, 1982; Ruddiman et al., 1989), in the south of the Angola basin (Bornhold, 1973; Diester-Haass, 1985), and farther north along the west African margin (Giresse and Barusseau, 1989).

Physical oceanography

Surface waters

The modern circulation in the Angola basin is relatively well known (Van Bennekom and Berger, 1984; Jansen et al., 1984; Piton and Kartavtseff, 1986). From north to south, five water masses can be described (Fig. 2):

(1) The Guinean Current flows eastward, carrying warm and low salinity waters into the Gulf of Guinea; it represents the tail end of the North Equatorial Countercurrent.

(2) The South Equatorial Current carries warm waters westward and, at the latitude of the Congo–Zaïre estuary, splits into two parts, one of which become the Angola Current.

(3) The South Equatorial Countercurrent flows eastward, although its temporal and spatial persistence is not well-defined.

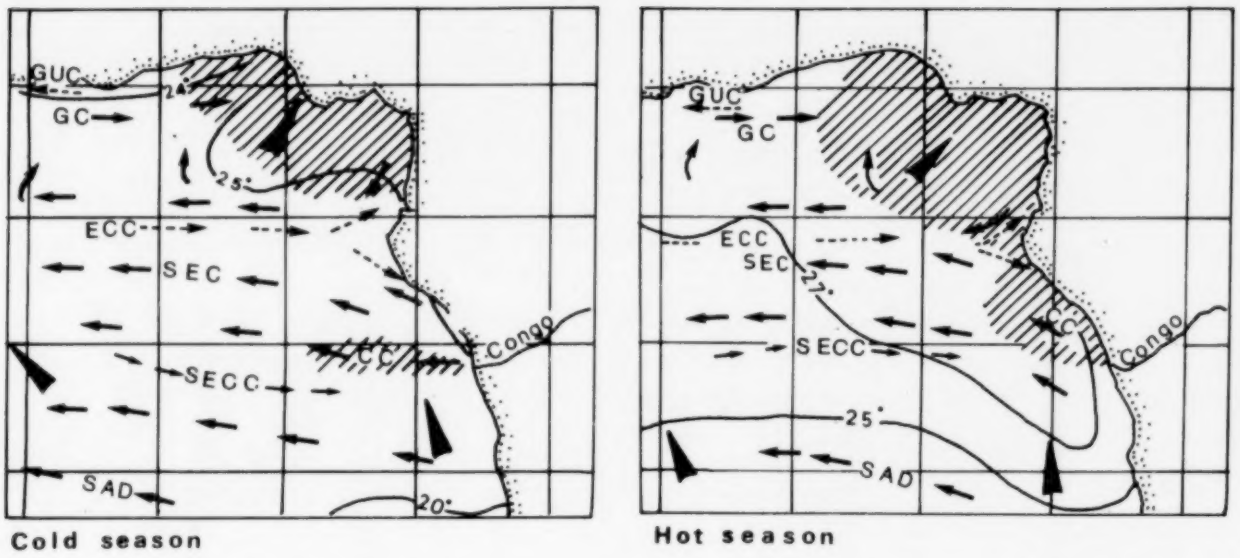

Fig. 2. Major currents in the Gulf of Guinea (from Piton and Kartavtseff, 1986). Surface currents: *SEC* = Equatorial current, *SECC* = south equatorial countercurrent, *GC* = Guinean current, *SAD* = south Atlantic drift and *CC* = Congo current. Subsurface currents: *ECC* = Equatorial countercurrent and *GUC* = Guinean undercurrent. Arrows: direction of dominant winds, isotherm curves; hatchings: salinity > 34%.

(4) The South Atlantic Drift carries relatively cool waters from the southeast, and is considered the continuation of the Benguela Current.

(5) The Congo–Zaïre river discharge flows west-northwest and then west.

Sub-surface waters

Two sub-surface currents are recognized (Fig. 2):

(1) The Guinea Undercurrent flows east to west along the north coast of Guinea.

(2) The Equatorial Countercurrent (*Lomonosov Current*) carries saline waters originating from the Brasilian margin; it diverges close to the African coast, one fraction continuing toward the Gulf of Biafra, the other extending to the south of Pointe-Noire (Congo).

During the austral winter and also in December–January, a coastal upwelling between the south of Congo and Cape Lopez affects and modifies the regional oceanographic pattern by pushing the Congo–Zaïre waters seaward.

During the austral summer, waters originating from fluvial discharge extend northward and join the low salinity waters of the Gulf of Guinea (Berrit, 1962).

Deep-waters circulation

The access of the Antarctic Bottom Water (AABW) to the Angola basin is limited by the Walvis Ridge (Metcalf et al., 1964). However, Connary and Ewing (1974) recorded flow through a channel across the West Walvis Ridge, which reaches 30° latitude (Van Bennekom and Berger, 1984; Fig. 3). The AABW in the Angola basin can be traced in thickness up to 200 m above the seafloor. In the equatorial area of the basin, an increase in bottom water temperatures reflects the diluting effect of the North Atlantic Deep Water (NADW) originating from the Labrador Sea.

Fluvial discharge to the Angola basin

On a regional scale, freshwater from the Congo–Zaïre dominates the runoff of the Angola basin: an annual supply of 40,900 $m^3\ s^{-1}$ represents close to 60% of the basin total. At the scale of our study, the Ogooue River is considered important as it supplies $138 \times 10^7\ m^3\ yr^{-1}$ (an order of magnitude less than the Congo–Zaïre River); other rivers, such as Kouilou and Nyanga, can be neglected. Negative rain anomalies and extended upwelling systems which induce low terrestrial temperature are found to be synchronous (Mahé et al., 1988).

The Congo–Zaïre River supplies 31 to 45 million tons of suspended matter annually, of which 13% is sand-sized and 15% is organic matter (Kinga-Mouzeo, 1986; Moguedet, 1988; Olivry et al., 1988). The significance of chemical weathering is

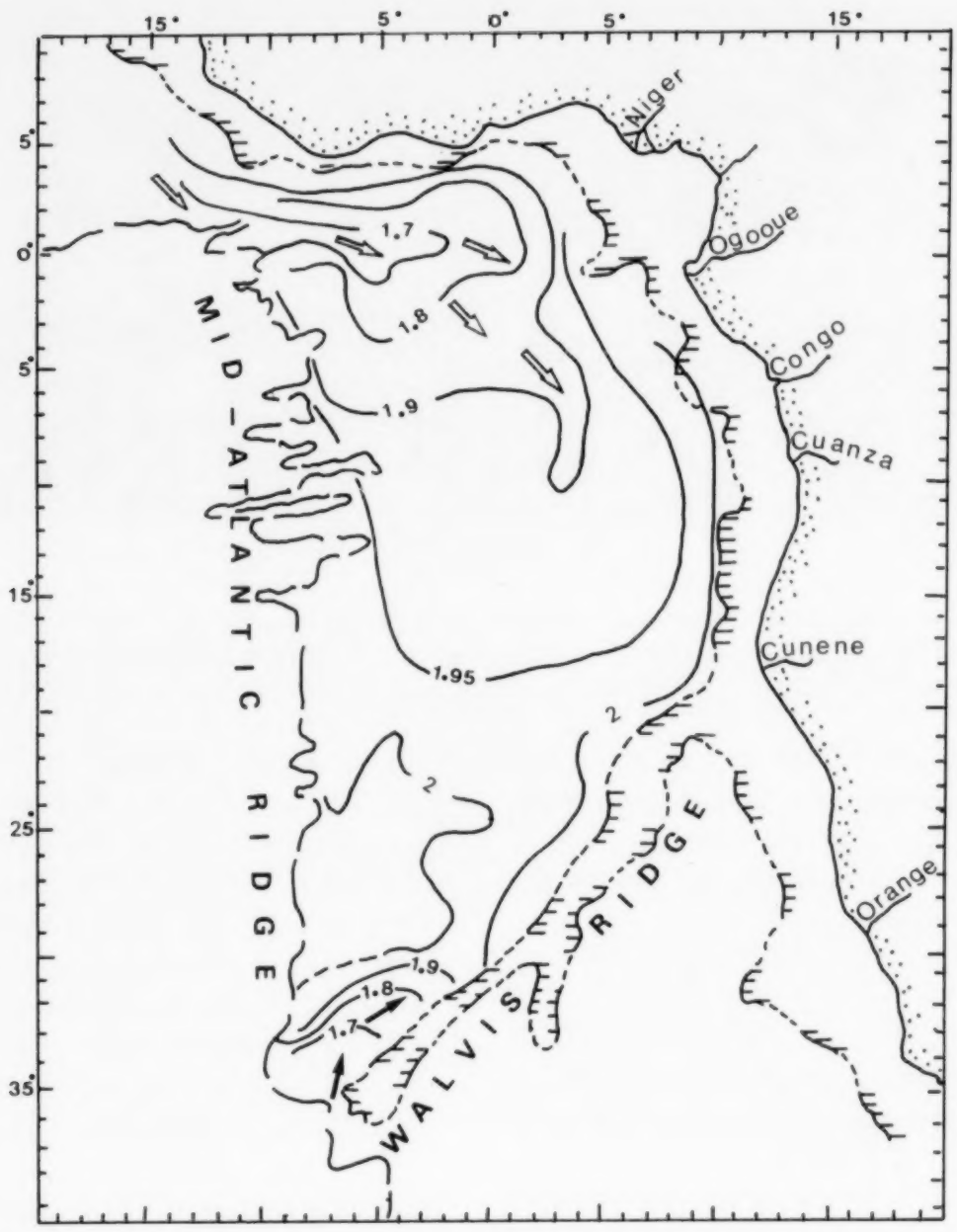

Fig. 3. Distribution of bottom water temperatures (from Van Bennekom and Berger, 1984); open arrows: NADW (North Atlantic Deep Water) circulation; closed arrows: AABW (Antarctic Bottom Water) circulation.

highlighted by a low proportion of suspended matter to total discharge (30%), which results from the extensive cover of the land by the Equatorial forest (50%).

Material and methods

The three cores were collected with a Kullenberg-type coring system. Gamma-densitometry curves and X-radiographs were acquired at the *Centre Océanologique de Bretagne* prior to splitting the cores. A detailed visual description of sedimentary structures and facies led to the sampling of the cores at 10 cm intervals (between major sedimentary structures); 541 samples were taken for analysis.

A classical set of measurements was performed; water content, $CaCO_3$, carbon and nitrogen contents, and fine-grain size-analyses on selected levels. X-ray diffractometry (CGR Theta Generator, anticathode of Cobalt) was performed on both clay-size material and on non-oriented silt-size particles.

Observation of the sand-size fractions (>40 μm) by binocular microscope allowed both quantitative and qualitative analysis of the different major components: fecal pellets, foraminifera, diatoms, sponge spicules, quartz grains and pyritic concre-

tions. Each component was counted in the whole sand-size fraction and reported as g^{-1} dry weight. Selected quartz grains were observed with a Hitachi S 520 scanning electron microscope.

About 15–20 specimens of the benthic foraminifer *Melonis barleeanum* were picked from each sample of core KW 23 for oxygen-isotopic determinations at the *Centre des Faibles Radioactivités* (L. Labeyrie, Gif-Sur-Yvette), reported to PDB standard.

Sedimentation rates expressed in cm yrs 10^{-3} and flux rates expressed in g cm^{-2} 10^{-3} yrs were calculated by the general formula:

$$S(d_2-d_1)=\frac{1}{t_2-t_1}\sum_{i=d_2}^{d_1} P_i(1-C_i)(d_2-d_1)$$

where:

$$P_i=\frac{(1-\omega_i)\rho_w\rho_s}{\omega_i\rho_s+(1-\omega_i)\rho_w}$$

t_2-t_1 = the time interval, t_1 = age at depth d_1, d = depth below core top, C_i = concentration of carbonate at depth d, ρ_w = water density and ρ_s = dry sediment density.

Bio- and chronostratigraphy

Core KW 23 is located 425 km from the Congo–Zaïre estuary (Fig. 1) at a depth of 2330 m of water. The $\delta^{18}O$ curve for the core (Fig. 4) is correlated with isotopic stages 1–9, following the

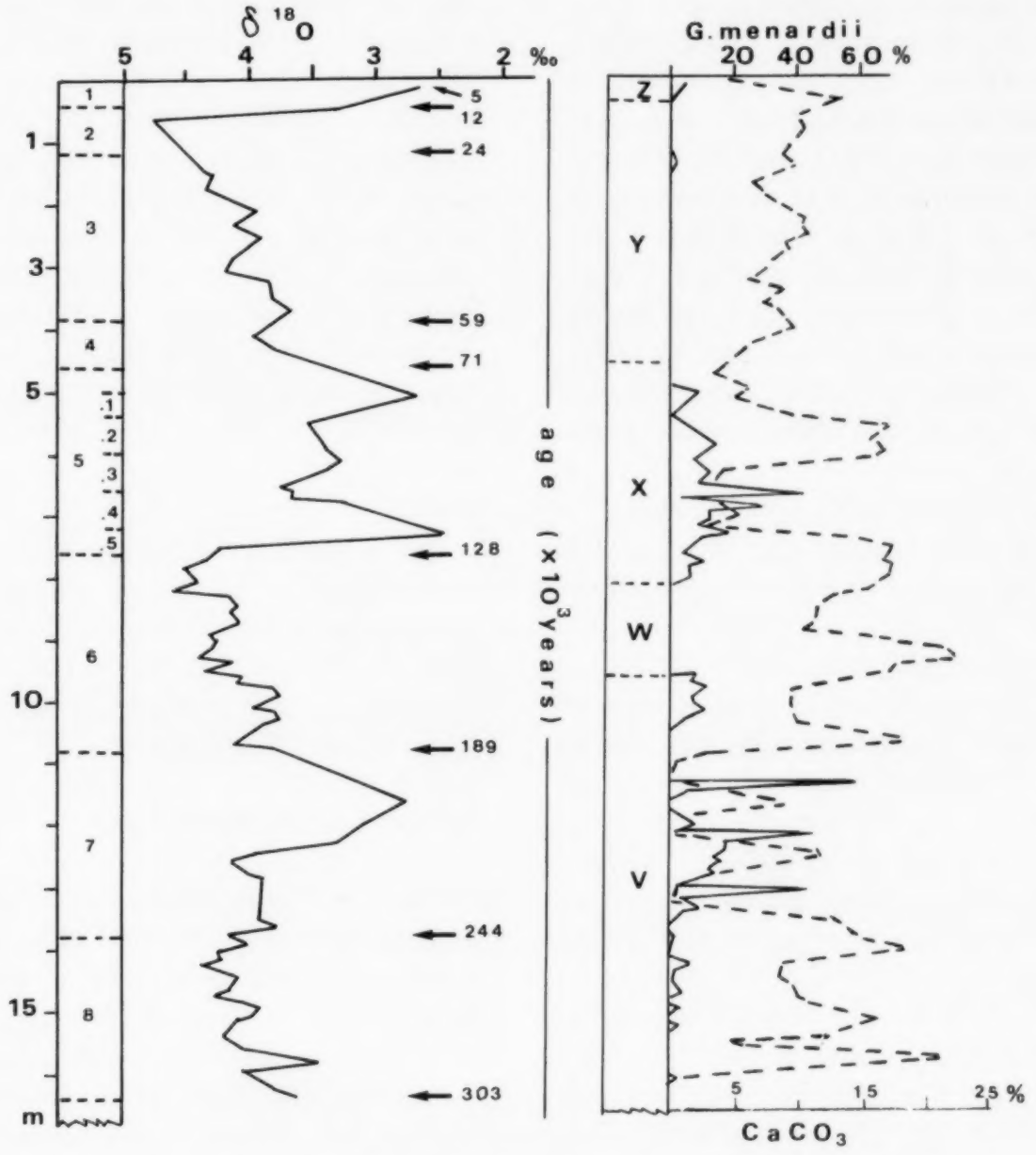

Fig. 4. Isotopic curve (^{18}O PDB) from *Melonis barleeanum* of core KW 23; correlated isotopic stages and datings from Imbrie et al. (1984). Vertical distribution of *G. menardii* (continuous line) and biozones; carbonate content (dashed line).

chronology established by Shackleton and Opdyke (1976) and revised by Imbrie et al. (1984): the top of the core is dated (^{14}C) at 5000 yrs B.P. (uppermost stage 1 is missing), while the stage 9/8 boundary at 16.40 m corresponds to 303,000 yrs. Most of the isotopic stages are characterized by second order fluctuations allowing sub-stage definitions. Sharp fluctuations (1.5–1.8‰) are recorded near the 2/1 and 6/5 stage boundaries and indicate dramatic changes in the isotopic composition of the deep waters in the Angola Basin. Similar isotopic changes were noted at the stages 2/1 and 6/5 boundaries in cores off Sierra Leone (Sarnthein et al., 1984), as well as in the North Atlantic where they are proposed to result from a syn-glacial cooling of the North Atlantic Deep Water (Duplessy et al., 1980).

Following the ecostratigraphic zonation of Ericson and Wollin (1968) using the abundance of *Globorotalia menardii,* core KW 23 was subdivised into warm (Z, X, V) and cold (Y and W) biozones (Fig. 4). The disappearance of *G. menardii* at the top of isotopic stage 5 may be related to selective dissolution. Biozone W, between 8.20 and 9.70 m, partly corresponds to isotopic stage 6. Strong variations in the abundance of *G. menardii* within biozone V indicate significant climatic fluctuations. The planktonic species *Neogloboquadrina hexagona,* a fairly good stratigraphic marker of warm stages in the deep-sea fan of Congo–Zaïre and in the Sierra Leone Rise (Zachariasse et al., 1984; Pflaumann, 1986), was not found to be reliable in this core.

Core KW 24 is located 520 km from the Congo–Zaïre estuary in 2334 m of water. Fluctuations of *G. menardii* define a foraminiferal biozonation as in KW 23. The similarity between the calcium carbonate curves of the two cores (Fig. 5), along with their proximity in similar depths, permits extension of the oxygen-isotope stratigraphy down to stage 8 by correlation of carbonate peaks (Fig. 5).

Core KW 25 (3994 m water depth) is situated 840 km from the Congo–Zaïre estuary, far from any river discharge. Fluctuations of *G. menardii* define a biozonation correlative to that in the other cores but including additional biozones; percentages exceed as much as 50% of the total foraminifera in biozones X, V and T (Fig. 6). The calcium carbonate curve, unlike those of other two cores, closely resembles the oxygen-isotope curves of cores from the Atlantic (Embley and Morley, 1980; Sarnthein et al., 1984). This is a common feature in Quaternary deep-sea sediments cores from the Atlantic Ocean (Embley and Morley, 1980). The occurrence of *N. hexagona* in warm biozones T, V and X, and its extinction 1.30 m from the top of the core (lower boundary of Y; Zachariasse et al., 1984), confirm the biozonation. A radiocarbon date on the total organic fraction at 7 cm gives an age of $13{,}960 \pm 700$ yrs B.P., confirming the absence of the Holocene in the core.

The extinction of the coccolith *Pseudoemiliana lacunosa* (LAD) which defines the top of nannozone 20 (Thierstein et al., 1977) occurs at 12.1 m in lower zone V; common species of nannozone 19 are found in the sediments overlying this level (C. Muller, pers. commun., 1987). It is estimatied that the LAD of *P. lacunosa* in Quaternary sediments lies at 474,000 yrs, within the middle of isotopic stage 12. However, in core KW 25, the disappearance of *P. lacunosa* is located 120 cm above the U/V boundary, which is dated to 470,000 yrs in the Sierra Leone Basin (Pflaumann, 1986). Two hypotheses can be made; (1) the estimated age of 474,000 years for this extinction is too old, or (2) the U/V boundary is older in the Angola Basin.

This *CARTUNE* scale established by Sarnthein et al. (1984) in the Sierra Leone Rise allows a precise correlation between the isotopic stages and biozones; the cold biozone U begins at the bottom of stage 15 and extends of stage 13, between 480,000 and 575,000 yrs (Fig. 6).

Sediment accumulation rates

Two types of calculations were used to approximate the accumulation rates of both the carbonate and the non-carbonate fraction. The first provides estimates in cm yrs 10^{-3} (sedimentation rates) without taking into account the degree of compaction of the sediments; this method allows comparison of our results with proximal studies. The second provides estimates in g cm^2 yrs 10^{-3} (flux rates) by assuming that the density of the sediment

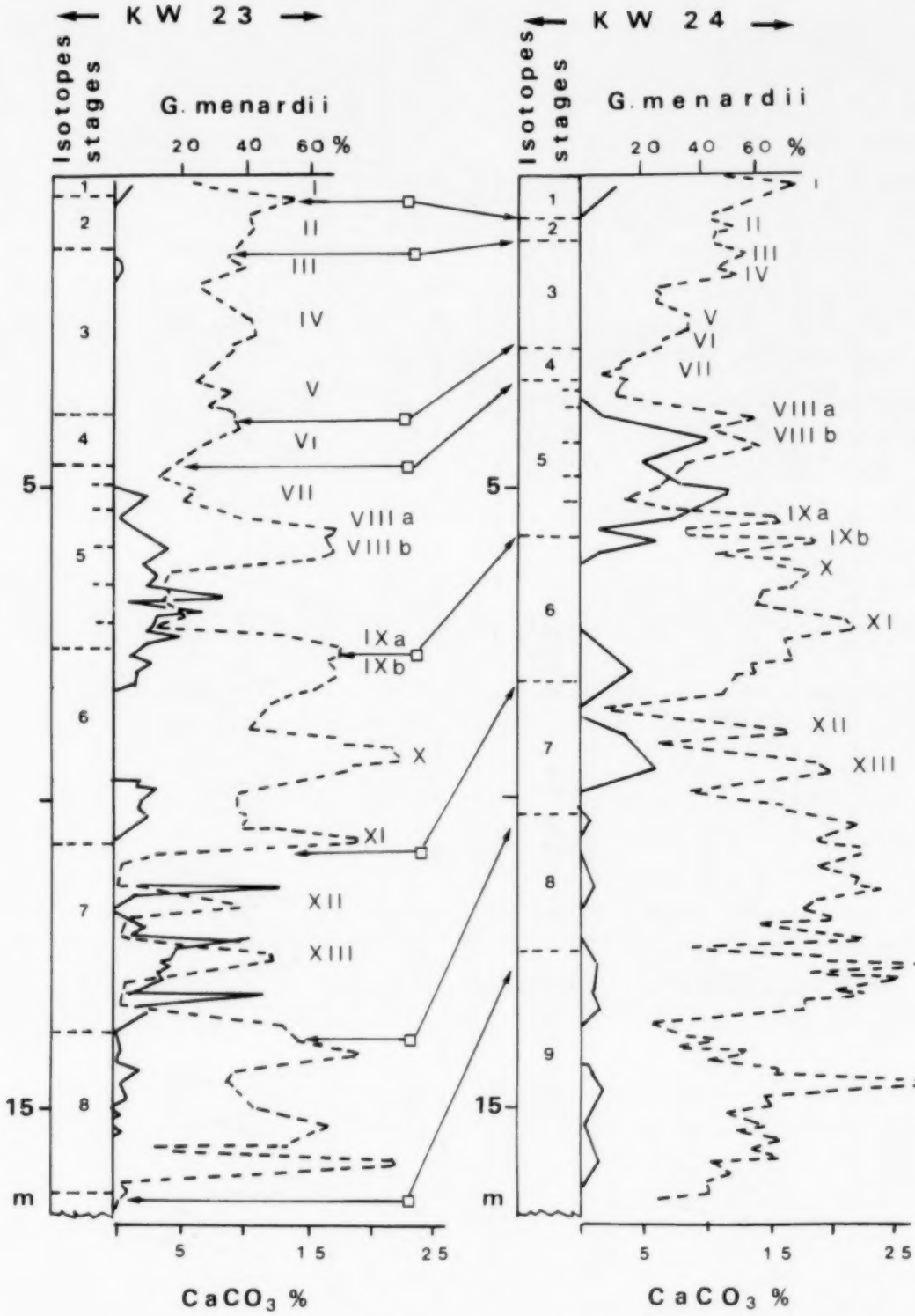

Fig. 5. Stratigraphic correlation of the two cores from 2300 m of water (KW 23 and KW 24); vertical distribution of *G. menardii* (continuous line), carbonate content (dashed line). Carbonate peaks are numbered I to XIII.

is a function of water content; this method has been used in cores from the Congo–Zaïre deep-sea fan (Jansen et al., 1984) and from the West African Margin (Giresse and Barusseau, 1989).

The resulting sedimentation rates for the two shallower cores are similar (3 to 8.5 cm yr 10^{-3}, Table 1) and are roughly half of the rates measured, at equivalent water depth, in the Congo–Zaïre middle fan (Bongo-Passi, 1984). They remain constant through time, and do not show any significant accelerations such as observed at the Y/Z boundary in Quaternary sediments off the Niger Delta (Pastouret et al., 1978), or off the Congo (Giresse et al., 1982). Sedimentation rates for core KW 25 (2.1 to 3.6 cm years 10^{-3}, Table 1) are lower than in the continental slope cores, as expected, but are

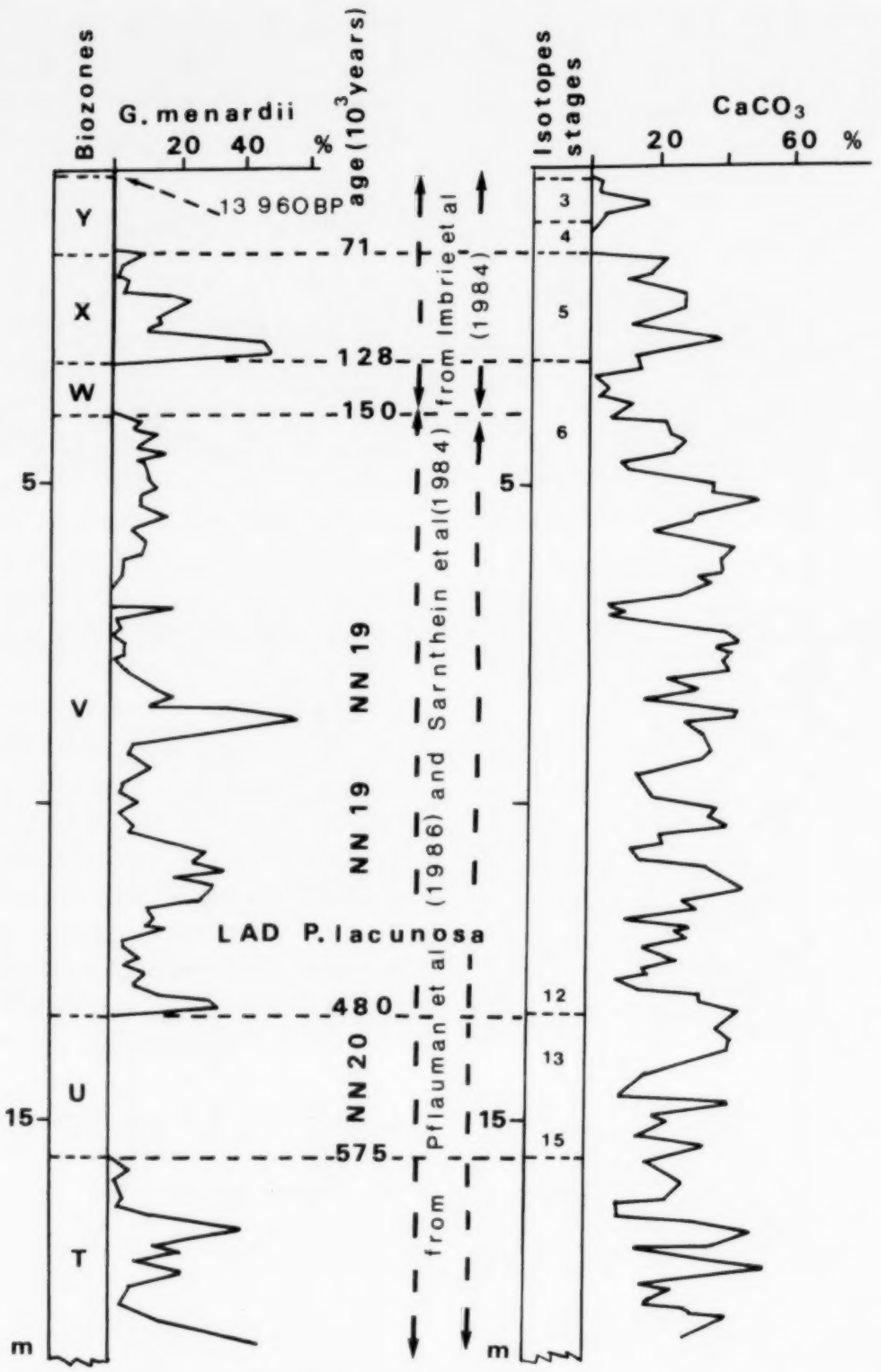

Fig. 6. Biostratigraphy and carbonate content of core KW 25.

also lower than in cores from the deep-sea fan of the Congo at about the same water depth (Jansen et al., 1984).

The cumulative curves of carbonate particle flux rate for the two shallower cores (Fig. 7) show several slight reductions which generally correspond to warm isotopic stages (5.0, 5.4, 7 for core KW 23, and 4, 5.0, 5.4 for core KW 24) while slight increases correspond to cool stages (5.2, 2 for KW 23, and, 8 for core KW 24). These changes in carbonate accumulation do not appear to affect the total flux rate which is linear throughout the middle and late Quaternary (Fig. 7); breaks are only noted within warm isotopic sub-stages 5.3 in core KW 23 and within 1, 5.3, 5.5 in core KW 24.

In core KW 25 (4000 m of water) the carbonate

TABLE I

Sedimentation rates (cm/10^3 years) of the three cores KW 23, KW 24, and KW 25

KW 23

Isotopic stages	Age (lower limit)	Thickness of intervals (cm)	Sedimentation rates (cm/10^3 yrs)
1	12,000	40	5.7
2	24,000	80	6.6
3	59,000	265	7.5
4	71,000	75	6.2
5.0	80,000	40	4.4
5.1	87,000	40	5.7
5.2	99,000	60	5
5.3	107,000	60	7.5
5.4	122,000	60	4
5.5	128,000	40	6.6
6	189,000	330	5.4
7	244,000	295	5.3

KW 24

Isotopic stages	Time range ($\times 10^3$ yrs)	Sedimentation rates (cm/10^3 yrs)
1	5–12	8.5
2	12–24	3.3
3	24–59	4.8
4	59–71	4.1
5.0	71–80	3.3
5.1	80–87	3.6
5.2	87–99	5
5.3	99–107	6.2
5.4	107–122	3
5.5	122–128	8.3
6	128–189	3.7
7	189–244	3.8
8	244–303	3.7

KW 25

	Z	Y	X	W	V	U
Sedimentation rates (cm/10^3 yrs)		2.12	3.20	3.63	2.28	2.42

flux rate (Fig. 7) fluctuates within cold biozones W and Y, where local severe dissolutions are present. As in the shallower cores, these changes do not affect the total flux rate prior to 75,000 yrs B.P.

Gamma-ray curves and visual lithologic logging show local zones of sediment, 1 to 2 cm thick, which are laminated and of different colour. The chronostratigraphic framework allows an estimated periodicity of 116 to 330 years for deposition of a single lamination. These zones are located randomly within the stratigraphy, but appear to be most closely related to biozones V and Y.

Biogenic components

Calcareous tests

Foraminifera represent the main component in all three cores. In the two shallower cores the carbonate percentages (2 to 23% for core KW 23 and 2 to 26% for core KW 24) increases within warm isotopic stages (1, various substages within 5, 6, 7 and 8). In core KW 25 the carbonate content is higher (O to 57%), and the major peaks correspond to warm biozones T, V and X; the contrast between the two latter biozones is greater than in KW 23 and KW 24.

Tests of benthic foraminifera are generally more resistant to dissolution processes than planktonic tests; a drop in the value of P/B (planktonic versus benthic foraminifera) is therefore related to dissolution (Thunnel, 1976; Diester-Haass, 1985). The P/B index roughly follows the carbonate curves, the relation being clearest in core KW 25 which has a higher range of carbonate contents and a longer duration of post-depositional processes. The two shallower cores are characterized by higher terrigenous flux rates, thus dilution processes would be expected to disturb the relation. Overall, an upward decrease in carbonate is present in core KW 25 (Fig. 8).

Fecal pellets and siliceous skeletons

The abundance of these particles is considered an approximate indicator of primary oceanic production, controlled by upwelling activity during cool periods. The abundance of mud-eating organisms is related to the nutrient flux on the seafloor, as has been demonstrated for the Congo continental margin (Zachariasse et al., 1984; Bongo-Passi, 1984) and the Senegal and Mauritania continental margins (Caralp, 1984).

In the two shallower cores, maxima in the number of diatoms are noted in isotopic stages 2, top 3 and throughout the bottom part of core KW 23; in stages 3, 4, 5.0 and top 6 and 8 in core KW

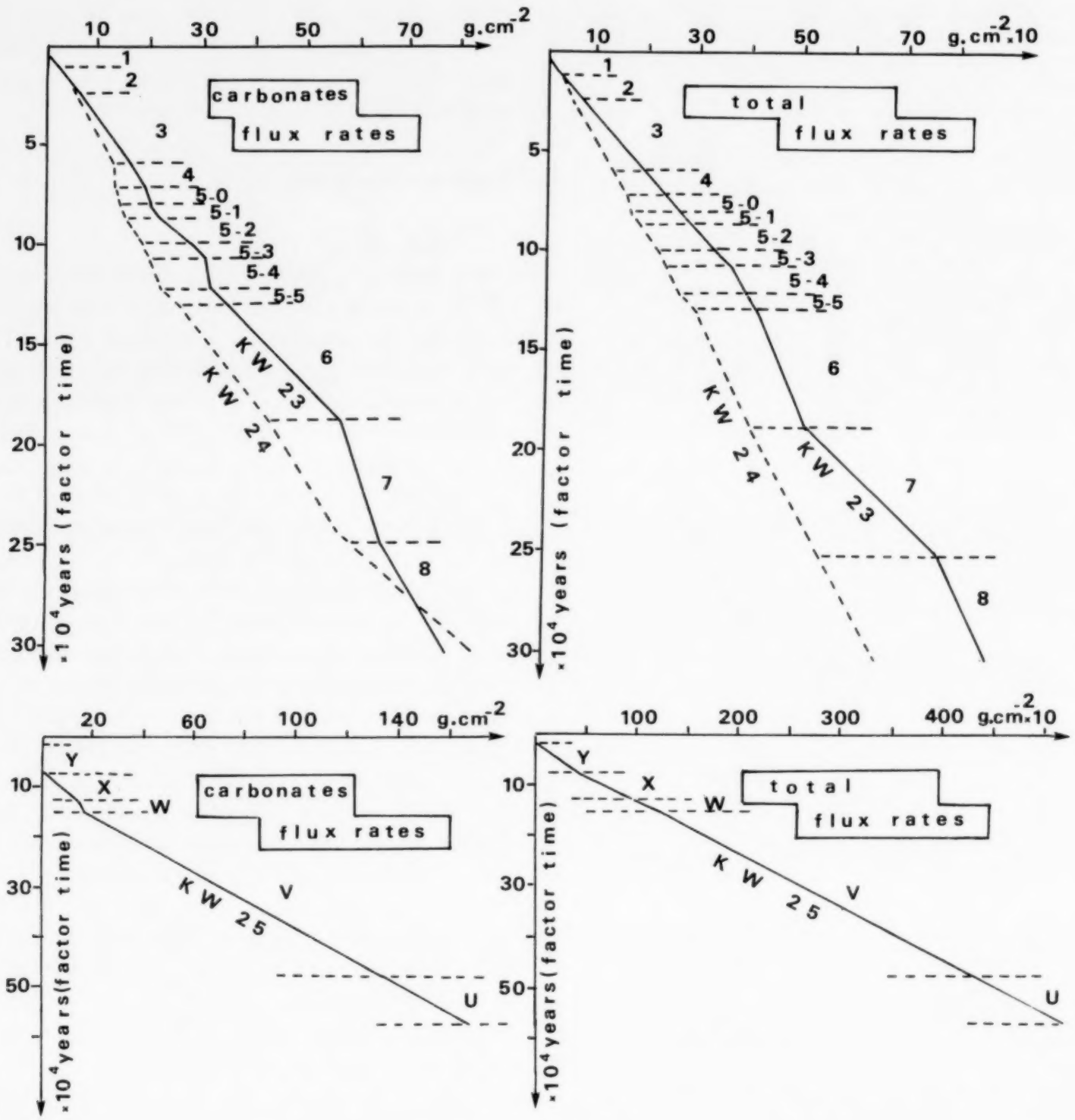

Fig. 7. Carbonate and total sediment accumulation rates of the three cores.

24 where the range of numbers is particularly contrasted. In core KW 23, the abundance of fecal pellets is high in stages 3, 5.4, base 6, top 7; sponge spicules are noted in stages 2, 3,7 and 8. In core KW 24, several stages correspond to a high number of fecal pellets (stages 5.0, 5.1, top 7, 9) and sponge spicules (stages 3, 4, bottom 7 and 8) (Fig. 9).

Peaks in diatoms and sponge spicule abundance in core KW 25 (4000 m of water), are found in biozones Y and V, while peaks in fecal pellets correspond to an increase of the benthic fauna at the bottom of Y, middle V and top T (Fig. 9). High oceanic production signals in zone V are clearly correlated with those in the Sierra Leone Basin (Pflaumann, 1986), where isotopic stage 6 is located at the top of zone V and in zone W. In the deep-sea fan of the Congo, Jansen et al. (1984) place isotopic stage 6 within zone W.

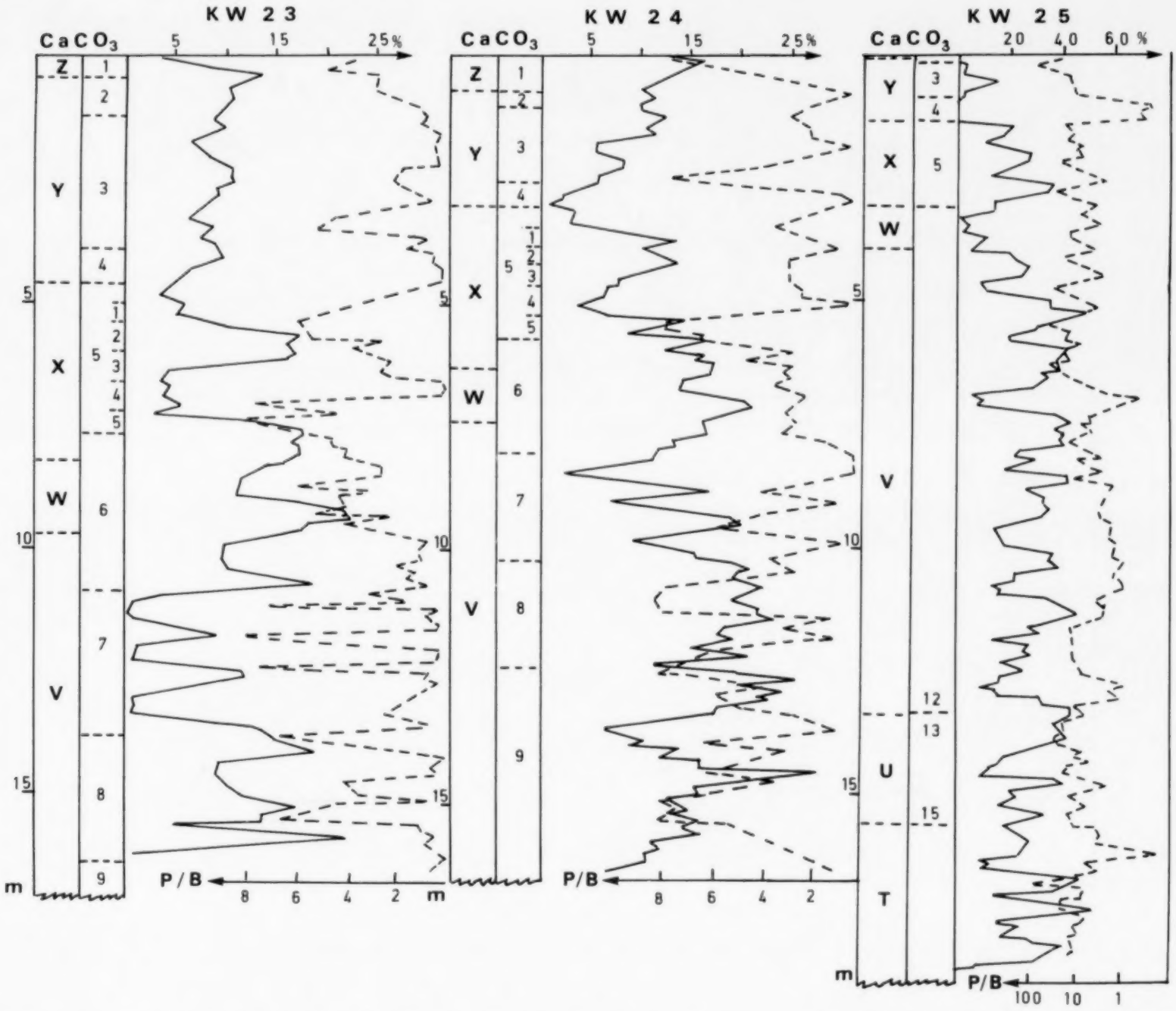

Fig. 8. Carbonate content (continuous line) against planktonic versus benthic foraminifers (P/B) curve (dashed line) for the three cores. Index P/B was calculated after counting 100 to 200 unbroken tests.

Organic carbon and nitrogen

Cores KW 23 and KW 24 show a very good correlation between carbon and nitrogen throughout the sedimentary column, indicating a constant and predominantly oceanic origin of the organic matter (Fig. 10). Only one level in core KW 24, below the Y–Z boundary, shows a sharp rise in the carbon content; this is considered to be a low relative eustatic sea level which induced terrigenous transportation of organic matter from the continental shelf. Carbon contents between 2 and 3% suggest these sediments have accumulated in a high productivity area (Johnson-Ibach, 1982).

An increase of C/N in the bottom sections of both cores results from diagenetic processes. In core KW 25, the same phenomenon is observed; the diagenetic effect appearing stronger in the bottom section of the core, prior to 400,000 yrs. Hence, the degradation time for organic matter in this area is close to that proposed by Jansen et al. (1984) for the Congo deep-sea fan (450,000–600,000 yrs), which implies more resistant organic matter than in typical oceanic areas

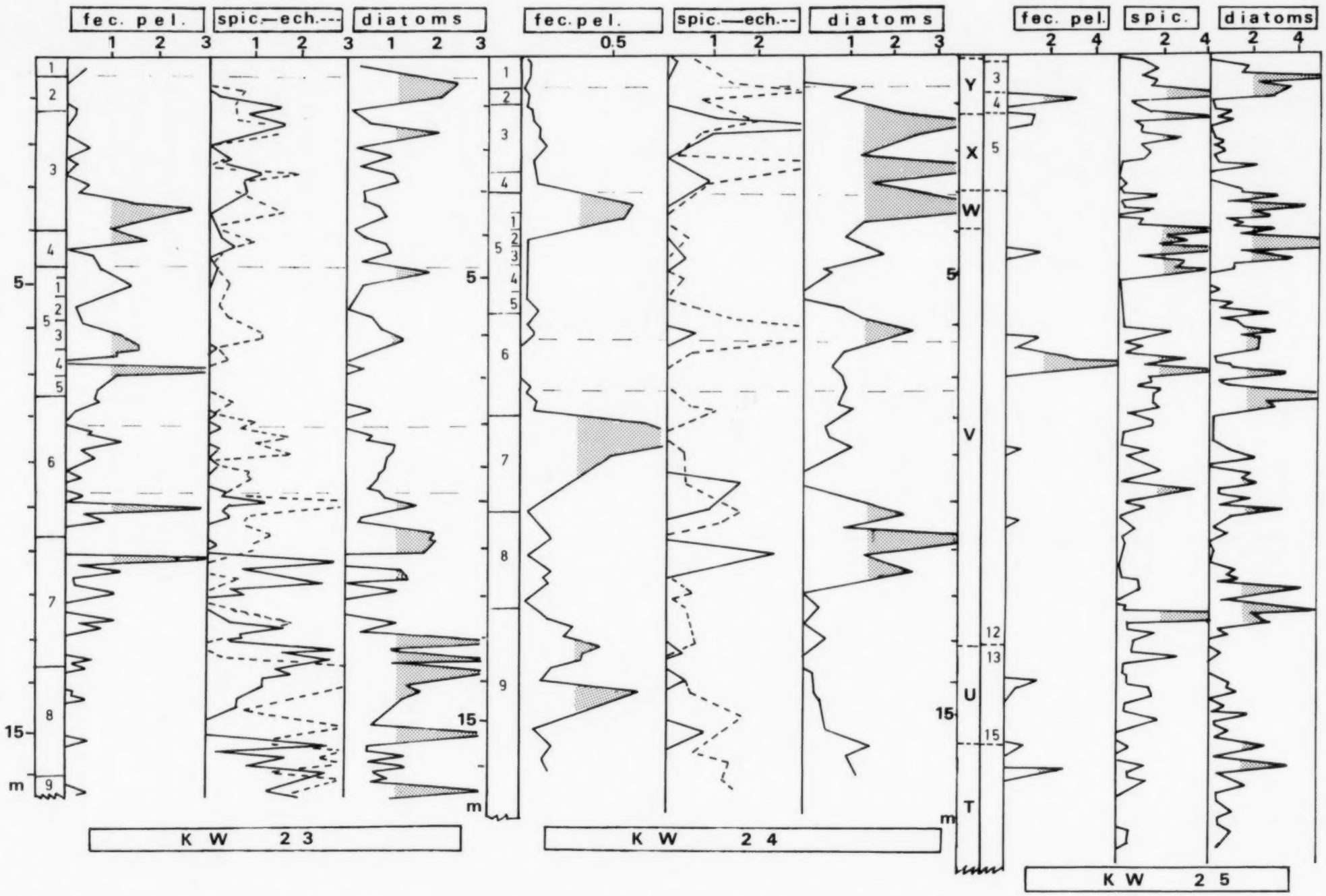

Fig. 9. Vertical distribution of the biogenic components: fecal pellets (KW 23: $\times 10^2$/g, KW 24: $\times 10^3$/g), sponge spikes (KW 23 and KW 24: $\times 10^2$/g, KW 25: $\times 10^3$/g), crinoid fragments (KW 23 and KW 24: $\times 10^2$/g, KW 25: $\times 10^3$/g), diatoms (KW 23 and KW 24: $\times 10$/g, KW 25: $\times 10^2$/g). Countings are related to weight of sand-sized fraction >40 μm.

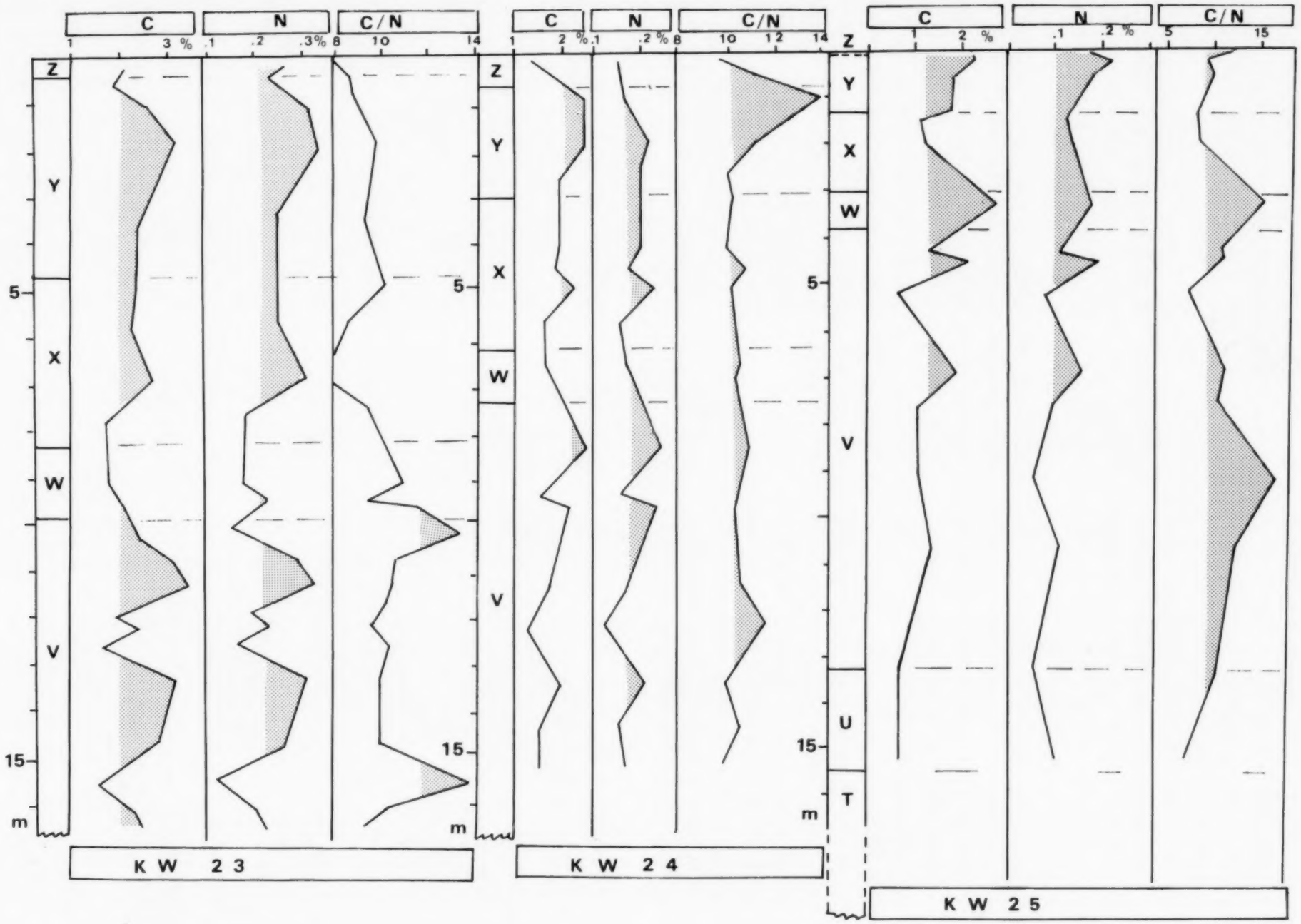

Fig. 10. Vertical distribution of organic carbon and nitrogen, and fluctuations of the C/N ratio among the 3 cores.

(Heath et al., 1977). Three peaks of C/N at the top of biozone Y, in W, and in the middle of V can be related to high terrigenous fluxes which disturb the oceanic input (Fig. 10).

On the whole, organic carbon and nitrogen peaks can be related to cold biozones, particularly the upper part of Y. In order to test a correlation between carbon content and carbonate dissolution, the X–Y–Z biozones of KW 25 were studied in detail (Fig. 11). In the greater part of the 32 analyzed levels, the intensification of dissolution effects on calcareous tests can be related to the carbon content, i.e., to productivity; shifts of the peaks may be due to the rate of microbial organic matter degradation which governed both methanogenesis and CO_2 availability; CO_2 release may also be displaced to the top.

Accumulation of organic matter on the seabed during periods of high primary production leads to decomposition in an aerobic environment, which creates favorable conditions for the dissolution or fragmentation of carbonate tests. Such a phenomena was previously reported for slope environments of the Panama Basin (Swift and Wenkam, 1978) and of the West equatorial Pacific (Berger et al., 1982).

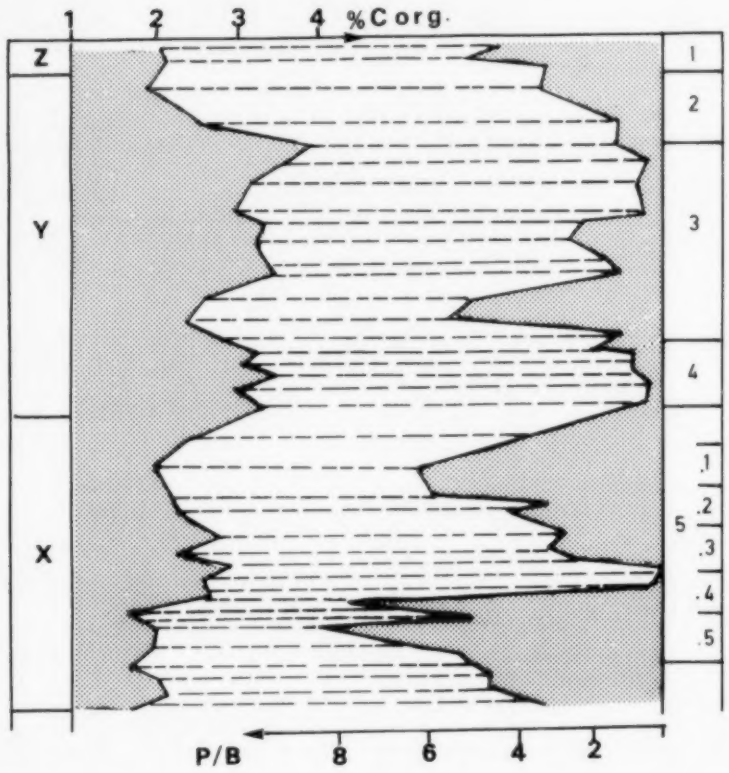

Fig. 11. Correlation between organic carbon content (% C_{org}) and *P/B* index (planktonic versus benthic foraminfera) in KW 25.

Quartz and clay minerals

Quartz

The abundance of quartz grains in marine sediments off the intertropical African margin has been repeatedly related to high terrigenous fluxes (Diester-Haass, 1976, 1983; Pastouret et al., 1978; Giresse et al., 1982) associated with pelitic deposition adjacent to the main river discharges. In the present study, this relationship seems less significant (Fig. 12). Quartz grains in the sand fractions (>50 μm) of each core are allways less than 1000 grains/10 g dry sediment, equivalent to 20 grains/100 g dry whole sediment; by contrast, concentration in pelitic sediments of the Congo

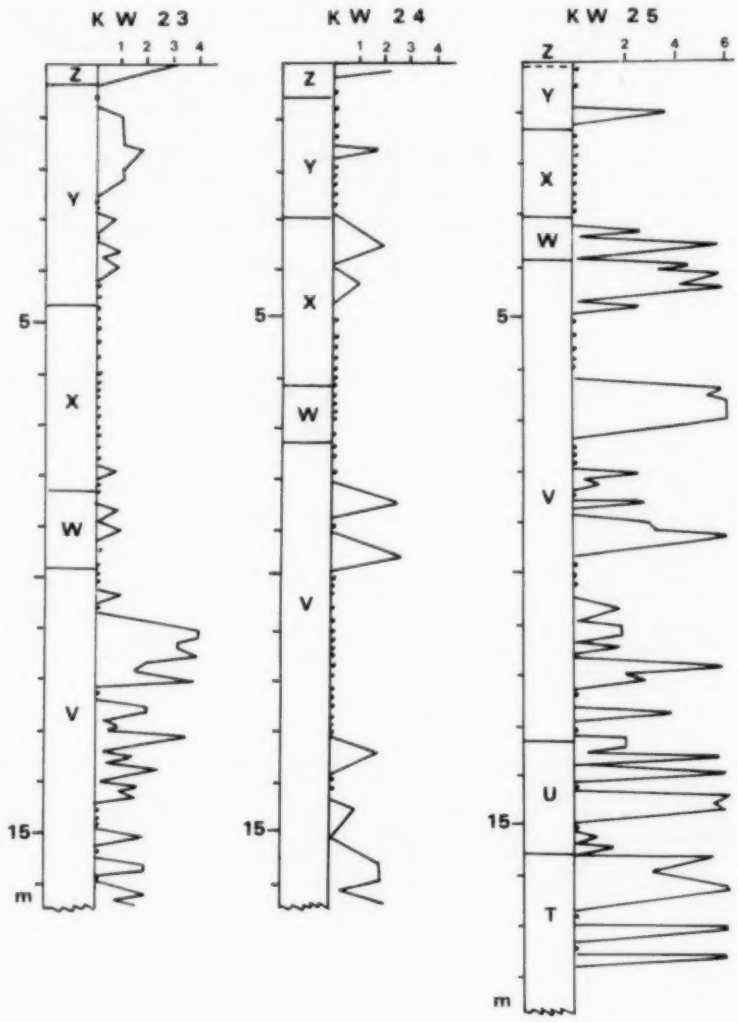

Fig. 12. Vertical distribution of quartz grains; grains were counted in the sandy fraction (>50 μm) of each level (O–6 means 0–1200 grains/10 g dry sediment).

deep-sea fan are 10 to 20 times higher (Giresse et al., 1982; Bongo-Passi, 1984). The vertical distribution of quartz grains in the three cores is generally erratic. Observed quartz specimens (SEM) are generally small (40–80 μm) and angular with frequent dissolution indices (pedogenetic stages), suggesting oceanic transportation and sorting from distant river mouths.

However, in KW 23 and KW 24 an increase of the quartz index within various cold isotopic stages in biozone Y suggests another scenario: in KW 25 (slower accumulation rate) fluctuations of abundance show some increase in the lower part of biozone Y, in W, in some levels of V and throughout the bottom section of the core. Two populations were noted:

(1) The majority of the grains show aeolian traces (aeolian cups with snail marks) with incipient quartz dissolutions; these aeolian traces are absent or unusual in biozones X and Z (Table 2; Fig. 13).

(2) Other grains show advanced dissolution, which in some cases have been modified by aquatic marks; several V marks are also observed; rounded grain shapes dominate this population.

What is the origin of these aeolian grains?

– Within some cold and dry periods of the Quaternary aeolian grains originating from the Sahara Desert accumulated on the sea floor, but such particles are usually found south of Sierra Leone (Stabell, 1986).

– Aeolian dust from the Namibian Desert has also been reported in previous studies, but according to Chester et al. (1972) such dust could not have reached the present study area.

– A possible source for the quartz grains reported here is aeolian dust from the Tchad area (Bilma–Faya–Largeau), following the Benoue

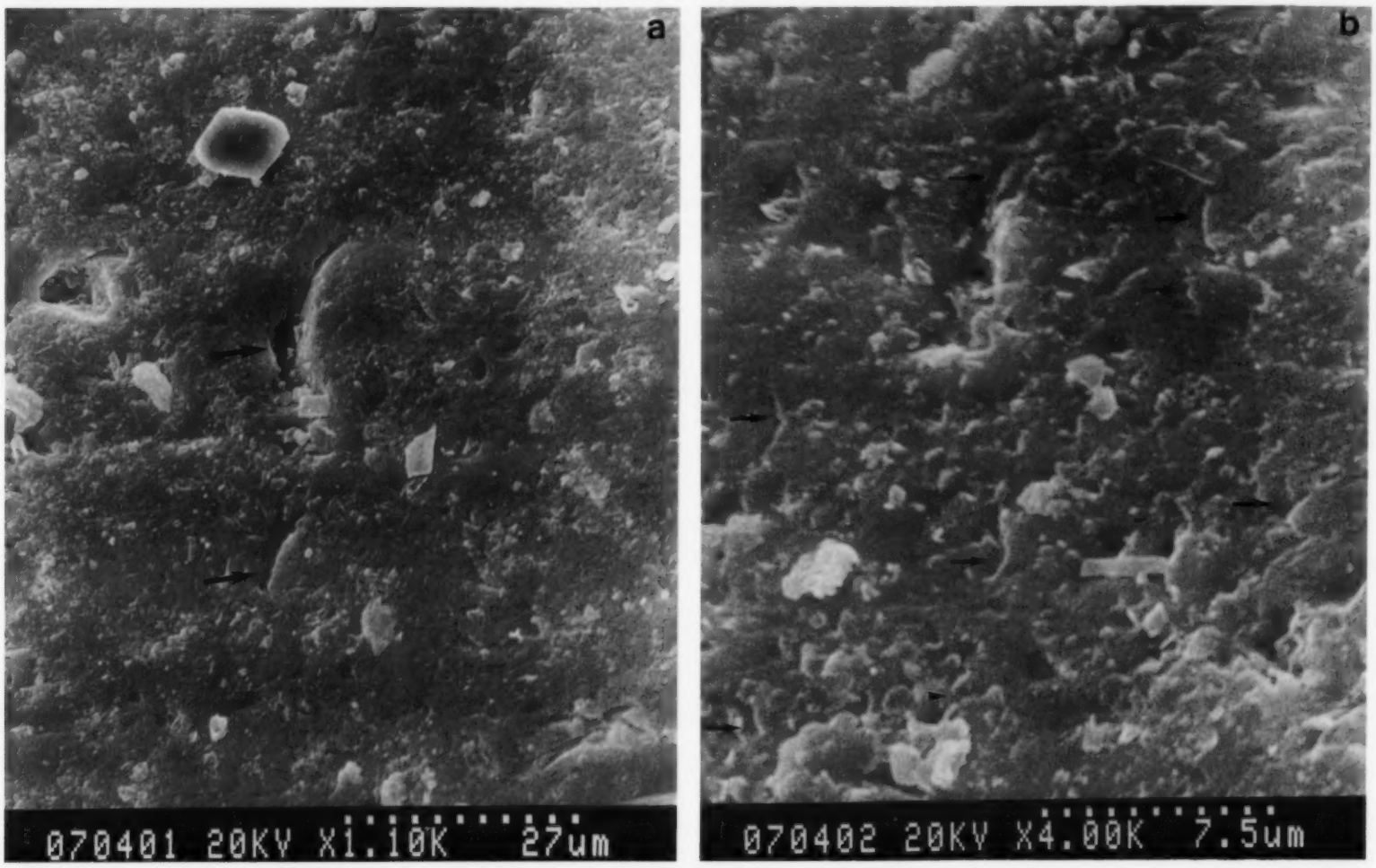

Fig. 13. SEM micrographs of surface textures. (a) Breakage surface with 10–15 μm aeolian cupules. (b) 2–3 μm aeolian marks and important coating of amorphous silica—this exfoliation film implies direct transportation without coastal influence (i.e. littoral drift).

TABLE 2

Summary of SEM examination of quartz grains from KW 25

Sample	Weak blunt edge	Nail marks cups	Conchoïdal breakage	Aquatic marks	Dissolution features	Plane breakage
4,62–4,64	*	*	*		*	*
6,83–6,85		*	*	*		*
7,03–7,05	*	*			*	
9,39			*	*		
15,84–15,86	*	*	*		*	*

Valley to be deposited in the Gulf of Guinea; this is an active process today during some days of the year (Bertrand, 1977; Kalu, 1979). Atmospheric circulation would have been more intense during cold and dry stages (Sarnthein et al., 1981), lending support to this hypothesis (Fig. 14).

Clay minerals

Kaolinite is the major component (generally 40 to 75%) of the clay minerals in the cores; it is complemented by 15 to 30% of smectites and up to 10% of illite. The Congo–Zaïre River is the main source of kaolinite in the Angola basin (Bornhold, 1973). Increasing distance from the river corresponds to a decrease of the kaolinite mean content; 68.3% in KW 23, 55% in KW 24 and 49% in KW 25 (Fig. 15). The distal location and greater water depth of core KW 25 could be the major factor leading to the difference in clay mineral content: light clay minerals such as interstratified illite–smectite are found in the deeper core; these light clay minerals could reach such a location more easily.

Kaolinite results from intense ferralitic pedogenesis on the adjacent land and from an increased terrigenous supply during warm periods. In the two shallower cores, the kaolinite content is quite erratic; the Y–Z biozone transition, as well as stages of X and V, are the most kaolinite-rich intervals, but do not allow accurate correlations between the two cores. In the deeper core, fluctuations in kaolinite content are greater (30–55%), and permit distinction of two parts of the core: from 5 m to the bottom, kaolinite is the dominant component, while above 5 m smectites with a poor crystallinity index become more important. The time scale involved for such a change is large: the climate appears to have been warmer and more humid before 350,000 yrs (top of isotopic stage 10).

The smectite crystallinity index in the lower part of KW 25 (generally <0.4) is lower than that in the upper part of the core (>0.5), as well as that of the shallower cores (about 0.7). This change within KW 25 could result from clay mineral transformation phenomena such as have been

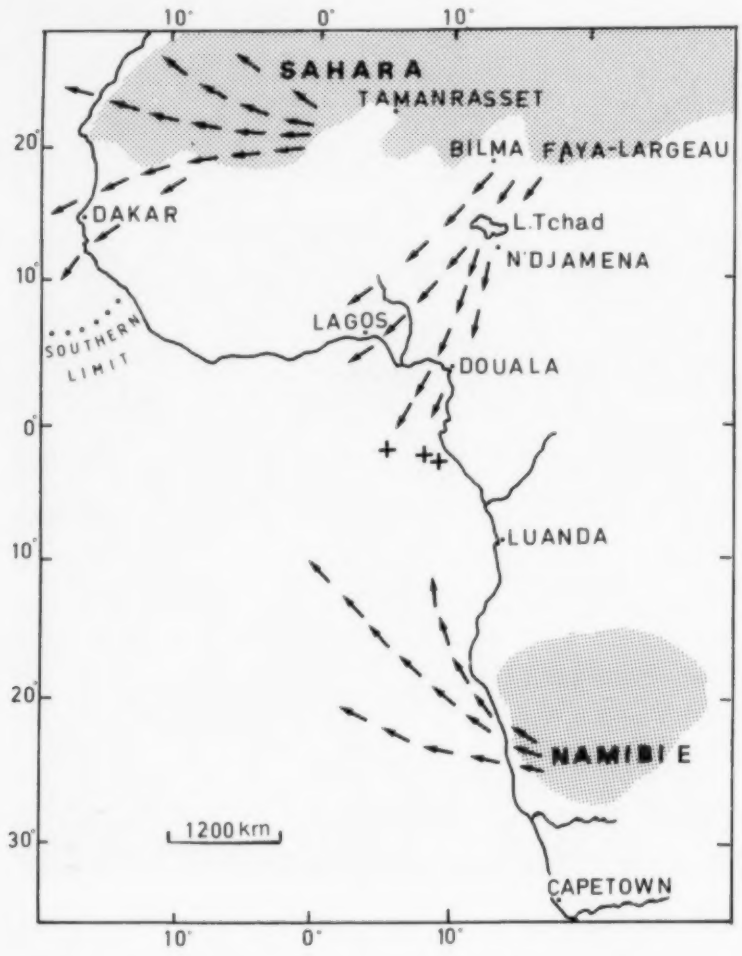

Fig. 14. Possible sources for aeolian dust during cold stages.

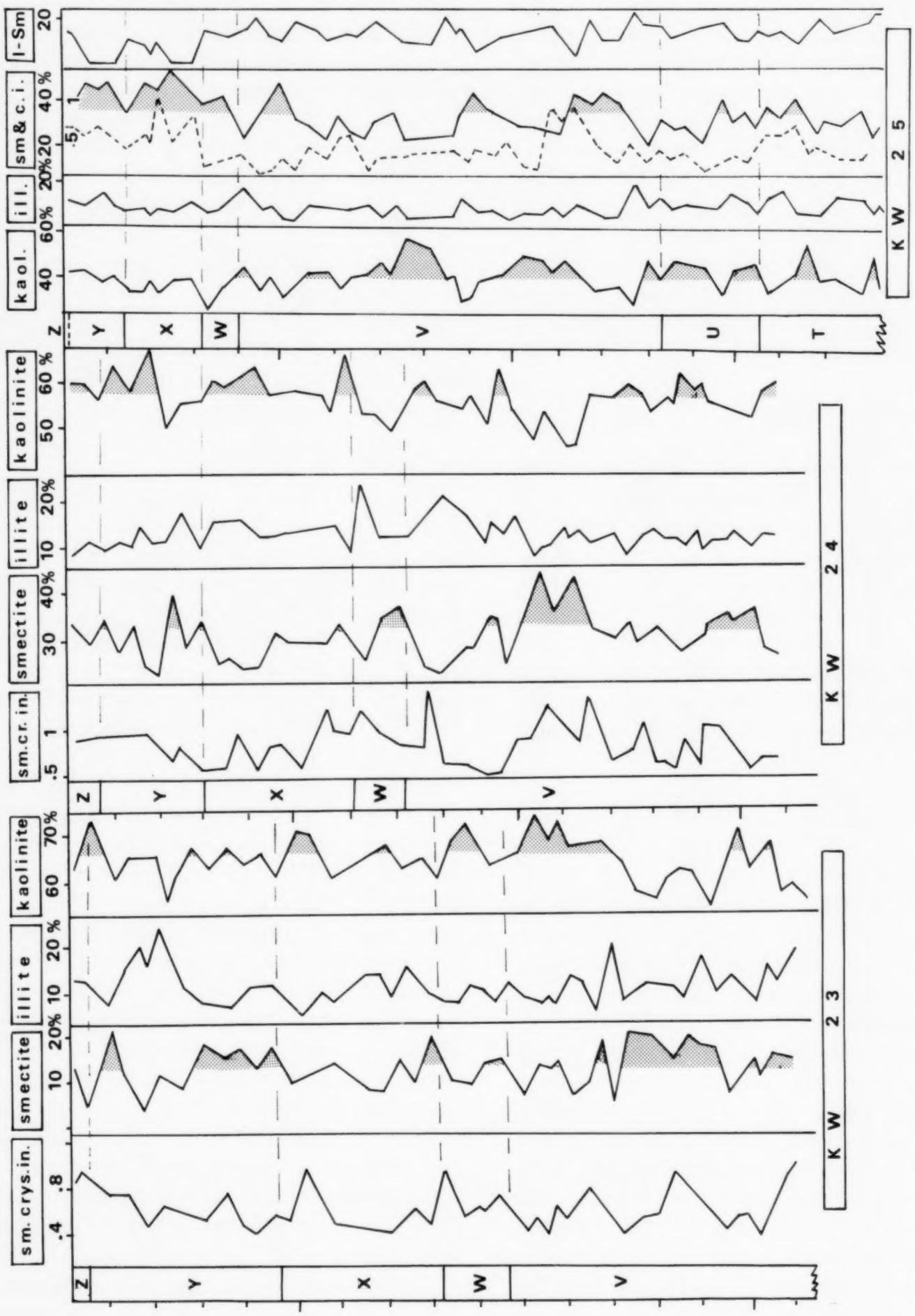

Fig. 15. Vertical distribution of the clay minerals (kaolinite, illite, smectites, interstratified illite–smectite, and smectite crystallinity index (0–1); smectite crystallinity index (dashed line) in KW 25; smectite crystallinity index half-height width versus height (weak index: well crystallized minerals).

reported from abyssal areas of the Atlantic Basin with low rates of sedimentation during the Mesozoic–Cenozoic (Holtzapfel et al., 1985). In contrast, smectites with poor crystallinity in the two shallower cores can be related to a terrigenous origin due to poorly developed pedogenesis (vertisol). The smectite content is higher during dryer isotopic stages 2, 3, 4 lower 7 and 8 in core KW 23, and 3, 4, 6, lower 7, 8 and 9 in core KW 24; however, the crystallinity index presents an erratic distribution, which is related to reworking of well-crystallized smectites from Mesozoic–Cenozoic outcroppings on the continental shelf (Jansen et al., 1984; Moguedet, 1988).

Discussion and conclusions

In a recent synthesis of climatic studies, Ruddiman et al. (1989) compared differend climatic scales during the Quaternary. Before 700,000 yrs B.P., fluctuations in the ice-cap volume of the northern hemisphere occurred at periods of about 41,000 yrs. Subsequently, fluctuations were of a larger period, approximately 100,000 yrs. Our cores from the equatorial area of the Atlantic Ocean contain characteristic cold and warm signals, which can be used to reconstruct the climatic history over the last 500,000 yrs (Fig. 16).

Oceanic fluctuations of ca. 100,000 yrs period

Interglacial stages

The early Holocene and isotopic stage 5 (particularly substage 5.5 which corresponds to a climatic optimum; Gardner and Hayes, 1976; Pflaumann, 1986) is taken as reference for reconstruction of previous interglacial episodes.

In the two shallower cores, the relatively greater abundance of calcium carbonate after 12,000 yrs B.P. suggests permanence of warm surface waters in this area, with only rare or weak upwellings: the northern spreading of the cold and productive waters is hereafter located at the south edge of the Congo–Zaïre plume (Van Bennekom and Berger, 1984). The same scheme is proposed for the record of the deep-sea sediments of the Congo–Zaïre fan (Jansen et al., 1984), in spite of higher sedimentation rates. Isotopic substage 5.5 (122,000–128,000 yrs) records a similar oceanic pattern in both cores. High amounts of carbonate particles are also observed in substage 5.5, and high values of the total foraminiferal number (unbroken tests) as well as of the planktonic/benthic ratio suggest a weak influence of dissolution processes. Sea surface waters characterized by high temperatures and low nutrient contents are consistent with the generally low abundance of diatoms and sponge spicules in the sediments.

In KW 25 at 4000 m of water, the lack of isotopic stratigraphy does not allow a precise reconstruction. However, warm biozone X with tropical and sub-tropical planktonic assemblages coincides with high carbonate content and low amounts of diatoms and sponge spicules.

Glacial stages

Core KW 23 contains oxygen-isotopic maxima within cold stages 2, 6.1 and 6.2. Incursions of cool sea-surface waters are recorded in all three cores, particularly by the planktonic foraminiferal fauna which is characterized by a high number of transitional and sub-polar species in stages 2, 4,6 and 8 and also in substages 5.2, 5.4, and 5.0 (Bonifay, 1987). In KW 23, some of these intervals (2, 4, 5.4) are marked by dissolution processes on the carbonate tests.

In the deep-sea sediments of the Congo–Zaïre fan, Jansen et al. (1984) defined levels for the CCD and the lysocline, during cold isotopic stages, of about 4300–4500 m and 3800–4000 m of water, respectively. These levels are deeper than the sampling depth of cores KW 23 and KW 24, and similar to the depth of KW 25. In the south equatorial Pacific, Berger et al. (1982) described dissolution effects on carbonate tests as a consequence of high CO_2 content in a microenvironment near the seabottom. In our three core sites, high dissolution levels are commonly correlated with a high number of diatoms (which are a good indicator of oceanic surface production) and with a high number of fecal pellets or sponge spicules (which characterize well developed benthic production).

The time intervals corresponding to these levels were found to be periods of high dissolution in areas of the south Angola Basin (Embley and

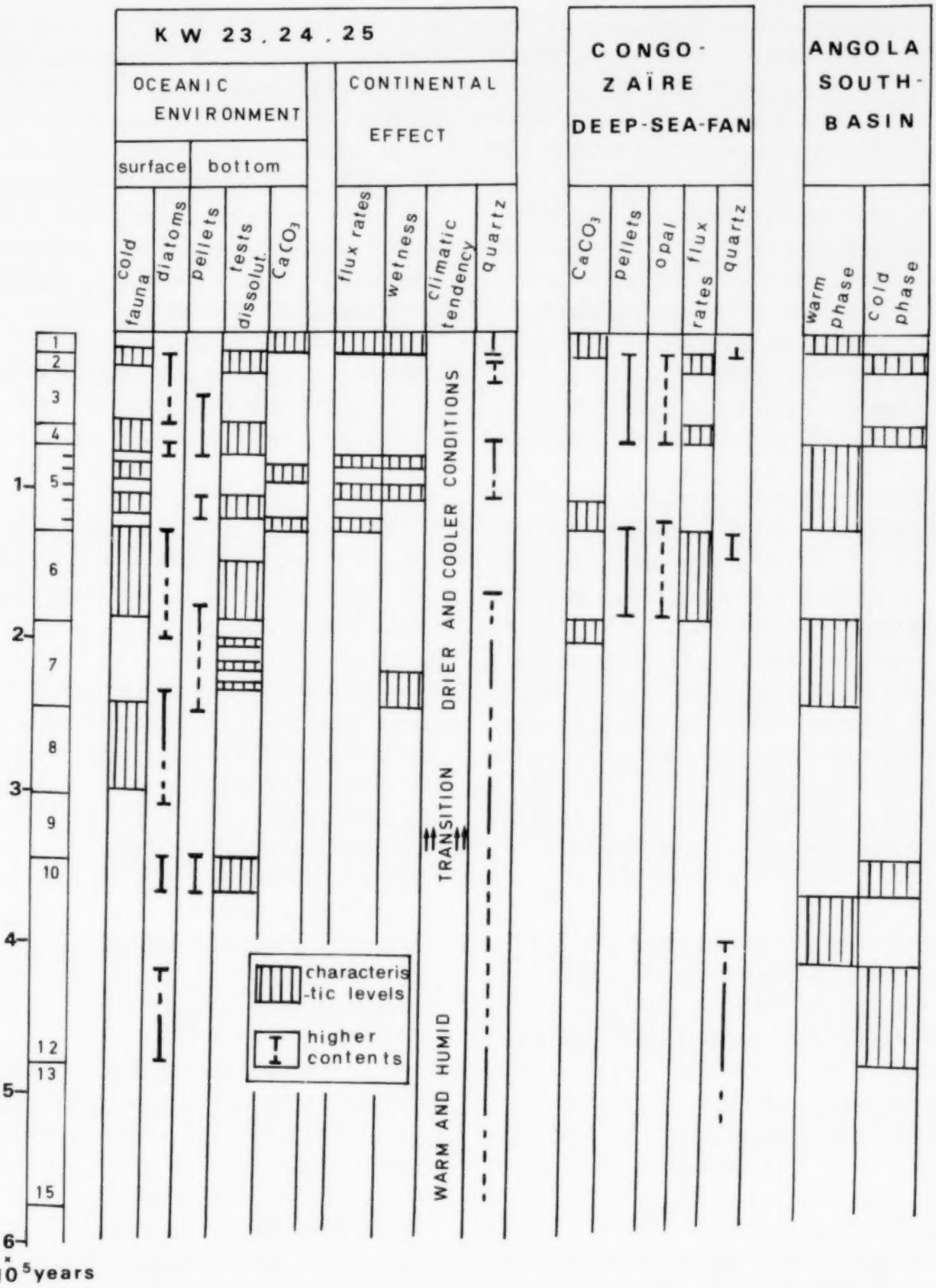

Fig. 16. Synthesis of climatic trend and oceanic changes in the three cores from the Angola Basin compared with results from the deep-sea fan of Congo–Zaïre (Jansen et al., 1984; Bongo-Passi, 1984) and the south of the Angola Basin (Embley and Morley, 1980); faunal distribution from Bonifay (1987).

Morley, 1980) and the Sierra Leone Rise (Pflaumann, 1986). In the Congo–Zaïre deep-sea fan in about 2000 m of water, dissolution has occurred during warm stages as a result of the large input of terrigenous matter from river runoff (Jansen et al., 1984).

Considering the minor influences of the AABW in this part of the Angola Basin (Van Bennekom and Berger, 1984), these dissolution processes cannot be explained by deep-water fluxes (Volat et al., 1980). Rather, fluxes of organic matter, and its subsequent degradation, appear to control the dissolution processes in the major part of the basin. A recent study on sediments off northwest Africa suggests a similar pattern for the last 270,000 years (Sarnthein and Thiedemann, 1989).

In contrast to the above scenario, some cold substages (6.0, 6.2) do not contain any indications of the blooms of oceanic production characteristic of a spreading of the upwelling systems. Hence, the high carbonate content of the these intervals is taken to be simply a consequence of a lack of dissolution. The nutrients of the cool sea-surface waters appear to be subject to important fluctuations (Labracherie, 1980; Stein, 1985).

Fluctuations of terrigenous input of 100,000 yr periods

The non-carbonate accumulation curves for the continental slope at 2300 m of water show a regular trend: in core KW 24 a steady increase is observed from 12,000 to 5,000 yrs B.P. This trend is distinct from those found at the end of isotopic stage 2 in the Niger and Congo–Zaïre fans (Pastouret et al., 1978; Giresse et al., 1982; Bongo-Passi et al., 1988). The linearity of the curves reflects the large distance of the cores from the main river discharges.

Clay minerals are the main components of the cored sediments. The Congo–Zaïre River is the principal source of an assemblage dominated by kaolinite (Kinga-Mouzeo, 1986), illite and smectite contents increase with distance from the river mouth (Van der Gaast and Jansen, 1984). This trend is more obvious towards the south of the basin (Bornhold, 1973). In core KW 23, some climatic optima (transition 1–2, substages 5.1, 5.5) are characterized by an increase in kaolinite content, and in poorly crystallized smectites and minor illite, attributed to the erosion of ferralitic soils comparable to those presently occurring on land. Sediments of cold stages (2, 4, 6) are enriched in poorly crystallized smectites and in illite, which are know to originate from poorly developed soils under dry climatic conditions (cf. the lacustrine deposits of Cameroun, Maley et al., 1990). Well crystallized smectites are also provided to the deep-sea during low sea-level periods by reworking of Mesozoic–Cenozoic outcroppings on the adjacent continental shelf (Jansen et al., 1984; Moguedet, 1988). At 4000 m of water, a slow sedimentation rate may allow the smectites to undergo transformation processes.

In the Congo–Zaïre deep-sea fan the abundance of quartz grains have been related to the importance of rainfall prior to development of the Equatorial Forest (Bongo-Passi, 1984). In the present study, at 2300 m of water, sand-size quartz grains are relatively few and their maxima number are associated with climatic optima. Within cold stages, quartz grains appear to have a distal origin: at 4000 m of water, a slow accumulation rate allows recognition of some well defined deposits of quartz grains, which include aeolian surface textures. The origin of these particles would probably be the Tchad area (via the Benoue Valley), rather than the south Sahara.

Long term climatic trend

In core KW 25 there is evidence for an important climatic as well as palaeoceanographic change in the late Quaternary, consisting of a progressive cooling since 400,000–500,000 yrs ago. This is inferred from the planktonic foraminifers (Bonifay, 1987), from the increase in the diatom numbers and in the smectite content, and from the reduction in aeolian quartz (Fig. 16).

On the continental slope off northwest Africa, a climatic cooling since around 450,000 yrs ago is suggested by the increased influence of upwellings (Stein and Sarnthein, 1984) and the increase in the paleoproductivity (Sarnthein et al., 1984). On the Sierra Leone Rise, Pflaumann (1986) found the highest winter sea-surface temperatures occurred

before 374,000 yrs. Off the Congo–Zaïre River, the high frequency of turbidity current deposits around the stage 9–10 boundary is consistant with a climatic cooling; subsequently, a warming since 400,000–300,000 yrs ago is suggested by a reduction in sediment accumulation (Jansen et al., 1986). There is no evidence for such a warming in our study.

A possible explanation for the evolution of the Pleistocene climate in this area is the modification of large-scale relief by tectonic uplift. The Tibetan uplift has been invoked to account for the increasing aridity of east Africa (Cerling et al., 1986) and for the increasing fluxes of aeolian particles from the south Sahara (Ruddiman et al., 1989). For the present study area, the development of the east African rift could have provided a similar topographic barrier which modified the tropospheric circulation, and hence the equilibrium of atmospheric humidity and insolation, beyond the barrier toward the west.

Aknowledgements

We thank the *Centre Océanologique de Bretagne* for supply of the cores; B.D. Bornhold for the core descriptions; L. Labeyrie for providing the oxygen-isotopic results; C. Muller for coccolith identification; G. Delibrias for the ^{14}C age dating. We also thank D. Praeg for reviewing this manuscript and correcting the English and anonymous referees for constructive reviews.

References

Berger, W.H., Bonneau, M.-C. and Parker, F.L., 1982. Foraminifera on the deep-sea floor; lysocline and dissolution rate. Oceanol. Acta, 5(2): 249–258.

Berrit, G.R., 1962. Contribution à la connaissance des variations saisonnières dans le Golfe de Guinée. Cah. Océanogr., 14: 633–643 and 719–729.

Bertrand, J.J., 1977. Action des poussières sub-sahariennes sur le pouvoir glaçogène de l'air en Afrique de l'Ouest. Doct. Thesis, Univ. Clermont-Ferrand, 197 pp. (Unpubl.).

Bongo-Passi, G., 1984. Contribution à l'étude lithostratigraphique, minéralogique et géochimique du delta sous-marin profond du fleuve Congo. Doct. Thesis, Univ. Toulouse, 215 pp. (Unpubl.).

Bongo-Passi, G., Gadel, F., Giresse, P., Kinga-Mouzeo and Moguedet, G., 1988. Séquences géochimiques et minéralogiques dans l'éventail détritique profond Quaternaire du fleuve Congo à 2000 et 4000 m de fond: sedimentogénèse et diagénèse. Bull. Soc. Géol. Fr., Sér. 8, IV (3): 437–452.

Bonifay, D., 1987. Interaction des accumulations terrigènes et océaniques dans le Quaternaire moyen et supérieur des marges profondes du Gabon et de la ride médio-guinéenne. Doct. Thesis, Univ. Perpignan, 185 pp.

Bornhold, B.D., 1973. Late Quaternary sedimentation in the eastern Angola Basin. Tech. Rep. Woods Hole Oceanogr. Inst., 73 (8): 1–213.

Caralp, M.H., 1984. Impact de la matière organique dans des zones de forte productivité sur certains foraminifères benthiques. Oceanol. Acta, 13: 509–514.

Cerling, T.E., Bowman, J.H. and O'Neil, J.R., 1986. An isotopic study of a fluvial–lacustrine sequence: the Plio-Pleistocene Koobi Fora sequence, East Africa. Palaeogeogr., Palaeoclimatol., Palaeoecol., 63: 335–356.

Chester, R., Elderfield, H., Griffin, J.J., Johnson, L.A. and Padgham, R.C., 1972. Eolian dust along the Eastern margins of the Atlantic Ocean. Mar. Geol., 13: 91–105.

Connary, S.D. and Ewing, M., 1974. Penetration of Antarctic bottom water from the Cape Basin into the Angola Basin. J. Geophys. Res., 79(3): 463–469.

Diester-Haass, L., 1976. Late Quaternary climatic variations in Northwest Africa deduced from East Atlantic sediment cores. Quat. Res., 6: 299–314.

Diester-Haass, L., 1983. Late Quaternary sedimentation processes on the West Africain continental margin and climatic history of the West-Africa (12–18°N). "Meteor" Forschungsergeb., Reihe C., 37: 47–84.

Diester-Haass, L., 1985. Late Quaternary sedimentation on the Eastern Walvis Ridge, SE Atlantic (HPC 532 and four piston cores). Mar. Geol., 65: 145–189.

Duplessy, J.C., Moyes, J. and Pujol, C., 1980. Deep water formation in the North Atlantic Ocean during the last ice age. Nature, 286: 479–482.

Embley, R.W. and Morley, J.J., 1980. Quaternary sedimentation and paleoenvironmental studies off Namibia (South-West Africa). Mar. Geol., 36: 183–204.

Ericson, D.B. and Wollin, G., 1968. Pleistocene climates and chronology in deep-sea sediments. Science, 162(3859): 1227–1243.

Gardner, J.V. and Hays, J.D., 1976. Response of sea-surface temperature and circulation to global climatic change during the past 200,000 years in the eastern Equatorial Atlantic Ocean. Geol. Soc. Am. Mem., 145: 221–246.

Giresse, P. and Barusseau, J.P., 1989. Quaternary accumulation rates by hemipelagic and gravity current sedimentation on the Atlantic margin of Africa: control factors of advective and vertical flows. Mar. Geol., 89: 279–297.

Giresse, P., Bongo-Passi, G., Delibrias, G. and Duplessy, J.C., 1982. La lithostratigraphie des sédiments hémipélagiques du delta profond du fleuve Congo et ses indicateurs sur les paléoclimats. Bull. Soc. Géol. Fr., Sér. 7, XXIV(4): 803–815.

Giresse, P., Kinga-Mouzeo and Schwartz, D., 1990. Breaks in the sedimentary and the environmental equilibrium in the Congo basin and incidences on the oceanic sedimentation during Quaternary. In: C.A. Kogbe and J. Lang (Editors), African Continent Sediments. J. Afr. Earth Sci., 12(1/2): 229–236.

Heath, G.R., Moore, T.C. and Dauphin, J.P., 1977. Organic

carbon in deep-sea sediments. In: N.R. Andersen and A. Malakoff (Editors), The Rate of Fossil Fuel CO_2 in the Oceans. Plenum, New York, pp. 605–625.

Holtzapfel, T., Bonnot-Courtois, C., Chamley, H. and Claver, N., 1985. Héritage et diagenèse des smectites du domaine sédimentaire nord-atlantique (Crétacé–Paléogène). Bull. Soc. Géol. Fr., Sér. 8, I(1): 25–33.

Imbrie, J., Hays, J.D., Martinson, D.G., McIntyre, A., Mix, A.C., Morley, J.J., Pisias, N.G., Prell, W.L. and Shackleton, N.J., 1984. The orbital theory of Pleistocene climate: support from a revised chronology of the marine $\delta^{18}O$ record. In: A.L. Berger, J. Imbrie et al. (Editors), Milankovitch and Climate. (NATO ASI Ser. C). Reidel, Dordrecht, 1: 269–305.

Jansen, J.H.F. and Van der Gast, S.J., 1988. Accumulation and dissolution of opal in Quaternary sediments of the Zaïre deep-sea fan (NE Angola Basin). Mar. Geol., 83: 1–7.

Jansen, J.H.F., Van Weering, T.C.E., Gieles, R. and Van Iperen, J., 1984. Middle and Late Quaternary Oceanography and climatology of the Zaïre–Congo fan and the adjacent Eastern Angola Basin. Neth. J. Sea Res., 17(2–4): 201–249.

Jansen, J.H.F., Kuijpers, A. and Troelstra, S.R., 1986. A mid-Brunhes climatic event: long term changes in global atmosphere and ocean circulation. Science, 232: 619–622.

Johnson-Ibach, L.E., 1982. Relationship between sedimentation rate and total organic carbon content in ancien marine sediments. Bull. Am. Assoc. Pet. Geol., 66(2): 170–188.

Kalu, A.E., 1979. The African dust plume: its characteristics and propagation across West Africa in winter. In: Saharan Dust. Wiley, New York, 14: 95–118.

Kinga-Mouzeo, 1986. Transport particulaire actuel du fleuve Congo et de quelques affluents; enregistrements quaternaires dans l'éventail détritique profond (sédimentologie, minéralogie et géochimie). Doct. Thesis, Univ. Perpignan, 251 pp. (Unpubl.).

Krinsley, D.H. and McCoy, F.W.: 1977. Significance and origin of surface texture on broken sands in deep-sea sediments. Sedimentology, 24: 857–862.

Labracherie, M., 1980. Les radiolaires témoins de l'évolution hydrologique depuis le dernier maximum glaciaire au large du Cap Blanc (Afrique du Nord-Ouest). Palaeogeogr., Palaeoclimatol., Palaeoecol., 32: 163–184.

Mahe, G., Olivry, J.C. and Lerique, J., 1988. La variabilité du régime des tributaires du Golfe de Guinée: indice de crises ou de changements climatiques. In: J.C. Olivry (Editor), Géodynamique de l'hydrosphère continentale. ORSTOM, Paris, pp. 115–120.

Maley, J., Livingstone, D.A., Giresse P., Thouveny, N., Brenac, P., Kelts, K., Kling, G., Stager, C., Haag, M., Fournier, M., Bandet, Y., Williamson, D. and Zogning, A., 1990. Lithostratigraphy, volcanism, paleomagnetism and palynology of Quaternary lacustrine deposits from Barombi-Mbo (West-Cameroon); preliminary results. J. Volcanol. Geotherm. Res., 42: 319–335.

Metcalf, W.G., Heezen, B.C. and Stalcup, M.C., 1964. The sill depth of the Mid-Atlantic Ridge in the Equatorial region. Deep-Sea Res., 11: 1–10.

Moguedet, G., 1988. Les relations entre le fleuve Congo et la sédimentation récente sur la marge continentale entre l'embouchure et le Sud du Gabon. Etude hydrologique, sédimentologique et géochimique. Doct. Thesis, Univ. Angers, 185 pp. (Unpubl.).

Olivry, J.C., Bricquet, J.P., Thiebaux, J.P. and Nkamdjou Sigha, 1988. Transport de matière sur les grands fleuves des régions intertropicales: les premiers résultats des mesures de flux particulaires sur le bassin du fleuve Congo. In: Sediment Budgets. Proc. Porto-Alegre Symp. IAHS Publ., 174: 509–521.

Pastouret, L., Chamley, H., Delibrias, G., Duplessy, J.C. and Thiede, J., 1978. Late Quaternary climatic changes in the Western Tropical Africa deduced from deep-sea sedimentation of the Niger delta. Oceanol. Acta, 1: 217–231.

Pflaumann, U., 1986. Sea-surface temperatures during the last 750,000 years in the Eastern Equatorial Atlantic: Planktonic foraminiferal record of "Meteor" cores 13519, 13521 and 16415. "Meteor" Forschungsergeb., Reihe C, 40: 137–161.

Piton, B. and Kartavtseff, A., 1986. Utilisation de bouées dérivantes à positionnement par satellite pour une meilleure connaissance de l'hydrologie de surface du golfe de Guinée. Doc. ORSTOM, Brest, 34, 41 pp.

Ruddiman, W.F., Sarnthein, M., Backman, J., Baldauf, J.G., Curry, W., Dupont, L.M., Janecek, T. Pokras, E.M., Raymo, M.E., Stabell, B., Stein, R. and Tiedemann, R., 1989. Late Miocene to Pleistocene evolution of climate in Africa and the low-latitude Atlantic: overview of Leg 108 results. In: W. Ruddimann et al., Proc. ODP, Sci. Results, 108: 463–484.

Sarnthein, M. and Tiedemann, R., 1989. Toward a high-resolution stable isotope stratigraphy of the last 3.4 million years: Sites 658 and 659 off northwest Africa. In: W. Ruddiman et al., Proc. O.D.P., 108: 167–185.

Sarnthein, M., Tetzlaff, G., Koopmann, B., Wolter, K. and Pflauman, U., 1981. Glacial and interglacial wind regimes over the eastern subtropical Atlantic and North-West Africa. Nature, 293: 193–196.

Sarnthein, M., Thiede, J., Pflaumann, U., Erlenkeuser, H., Fütterer, O., Koopmann, B., Lange, H. and Seibold, E., 1982. Atmospheric and oceanic circulation patterns off northwest Africa during the past 25 million years. In: U. von Rad et al. (Editors), Geology of the Northwest African Continental Margin. Springer, Berlin, pp. 545–603.

Sarnthein, M., Erlenkeuser, H., Von Grapenstein, R. and Schroder, C., 1984. Stable isotope stratigraphy for the last 750,000 years: "Meteor" core 13519 from the Eastern Equatorial Atlantic. "Meteor" Forschungsergeb., Reihe C, 38: 9–24.

Shackleton, N.J. and Opdyke, N.D., 1976. Oxygen-isotope and paleomagnetic stratigraphy of Pacific core V 38-239. Late Pliocene to Latest Pleistocene. Geol. Soc. Am. Mem., 145: 449–464.

Stabell, B., 1986. Variations of diatom flux in the eastern equatorial Atlantic during the last 400,000 years ("Meteor" cores 13519 and 13521). Mar. Geol., 72: 305–323.

Stein, R., 1985. Late Neogene changes of paleoclimate and paleoproductivity off Northwest Africa (DSDP site 397). Palaeogeogr., Palaeoclimatol., Palaeoecol., 49: 47–59.

Stein, R. and Sarnthein, M., 1984. Late Neogene events of atmospheric and oceanic circulation patterns offshore northwest Africa: high resolution record from deep-sea sediments. Palaeoecol. Afr., 16: 9–36.

Swift, S.A. and Wenkam, C., 1978. Holocene accumulation

rates of calcite in the Panama Basin. Lateral and vertical variations in calcite dissolution. Mar. Geol., 27: 67–77.

Thierstein, H.R., Geitzenauer, K.A. and Molfino, B., 1977. Global synchroneity of Late Quaternary coccolith datum levels validation by oxygen isotopes. Geology, 5: 400–404.

Thunnel, R.C., 1976. Optimum indices of calcium carbonate dissolution in deep-sea sediments. Geology, 4: 525–528.

Tiedemann, R., Sarnthein, M. and Stein, R., 1989. Climatic changes in the western Sahara; aeolo-marine sediment record of the last 8 millions years (sites 657–661). In: W. Ruddiman et al., Proc. ODP, Sci. Results, 108: 241–277.

Van Bennekom, A.J. and Berger, G.W., 1984. Hydrography and silice budget of the Angola Basin. Neth. J. Sea. Res., 17(2): 149–200.

Van der Gast, S.J. and Jansen, J.H.F., 1984. Mineralogy, opal and manganese of Middle and Late Quaternary sediments of the Zaïre (Congo) deep-sea fan; Origin and climatic variation. Neth. J. Sea Res., 17(2–4): 313–341.

Van Weering, T.C.E. and Van Iperen, J., 1984. Fine grained sediments of the Zaïre deep-sea-fan, southern Atlantic Ocean. In: D.A.V. Stow and D.J.W. Piper (Editors), Fine Grained Sediments: Deep Water Processes and Facies. Geol. Soc. London Spec. Publ., pp. 93–113.

Volat, J.L., Pastouret, L. and Vergnaud-Grazzini, C., 1980. Dissolution and carbonate fluctuations in Pleistocene deep-sea cores: A review. Mar. Geol, 34: 1–28.

Zachariasse, W.J., Schmidt, R.R. and Van Leeuwen, R.J.W., 1984. Distribution of foraminifera and calcareous nannoplankton in Quaternary sediments of the eastern Angola Basin in response to climatic and oceanic fluctuations. Neth. J. Sea Res., 17(2–4): 250–275.

Marine Geology, 106 (1992) 131–139
Elsevier Science Publishers B.V., Amsterdam

Thermoluminescence dating of dunes at Cape St. Lambert, East Kimberleys, northwestern Australia

Brian G. Lees[a], Lu Yanchou[b] and David M. Price[c]

[a]*Department of Geography, Australian National University, Box 4, Canberra, ACT 2601, Australia*
[b]*Xian Laboratory of Loess and Quaternary Geology, Academica Sinica, Box 17, Xian, Shaanxi Province, People's Republic of China*
[c]*Department of Geography, University of Wollongong, Box 1144, Wollongong, NSW 2500, Australia*

(Received June 14, 1991; revision accepted October 14, 1991)

ABSTRACT

Lees, B.G, Lu Yanchou and Price, D.M., 1991. Thermoluminescence dating of dunes at Cape St Lambert, East Kimberleys, northwestern Australia. *Mar. Geol.*, 106: 131–139.

Quaternary lithostratigraphic units in coastal dunes have been dated in the dune field at Cape St. Lambert, near the mouth of the Berkeley River in the East Kimberley Region, northwestern Australia, using coarse fraction thermoluminescence (TL) dating. Twelve TL dates were measured. Four main chronostratigraphic units were identified. The oldest dunes appear to have been produced from offshore deposits reworked by rising sea level about 5000 years ago. Two sequences of younger, stable dunes derive from the river mouth sediments of the Berkeley River and date to about 3000 years ago and 1600 years ago respectively. The presently active dunes appear to have been initiated within the last 1000 years. A period of increased climatic variability, from 3000 yrs B.P. to the present, appears to be responsible for most of the late Holocene units identified at Cape St. Lambert.

Introduction

There has been considerable debate over a number of years about the processes which led to the formation of transgressive coastal dunes during the late Quaternary. Much of this has been summarised by Pye (1984), but the main hypotheses are that these are either random events related to local sediment budget changes, or non-random events associated with either glacial low sea levels (Coaldrake, 1962), marine transgressions (Cooper, 1958), cycles of storminess (Thom, 1978), anthropogenic disturbance, or changes in wetness.

Thermoluminescence (TL) dating of late Quaternary units in three coastal dunefields in the eastern part of northern Australia; Cobourg Peninsula, Shelburne Bay and Cape Flattery, provides evidence to show that dune emplacement has been both episodic and synchronous over a wide area (Lees et al., 1990). This suggests very strongly that these are non-random events. However, with information from only three dunefield sites there is insufficient data to confidently extrapolate these characterisations to the region. This investigation of the Cape St. Lambert dunefield (Fig. 1) is part of a project to increase the data set by investigating other dunefield sites, and also by providing more detailed information on sites already reconnoitered. A more complete data set will allow interpretation of these late Quaternary depositional environments to be carried out with more confidence and precision. Work is in progress in the dunefields around Cape Arnhem, and on Groote Eylandt. Further dating is also being undertaken in Shelburne Bay dunefield.

In northern Australia large coastal dunefields are common along the eastern coasts of Cape York

Correspondence to: B.G. Lees, Australian National University, Department of Geography, G.P.O. Box 4, Canberra, ACT 2601, Australia.

0025-3227/92/$05.00

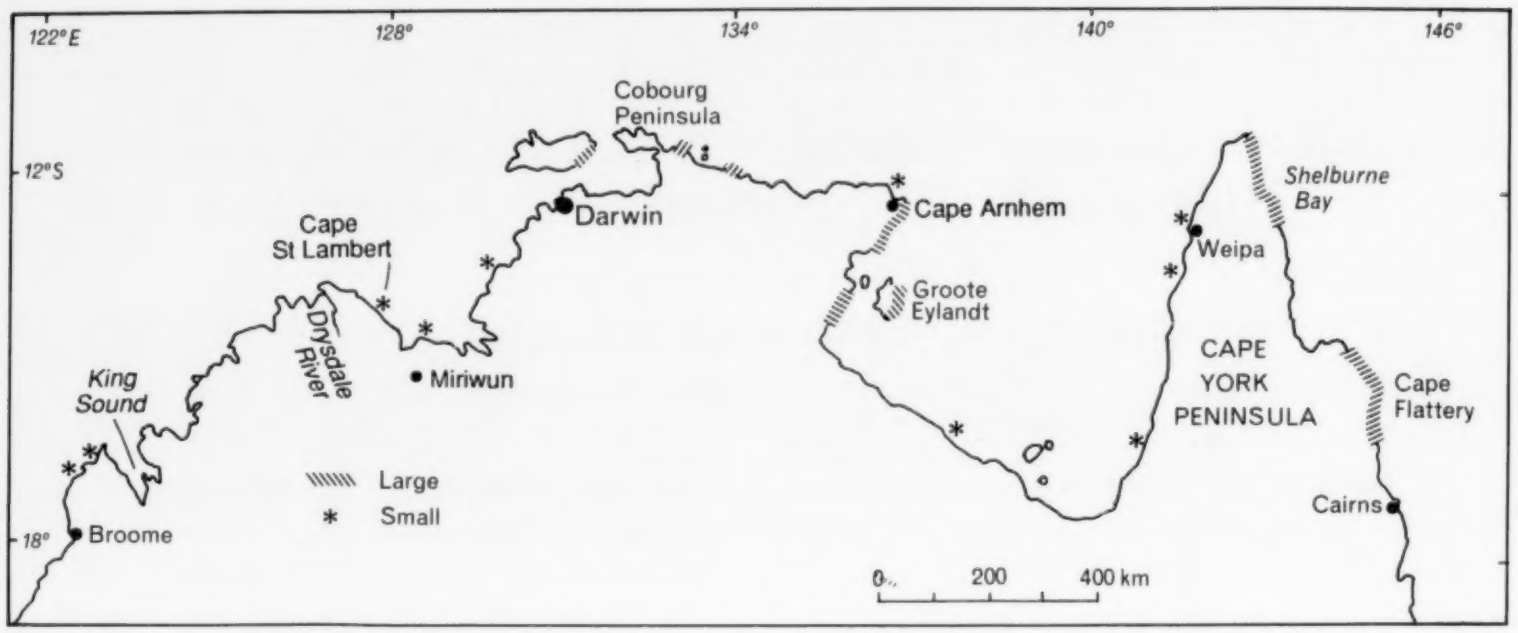

Fig. 1. The distribution of major coastal dunefields in northern Australia (after Galloway et al., 1980).

and Arnhem Land. West of Cape Arnhem coastal dunefields become smaller and less common. To the west of Darwin coastal dunefields are rare. Although there are some dunes on the western side of King Sound, and near the mouth of the Drysdale River, the Cape St. Lambert dunefield is the most westerly coastal dunefield in northern Australia (Fig. 1). This is the driest of northern Australia's coastal dunefields (Fig. 2). It is also the windiest. On the east Kimberley coast the dominant southeast trades are reinforced by circulation around the high pressure systems typical of the continental pressure patterns during the dry season. This makes it a particularly interesting site as it is, and presumably has been throughout the late Holocene, more susceptible to mobilisation than wetter, or less windy, locations.

The dunefield at Cape St. Lambert is much

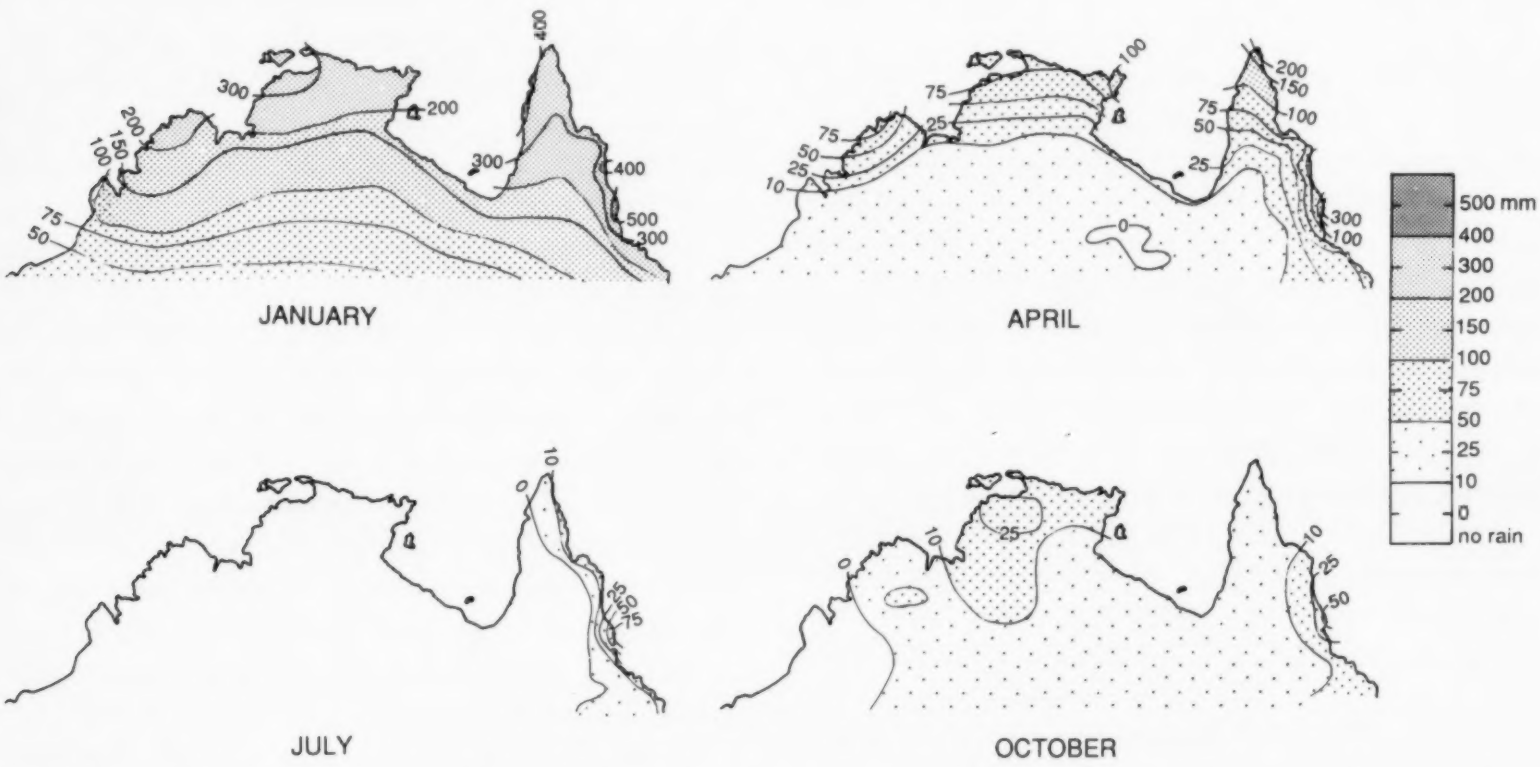

Fig. 2. Seasonal rainfall across northern Australia showing the variation in the length of the dry season from site to site.

smaller than those previously described in eastern Cape York and Arnhem Land (Lees et al., 1990). It extends along the coast north of the mouth of the Berkeley River for about 8 km, and inland from the coast about 1.5 kilometers (Fig. 3). Despite its small size, it contains some very large elongate parabolic dunes. The largest of these is about 5 kilometers long and has an advancing slip face 91 m high. The dunes are aligned with the dominant southeast trade winds.

The East Kimberley coast is strongly fault controlled. For most of its length it is characterised by steep rocky cliffs with narrow, structurally controlled river valleys. Only for a short distance to the immediate north of the mouth of the Berkeley River, and in a few small embayments beyond this, are sediments found on the open coast. Like most of the large coastal dune fields in northern Australia, the dunes here are associated with a major river delivering material to an easterly facing coast.

Methodology

Because of access problems field work in the Cape St. Lambert dune field was limited to a 4 day period in July 1989. Preliminary geomorphological mapping, carried out in advance using aerial photography, was field checked across a number of transects.

Representative samples for TL dating were collected from the dunefield units identified during geomorphological mapping. Samples were collected from covered trenches and sealed in steel cans in total darkness. Each sample was matched for reference, where possible, with a surface sample assumed to have been zeroed in sunlight. The samples were divided between two laboratories. Five of the samples were submitted to the Xian Laboratory of Loess and Quaternary Geology and seven to the University of Wollongong TL laboratory. Both of the laboratories dated the coarse fraction (90–125 μm) of the samples using similar methodologies. This was not intended as a comparative analysis and the only paired samples were W896 and XAL096, XAL097 and XAL098, W894 and W895, and XAL100 and W897 (Fig. 3).

The preparation procedure for those samples processed at Xian was described in Lu Yanchou et al. (1987) and Lees et al. (1990). Age determinations and sample characteristics are shown in Table 1.

The preparation procedure for those samples processed at Wollongong has been described in Nanson et al., (1991). The additive TL dating method (Aitken, 1985) was used by the Wollongong laboratory in their determinations. The ages shown in Table 2 are the mean of a series of analyses performed at 25°C intervals throughout the stated temperature range and are presented to within 1 SD. Values subscripted UV represent TL ages calculated with reference to the TL level attained following 48 hours UV bleaching under an intense sun lamp (Phillips MLU 300 W). These

TABLE 1

Thermoluminescence results and analysis data for dunesand samples collected from Cape St. Lambert (Xian Laboratory of Loess and Quaternary Geology)

Remark	U (ppm)	Th (ppm)	K_2O (%)	Water (%)	Dose rate D (μGy/yrs)	Plateau (°C)	Palaeodose (Gy)	TL Age (Years B.P.)
XAL096	1.34	2.16	0.07	1.5	735	340–370	4.08 ± 0.58	5600 ± 800
						(330–350	5.10 ± 1.20	6900 ± 1600)*
XAL097	0.81	1.44	0.07	3.0	540	300–350	0.83 ± 0.11	1500 ± 200
XAL098	0.48	1.27	0.07	2.0	440	350–370	0.69 ± 0.07	1600 ± 200
XAL099	0.48	1.36	0.05	3.0	426	320–350	2.01 ± 0.21	4700 ± 500
						(320–350	5.73 ± 0.44	13,400 ± 1000)*
XAL100	1.20	2.68	0.13	2.7	805	300–340	2.73 ± 0.25	3400 ± 300

*The palaeodose P = EDn-EDs, where EDs was derived from the XAL097 surface sample, the youngest surface sample in the location.

TABLE 2

Thermoluminescence results and analysis data for dunesand samples collected from Cape St. Lambert (University of Wollongong Laboratory)

Remark	Analysis temp. range (°C)	(Grays)(P_{UV})	K content (%)	Rb content (ppm)	Water (%)	Specific activity (Bg./kg)	Annual radiation (μGy/yrs)	TL age (TL_{UV}) (yrs B.P.)
W894	275-425	0.21	0.100	2.0	1.6	14.9	558	400 ± 200
W895	300-450	0.43	0.100	2.0	1.5	17.2	602	700 ± 250
W896	300-425	2.62	0.058	2.0	2.0	16.3	537	4900 ± 1350
W897	275-425	1.52	0.058	1.5	2.6	15.2	513	2950 ± 900
W898	325-400	0.34	0.050	1.5	1.8	9.7	395	850 ± 500
W899	350-400	0.24	0.050	1.5	2.4	11.1	419	550 ± 200
W900	300-425	1.7	0.108	2.0	2.5	38.1	1024	1650 ± 450

The palaeodose (P_S) is not shown as TL_S value for W896 is lower than TL_{UV} suggesting zeroing by fire.

are normally assumed to indicate absolute maximum possible TL ages as this degree of bleaching is unlikely to be attained due to solar exposure alone.

The University of Wollongong laboratory normally evaluates the sample palaeodose (P) by fitting the values of TL_n and TL_s (the mean TL levels measured from unbleached and surface residual samples respectively) to the TL growth curve, thus $P = P_n - P_s$. However the TL of some of the surface samples submitted to Wollongong were found to be lower than TL_{UV}. This suggests that some of the surface samples may have been subject to zeroing during grass fires in the year prior to collection. Under these circumstances, the surface samples were not used to calculate TL_S.

The possibility that some of the surface samples have been partially zeroed by fire brings into question the assumption that the TL of the sample was reset prior to burial only by insolation. Surface samples associated with samples W894, W895, W896 all had TL_{UV} levels higher than the TL level of the surface sample. The other surface samples did not appear to have been affected. The ratios of TL_{UV}/TL of the affected surface samples are 1.5536, 1.3352, and 1.7667 for samples W894, W895, and W896 respectively. It is impossible for this to occur unless the TL of these surface samples had been substantially lowered by fire. Fire is an annual phenomenon in the open forests of northern Australia and frequently occurs as a result of lightning strikes during the build-up to the wet season. Zeroing of the surface layer by fire will be most likely to occur on stable, vegetated surfaces as bare, mobile surfaces lack any fuel to support a fire. Thus it would be expected that the bulk of the sediment being incorporated into a deposit would not have experienced exposure to fire. Only when the fire tolerant northern Australian vegetation fails to recover from burning, perhaps due to the failure of the following wet season to produce rain, might this thin layer of 'fired' material become mobile and be incorporated into a deposit. Whilst the TL_{UV} ages are therefore still considered to provide maximum ages for the samples, this additional uncertainty in one of the major assumptions underlying the TL age determinations makes comparison with ^{14}C age determinations vital.

Cross-checking the TL ages with local ^{14}C is difficult in these freely drained deposits. The environment is not conducive to the preservation of organic material and none was found in the dunefield. The nearest, well-dated eolian sequence is at Miriwun, a rock shelter about 50 km south of Kununurra (Fig. 1). Here a period of apparently more arid conditions has resulted in a sequence of fine silty deposits. The lower unit contains charcoal which dates to 17,980 ± 1170 yrs B.P. (ANU 1008) (Dortch, 1977). This is separated by an erosional contact from a similar overlying deposit which dated to 2970 ± 120 yrs B.P. (SUA 142 corrected date; Barbetti pers. comm, 1984). Over this, and also separated by an erosional contact, is a more recent eolian deposit which dates to 1675 ± 185 yrs

B.P. (SUA 141). The most recent, surface, deposit is undated. This deposit provides a useful comparison and control on the dunefield chronostratigraphy.

Description of sample sites

The dunefield at Cape St. Lambert, although small, is very complex with several large, active, elongate parabolic dunes reworking older stabilised dunes. The oldest unit identified formed a sand plain which extended 2 km to the west of the elongate parabolic dunes (Unit D; Fig. 3). This unit showed some soil profile development with a shallow (60 cm) A horizon overlying a light reddish-brown (5YR 6/6) B horizon. Samples were collected from a depth of 1.5 m. The forward progress of the elongate parabolic dunes has exposed a number of fragmented palaeosol sections (Units A, B, C and D; Fig. 3). Two sections were sampled. The other major feature sampled was a steep, lightly grassed dune ridge which paralleled the shoreline to the north of Cape St. Lambert (Unit A; Fig. 3). All of the units identified were composed of fine to medium sand. The presence of large-scale cross-bedding, with foresets close to the angle of rest, indicate that all of the palaeosols had been formed in aeolian deposits.

Large fragments of pisolithic laterite rubble (Unit E; Fig. 3) on the shoreline indicate the erosion of older units which could not be identified during fieldwork.

Results

Samples collected from the sand plain (Unit D; Fig. 3) gave TL ages of 4900 ± 1350 yrs (W894,TL_{UV}) and 5600 ± 800 yrs (XAL096).

Samples from palaeosols exposed in section by the movement of the largest of the elongate parabolic dunes gave[a] TL ages of 4700 ± 500 yrs (XAL099) from the oldest unit identified (Unit D), 2950 ± 900 yrs (W897,TL_{UV}) and 3400 ± 300 yrs (XAL100) from a mottled light yellow–orange unit (Unit C), and 1650 ± 450 yrs (W900, TL_{UV}) and 550 ± 200 yrs (W899, TL_{UV}) respectively from the two youngest units (Units B and A). The latter are of undifferentiated dull orange fine to medium sand.

Samples from two units exposed in the active elongate parabolic dune to the north of the largest dune gave similar ages. These are also of undifferentiated pale yellow fine sand and gave TL ages of 1500 ± 200 yrs (XAL097) and 1600 ± 200 yrs (XAL098) for the lower unit (Unit B), and 850 ± 500 yrs (W898, TL_{UV}) for the upper unit (Unit A).

Samples from the steep, lightly grassed dune ridge which parallels the shoreline to the north of Cape St. Lambert gave ages of 400 ± 200 yrs (W894, TL_{UV}) and 700 ± 250 yrs (W895, TL_{UV}).

The TL characteristics of samples W898, W899 and W900 indicate that they have impurity level ratios (see Table 2) that are different from those of the remaining samples submitted to the Wollongong laboratory. This may suggest a different sediment source or sample history. Similar differences can be seen between some of the Xian samples in Table 1.

The dates of the two late Holocene units at Miriwun [2970 ± 120 yrs B.P. and 1675 ± 185 yrs B.P.] are very close to the TL ages derived for chronostratigraphic units B [2950 ± 900 yrs (W897) and 3400 ± 300 yrs XAL100)] and C [1500 ± 200 yrs (XAL097), 1600 ± 200 yrs (XAL098) and 1650 ± 450 yrs (W900)] at Cape St. Lambert (Fig. 3). The grouping of the TL ages for these units, the similarity of the ^{14}C dates from Miriwun, and the close correspondence between the results from the two TL laboratories, all give some confidence that the age of these units have been assessed correctly. The youngest chronostratigraphic unit, which has four TL ages indicating emplacement during the last 1000 years, has no soil profile development and the TL ages appear reasonable. This unit may correspond to the upper, undated, unit at Miriwun.

There is no correspondence between the oldest chronostratigraphic units at Miriwun and Cape St. Lambert. This is because the two sites are not directly comparable. Miriwun is remote from coastal influences and is an accumulation of silty, loess-like sediment. The lower unit here corresponds to the period of widespread dune activity associated with the last glacial maximum already

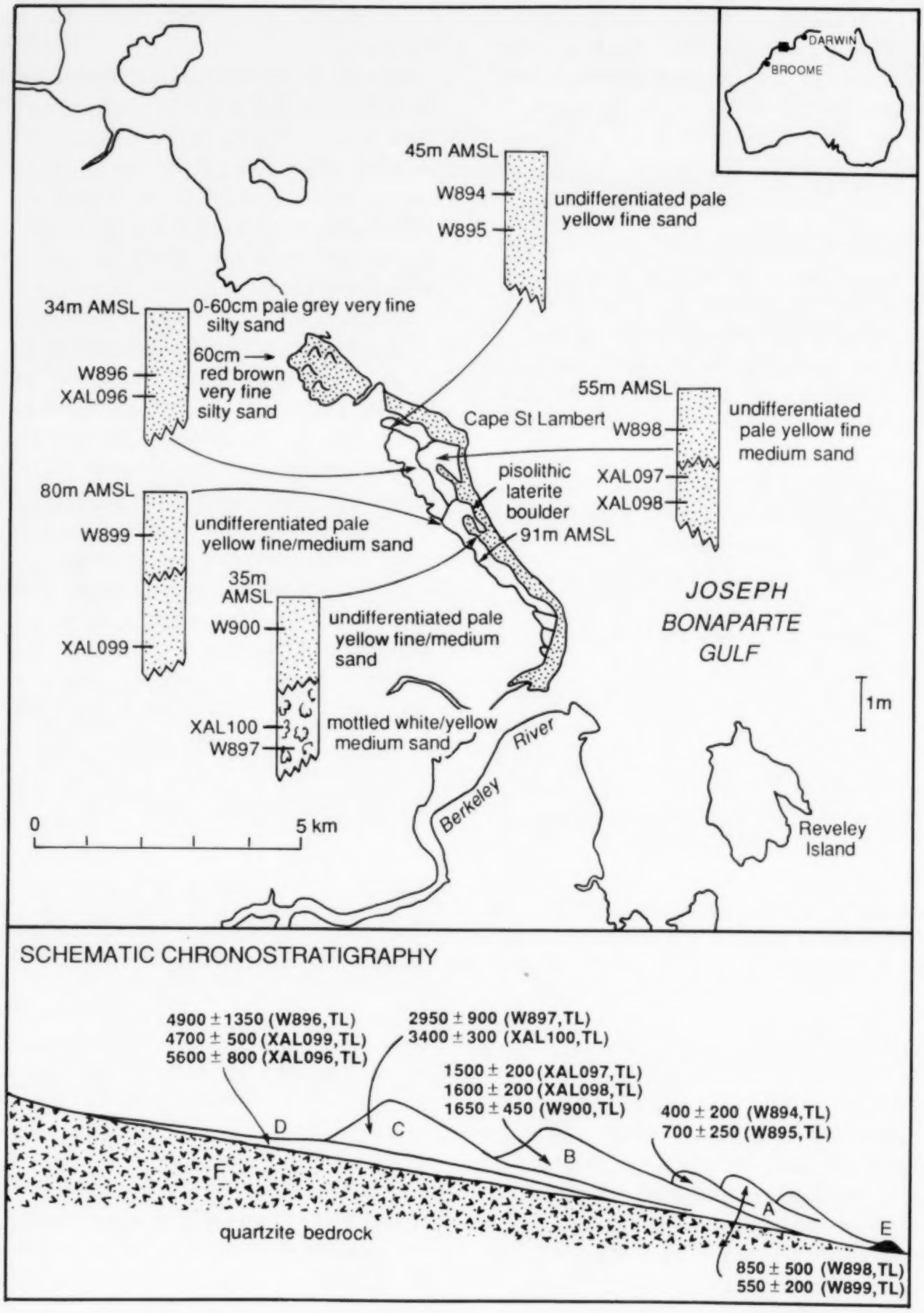

Fig. 3. Map showing sample location, core diagrams, and schematic stratigraphy of the Cape St. Lambert sites. Units *A* to *D* are dunesand units, unit *E* represents the pisolitic laterite rubble which remains following the reworking of older units.

identified in other northern Australian dunefields (Lees et al., 1990). The colour and TL characteristics of the sediments forming the oldest of the units identified at Cape St. Lambert, the mid-Holocene unit, suggest that it may have been reworked from an older palaeosol. These differ from the sediments which comprise the most recent units which are clearly derived from the mouth of the Berkeley River. The TL characteristics of this material are distinctly different to that of the older unit, and those units derived from the reworking of this older unit.

The TL ages for the mid-Holocene unit (Unit D) [4900 ± 1350 yrs (W896), 4700 ± 500 yrs (XAL099) and 5600 ± 800 yrs (XAL096)] are compatible with emplacement following reworking of older, offshore deposits by rising sea level. Sea level reached its present level about 5500 yrs B.P. in the South Alligator area, the closest site at which it has been assessed (Woodroffe et al., 1987). This conclusion is reinforced by the presence of a small amount of pisolitic laterite rubble on the shoreline near Cape St. Lambert which supports the inference that older deposits were present and have been completely reworked by rising sea level. The absence of a comparable mid-Holocene unit in the deposit at Miriwun, which is remote from coastal influences, adds some weight to this interpretation. Work in progress on the dunefields at Cape Arnhem and on Groote Eylandt is returning similar results.

Discussion

The dunes at Cape St. Lambert fall into two groups, those which have resulted from the reworking of offshore deposits by rising sea level, and those which have their origins in the deflation and alongshore transport of the river mouth sediments from the Berkeley River. The former source may be reworked fluvial and fluvio-deltaic sediments of the Berkeley, Ord and Victoria Rivers (Lees, 1992a). These would have been exposed on the shelf during the last glacial and subjected to deflation, which produced dunes and, at a distance, loess deposits like that found at Miriwun.

Earlier work in the coastal dunefields of the eastern part of northern Australia (Lees et al., 1990) identified a phase of dune emplacement during the late Holocene (ca. 2700–1800 yrs B.P.) and an early Holocene phase of dune emplacement (ca. 8600–7500 yrs B.P.) in two out of the three dune fields, and a late Pleistocene episode (ca. 24 000–17 000 yrs B.P.) in both the Cape York dune fields. The late Holocene event falls into the 2800–1600 yrs B.P. period suggested by Lees and Clements (1987) as being a time of reduced wet season precipitation across northern Australia. The early Holocene event was identified as being the Cooper–Thom event of Pye (1984), a period of dune instability initiated by shoreline erosion associated with rising sea level. The data from the Kimberley region follows this general pattern, but there are some significant differences.

The lowest unit at Miriwun confirms that a late Pleistocene episode of deflation, dating to the last glacial maximum, occurred in the Kimberley region. At Cape St. Lambert, rising sea level has apparently completely reworked this, and possibly older, units.

The stabilisation of the mid-Holocene unit at Cape St. Lambert closely matches the time of stabilisation of sea level in northern Australia. Coupled with the absence of this unit from the Miriwun sequence, a site remote from coastal influence, the evidence suggests that this represents the end of a period of dune instability initiated by shoreline erosion associated with rising sea level. This further supports the Cooper-Thom hypothesis expounded by Pye (1984).

The two late Holocene units at Cape St. Lambert, which date to c. 3000 yrs B.P. and 1600 yrs B.P. are quite distinct. The close correspondence of age assessment both between the two TL laboratories and the ^{14}C from Miriwun gives some confidence that the age of the units has been assessed correctly. Ages from the currently active dunes suggest that these have been initiated within the last thousand years. These are quite distinct from the underlying (c. 1600 yrs B.P.) unit and also appear to represent distinct, but temporally close, events. This indicates that the single late Holocene period of widespread regional change in climatic conditions identified by Lees and Clements (1987), between 2800 and 1600 yrs B.P., may in fact

encompass a number of distinct, but temporally close, climatic events.

Detailed re-examination of a chenier sequence on the Victoria Delta (Lees, 1992b), on the southern shoreline of Joseph Bonaparte Gulf, showed that five chenier ridges formed rapidly over a thousand year period from about 2020 yrs B.P.* to about 1210 yrs B.P.*. These are separated by about 700 m of tidal mud flat from the most recent chenier ridge, for which no good age is available. This appears to have formed within the last thousand years. There are no older cheniers present. Although cheniers can be an ambiguous indicator of environmental change, the most probable cause of this change in the mode of shoreline progradation, on the evidence currently available, was decreased fluvial input due to climatic changes in the Victoria catchment. While there is no chenier ridge to match the c. 3000 yrs B.P. eolian event, the marked break between the five dated ridges and the most recent ridge clearly support the interpretation that the dune emplacements c. 1600 yrs B.P. and c. 700 yrs B.P. represent separate climatic events, probably periods of reduced rainfall. While the lack of older ridges (c. 3000 yrs B.P.) might suggest that this was either a less severe, or less prolonged, period of reduced rainfall, it is important to note that where chenier building and dune transgression (Units A and B) took place at the same time in a region (and the other causes of chenier formation can be excluded), it is reasonable to infer that reduced rainfall was the cause. However, if episodic dune transgression took place at a time when mud was being deposited on the shoreface (Unit C), then a period of increased windiness must also be considered as a possibility.

Conclusion

The single, discrete, period of changed environmental conditions (2800–1600 yrs B.P.) hypothesised by Lees and Clements (1987) is not supported by the evidence presented here. The data, when considered in conjunction with the chronostratigraphy of other depositional environments in the area (Lees, 1992b), clearly suggest that a period of increased climatic variability, from 3000 yrs B.P. to the present, is responsible for most of the late Holocene units identified at Cape St. Lambert. During this time three dune initiation and stabilisation events took place. The synchroneity of the two late Holocene dune transgressions with the progradation of fine sandy cheniers, and the apparent stability of the dunefield during the period when mud flat progradation took place, indicate very strongly that these are probably short periods of decreased wet season rainfall, the timing and duration of which are difficult to resolve more precisely using the methods shown here. The initial assumption that this site might be more sensitive to climatic variation than the more easterly dunefields appears to have been well founded.

Acknowledgements

Samples were collected with the assistance of the crew of the Oceanic Research Foundation research vessel, *Thistlethwaite*. We would like to thank Don Richards, Captain Peter Gill and his crew, and Ian Brokenshire, David Lake, Kris Pedler, Ron Sim, and Jim Spears for their considerable help. Financial support for this work came from the Australian Research Council and the Australian National University Faculties Research Fund. Diagrams were drawn by Val Lyon.

References

Aitken, M.J., 1985. Thermoluminescence Dating. Academic Press, London, 359 pp.

Coaldrake, J.E., 1962. The coastal dunes of southern Queensland. Proc. Roy. Soc. Queensl., 72: 101-116.

Cooper, W.S., 1958. Coastal sand dunes of Oregon and Washington. Mem. Geol. Soc. Am., 72.

Dortch, C.E., 1977. Ancient grooved stone axes from analluvial terrace on Stonewall Creek, Kimberley, Western Australia. J. R. Soc. West. Aust., 60: 23-30.

Galloway, R.W., Storey, R., Cooper, R., and Yapp, G.A., 1980. Coastal Lands of Australia. CSIRO Aust. Div. Land Use Res. Tech. Memo., 80(24).

Lees, B.G., 1992a. Recent terrigenous sedimentation in Joseph Bonaparte Gulf, north western Australia. Mar. Geol., 103: 199–213.

Lees, B.G., 1992b. The development of a chenier sequence on the Victoria Delta, Joseph Bonaparte Gulf, northern Australia. Mar. Geol. 103: 215–224.

Lees, B.G. and Clements A.M., 1987. Climatic implications of chenier dates in northern Australia. Radiocarbon, 29(3): 311–317.

Lees, B.G., Lu Yanchou and Head, J., 1990. Reconnaissance thermoluminescence dating of northern Australian coastal dune systems. Quat. Res, 34: 169–185.

Lu Yanchou, Mortlock, A.J., Price, D.M. and Readhead, M.L., 1987. Thermoluminescence dating of coarse grain quartz loess from the Malan Loess at Zhaitang section, China. Quat. Res. 28: 356–363.

Nanson, G.C., Price, D.M., Short, S.A., Young, R.W. and Jones, B.G., 1991. Comparative uranium–thorium and thermoluminescence dating of weathered Quaternary alluvium in the tropics of northern Australia. Quat. Res, 35: 347–366.

Pye, K., 1984. Models of transgressive coastal dune building episodes and their relationship to Quaternary sea level changes: a discussion with reference from eastern Australia. In: M. Clark (Editor), Coastal Research: U.K. Perspectives. Geobooks, Norwich. pp. 81–104.

Thom, B.G., 1978. Coastal sand deposition in southeast Australia during the Holocene. In: J.L. Davies and M.A.J. Williams (Editors), Landform Evolution In Australasia. Australian National University Press, Canberra, pp. 197–214.

Woodroffe, C.D., Thom, B.G., Chappell, J., Wallensky, E., Grindrod, J. and Head, J., 1987. Relative sea level in the South Alligator River region, north Australia, during the Holocene. Search, 18: 198–200.

Marine Geology, 106 (1992) 141–148
Elsevier Science Publishers B.V., Amsterdam

Stable isotopic composition of carbonate-cemented recent beachrock along the Mediterranean and the Red Sea coasts of Egypt

H. Holail and M. Rashed

Geology Department, Alexandria University, Alexandria, Egypt

(Received February 19, 1991; revision accepted November 12, 1991)

ABSTRACT

Holail, H. and Rashed, M., 1992. Stable isotopic composition of carbonate-cemented beachrock along the Mediterranean and the Red Sea coasts of Egypt. *Mar. Geol.*, 106: 141–148.

Recent beachrocks on the Mediterranean and the Red Sea coasts of Egypt have been studied. In the Mediterranean beachrock skeletal particles (mainly molluscan fragments) are the most abundant grain type comprising approximately 60% of the framework grains; intraclasts make up the remaining 40%. In contrast, the Red Sea beachrocks are dominantly composed of igneous and metamorphic crystalline basement rock fragments that range in dimension from large boulders in proximal parts of the fan to gravels, sands and silts in the distal parts.

High energy conditions as well as the presence of relatively coarse, high porous and permeable sediments ensure that adequate volumes of supersaturated water are able to move through the pore system to accomplish the cementation process. Textural study (light and SEM microscope) on samples from both localities reveals that high-Mg calcite cements occur as thick to thin bladed isopachous crusts, which sometimes occlude all pore spaces. Aragonite cements are also present as thin circumgranular acicular crusts. However, some samples along the Red Sea coast contain high-Mg calcite displaying scalenohedral crystal forms.

The isotopic composition of these beachrock cements generally show high values of $\delta^{18}O$ and $\delta^{13}C$. In the Mediterranean beachrock cements the $\delta^{18}O$ and $\delta^{13}C$ values range from -0.4 to $+1.2$ and from $+1.0$ to $+2.1$‰ PDB, respectively, whereas the $\delta^{18}O$ and $\delta^{13}C$ values of Red Sea beachrock cements range from -0.1 to $+1.2$ and from $+2.1$ to $+4.5$‰ PDB, respectively.

The oxygen and carbon isotopes, together with the texture and mineralogical composition of these cements, are good indicators of the conditions of primary cementation and reflect the gross of stable isotopic and chemical composition of marine water.

Introduction

Numerous studies have demonstrated that cementation is a slow process (Bathurst, 1975; Lighty, 1985; Pierson and Shinn, 1985; Moore, 1985; Saller, 1986). Beachrocks exceptionally undergo rapid cementation (lithification) in tens of years (Land, 1970; Friedman and Gavish, 1971; Alexandersson, 1972; Krumbein, 1979; Meyers, 1987; El-Sayed, 1988; Amieux et al., 1989; Schillings and Richter, 1989; Strasser et al., 1989; Guo and Friedman, 1990). Such fast rates of cementation may depend on high levels of supersaturation for $CaCO_3$ and may accompany one of the following mechanisms: (1) direct precipitation from seawater, (2) mixing of seawater with freshwater (Schmalz, 1971; Moore, 1973), (3) evaporation of ground water in arid climates (Ginsburg, 1953; Russell, 1962), and (4) degassing of CO_2 (Hanor, 1978).

In general, beachrocks occur in the tropical and sub-tropical beaches as a layer of cemented beach sediments and occupy a position within intertidal and low supratidal zones. Cement typically consists of aragonite, high-Mg calcite, or a mixture of the

Correspondence to: H. Holail, University of Qatar, Faculty of Science, Department of Geology, P.O. Box 2713, Doha, Qatar.

0025-3227/92/$05.00

two (Stoddart and Cann, 1965). Alexandersson (1972) has noted that the cement of the Mediterranean beachrocks represents a major occurrence of Mg-calcite, whereas the precipitation of aragonite is a subordinate process.

This study documents the mineralogical composition and evolution of the beackrock cements along the Mediterranean and Red Sea coasts of Egypt. Sampling of the cements for isotopic analysis will aid in quantifying the evolution of fluid chemistry through cementation process. Significantly, this study attempts geochemical documentation of marine cementation. Comparison of features observed in both localities may shed light on the temporal relationships and genetic processes of beachrock cementation on regional scale.

Analytical procedures

Two outcrops of beachrocks along the Mediterranean and Red Sea coasts were studied and sampled along the coasts (Fig.1). Twenty specimens were taken from each locality to study and compare the macroscopic textures and the microfabrics of beachrock cements at the two localities. The fabric analysis was performed on polished thin sections utilizing a petrographic microscope and on fractured chips using a Scanning Electron Microscope (SEM). Standard staining techniques (Dickson, 1966) and X-ray diffraction were used to study carbonate cement mineralogy. Calcite crystal lattice d-spacings were corrected using quartz as an internal standard.

Preliminary examination of the carbon-oxygen isotopic composition of beachrock cements were concentrated on a suite of 30 samples from the two study localities. A microscope-mounted drill assembly was employed to extract 0.2 to 0.5 mg of powdered carbonate cement from polished slabs. Pure aragonite and/or high-Mg calcite cements were impossible to obtain and the analysed cements are a mixture of the two, where the high-Mg calcite cement is more dominant. The powder samples were roasted under vacuum for 1 h at 100°C not at 380°C. This is to eliminate any possibilities of aragonite inversion to calcite. Samples were subsequently reacted with anhydrous phosphoric acid at 50°C in a reaction/extraction line coupled directly to the inlet of a VG Micromass 602D ratio mass spectrometer. All analyses were converted to PDB and corrected for ^{17}O as described by Craig (1957). Measured precision is 0.07 for $\delta^{18}O$ and 0.06 for $\delta^{13}C$.

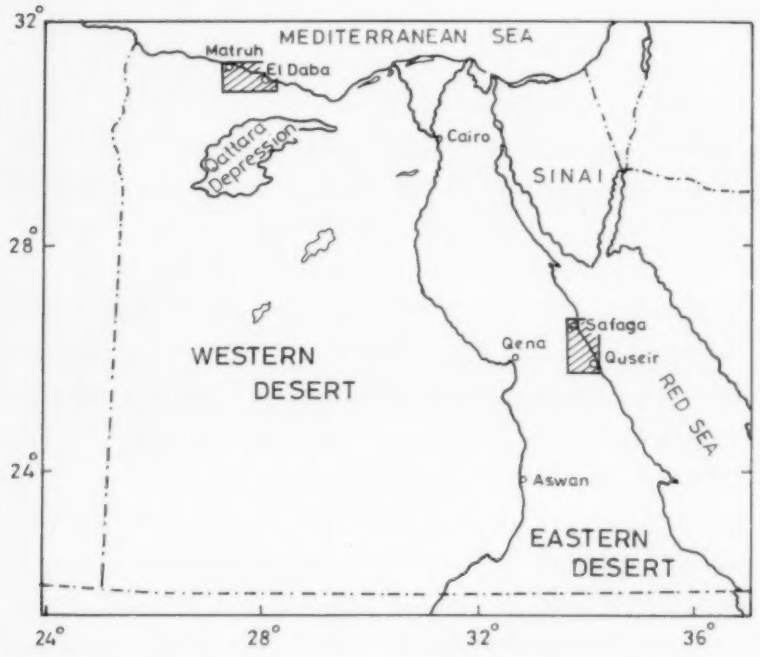

Fig.1. Map of Egypt showing locations of study sites.

General geological setting

Beachrocks are exposed in a narrow intertidal zone along the Mediterranean and the Red Sea coasts of Egypt. Along the Red Sea coastline a consideable volume of terrigenous sediments, which are mainly composed of igneous and metamorphic rocks, is supplied to the intertidal zone from the adjacent uplifted land areas (Precambrian Arabo Nubian massifs). The uppermost intertidal zone is covered with boulders and gravel cemented into beachrocks. Meanwhile, the intertidal flats consist of well-sorted sands, and the beachrocks are highly developed.

The studied Mediterranean beachrocks are similar to those studied along the Mediterranean coast of Israel (Magaritz et al., 1979). The skeletal particles are the most abundant grain type (mainly aragonitic molluscan fragments). Moreover, streams draining through sedimentary terrains exclusively carry sediments derived from Miocene–Pliocene rocks into the Mediterranean intertidal zone. The Mediterranean coast is bordered by

limestone cliffs, eroded by the sea and wind. Beachrocks are onlapping the base of these cliffs. Traces of erosion are visible along the coast, showing the effects of the wave attacks on the coastline. The most obvious sedimentary structures in the Mediterranean and Red Sea beachrocks are gentle, large seaward dipping slabs in the foreshore zone.

The occurrence of beachrocks at sea level over large parts of the Mediterranean and Red Sea coasts suggests that cementation is currently active. Moreover, fragments of pottery and glass artifacts were found cemented into these beachrocks. Therefore, the maximum age for cementation under such circumstances can be no more than a few hundred years.

The climate for much of the Mediterranean and Red Sea coasts of Egypt has been consistently described as substantially semi-arid to arid, with rainfall ranging from 150–200 mm/yr to 10–70 mm/yr along the Mediterranean and the Red Sea coasts, respectively. The salinity of the Mediterranean surface waters varies between 39 and 39.4‰, where the salinity of the Red Sea surface water is ranging from 40 to 42.5‰.

Results and discussion

Petrography

Studies of modern occurrences of beachrock from other localities demonstrate that the usual cement in such rocks is formed as a result of direct precipitation of high-Mg calcite and/or aragonite from solution within the beachrock. Cementation occurs in two stages: an initial cryptocrystalline high-Mg calcite rim first coats the grains, followed by growth of fibrous carbonate (generally high-Mg calcite or aragonite) commonly as isopachous coatings around the framework grains (Friedman, 1968, 1975; Alexandersson, 1969; Gavish and Friedman, 1969; Moore, 1971; Meyer, 1987). The presence of such cementing agents in most beachrocks suggests that the cement was formed in contact with seawater (Folk, 1974), where in fresh water the low concentration of Mg ions favours formation of low-Mg calcite cement.

In this study the development of an initial stage of high-Mg cryptocrystalline calcite rims around framework grains is most extensive in the Red Sea beachrock (Fig.2A). These cryptocrystalline calcite rims are relatively thick with dark color and consist of equidimensional crystals of high-Mg calcite. A similar cryptocrystalline calcite rim has been termed micritic rim (e.g. Alexandersson, 1972; Moore, 1973; Land and Moore, 1980). Alexandersson (1972) has noted that the dark colors of such rims are associated with the cryptocrystalline form of cement. In some Red Sea beachrocks, double cryptocrystalline rims of high-Mg calcite suggest two stages of algal activity. In contrast, the cryptocrystalline calcite rims of the Mediterranean beachrock are less abundant, less developed and occur as thin irregular layers coating the allochem grains (Fig.3A).

The most common cement in the studied beachrocks consists of fringes of high-Mg calcite (Figs.2B,C and 3). The high-Mg calcite crystals commonly form isopachous rims around the grains and the cryptocrystalline rims. X-ray diffraction analyses of this cement show a main phase of calcite with a d $10\bar{1}4$ spacing of about 2.99 Å, which corresponds to a variable amount of substitution of Mg for Ca in the calcite lattice. In the Red Sea beachrock, the isopachous rims are characterized by slightly coarser and more elongated crystals with faces showing pitting (Fig.2B). Moreover, this cement is more abundant and thicker than in the Mediterranean beachrock. James et al. (1976) attributed the formation of fringes surrounding cryptocrystalline calcite rims to progressive and more complete cementation in older sediments. In some samples of the Red Sea beachrock, the high-Mg calcite cement displays a scalenohedral crystal form which occurs together with a aragonite lath cements (Fig.2D).

The least common cements in the studied beachrocks consist of aragonite needles and lathes (Figs.2 and 3). In the Red Sea beachrock, aragonite crystals are elongate and display broader lath-like shapes (Fig.2D), whereas in the Mediterranean beachrock, aragonite crystals are relatively less abundant, small and display needle shapes (Fig.3D).

The complex interrelationship and irregular distribution of the various types of cement indicate a large variety of parameters controlling beachrock

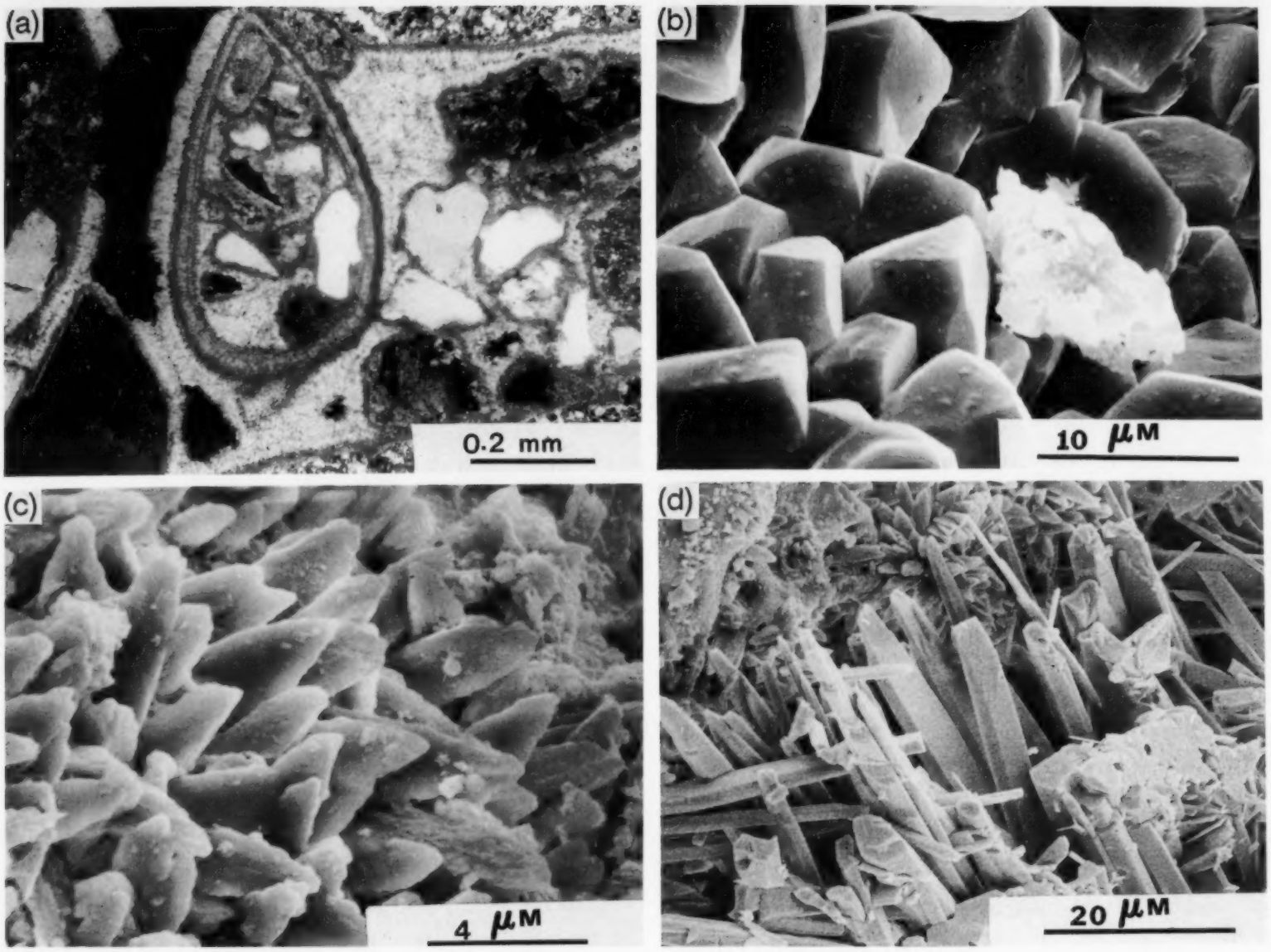

Fig.2. Photomicrograph and SEM micrographs of Red Sea beachrock samples. (A) Photomicrograph of high-Mg calcite isopachous fringe cements and cryptocrystalline calcite rims; note how regular these cements development are compared to Fig.3A. (B) SEM micrograph of fringe cements, note that surfaces show pitting. (C) SEM micrograph of scalenohedral crystals of high-Mg calcite. (D) SEM micrograph of lath-shaped aragonite crystals as marine cement; note that aragonite fabric is an open structure.

cementation. The growth of aragonite crystals in the studied beachrocks might be related to seawater supersaturation and enhancement of conditions for precipitation by temperature, evaporation, and perhaps by fluctuation of pH and pCO_2 due to photosynthesis by algae living in and on beach grains. Therefore, it appears that the abundance of aragonite cements in the Red Sea beachrock might be more related to the prevalence of the previous conditions during the cementation process. Moreover, salinity might have played a role in this case. Zhong and Mucci (1989) indicated that salinity variations alone do not have a significant effect on both the precipitation rates and overgrowth composition of calcite and aragonite under constant saturation conditions.

Petrographic investigations do not show evidence of the influence of meteoric water on the precipitation of the beachrock cement and, therefore, in this study the hypothesis of meteoric–seawater mixing has not been invoked to explain the cementation process of the Mediterranean and Red Sea beachrocks.

Stable oxygen and carbon isotopes

The $\delta^{18}O$ values of the Mediterranean beachrock cements range from -0.4 to $+1.2$‰ PDB with a

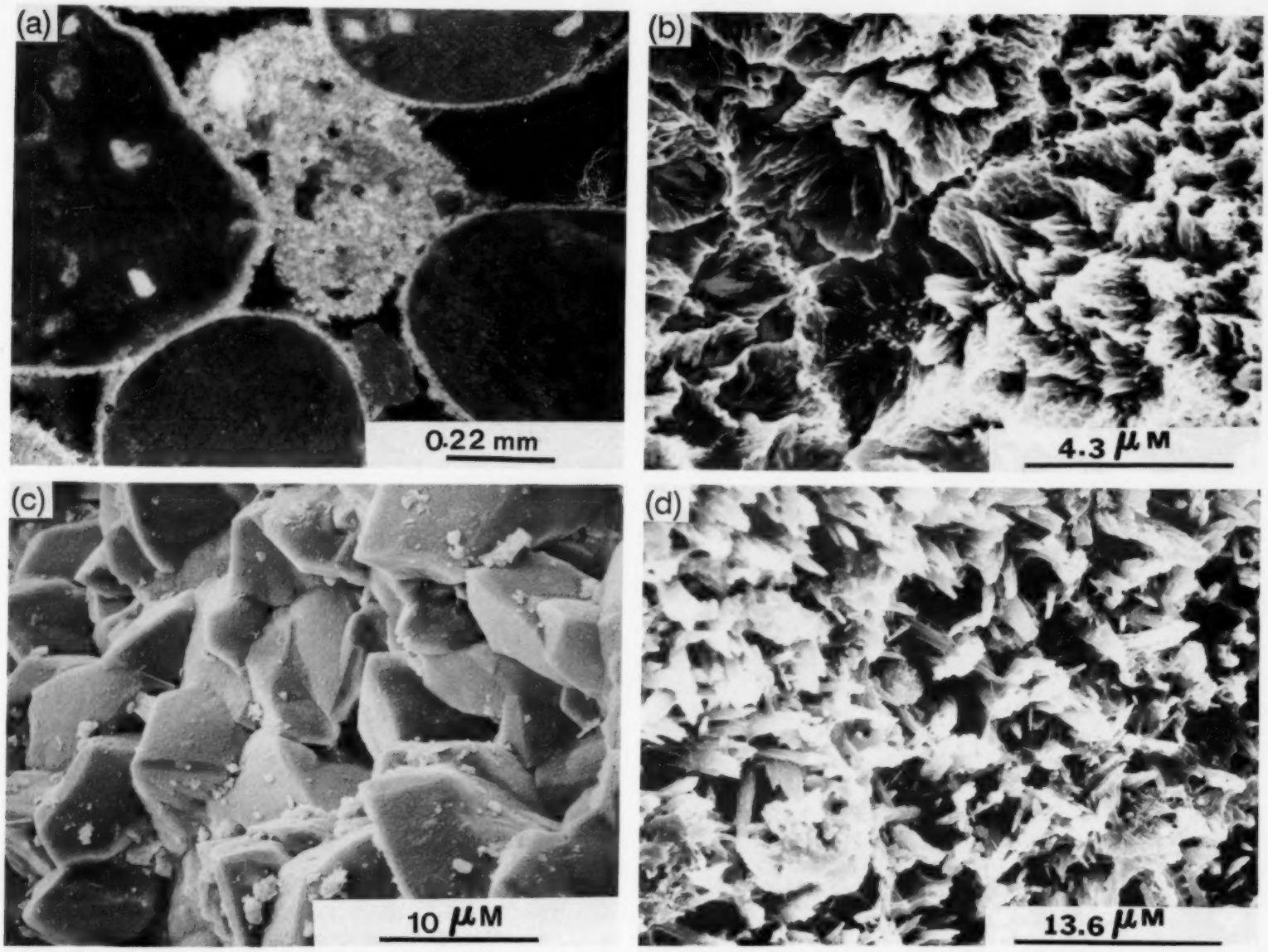

Fig.3. Photomicrograph and SEM micrographs of Mediterranean beachrock samples. (A) Photomicrograph of isopachous fringes of high-Mg calcite cement surrounding framework grains, note that cryptocrystalline calcite rims are poorly developed. (B) and (C) SEM micrographs of high-Mg calcite as cryptocrystalline and isopachous rims, note the rhomb terminations of fringe calcite crystals. (D) SEM micrograph of aragonite needles as marine cement.

mean of +0.5‰ PDB, whereas the $\delta^{18}O$ values of the Red Sea beachrock cements range from −0.1 to +1.2‰ PDB with a mean of +0.5‰ PDB (Fig.4). Therefore, it appears that the mean values of oxygen isotopic composition are identical for the cements of both localities.

The small oxygen isotopic heterogeneity within the cement of each locality suggests the absence of a progressive shift in temperature or composition of precipitation waters during cement growth, and might indicate that oxygen isotopic composition of waters and temperature remained relatively constant during cement precipitation. Moreover, the oxygen isotopic values of the beachrock cements in this study are within the range of values considered typical for carbonate cement formed in equilibrium with present-day seawater (Milliman, 1974).

The mean $\delta^{13}C$ values of beachrock cements from both localities represent an isotopically heavy composition which is explained most easily by precipitation from seawater. These values for the Mediterranean beachrock cements range from +1.0 to +2.1‰ PDB with a mean of +1.6‰ PDB, whereas the $\delta^{13}C$ values of the Red Sea beachrock cements range from +2.1 to +4.5‰ PDB with a mean of +3.3‰ PDB. Therefore, the carbon isotopic compositions are most enriched in ^{13}C in the Red Sea beachrock cements relative to the Mediterranean beachrock cements. Friedman

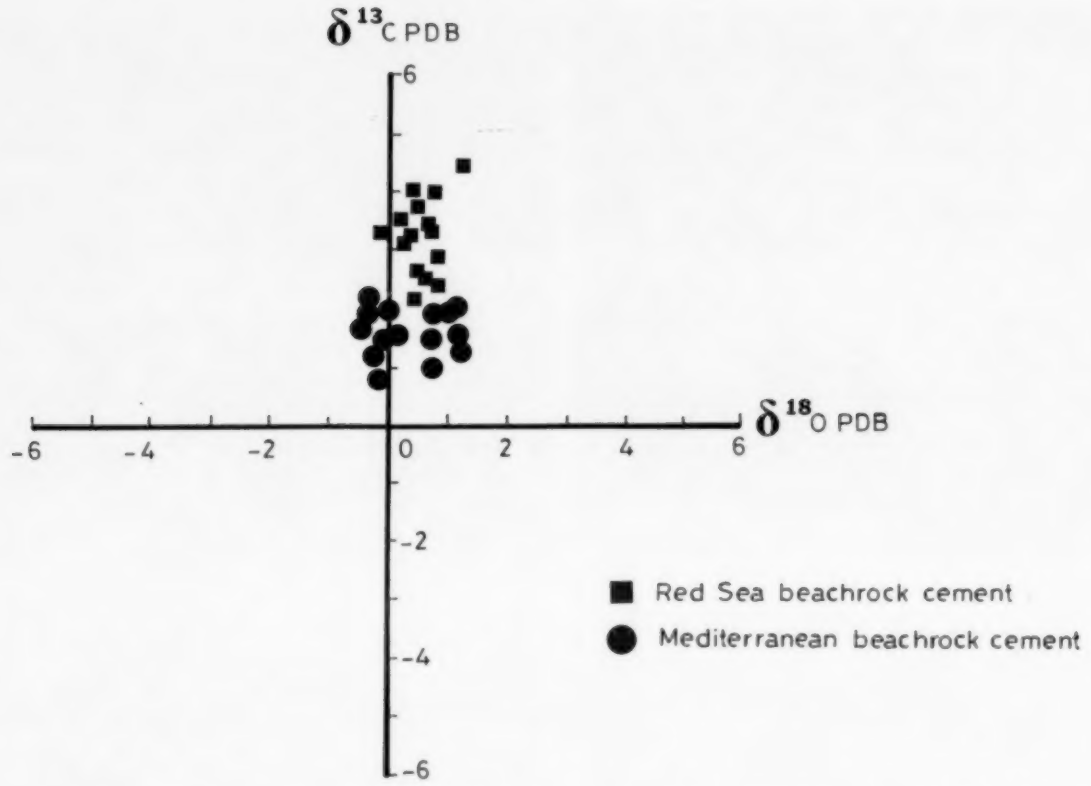

Fig.4. Stable carbon and oxygen isotope compositions of Mediterranean and Red Sea beachrock carbonate cements.

(1991) reported that methane is involved in Holocene beachrock formation along the Egyptian shores of the Mediterranean; $\delta^{13}C_{PDB}$ reaches level of $-39.3‰$ for dolostone samples.

In the previous section, it has been shown that concentration of 100% high-Mg calcite and/or aragonite cements was impossible to obtain. Therefore, the analysed cements in this study are a mixture, where high-Mg calcite cements are more dominant. Due to this fact, it is difficult to estimate the relative enrichment of $\delta^{18}O$ values which might be related to fractionation of oxygen during the precipitation of the aragonite cement.

Comparisons between the isotopic compositions of the cements in the present study and the isotopic compositions of modern marine carbonate and modern beachrock cements in other localities are important for understanding the diagenetic system resulting from early marine lithification (Fig.5). The precipitation of submarine cements of high-Mg calcite and aragonite minerals in present-day, warm shallow seawater is marked by relatively heavy $\delta^{18}O$ and $\delta^{13}C$ $+3‰$ and $+3.5\pm1.5‰$ PDB, respectively (Milliman, 1974; Hudson, 1977; James and Choquette, 1984). The isotopic compositions of the beachrock cements analysed in this study are within the range of present-day marine cements values (Fig.5). In the same scenario, stable oxygen and carbon isotopic compositions of the beachrock cements in this study are similar to other modern beachrock cements from other localities, including high-Mg calcite and aragonite cements from Enewetak and Bikini (Margaritz et al., 1979; Gonzalez and Lohmann, 1985; Beier, 1985).

Finally, beachrock cements in the present study have a $\delta^{18}O$ values similar to the predicted and modern marine calcite cement values. The oxygen isotopic composition of these cements formed under equilibrium conditions is a function of the oxygen isotopic composition and temperature of the water from which it precipitated. It is therefore reasonable to conclude that the beachrock cements are in oxygen isotopic equilibrium with essentially seawater. Moreover, the carbon isotopic composition is also similar to carbon isotopic composition of calcite cement formed in marine diagenetic environments in other semiarid to arid recent settings. This interpretation is also compatible with the conclusion that high-Mg calcite and aragonite beachrock cements indicate precipitation strictly from seawater.

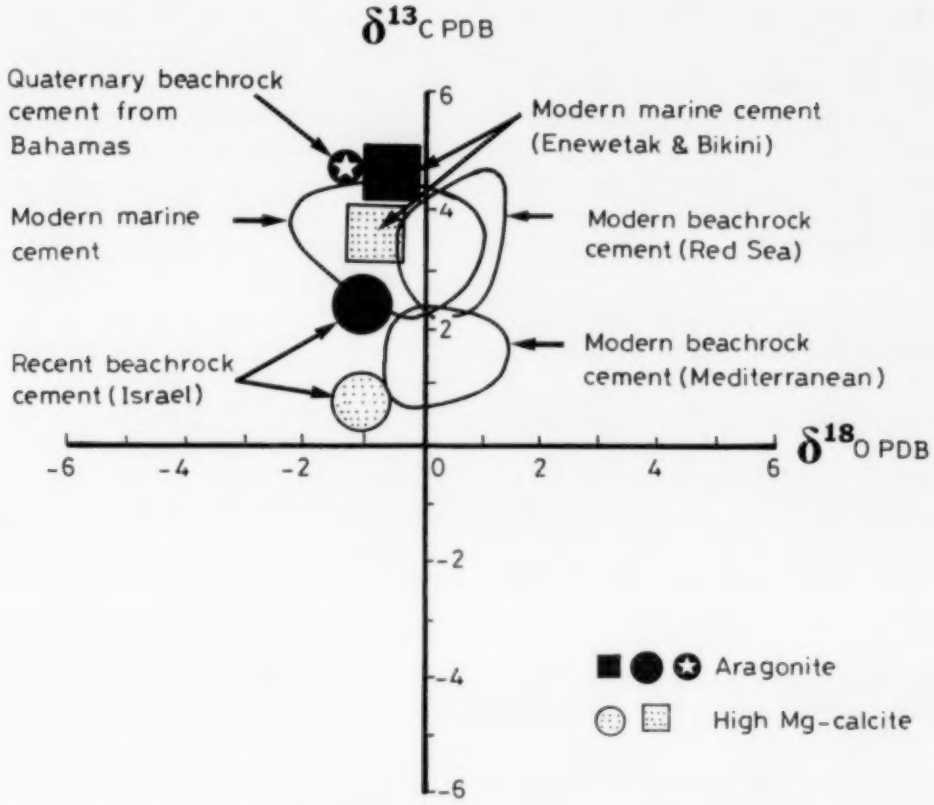

Fig.5. Stable carbon and oxygen isotope compositions of groups of beachrock carbonate cements and modern marine cement. Field of modern marine cements is from Hudson (1977). Values of high-Mg calcite and aragonite cements from Enewetak and Bikini are from Gonzalez and Lohmann (1985). Values of high-Mg calcite and aragonite from Israel from Margaritz et al. (1979). Values of aragonite cement of Quaternary Bahamian beachrock from Beier (1985).

Conclusions

(1) The cement of the Mediterranean and Red Sea beachrocks represents a major occurrence of marine-precipitated high-Mg calcite and aragonite.

(2) The cement samples (mixture of high-Mg calcite and aragonite) from the Mediterranean and Red Sea beachrocks show no trend with respect to oxygen isotope and a relatively enriched trend with respect to carbon isotope toward the Red Sea beachrock cements.

(3) Oxygen and carbon isotopic values, together with the mineralogical composition of the beachrock cements, are good indicators of precipitation strictly from seawater.

References

Alexandersson, T.E., 1969. Recent littoral and sublittoral high magnesium calcite lithification in the Mediterranean. Sedimentology, 12: 47–61.

Alexandersson, T.E., 1972. Mediterranean beachrock cementation: Marine precipitation of Mg-calcite. In: D.J. Stanley (Editor), The Mediterranean Sea. Dowden, Hutchinson and Ross, Stroudsburg, pp. 203–223.

Amieux, P., Bernier, P., Dalongeville, R. and Medwecki, V., 1989. Cathodoluminescence of carbonate-cemented Holocene beachrock from the Togo coastline (West Africa): an approach to early diagenesis. Sediment. Geol., 65: 261–272.

Bathurst, R.G., 1975. Carbonate sediments and their diagenesis. (Developments in Sedimentology, 12.) Elsevier, Amsterdam, 658 pp.

Beier, J.A., 1985. Diagenesis of Quaternary Bahamian beachrock: petrographic and isotopic evidence. J. Sediment. Petrol., 55: 755–761.

Craig, H., 1957. Isotopic standards for carbon and oxygen and correction factors for mass spectrometric analyses of carbon dioxide. Geochim. Cosmochim. Acta, 12: 133–149.

Dickson, J.A., 1966. Carbonate identification and genesis as revealed by staining. J. Sediment. Petrol., 36: 491–505.

El-Sayed, M.Kh., 1988. Beachrock cementation in Alexandria, Egypt. Mar. Geol., 80: 29–35.

Folk, R.L., 1974. The natural history of crystalline calcium carbonate: Effect of magnesium content and salinity. J. Sediment. Petrol., 44: 40–53.

Friedman, G.M., 1968. The fabric of carbonate cement and matrix and its dependence on the salinity of water. In: G. Muller and G.M. Friedman (Editors), Recent Development of Carbonate Sedimentology in Central Europe. Springer, New York, pp.21-32.

Friedman, G.M., 1975. The making and unmaking of lime-

stones ore the downs and ups of porosity. J. Sediment. Petrol., 45: 379–398.

Friedman, G.M., 1991. Methane-generated lithified dolomite rock (dolostone) of Holocene age: Eastern Mediterranean. J. Sediment. Petrol., 61: 188–194.

Friedman, G.M. and Gavish, E., 1971. Mediterranean and Red Sea (Gulf of Aqaba) beachrock. In: O.W. Bricker (Editor), Carbonate Cements. (Johns Hopkins University, Studies in Geology, 19.), pp.13–16.

Gavish, E. and Friedman, G.M., 1969. Progressive diagenesis in Quaternary to late Tertiary carbonate sediment: sequence and time scale. J. Sediment. Petrol., 39: 980–1006.

Ginsburg, R.N., 1953. Beachrock in south Florida. J. Sediment. Petrol., 23: 85–92.

Gonzalez, L.A. and Lohmann, K.C., 1985. Carbon and oxygen isotopic composition of Holocene reefal carbonates. Geology, 13: 811–814.

Guo, B. and Friedman, G.M., 1990. Petrophysical characteristics of Holocene beachrock. Carbonates Evaporites, 5: 223–243.

Hanor, J.S., 1978. Precipitation of beachrock cements: Mixing of marine and meteoric waters vs. CO_2 degassing. J. Sediment. Petrol., 48: 489–501.

Hudson, J.D., 1977. Stable isotopes of limestone lithification. J. Geol. Soc. London, 133: 637–660.

James, N.P. and Choquette, P.W., 1984. Diagenesis limestones—The meteoric diagenetic environment. Geosci. Can., 11: 161–194.

James, N.P. and Ginsburg, R.N., Marszalek, D.S. and Choquette, P.W., 1976. Facies and fabric specificity of early subsea cements in shallow Belize (British Honduras) reefs. J. Sediment. Petrol., 46: 523–544.

Krumbein, W.E., 1979. Phytolithotropic and chemoorganotrophic activity of bacteris and algae related to beachrock: Geomicrobiol. J., 1: 139–203.

Land, L.S., 1970. Phreatic vs. vadose meteoric diagenesis of limestones: Evidence from a fossil water table. Sedimentology, 14: 175–185.

Land, L.S. and Moore, C.H., 1980. Lithification, micritization, and syndepositional diagenesis of biolithites on the Jamaican Island slope. J. Sediment. Petrol., 50: 357–369.

Lighty, R.G., 1985. Preservation of internal reef porosity and diagenetic sealing of submerged Early Holocene Barrier Reef, Southeast Florida shelf. In: N. Schneidermann and P.M. Harris (Editors), Carbonate Cements. SEPM, Spec. Publ., 36: 123–152.

Magaritz, M., Gavish, E., Bakler, N. and Kafri, U., 1979. Carbon and oxygen isotope composition indicators of cementation environment in Recent, Holocene, and Pleistocene sediments along the coast of Israel. J. Sediment. Petrol., 49: 401–412.

Meyers, H.J., 1987. Marine vadose beachrock cementation by cryptocrystalline magnesian calcite. J. Sediment. Petrol., 57: 558–570.

Milliman, J.D., 1974. Marine carbonates. Springer, Berlin, 375 pp.

Moore, C.H., 1971. Beachrock cements, Grand Cayman Islands. In: O.W. Bricker (Editor), Carbonate Cements. (Johns Hopkins University, Studies in Geology, 19.), pp. 9–12.

Moore, C.H., 1973. Intertidal carbonate cementation, Grand Cayman, West Indies. J. Sediment. Petrol., 43: 591–602.

Moore, C.H., 1985. Upper Jurassic subsurface cements: A case History. In: N. Schneidermann and P.M. Harris (Editors), Carbonate Cements. SEPM, Spec. Publ., 36: 291–308.

Pierson, B.J. and Shinn, E.A., 1985. Cement distribution and carbonate mineral stabilization in Pleistocene limestones of Hogsty Reef, Bahamas. In: N. Schneidermann and P.M. Harris (Editors), Carbonate Cements. SEPM, Spec. Publ., 36: 153–168.

Russell, R.J., 1962. Origin of beachrock. Z. Geomorphol., 6: 1–16.

Saller, A.H., 1986. Radiaxial calcite in Lower Miocene strata, subsurface Enewetak Atoll. J. Sediment. Petrol., 56: 743–762.

Schillings, R.W. and Richter, D.K., 1989. Rezente Beachrockbildung an den Kusten Griechenlands. Geol. Palaontol. Mitt. Innsbruck, 16: 96–98.

Schmalz, R.F., 1971. Formation of beachrock at Enewetak Atoll. In: O.W. Bricker (Editor), Carbonate Cements. (Johns Hopkins University, Studies in Geology, 19.), pp.17–24.

Stoddart, D.R. and Cann, J.R., 1965. Nature and origin of beachrock. J. Sediment. Petrol., 35: 243–247.

Strasser, A., Davaud, E. and Jedoui, Y., 1989. Carbonate cement in Holocene beachrock: example from Bahiret el Biban, south eastern Tunisia. Sediment. Geol., 62: 89–100.

Zhong, S. and Mucci, A., 1989. Calcite and aragonite precipitation from seawater solution of various salinities: Precipitation rates and overgrowth compositions. Chem. Geol., 78: 283–299.

Marine Geology, 106 (1992) 149–164
Elsevier Science Publishers B.V., Amsterdam

Possible microbial origin of phosphorites on Error Seamount, northwestern Arabian Sea

V. Purnachandra Rao[a], M. Lamboy[b] and R. Natarajan[c]

[a]*National Institute of Oceanography, Dona Paula, Goa 403 004, India*
[b]*Department of Geology, University of Rouen, Rouen, France*
[c]*National Geophysical Research Institute, Uppal Road, Hyderabad 500 007, India*

(Received March 7, 1991; revision accepted November 6, 1991)

ABSTRACT

Purnachandra Rao, V., Lamboy, M. and Natarajan, R., 1992. Possible microbial origin of phosphorites on Error Seamount, northwestern Arabian Sea. *Mar. Geol.*, 106: 149–164.

Petrographical, mineralogical and microprobe analysis of phosphorites from Error Seamount, in the northwestern Arabian Sea, demonstrates that microbial processes played an important role in the early diagenetic formation of the phosphorites during subaerial exposure of the seamount.

The phosphorites on Error Seamount occur as laminated crusts and massive slabs. Low-magnesium calcite and carbonate fluorapatite are the major minerals of the phosphorites, with goethite being important only in the massive slab phosphorites. Elemental sulphur, pyrrhotite, gypsum and chlorite are the mineral phases present in the acid-insoluble residues of the phosphorites. Elemental sulphur, which is exclusively formed by microbial processes, occurs as submicrometre-sized granules on gypsum surfaces.

The laminated crust phosphorites consist of organic-rich and organic-poor laminae interlayered with ghost pellets, index fossils of Oligocene to lower Miocene age, peloids and coated grains. Massive slab phosphorites are fine-grained, and consist of goethitic and non-goethitic zones. Non-goethitic zones comprise mainly microsphorite with Oligocene to lower Miocene fossils and microfossils. Goethitic zones contain abundant Quaternary skeletons.

Microprobe analyses of the Error Seamount phosphorites indicate that the geochemistry of these phosphorites is similar to that of the Tertiary seamount phosphorites in the Atlantic and Pacific Ocean and that they are enriched in Ca and depleted in P compared to other seamount and island phosphorites in the Indian Ocean.

Microbial activity is evident in both types of phosphorites and occurs in the form of microborings in peloids and on skeletal fragments, encrustation of phosphate crystals on hollow, globular microstructures and phosphate sheaths enclosing organic filaments. The presence of calcite rim cements, microspar-filled patches and recrystallised grains indicates exposure of the seamount under subaerial conditions, during which phosphatisation took place.

Introduction

Two important processes have been reported for the formation of seamount phosphorites (Cullen and Burnett, 1986): (1) the mobilisation of guano-derived phosphate initially deposited on emergent islands and (2) the replacement of calcite by apatite during diagenesis. In recent years, however, the role of microbial processes in phosphogenesis has received considerable attention (O'Brien et al., 1981; Lucas and Prévôt, 1984; Prévôt and Lucas, 1986; Southgate, 1986; Lamboy and Monty, 1987; Rao and Nair, 1988; Soudry and Lewy, 1988; Soudry and Southgate, 1989; Lamboy, 1990a, b; Rao and Burnett, 1990). The evidence of microbial participation so far reported comes from phosphorites on land, from seafloor phosphorites in coastal regions and seamount phosphorites in the Pacific Ocean. The purpose of this paper is to demonstrate the effect of microbial activity in the formation of phosphorites on Error Seamount, in the northwestern Arabian Sea, and to report the discovery of elemental sulphur in the phosphorites. The phosphorites were recovered by dredging the flanks of the seamount at depths ranging from 400 to 460 m. Error Seamount (Fig.1) rises to a water depth of 370 m.

0025-3227/92/$05.00

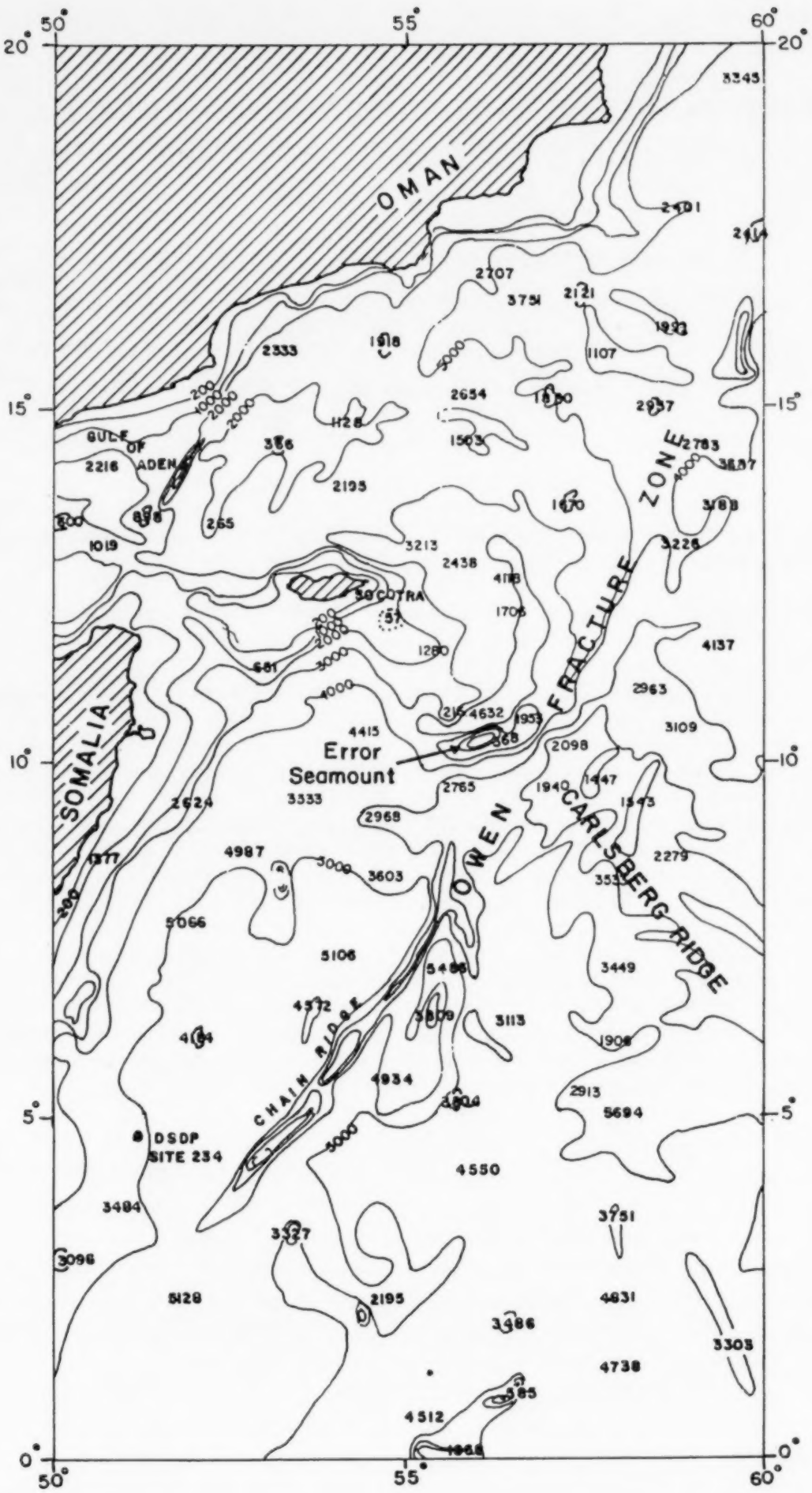

Fig.1. Location of Error Seamount.

Petrology of the phosphorites

The Error Seamount phosphorites (ESP) are associated with coralline algal limestones and occur as two different morphologies: (1) laminated crusts and (2) massive slabs.

Laminated crust phosphorites

The laminated crust phosphorites are about 10 cm thick and exhibit distinct layers in their basal parts and vaguely laminated structures in their upper parts (Fig.2a). The lower layering is in the form of domal laminae, reflecting the morphology of the surface on which the layering was formed. In thin section the basal parts of the crusts are characterised by alternating layers of smooth, light brown microcrystalline phosphate and a dense brown cryptocrystalline phosphate mosaic containing scattered carbonate particles. The thickness of the dark laminations varies from place to place (Fig.2b). Vertical extensions of indeterminate black material (probably organic matter) have also been observed (Fig.2c). The dark phosphate microlaminations are overlain by and interspersed with "ghost" pellets. Some of the skeletal components identified are filamentous algae, bryozoa, molluscs, and index fossils such as coralline algae (Lithothamniae), and benthic foraminifera (Miogypsinidae and Gypsinidae); these components suggest that the age range of the crust material is Oligocene to lower Miocene. Crystals that morphologically resemble gypsum are rare components. Micritised grains are common, as are peloids and other grains coated by layers of micritic phosphate (Fig.3a and b). The cement is mostly microcrystalline phosphate, but calcite spar is also present in the upper parts of the crust. Carbonate cements are localised

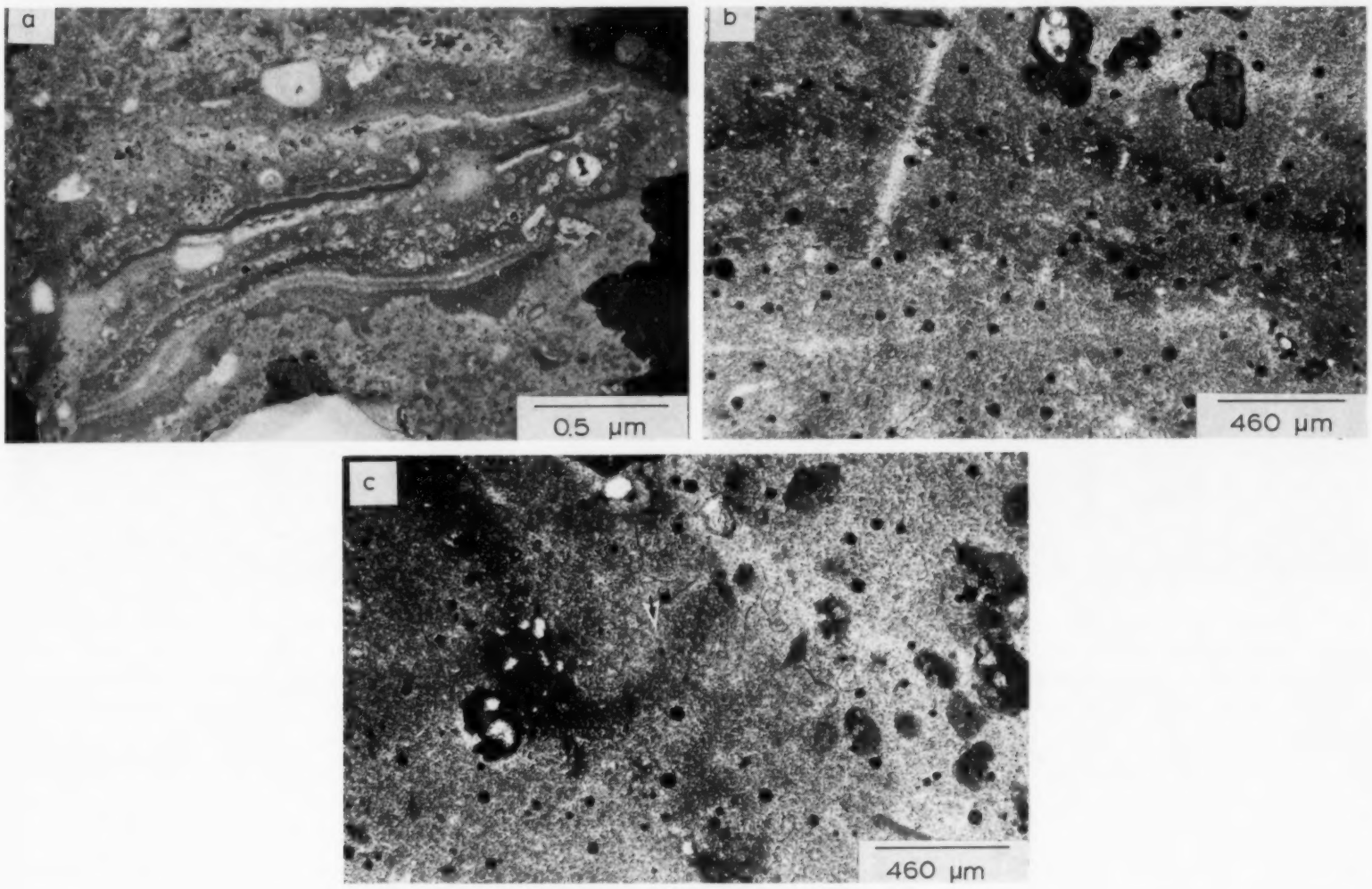

Fig.2. Laminated crust phosphorites. (a) Polished section showing distinct laminations in the basal parts. (b) Thin laminations; the colour of the lamination may be due to dark material. (c) Vertical extensions (arrows) of black material indicating that the organic matter was carried along these paths to the basal parts of the sediment to form laminated crusts. Figs.2b and c are both plane polarised light (PPL) photomicrographs.

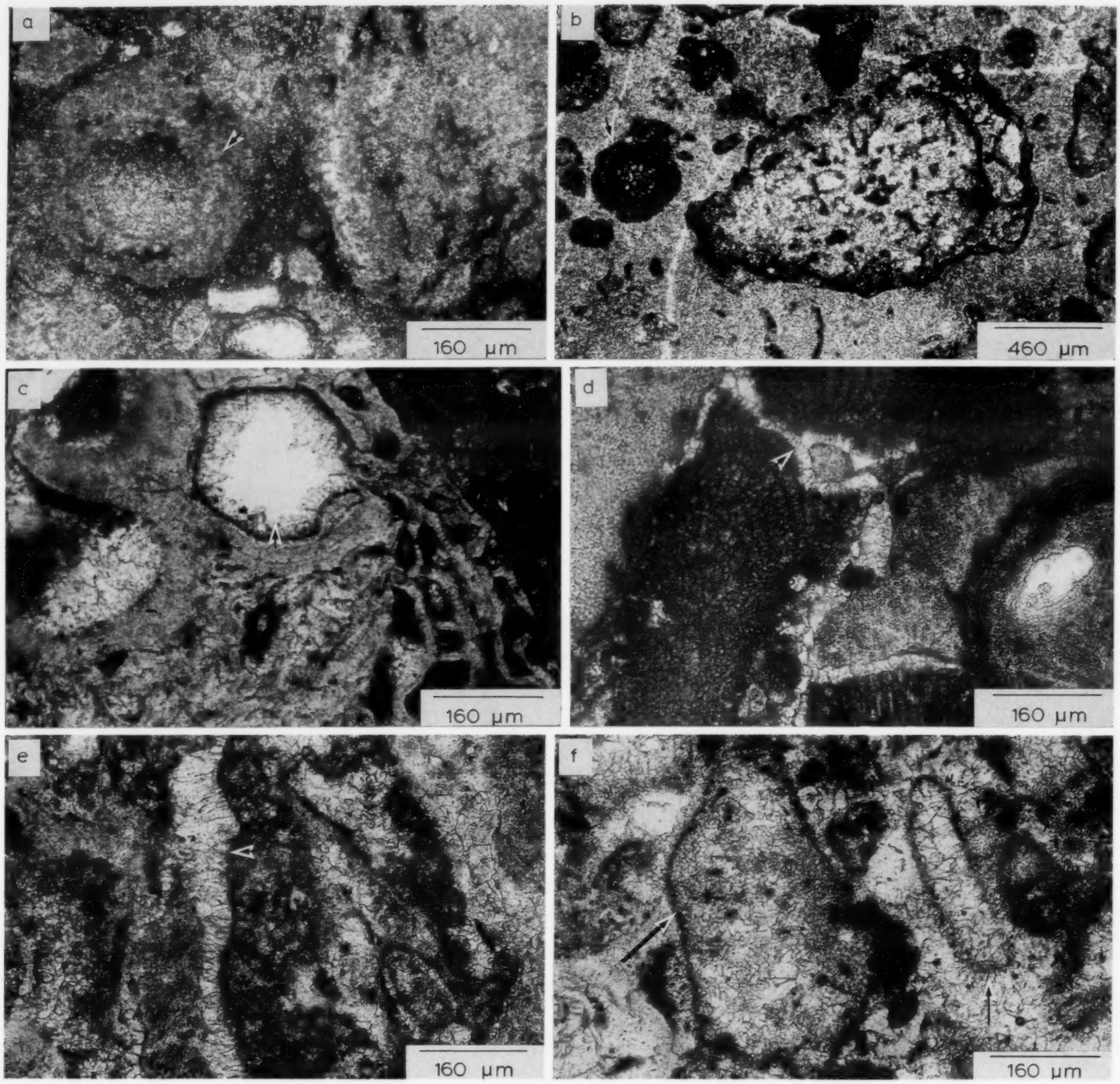

Fig.3. PPL photomicrographs. (a) Phosphatic peloid (arrow) formed by the aggregation of microcrystalline phosphate. (b) Spar crystal showing micritisation and organic coating at the periphery; a coated grain (arrow) can also be seen. (c) Voids in a skeletal fragment showing calcite crystallisation at the inner periphery (arrow). (d) Sparry calcite as cementing material (arrow) for the bioclasts. (e) Sparry calcite (arrow) in the fractures that developed around grains. (f) Skeletal grains recrystallised to microspar (arrows).

to grain contacts and extend into the voids. Internal voids of bioclasts are also partially occluded or completely replaced by microspar (Fig.3c). Elsewhere, sparry calcite has filled all voids (Fig.3d). Microspar crystallisation is often irregular in the matrix and is concentrated around bioclastic fragments as if filling cracks (Fig.3e). Some of the bioclasts have recrystallised to microspar (Fig.3f). The sparry calcites consist of rounded to oval opaque bodies and associated

rod-shaped structures and are similar to structures formed by bacterial origin in the sparry calcites of stalactites from the Grand Caymen Islands (Jones and Motyka, 1987; Fig.3b).

Massive slab phosphorites

Massive slab phosphorites consist of fine-grained phosphates with surface borings (Fig.4a). Iron-

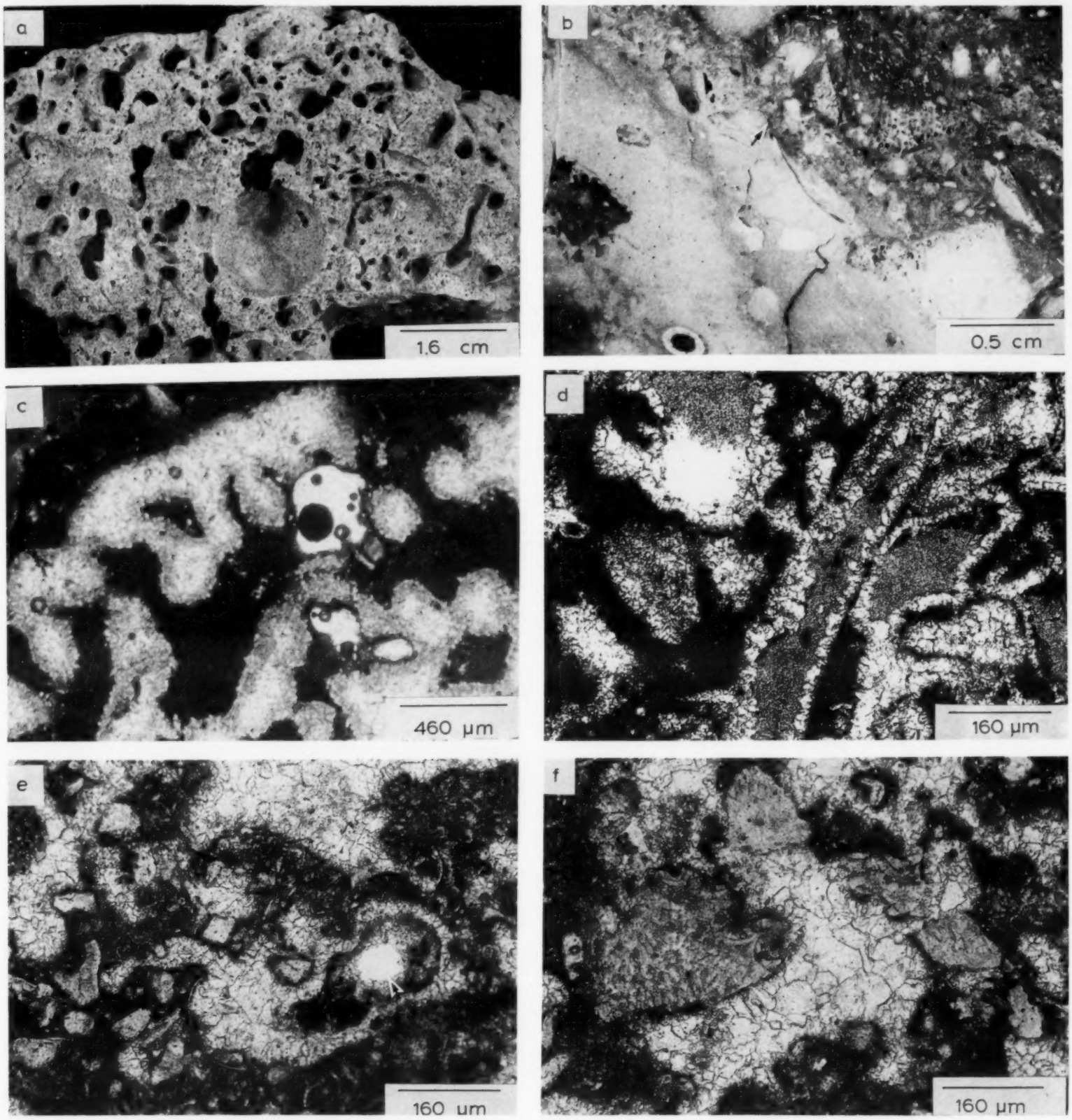

Fig.4. Massive slab phosphorites. (a) Hand specimen showing bored surfaces. (b) Polished section showing goethitic and non-goethitic zones; arrow points to the goethitic portion. (c) Boring cavities infilled with microsphorite. (d) Calcite fringe cement around phosphatised material. (e) Irregular distribution of sparry calcite in the matrix; rounding of pore space can also be seen (arrow). (f) Sparry calcite accumulated at grain contacts resembling gravitational cements. Figs.4c–f are PPL photomicrographs.

oxide impregnation enables us to distinguish goethitic and non-goethitic zones in these phosphorites (Fig.4b).

Thin sections show that the non-goethitic zones are largely composed of microcrystalline phosphate, similar to microsphorite (cf. Riggs, 1979), with few algal and foraminiferal skeletal particles. Boring cavities filled with microsphorite are present. The borings are about 50 μm in diameter and penetrate perpendicular to the surface; the boreholes are parallel with lobate extensions (Fig.4c). Crustose coralline algal bodies morphologically resembling the fore-reed genus *Mesophyllum* (cf. Buchbinder, 1977) are recorded from this zone, together with the Oligocene–lower Miocene benthic foraminifer *Miolepidocyclina*, suggesting that this zone corresponds chronologically to the material in the laminated crust phosphorites. Rounded grains and cemented composite grains represent allochthonous material stripped from poorly lithified sediment by wave and current action that was subsequently rounded, transported and deposited with the microsphorite.

The goethitic zones of the massive slab phosphorites contain abundant tests of the planktonic foraminifera *Orbulina universa* d'Orbigny, *Globorotalia truncatulinoides* (d'Orbigny), *Globorotalia* spp. and *Globigerina* spp., demonstrating that the age of this material is Quaternary. The cements in this zone are phosphatic as well as goethitic and hardly any diagenetic textures can be recognised. The transition zone between goethite and non-goethite layers shows freshwater phreatic cements, including rim cements (Fig.4d) precipitated during the replacement and formation of dissolution cavities in the bioclasts. Irregular distribution of microspar patches with rounding of pore spaces (Fig.4e) and microspar-filled patches at grain boundaries (Fig.4f) which resemble gravitational cements are also common.

Examination of freshly broken surfaces of the ESP with an SEM equipped with an energy dispersive X-ray analyser has revealed that the laminated crust phosphorites consist of globular structures coated with phosphate crystals (Fig.5a). The globular structures are about 10 μm across, circular to ovoid in outline, and coated by minute (1 μm) phosphate crystals. Some of these structures appear to be hollow, with a narrow aperture. Bare phosphatised filaments enclosed in phosphate sheaths are found elsewhere (Fig.5b). In some places phosphate crystals are attached to the filaments and sheaths (Fig.5c–f); the sizes, textures and morphologies of these crystals vary considerably. The size of the filaments also varies, from 0.1 to 10 μm. The non-goethitic zone of the massive slab phosphorites contains abundant coccoliths, and phosphatised organic filaments. Coccoliths partially replaced by carbonate fluorapatite (Fig.6a). Well-developed hexagonal carbonate fluorapatites are found in the cavities (Fig.6b). In the goethitic zone completely replaced foraminiferal tests have been observed, with some chambers densely filled with carbonate fluorapatite while others remain quite empty (Fig.6c). Secondary calcite in the cavities is precipitated as acicular crystals, upon which carbonate fluorapatite has developed (Fig.6d).

Mineralogy

Study of the bulk mineralogy indicates that low-magnesium calcite and carbonate fluorapatite are the important mineral constituents in both types of phosphorites, with the goethite being present only in the massive slab phosphorites (Fig.7). To separate the minor minerals, powdered samples were treated with 3 *M* HCl and the insoluble residue was washed and filtered onto 0.4 μm Nucleopore filters. Microscopic observations of this residue indicated that sulphur granules were scattered throughout the material, being especially prominent on the surfaces of gypsum crystals. Examination with the SEM revealed that these surfaces (Fig.8) show solution features and are segmented into rounded aggregates of 4–5 μm in diameter. These aggregates consist of submicrometre-sized sulphur granules, which implies that replacement of gypsum by elemental sulphur has taken place. A similar process was reported by Ivanov in 1968 for sedimentary sulphur deposits in Lake Eyre. X-ray diffraction analysis (Fig.9) of the insoluble residues confirmed the presence of elemental sulphur and minor amounts of

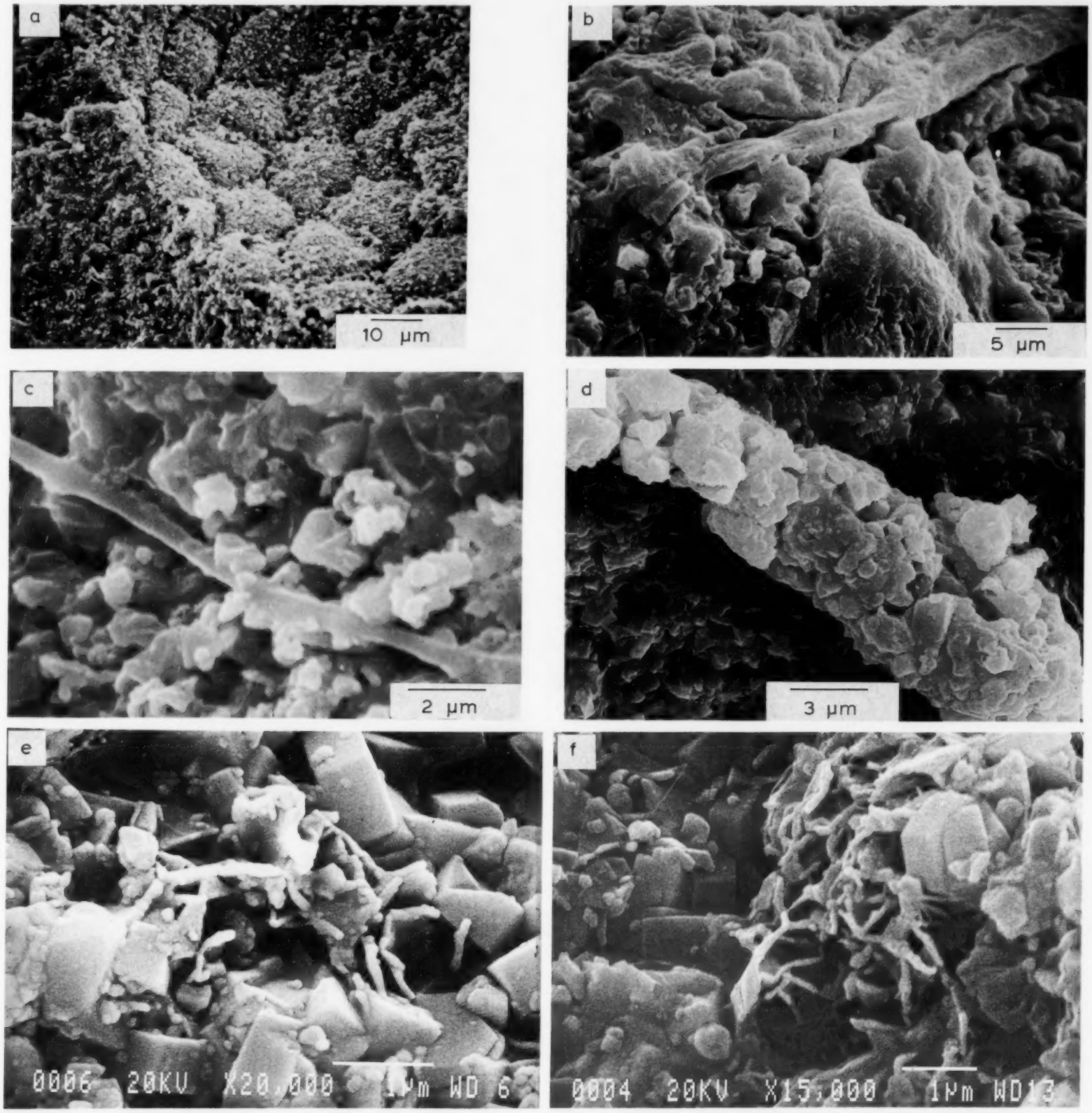

Fig.5. SEM micrographs. (a) Spherical to ovoidal microstructures encrusted with phosphate crystals. (b) Filaments enclosed in a phosphatic sheath. (c)–(f) Carbonate fluorapatite crystals attached to filaments; note that the diameter of the filaments and nature of the phosphatic crystals encrusted varies in each micrograph.

chlorite and gypsum in the laminated crust phosphorites, and goethite, elemental sulphur, pyrrhotite and gypsum in the massive slab phosphorites. Elemental sulphur peaks are prominent in laminated crust phosphorites (Fig.9a) where the iron content is lowest (column C, Table 1), suggesting that sulphur is not a product of weathering of sulphides.

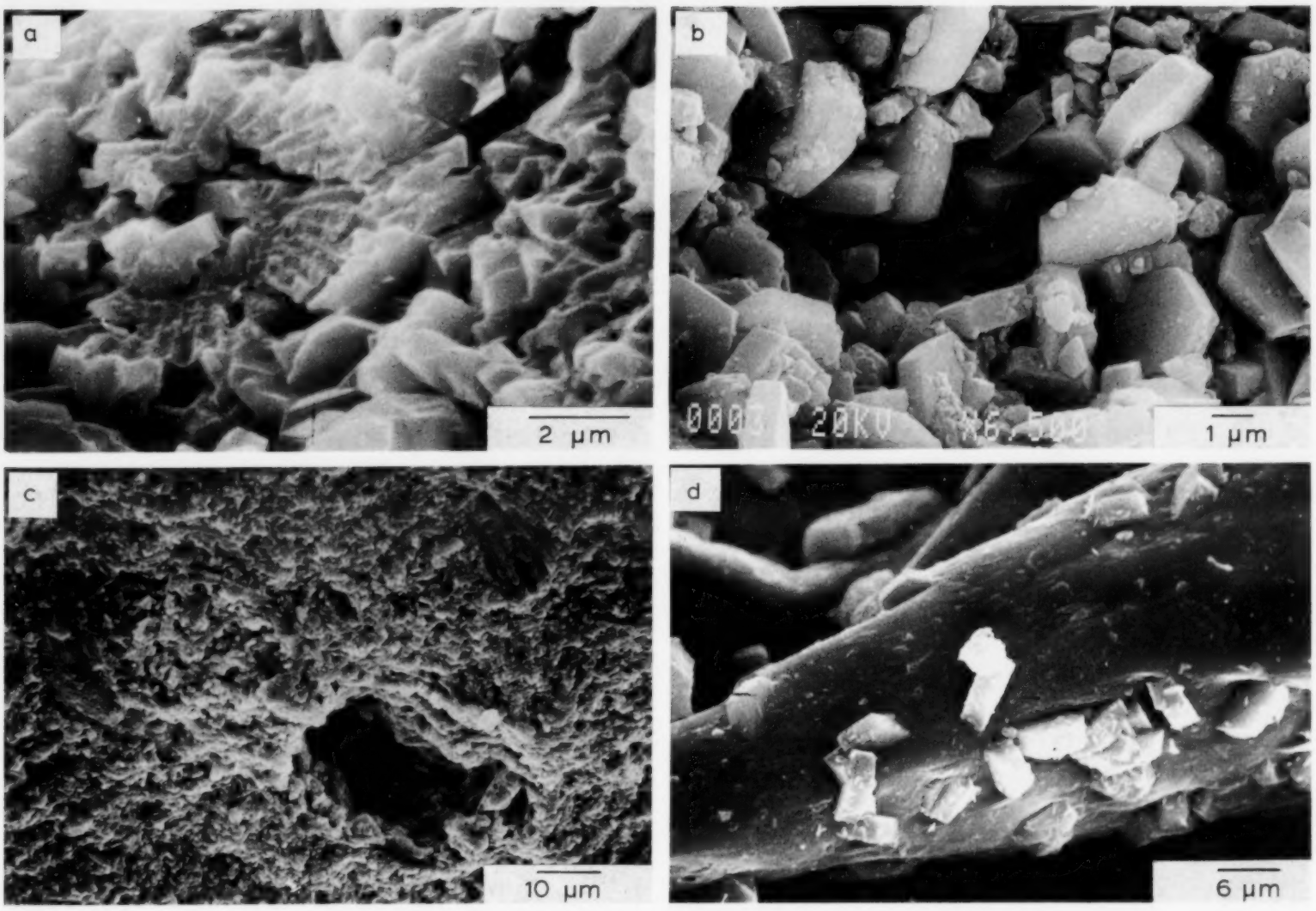

Fig.6. SEM micrographs. (a) Coccoliths being replaced by carbonate fluorapatite. (b) Well-developed carbonate fluorapatite crystals in cavities. (c) Phosphatised foraminiferal grain showing one chamber completely filled with carbonate fluorapatite crystals; the right-hand chamber is empty. (d) Carbonate fluorapatite crystallisation on acicular calcite crystals.

Geochemistry

Microprobe analyses of the ESP (Table 1) indicate that the elemental concentrations in the goethitic part of the massive crust phosphorites (Quaternary in age) are distinctly different from those of non-goethitic massive crust and laminated crust phosphorites (both Oligocene to lower Miocene in age). The elemental concentrations of non-goethitic massive crust and laminated crust phosphorites are comparable, except that the former contains slightly more P, Ca and Fe and less Si, Al and Mg. P_2O_5 contents ranges up to 33%. It appears that the ESP are enriched in Ca and depleted in P compared to other seamount and island phosphorites in the Indian Ocean. Si, Al, K and Na are lower and Ca and Mg are higher in the ESP when compared to the continental margin phosphorites in the Indian Ocean. The isolated position of Error Seamount may explain the depletion of terrigenous material in its phosphorites. The elemental concentrations of ESP are in agreement with those in other Tertiary phosphorites of seamounts of the Atlantic and Pacific Ocean (Table 1). The CaO/P_2O_5 ratio is about 1.95, which is higher than that found for pure carbonate fluorapatite (1.54; McClellan and Lehr, 1969). The structural CO_2 content of the carbonate fluorapatite varies from 5.2 to 5.95 and the average CO_3/PO_4 ratio is 0.25. Similar values for structural CO_2 were reported by McArthur (1984) in replacement-type phosphorites. The "a"-cell dimensions range from 9.32 to 9.33 Å. The smaller "a"-cell dimensions and the high CO_3/PO_4 ratio in the

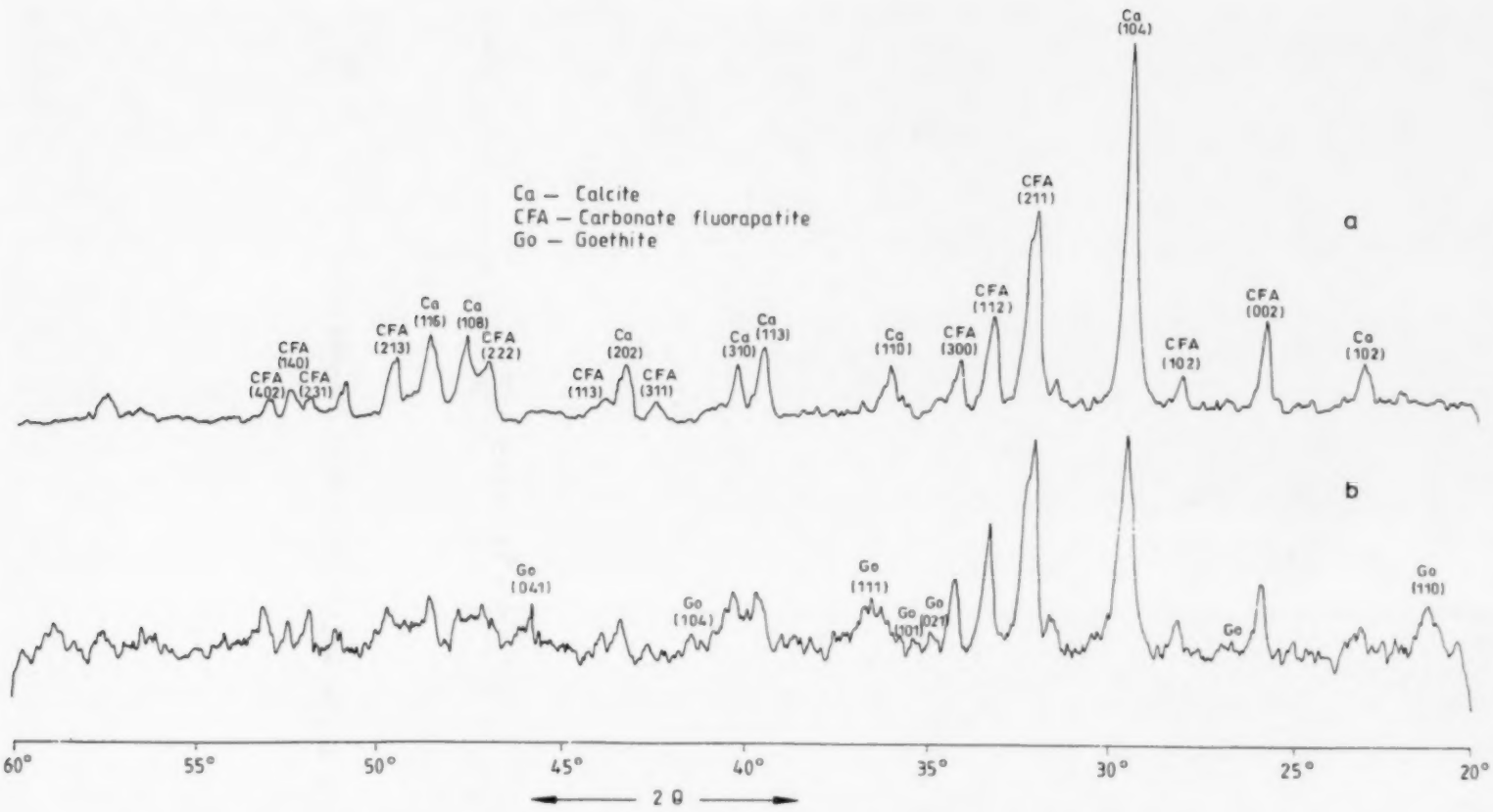

Fig.7. Whole-rock X-ray diffractograms. (a) Laminated crust phosphorite. (b) Massive slab phosphorite.

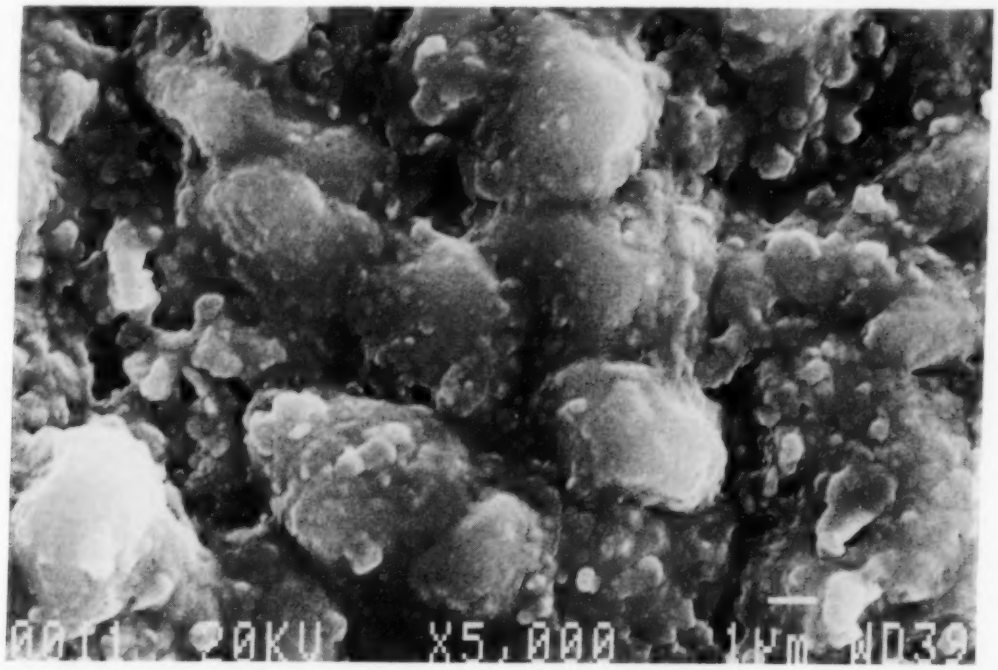

Fig.8. SEM micrograph of gypsum surface showing dissolution features, segregation of spheroidal forms and submicrometre-sized sulphur grains.

carbonate fluorapatites reveal that the phosphorites are unaltered. This supports the hypothesis that phosphogenesis preceded the onset of oxidising conditions when layers impregnated by goethite probably formed.

Age and genesis of phosphorites

Petrographic studies suggest that the Error Seamount phosphorites are the products of two phosphogenic events, one of which occurred between

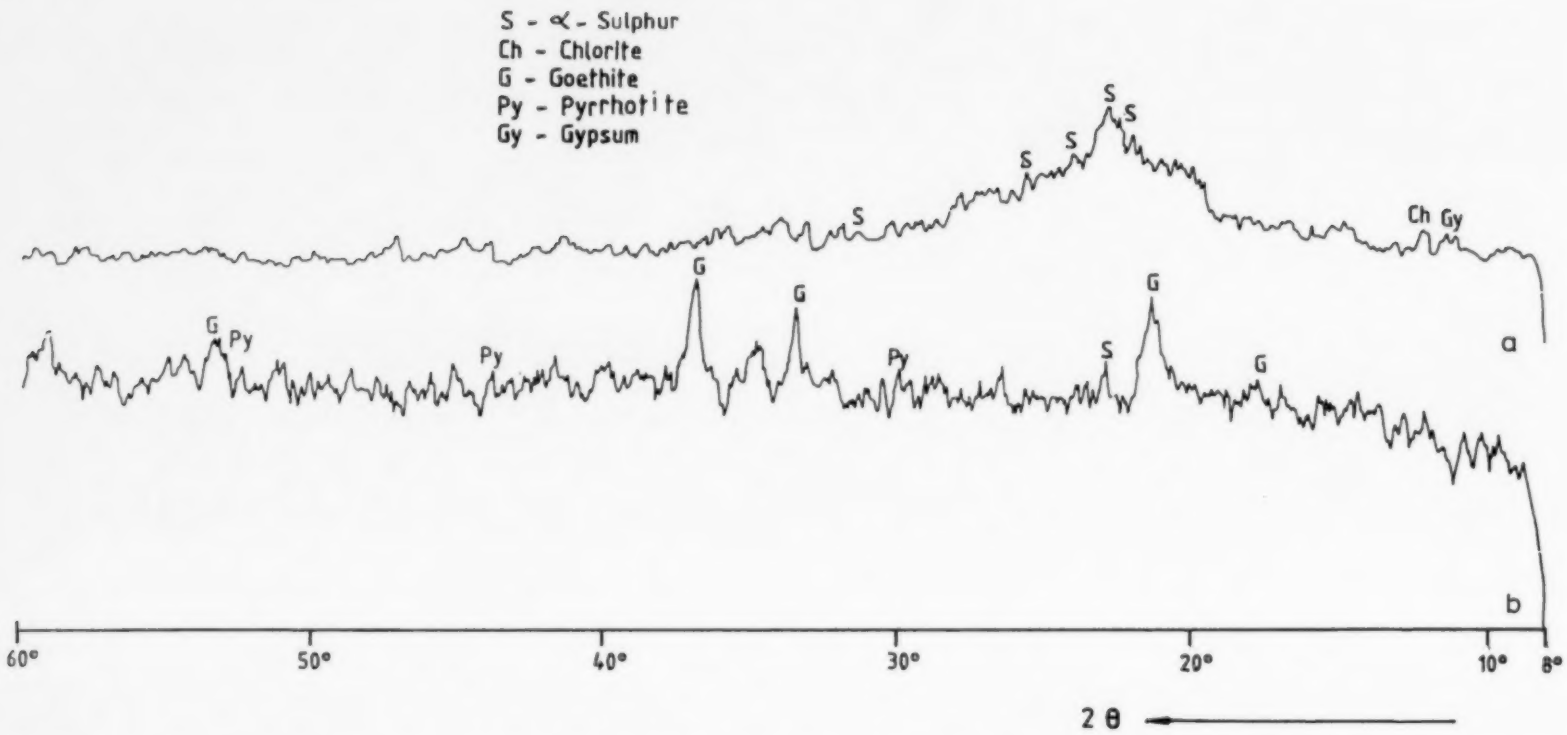

Fig.9. X-ray diffractograms of acid-insoluble residues. (a) Laminated crust phosphorite. (b) Massive slab phosphorite.

the Oligocene and early Miocene, the other occurring in the Quaternary.

Laminated crust phosphorites

Distinct laminations in the basal parts of the crust mainly reflect the presence of a dark brown pigment, probably organic matter, in the darker layers. Processes/products such as calcrete formation, lichen development and cryptalgal structures produce laminated structures in limestones. Read (1976) and Klappa (1979a) reported the characteristic features of laminated calcretes and cryptalgal laminations and lichen-produced laminations in calcretes and subsurface calcretes. The laminations in the phosphorites vary in thickness and follow topographic irregularities in the underlying surface (Fig.2a). The vertical extensions (Fig.2c) of black material may represent the paths of organic detritus carried to the lower portions. The dark laminations consist of skeletal material, unlike the laminations produced by lichens, which are amorphous (Jones and Kahle, 1985). Subaerial diagenetic textures (described below) are associated with the laminated structures. It is therefore suggested that the process of crust formation on Error Seamount is a subsurface process which may have resembled those entailed in calcrete formation (Multer and Hoffmeister, 1968; Read, 1974), involving dissolution of carbonate, decomposition of organic matter and phosphorous enrichment in interstitial waters which subsequently reached the base of the sediment profile. Some of the organic detritus might have washed down from the upper layers of sediment, filled cavities and finally precipitated as laminated crusts.

Evidence of subaerial exposure

Sparry calcite occurs as rim cement localised at grain contacts (Figs.3c, 3d and 4e) and as fringe cement (Fig.4d). These fabrics are characteristic of phreatic freshwater conditions.

Microspar patches around grains (Fig.3e) indicate that freshwater may have percolated into the fractures that developed during subaerial exposure, the fluid subsequently crystallised to microspar. Pockets of microspar-filled patches at grain boundaries (Fig.4e and f) and recrystallised bioclastic material (Fig.3f) may have developed due to freshwater solutions which remained for longer periods at those places where crystallisation had taken place to form sparry calcite. These cements occur in the upper parts of laminated crust phosphorites and in transitional parts of the crust between goethitic and non-goethitic layers of the massive

TABLE 1

Microprobe analyses of Error Seamount phosphorites and comparison with other seamounts, islands and continental margin phosphorites of the Indian Ocean and seamount phosphorites of the Atlantic and Pacific Ocean

	(A) 10*	(B) 15*	(C) 12*	(D)	(E)	(F)	(G) 25*	(H)	(I)	(J)	(K) 20*
SiO_2	2.17	0.25	2.44	4.66	–	3.10	5.21	13.30	9.69	2.78	1.99
Al_2O_3	3.40	0.19	1.33	2.29	–	2.28	2.05	4.45	1.57	–	0.56
Fe_2O_3**	67.74	2.53	0.46	–	–	5.75	4.37	7.55	–	–	0.68
MgO	3.21	0.49	0.86	1.41	0.81	1.10	2.44	11.10	1.31	0.80	0.45
CaO	2.29	51.97	47.58	45.35	45.52	43.90	45.92	25.80	38.51	50.40	47.57
Na2O	0.39	0.83	0.71	–	0.82	0.89	0.06	0.79	0.62	–	0.92
K_2O	0.17	0.13	0.33	–	–	0.44	0.34	0.80	0.98	0.13	0.10
P_2O_5	3.03	26.46	24.16	27.80	28.60	28.00	24.82	6.20	14.95	25.30	27.40
SO_3	0.17	0.97	1.06	–	–	–	–	–	–	–	1.70
F	–	1.20[1]	1.05[1]	2.58	0.82	1.97	1.20	–	1.95	1.99	–
CO_2[a]	–	5.95	5.20	–	–	–	–	–	–	–	–
CaO/P_2O_5	0.76	1.96	1.97	1.63	1.59	1.57	1.85	4.16	2.58	–	1.74
MgO/P_2O_5	1.06	0.018	0.036	0.05	0.028	0.039	0.098	1.79	0.088	0.031	0.016
Na_2O/P_2O_5	0.13	0.031	0.029	–	0.029	0.032	0.002	0.13	0.041	–	0.034
SO_3/P_2O_5	0.056	0.037	0.043	–	–	–	–	–	–	–	0.058

(A), (B) and (C) = Error Seamount phosphorites (this paper): (A) = Geothitic portion of the massive slab phosphorites; data not used for comparison. (B) = Non-goethitic portion of the massive slab phosphorites. (C) = Laminated crust phosphorites.
Other phosphorites:
(D) = unnamed seamount (13°45′S, 99°56′E), Baturin (1982)
(E) = Remire Island, Braithwaite (1968)
(F) = Socotra Island shelf, Gevork'yon and Chugunnyy (1970)
(G) = western shelf of India (off Goa), Rao et al. (1990)
(H) = western shelf of India (off Quilon), Baturin (1982)
(I) = Agulhas Bank (African shelf), Cronan (1980)
(J) = Annon Seamount (Atlantic Ocean), Jones and Goddard (1979)
(K) = Pacific seamounts, Burnett et al. (1987)
* Number of spots analysed (microprobe)
** Total iron expressed as Fe_2O_3
[1] Fluoride ion electrode method, Edmond (1969)
[a] Gulbrandsen (1970) method.

slab phosphorites. This may imply that the sediments in phosphorites experienced subaerial conditions at the time of consolidation.

Identification of micro-organisms

Several workers have attempted to distinguish the various groups of organisms (algae, fungi, root hairs, bacteria and actinomycete) based on the size, mode of branching and some of the morphological characteristics of the filaments and borings. It has been suggested that the larger diameter filaments (>4 μm) originate from algae (Kendrick et al., 1982) and root hairs (5–17 μm; Klappa, 1979b), while smaller diameter filaments (1–4 μm) are produced by fungi (Perkins and Halsey, 1971; Rooney and Perkins, 1972). The very small filaments (<1 μm) are produced by bacteria (Folk et al., 1985). However, distinctions based solely on size may not be a reliable criteria, because fungal filaments ranging from 0.9 to 10 μm in diameter (Tsuneda, 1983; Klappa, 1979b) and blue-green and green algae of 0.5 to 20 μm in diameter have been reported as being associated with vadose settings. It is therefore necessary to consider other morphological characteristics of the filaments. However, Jones (1989) has suggested that most of the important taxonomical characteristics were lost due to calcification in the vadose evironment and that it is thus difficult to assign the organisms to

their taxonomic groups. The diameters of the filaments (0.1–10 μm) and borings (a few micrometres to 50 μm) observed in the present study indicates organisms ranging from bacteria to green algae. However, in view of the above, no attempt has been made to classify them and the collective term "microbial organisms" has been used in this paper.

Non-goethitic zone

The age of the non-goethitic zone of the massive slab phosphorites corresponds to that of the laminated crust phosphorites, despite the dominance of microsphorite in the non-goethitic zone. Microsphorite in phosphorite is analogous to micrite in limestones (Riggs, 1979). Micrites originate by several processes (Jones and Motyka, 1987), either by (a) inorganic precipitation, (b) by organic precipitation (either directly or indirectly), (c) by replacement of spar crystals, or (d) at locations distal to the eventual place of deposition, subsequently to be transported and deposited in a low-energy environment.

The abundance of coccoliths (Fig.6a) indicates that most of the fine-grained material may be a nanno ooze. However, micrite/lime muds derived from other sources may have also contributed to the original sediments. For example, composite grains and several rounded skeletal fragments embedded in the matrix suggest the possibility that some micrite formed by erosion of the algal limestones, and might have been carried to the site of formation. Several allochems and spar calcites contain borings produced by micro-organisms (Fig.3b). Hence, micrite resulted due to the breakdown of grains by micro-organisms and by spar-micritisation (Kahle, 1977) could have contributed to the original sediments. It is assumed, therefore, that the initially formed lime muds/micrite were subsequently phosphatised during subaerial diagenesis to form microsphorite. Rocks with a mudstone fabric formed by subaerial diagenesis have been recognised in the calcretes of Shark Bay, Australia (Read, 1974). Micritisation of grains, and grains coated by micritic phosphate, may be the products of diagenesis.

Goethitic zone

The age of the goethitic zone of the massive slab phosphorites is Quaternary. During submergence of the seamount in the Quaternary, an open-ocean fauna and flora was deposited above the non-goethitic zone and became diagenetically altered to phosphorite. Goethite is an important mineral in this goethitic zone, together with carbonate fluorapatite and calcite. Microprobe analysis shows that the P_2O_5 content is lowest (average 3.03) (range from 2 to 6%) (Table 1). Berner (1990) and O'Brien et al. (1990) suggested adsorbed phosphate on FeOOH during Fe-redox cycling as a possible source of phosphate in phosphorites. This is considered unlikely to be the major process on Error Seamount because: (a) iron and phosphate in this zone show a strong negative correlation, and (b) if phosphate and iron were introduced to the crust through a sediment mixing process one would expect the whole crust to be "ferruginised"; this is not the case here as iron is confined only to the goethitic zone. Since phosphogenesis takes place in suboxic to anoxic environments, it must have preceded the onset of oxidising conditions that led to the impregnation of layers by goethite. The origin of the goethitic zone relates, therefore, to sea-level changes in the early diagenetic stage of phosphorite formation. The presence of borings on surfaces of massive slab phosphorites also provides evidence of subaerial or very shallow marine oxic conditions (Bathurst, 1975).

Process of phosphogenesis on Error Seamount

SEM studies indicate that two important processes have been involved in phosphatisation on Error Seamount. The first involves the phosphatisation of organic filaments and precipitation by phosphate crystals of microbial cell-like structures. The second entails the replacement of calcite by apatite, and the infilling of foraminiferal chambers by apatite crystals. Phosphate crystals formed on cell-like structures with hollow centres (Fig.5a) may indicate that phosphatisation was an early diagenetic process, which took place before complete disintegration of associated organic matter. Further, the enclosure of filaments in phosphatic

sheaths (Fig.5b) suggests that phosphatisation probably occurred through direct microbial precipitation rather than by replacement of calcite by apatite.

Previous investigations of carbonate sediments (Kobluk and Risk, 1977; Klappa, 1979b) have suggested that calcification apparently takes place mostly on dead filaments. The subaerial conditions of the seamount are evident from thin-section studies. During early diagenesis the phosphate is released from the decomposition of organic matter associated with the sediments and with organic structures. Bacteria associated with the decay of organic matter may therefore have created a suitable environment for the precipitation of apatite. Precipitation of apatite could also have been achieved by intense evaporation resulting in an increase in pH and temperature in the sediment interstices. The encrustation of filaments and cell-like structures by apatite crystals suggests that the organic structures acted as a source as well as a suitable substrate for phosphate mineralisation (Southgate, 1986). The size, nature and morphology of the phosphate coatings on filaments (Fig.5c–f) may be related to the nature and chemical constituents of the organic structures, and thus are species-specific. Pentecost and Riding (1986) suggested that the polysaccaride sheaths of filaments provide a suitable nucleation site for carbonate crystals. It therefore seems reasonable to infer that microbial processes played an analogous major role in the phosphatisation on Error Seamount. Several workers (Soudry and Champetier, 1983; Southgate, 1986; Lamboy and Monty, 1987; Soudry and Lewy, 1988; Soudry and Southgate 1989) have reported microbial influences in phosphate mineralisation, and others (Cayeux, 1936; Oppenheimer, 1958; O'Brien et al., 1981; Riggs, 1982; Zanin et al., 1985; Rao and Nair, 1988; Rao and Burnett, 1990) have demonstrated phosphate enrichment in bacterial cell-like structures suggesting that bacteria were in some way related to phosphorite formation. Lucas and Prévôt (1984) and Prévôt and Lucas (1986) synthesised apatite from organic matter in non-sterile conditions, and suggested that bacterial mediation is necessary for apatite formation.

The second phosphogenesis process, namely the replacement of carbonate by phosphate, is evident in the massive slab phosphorites (Fig.6a). It may be that at least part of the phosphate released to the interstitial waters subsequently replaced the carbonates, filled the cavities and precipitated around the skeletal particles to form coated grains. The dense packing by carbonate fluorapatite of one chamber, whereas the adjacent chamber (Fig.6c) remains unfilled, may correspond to the absence of microbes in the latter chamber.

Mineralogy

The bulk mineralogy of the phosphorites was discussed at length in an earlier paper (Rao, 1986). This established that the minerals observed in the phosphorites do not represent the original minerals of the constituent skeletal components. The stable carbonate mineral phase, low-magnesium calcite and carbonate fluorapatite were products of early diagenesis during subaerial exposure of the seamount summit. The presence of elemental sulphur in the phosphorites, however, was not reported earlier. Elemental sulphur forms either through direct oxidation of organic matter, or through reduction of mineral sulphate to H_2S which is subsequently oxidised. Since the oxidation of sulphide to elemental sulphur in sedimentary rocks is thought to occur exclusively through microbial processes (Kostov, 1968), its presence in phosphorites may suggest that there were two important interrelated processes at work. Intense bacterial activity (sulphate reduction and sulphide oxidation) apparently existed in the carbonate sediments during early diagenesis and, as a result, elemental sulphur accumulated. A contemporaneous and interrelated process was the release of phosphate to the sediment interstitial waters under microbial influences. Slansky (1979) suggested that the most favourable environment for phosphorite formation is near the boundary between suboxic and anoxic conditions within the sedimentary environment. On the other hand, Burnett and Veeh (1977) suggested that strongly reducing conditions may not be conducive to phosphorite formation. In the present instance, sulphate-reducing conditions on Error Seamount must have existed in close proximity to the sulphide-oxidising bacteria responsible

for elemental sulphur formation. It is possible that pyrrhotite formed through reaction between elemental sulphur and free iron diffusing out of the adjacent anoxic sediment. The chlorites (see Fig.9) also may have formed during diagenesis. It is therefore suggested that the presence of elemental sulphur in both the massive slab and laminated crust phosphorites augments the evidence for microbial activity playing an important role in the phosphate mineralisation on Error Seamount.

Conclusions

Error Seamount was subaerially exposed during the Oligocene to early Miocene, at which time carbonate sediments derived from the erosion of algal growths were deposited on the flanks of the seamount. Microbial decomposition of organic matter associated with the carbonate sediments released phosphate to the interstitial waters. This phosphate along with some organic matter was washed down to subsurface depths and produced laminated phosphatic crusts. The non-goethitic zone of the massive slab phosphorites apparently formed by similar processes at the same time. During early diagenesis, microbial processes played a major role in phosphate release and phosphate precipitation. The goethitic zone of the massize slab phosphorites formed in the Quaternary, the iron oxide impregnation presumably taking place in the early diagenetic stage of the phosphorite formation during sea-level changes. The Quaternary phosphorites occur directly on Oligocene to lower Miocene phosphorites (non-goethitic zone of the massive slab phosphorite). The absence of middle Miocene to Pliocene fauna may indicate a period of non-deposition, and subaerial conditions probably held sway at the summit of Error Seamount during that time.

Cullen and Burnett (1986) described both peaked seamounts and flat-topped guyots in the tropical southwest Pacific Ocean. They found that phosphorites on peaked seamounts were exclusively marine in origin, whereas phosphorites recovered from the guyots commonly showed evidence of an insular origin, with phosphate perhaps derived from avian guano. Cullen (1988) further reported the filamentous structures, broadly comparable to those described in this paper, in guano-derived phosphates of the Bounty Islands, suggesting a microbial role even in insular settings. Error Seamount is a flat-topped seamount located in tropical waters of the northwestern Indian Ocean. The phosphorites on this seamount were formed in quite different environmental settings and it is clear that not all phosphorites on flat-topped seamounts are necessarily of insular origin.

Acknowledgments

Part of this research was completed while the senior author was a visiting scientist at the Department of Oceanography, Florida State University and at the Department of Geology, University of Rouen, France. Rao's travel was funded by UNESCO and all research was supported through a grant to Prof. Bill Burnett from the National Science Foundation (OCE8520724). We thank W. Landing and P. Larock for helpful discussion, Dr. P.A. Dupeuble for identifying the index fossils and N. Azzouzi and A. Watkins for assistance. Rao wishes to thank the Directors of the National Institute of Oceanography (NIO) and the National Geophysical Research Institute (NGRI) for facilities and Dr. S.M. Naqvi, Mr. P.S.N. Murty and Mr. R.R. Nair for their encouragement. We thank Dr. David J. Cullen and Prof. Brian Jones and Prof. Bill Burnett for the critical review of the earlier versions of the manuscript. Photographic work was carried out by V.M. Date and Karim Shaik Ali of NIO. We would also like to thank two anonymous reviewers for their comments which helped in improving the manuscript.

References

Bathurst, R.G.C., 1975. Carbonate Sediments and their Diagenesis. Elsevier, Amsterdam, 658 pp.

Baturin, G.N., 1982. Phosphorites on the Sea Floor. Elsevier, Amsterdam, 343 pp.

Berner, R.A., 1990. Diagenesis of phosphorous in sediments from non-upwelling areas. In: Phosphate Deposits of the World, Vol.3. Cambridge University Press, pp.27–32.

Braithwaite, C.J.R., 1968. Diagenesis of phosphatic carbonate rocks on Remire Islands, Amirantes, Indian Ocean. J. Sediment. Petrol., 38: 1194–1212.

Buchbinder, B., 1977. Systematics and palaeoenvironments of calcareous algae from the Miocene (Tortonian) Tziqlag formation, Israel. Micropalaeontology, 23: 415–435.

Burnett, W.C. and Veeh, H.H., 1977. Uranium-series disequilibrium studies in phosphorite nodules from the west coast of South America. Geochim. Cosmochim, Acta, 41: 755–764.

Burnett, W.C., Cullen, D.J. and McMurtry, G.M., 1987. Open-ocean phosphorites: In a class by themselves? In: P.G. Teleki, M.R. Dobson, J.R. Moore and U. Von Stackelberg (Editors), Marine Minerals: Advances in Research and Resource Assessment. Reidel, pp.119–134.

Cayeux, L., 1936. Existence de nombreuses bacteries dans les phosphates sedimentaires de tout âge. C.R. Acad. Sci. Paris, 23: 1198–1200.

Cronan, D.S., 1980. Underwater Minerals. Academic Press, London, 360 pp.

Cullen, D.J., 1988. Mineralogy of nitrogenous guano on the Bounty Islands, SW Pacific Ocean. Sedimentology, 35: 421–428.

Cullen, D.J. and Burnett, W.C., 1986. Phosphorite associations on seamounts in the tropical southwest Pacific Ocean. Mar. Geol., 71: 214–236.

Edmond, C.R., 1969. Direct determination of fluoride in phosphatic rock samples using the specific ion electrode. Bull. Anal. Chem., 41: 1327–1328.

Folk, R.L., Chafetz, H.S. and Tiezzi, P.A., 1985. Bizarre forms of depositional and diagenetic calcite in hot-spring travertines, central Italy. In: N. Schneidermann and P.M. Harris (Editors), Carbonate Cements. SEPM Spec. Publ., 36: 349–369.

Gevork'yon, V.Kh. and Chugunnyy, Yu.G., 1970. Phosphatic nodules in the bottom sediments of the Gulf of Aden. Oceanology, 10: 232–241.

Gulbrandsen, R.A., 1970. Relation of carbon dioxide content of apatite of the Phosphoria Formation to regional facies. U.S. Geol. Surv. Prof. Pap., 700-B: B9–B13.

Ivanov, M.V., 1968. Microbial Processes in the Formation of Sulfur Deposits. Isr. Programme Sci. Transl., Jerusalem, 298 pp.

Jones, B., 1989. The role of microorganisms in phytokarst development on dolostones and limestones, Grand Cayman, British West Indies. Can. J. Earth Sci., 26: 2204–2213.

Jones, B. and Kahle, C.F., 1985. Lichen and algae: Agents of biodiagenesis in karst breccia from Grand Cayman Island. Bull. Can. Petrol. Geol., 33: 446–461.

Jones, B. and Motyka, A., 1987. Biogenic structures and micrite in stalactites from Grand Cayman Island, British West Indies. Can. J. Earth Sci., 24: 1402–1411.

Jones, E.J.W. and Goddard, D.A., 1979.Deep-sea phosphorite of Tertiary age from Annon Seamount, eastern equatorial Atlantic. Deep-Sea Res., 26A: 1363–1379.

Kahle, C.F., 1977. Origin of subaerial Holocene calcareous crusts: role of algae, fungi and sparmicritization. Sedimentology, 24: 413–435.

Kendrick, B., Risk, M.J., Michaelides, J. and Bergman, K., 1982. Amphibious microborers; bioeroding fungi isolated from live corals. Bull. Mar. Sci., 32: 862–867.

Klappa, C.F., 1979a. Lichen stromatolites: Criteria for subaerial exposure and a mechanism for the formation of laminar calcretes. J. Sediment. Petrol., 49: 379–400.

Klappa, C.F., 1979b. Calcified filaments in Quaternary calcretes: Organomineral interactions in the subaerial vadose environment. J. Sediment. Petrol., 49: 955–965.

Kobluk, D.R. and Risk, M.J., 1977. Calcification of exposed filaments of endolithic algae, micrite envelope formation and sediment production. J. Sediment. Petrol., 47: 517–528.

Kostov, I., 1968. Mineralogy. Oliver and Boyd, Edinburgh, 587 pp.

Lamboy, M., 1990a. Microbial mediation in phosphatogenesis. New data from the Cretaceous phosphatic chalks of northern France. In: A.J.G. Notholt and I. Jarvis (Editors), Phosphorite Research and Development. Geol. Soc. London Spec. Publ., 52: 157–167.

Lamboy, M., 1990b. Microstructure of a phosphatic crust from the Peruvian continental margin: phosphatised bacteria and associated phenomena. Oceanol. Acta, 13: 439–451.

Lamboy, M. and Monty, C.L.V., 1987. Bacterial origin of phosphatised grains. Terra Cognita, 7: 207 (Abstr).

Lucas, J. and Prévôt, L., 1984. Apatite synthesis by bacterial activity from phosphatic organic matter and several calcium carbonates in natural fresh and sea water. Chem. Geol., 42: 101–118.

McArthur, J.M., 1984. Francolite geochemistry compositional controls during formation, diagenesis, metamorphism and weathering. Geochim. Cosmochim. Acta, 49: 23–35.

McClellan, G.H. and Lehr, J.R., 1969. Crystal chemical investigations on natural apatites. Am. Mineral., 54: 1374–1391.

Multer, H.G. and Hoffmeister, J.E., 1968. Subaerial laminated crusts of the Florida Keys. Geol. Soc. Am. Bull., 79: 183–192.

O'Brien, G.W., Harris, J.R., Milnes, A.R. and Veeh, H.H., 1981. Bacterial origin of East Australian continental margin phosphorites. Nature, 294: 442–444.

O'Brien, G.W., Milnes, A.R., Veeh, H.H., Heggie, D.T., Riggs, S.R., Cullen, D.J., Marshall, J.F. and Cook, P.J., 1990. Sedimentation dynamics and redox iron-cycling: controlling factors for the apatite–glauconite association on the East Australian continental margin. In: A.J.G. Notholt and I. Jarvis (Editors), Phosphorite Research and Development. Geol. Soc. London Spec. Publ., 52: 61–86.

Oppenheimer, C.H., 1958. Evidence of fossil bacteria in phosphate rocks. Inst. Mar. Sci. Publ., 5: 156–159.

Pentecost, A. and Riding, R., 1986. Calcification in cyanobacteria In: B.S.C. Leadbeater and R. Riding (Editors), Biomineralisation in Lower Plants and Animals. The Systematics Association. Special Volume 30. Clarendon, Oxford, 400 pp.

Perkins, R.D. and Halsey, S.D., 1971. Geologic significance of microboring fungi and algae in Carolina shelf sediments. J. Sediment. Petrol., 41: 843–853.

Prévôt, L. and Lucas, J., 1986. Microstructure of apatite-replacing carbonate in synthesised and natural samples. J. Sediment. Petrol., 56: 153–160.

Rao, V.P., 1986. Phosphorites from the Error Seamount, Northern Arabian Sea. Mar. Geol., 71: 177–186.

Rao, V.P. and Burnett, W.C., 1990. Phosphatic rocks and manganese crusts from seamounts in the EEZ of Kiribati and Tuvalu, Central Pacific Ocean. In: B. Keating and B. Bolton (Editors), Geology and Offshore Mineral Resources of the Central Pacific Basin. AAPG/Circ. Pac. Monogr. Ser., 15: 285–296.

Rao, V.P. and Nair, R.R., 1988. Microbial origin of the phosphorites of the western continental shelf of India. Mar. Geol., 84: 105–111.

Rao, V.P., Natarajan, R., Parthiban, G. and Mascarenhas, A.,

1990. Phosphatised limestones and associated sediments from the western continental shelf of India. Mar. Geol., 95: 17–29.

Read, J.F., 1974. Calcrete deposits and Quaternary sediments, Edel Province, Shark Bay, Western Australia. Am. Assoc. Pet. Geol. Mem., 22: 250–282.

Read, J.F., 1976. Calcretes and their distinction from stromatolites. In: M.R. Walter (Editor), Stromatolites (Developments in Sedimentology, 20.) Elsevier, Amsterdam, pp.55–73.

Riggs, S.R., 1979. Petrology and Tertiary phosphorite system of Florida. Econ. Geol., 74: 195–220.

Riggs, S.R., 1982. Phosphatic bacteria in the Neogene phosphorites of the Atlantic Coastal Plain–Continental Shelf System. IGCP Proj. 156, Phosphorite News Lett., 11: 34.

Rooney, W.S. and Perkins, R.D., 1972. Distribution and geologic significance of microboring organisms within sediments of the Arlington Reef Complex, Australia. Bull. Geol. Soc. Am., 83: 1139–1150.

Slansky, M., 1979. Geology of Sedimentary Phosphates. North Oxford Academic Publ., U.K., 210 pp.

Soudry, D. and Champetier, Y., 1983. Microbial processes in the Negev phosphorites (Southern Israel). Sedimentology, 30: 411–423.

Soudry, D. and Lewy, Z., 1988. Microbially induced formation of phosphate nodules and megafossil moulds. Palaeogeogr., Palaeoclimatol., Palaeoecol., 64: 15–34.

Soudry, D. and Southgate, P.N., 1989. Ultrastructure of a middle Cambrian primary non-pelletal phosphorite and its early formation into phosphate vadoids: Georgina Basin, Australia. J. Sediment. Petrol., 59: 53–63.

Southgate, P.N., 1986. Cambrian phoscrete profiles, coated grains and microbial processes in phosphogenesis, Georgina Basin, Australia. J. Sediment. Petrol., 56: 429–441.

Tsuneda, A., 1983. Fungal Morphology and Ecology. Mostly Scanning Electron Microscopy. Tokyo Press.

Zanin, Y.M., Letov, S.V., Krasil'nikova, N.A. and Mirtov, Y.V., 1985. Phosphatised bacteria from Cretaceous phosphorites of the east European platform and Paleogene phosphorites of Morocco. In: J. Lucas and L. Prévôt (Editors), Sciences Géologiques, Mem. 77, pp. 79–81.

Marine Geology, 106 (1992) 165–168
Elsevier Science Publishers B.V., Amsterdam

Book Reviews

Geological Evolution of Antarctica. M.R.A. Thomson, J.A. Crame and J.W. Thomson (Editors). (World and Regional Geology, 1) Cambridge University Press, Cambridge, 1991, xiii + 722 pp. £50, US $89.50 (hardcover), ISBN 0-521-37266-6.

What is the most desirable form of title, all things considered, for books issuing from serial conferences? A neat answer was found in 1981 by the editors of the proceedings of the Fifth International Gondwana Symposium. They called their volume *Gondwana Five*.

In the same way an accurate and sufficient title for the volume under review could have been *Antarctic Earth Sciences Five*. The book simply is not a coherent volume on the Geological Evolution of Antarctica, but is a collection of 138 papers presented by 203 authors at the Fifth International Symposium on Antarctic Earth Sciences in Cambridge, England in 1987.

After that caveat I hasten to add that the volume is a scholarly and faultlessly-produced example of its type, and is up to the standards set by the first four volumes in the series, which were issued in 1964, 1972, 1982 and 1983. All are now collectors' items. The 1983 volume was produced very quickly, and was made manageable in size by using very small print. The others, including the 1991 volume, are rather massive and heavy prestige publications, perhaps reflecting a certain degree of international competition. They range in size from 700 to over 1100 pages but all have been sold at a relatively low price because of support from national Antarctic organisations.

All are bargains. The cost of the Antarctic work reported by the 203 authors of this volume came to US$51 million when I did some adding, on the back of an envelope, of the costs of salaries, ships, aircraft, polar bases, land transport, food, fuel, Antarctic clothing, laboratories back home and administration. That is a notional cost of about $70,637 per page for the 722 pages of the 1991 volume, or roughly $70 per word. The cost to the buyer of the book is 12.4 cents a page. (In 1959 the cost of the International Geophysical Year was estimated at 3 cents a published word, but the calculations were made on the back of a very small envelope).

The 722 pages are divided into four sections corresponding to geological provinces, a fifth section on Gondwana break-up and a sixth on Cenozoic paleoenvironments.

Section one, on the East Antarctic craton is particularly frustrating. There are interpretive papers, some with more controversial interpretations than others, like the analysis of intrusive Mawson charnockites by Young and Ellis; but most are descriptive and they do not tie together. The editors are not at fault of course, because with a symposium volume they just had to take what was contributed by Australian, British, Chinese, German, Indian, Japanese, South African, Soviet and United States authors. A summation or synthesis was not feasible at the meeting, but perhaps could have been considered during the compilation of the volume.

The other three sections on provinces are similar in style to section one, and cover the Transantarctic Mountains, the Weddell Sea–Ross Sea region where geophysics comes into its rightful place, and the Pacific Margin which in this volume means only the region from the Scotia Arc to the Antarctic Peninsula and Thurston Island. What is wrong with the name West Antarctica? Perhaps that name was not used because there is essentially nothing in the volume on the Ellsworth Mountains.

That is a reflection of the fact that nearly all the non-Soviet field parties in the deep interior of Antarctica have been put in place by US aeroplanes. It is dangerous and costly work, but the parties of other nations have been supported freely, with extraordinary skill, generosity and friendliness. The US planes have provided in effect a free international shuttle service, but they cannot go everywhere in the short Antarctic summer seasons, and the Ellsworths are a long, long way from McMurdo. They have been off-program for some time.

The final section of the book consists of 17 papers on Cenozoic paleoenvironments, and is the most important part of the volume for marine scientists. This is the only section with an overview (by Peter Webb), followed by papers about the first record of dinosaurs in Antarctica, fossil forests, the glacial history as determined by drillholes, the amazing climatic and tectonic history preserved in the Sirius Group along the Beardmore Glacier and the abundant vertebrate fossils of the marine plain in the Vestfold Hills at the edge of the Indian Ocean.

Obviously all Antarctic geologists, several hundreds of them now, have to try to buy this volume as a key part of their personal libraries, or persuade their institutions to buy it. Many Gondwana earth scientists have to decide the same way. The book would be a luxury in the personal libraries of marine geologists, but is a very reasonable purchase for their institutional libraries. Partly this is because the Pacific margin section contains papers on the interactions between the South Pacific and South Atlantic Oceans and Antarctica. More significantly, access to leading Antarctic literature has become important suddenly to North American and European geologists because of the thrilling emergence of the SWEAT hypothesis in a series of papers in 1991. Put as briefly as possible this hypothesis states that North America was part of proto-Gondwana, fitting into the space that is now the South Pacific, and against the west side of South America, the east side of Australia and the east side of the Transantarctic Mountains. The northward break-out of North America if it occurred, and that is under debate, was similar to the northward movement of India, and for roughly the same distance. It possibly caused the closing of the Iapetus Ocean, just as the later Indian closure caused the Himalayas. This concept is causing vigorous reappraisal of regional correlations over large parts of the globe. Consequently it is going to be desirable for many people to have access to some of the leading volumes on Antarctic geology. This volume is one of them. It is selling at a very reasonable price for a large hardback.

It is a primary source work, and it is recommended for the libraries of universities and other organisations involved in global geological research.

H.J. HARRINGTON (Canberra, A.C.T.)

Nannofossils and Their Applications. Jason A. Crux and Shirley E. van Heck (Editors). Ellis Horwood Limited, Chichester, England, for The British Micropalaeontological Society, 1989, xi + 356 pp., £69.50 (hardcover), ISBN 0-7458-0237-0 (Ellis Horwood Ltd.), ISBN 0-470-21203-9 (Halsted Press).

This volume is a collection of 14 well-illustrated papers selected from those presented at the Fourth Meeting of the International Nannoplankton Association in London, 1987. All of the papers represent new contributions and very little of the information has been published elsewhere. The book is organized around three topics: Morphology, Systematics and Evolution; Palaeoenvironmental and Palaeogeographical Applications; and Biostratigraphical Applications.

In the first section Jeremy R. Young describes a variety of heterococcolith rim structures and their relationship to developmental processes in an attempt to relate intracellular development of coccoliths to the variability of forms observed in the fossil record. Marie-Pierre Aubry discusses the difficulties of reconciling the taxonomy of living and fossil calcareous nannoplankton and the problem of following their evolution across a major event, the Cretaceous–Tertiary boundary. Liam Gallagher provides a critical review of taxonomy, structure and evolution of the complex and confusing group of nannofossils assigned to the genus *Reticulofenestra*. In the context of describing the optical properties and microcrystallography of the Arkhangelskiellaceae and other Late Cretaceous calcareous nannofossils, Shimon Moshkovitz and Kenneth Osmond provide an excellent introduction to the optics of calcareous nannofossils. They show the effects observed with a gypsum plate using color illustrations. Paul R. Brown and M. Kevin E. Cooper present a comparative account of three peculiar conical species.

The second section, devoted to paleoenvironmental and paleogeographic interpretation also consists of five papers. The first, by Gunilla Gard, documents changes in relative abundances of coccoliths, particularly *Coccolithus pelagicus*, during Late Pleistocene glacials and interglacials in the high and mid-latitude Atlantic and Indian Oceans. The other four papers in this section are concerned

with interpretation of Early Cretaceous coccolith assemblages. Jörg Mutterlose discusses the connections between the Tethys and central Europe. Jason A. Crux provides a thorough discussion of zonation schemes for Lower Cretaceous nannofossils in northwestern Europe. This important paper includes with 14 plates illustrating the stratigraphically and paleobiogeographically important species. Joseph L. Applegate, James A. Bergen, J. Mitchener Covington and Sherwood W. Wise, Jr. document the differing ranges of calcareous nannofossil species in Lower Cretaceous sediments along the northern margin of the young Atlantic and in the North Sea. M. Kevin E. Cooper evaluates provincialism among major groups of Late Jurassic–Early Cretaceous (Kimmeridgian to Valanginian) calcareous nannofossils on a global scale.

The third section is mostly devoted to biostratigraphy, but two of the four papers also discuss paleoenvironmental interpretation. José-Abel Flores and Francisco-Javier Sierro provide new information on Late Miocene water mass changes in the Atlantic adjacent to the Mediterranean, suggesting a general Tortonian–Messinian cooling trend on which minor climate fluctuations are superposed. Osman Varol introduces a detailed Paleocene calcareous nannofossil biostratigraphic zonation scheme for the North Sea as well as describing the nannofossil distribution in the remarkably complete Kokaksu Section in Turkey. Vedia Toker lists Paleocene–Eocene calcareous nannofossil zones that can be recognized at eight widely separated sections in Turkey, combining these to produce a composite zonation. Magdy H. Girgis describes the results of morphometric analysis of *Arkhangelskiella* and the stratigraphic and paleoenvironmental importance of the group.

The editors have done an excellent job of insuring uniformity of format and have maintained high standards for the illustrations. The book includes a complete index to the genera and species mentioned in the text, on tables or in figures.

This work is indispensable for nannofossil specialists dealing with the Lower Cretaceous or Europe and belongs in every reference library with a micropaleontological clientele.

WILLIAM W. HAY (Kiel, Germany)

Carbonate Diagenesis and Porosity (*Developments in Sedimentology, Vol. 46.*) C.H. Moore. Elsevier Science Publishers, Amsterdam, 1989, 338 pp. (ISBN 0-444-87416-X (paperback, Dfl 90), 0-444-87415-1 (hardback, Dfl 180).)

This book is by a very well known researcher in the applied aspects of carbonates and has arisen from many years of preparation of short courses for industry, and it will prove to be a very useful introduction to the topic of carbonate diagenesis both for students (at the post-graduate level) and to oil industry geologists.

The book contains nine chapters. The first two cover a brief look at carbonate versus siliciclastic deposystems and the classification and nature of carbonate porosity. These are followed by a chapter introducing the major diagenetic regimes, followed by six more chapters, each of which is devoted to one regime: "normal" marine diagenetic environments, evaporative marine environments, two chapters on meteoric environments, one on dolomitization, and finally a chapter on the burial diagenetic environment.

This book is written in an easy-to-read style in a single-column format with very clear diagrams. I noted minor repetition of illustrations, which considering printing costs, is surprising. Many of the photo illustrations are too small to be of any real use, but generally the photomicrographs are good.

The book could well be re-formatted to produce a much smaller (and cheaper) volume, but it might well then lose its attractive "user-friendly" look.

Although there is no section on techniques the book does cover these where appropriate, and wisely discusses pitfalls in the usage of the techniques.

I like the book but the experienced carbonate geologist will not find much that is new. However, the book, in its style and format, is aimed as an introduction to the topic and fills this role well. The basics are introduced gently and the text contains numerous case studies from the oil industry and (knowing the author's experience) the heavy emphasis on the Jurassic Smackover reservoirs of the southern USA is understandable. The references provided are not exhaustive but do provide the key papers for the reader.

Most post-graduate students studying carbon-

ates will find this book of use only initially and will soon require more detailed text. The strength of the book lies in its integration of reservoir case studies and thus it will be of most use to exploration geologists and to new production geologists requiring an introduction to carbonate diagenesis and porosity.

The book is well worth the price for anyone wanting a good, clear introduction to carbonate diagenesis with an emphasis on hydrocarbon reservoirs.

PAUL WRIGHT (Reading, U.K.)

NOTES FOR ELECTRONIC TEXT PREPARATION

1. General

The word-processed text should be in single column format. Keep the layout of the text as simple as possible; in particular, do not use the word-processor's options to justify the text or to hyphenate the words.

2. Text preparation

The electronic text should be prepared in a way very similar to that of conventional manuscripts (see also Guide for Authors). The list of references, tables and figure captions should be compiled separately from the main text. Do *not* reserve space for the figures and tables in the text; instead, indicate their approximate locations, either directly in the electronic text or on the manuscript.

3. Submission

The final text should be submitted both in manuscript form and on diskette. Use standard 3.5″ or 5.25″ diskettes for this purpose. Both double density (DD) and high density (HD) diskettes are acceptable. Ensure, however, that the diskettes are formatted according to their capacity (HD or DD) before copying the files onto them.

Storage of the main text, list of references, tables and figure captions in separate text files with clearly identifiable file names (for example, with extensions .TXT, .REF, .TBL, .FIG) is required.

The format of the files depends on the wordprocessor used. Texts made with DEC WPS PLUS, DisplayWrite, First Choice, IBM Writing Assistant, Microsoft Word, Multimate, PFS:Write, Professional Writer, Samna Word, Sprint, Total Word, Volkswriter, Wang PC, WordMARC, WordPerfect, Wordstar, or files supplied in DCA/RFT format can be readily processed. In all other cases the preferred text format is ASCII.

Essential is that the name *and* the version of the wordprocessing program and the type of computer on which the text was prepared is clearly indicated on the diskette label or the accompanying checklist.

Authors are cncouraged to ensure that **the disk version and the hardcopy must be identical**. Discrepancies can lead to proofs of the wrong version being made.

Illustrative material (original figures or high-quality glossy prints, or photographs showing sharp contrast) should be included separately.

ELECTRONIC TEXT CHECKLIST

Please complete this list where appropriate and include it with the diskette.

Journal : _____

Title : _____

_____

Author(s) : _____

Computer

☐ IBM compatible
☐ Macintosh[1]

Diskette

☐ formatted with MS-DOS/PC-DOS
☐ formatted with Macintosh OS

File format (if different from wordprocessor's original format)

☐ ASCII
☐ DCA/RFT
☐ DEC/DX

Wordprocessor

☐ DEC WPS PLUS[2] version: _____
☐ DiplayWrite[3] version: _____
☐ First Choice version: _____
☐ IBM Writing Assistant version: _____
☐ Microsoft Word version: _____
☐ Multimate version: _____
☐ PFS:Write version: _____
☐ Professional Writer version: _____
☐ Samna Word version: _____
☐ Sprint version: _____
☐ Total Word version: _____
☐ Volkswriter version: _____
☐ Wang PC version: _____
☐ WordMARC version: _____
☐ WordPerfect version: _____
☐ Wordstar version: _____

☐ Other (specify)[4]: _____

Diskette contents : _____

_____

_____

Remarks : _____

_____

_____

[1] In view of the further text processing on a MS-DOS compatible system submission of text files on MS-DOS formatted diskettes is recommended.
[2] Files should be submitted in DX format (option "CV" from the DEC-WPS Document Processing Menu).
[3] Files created with DisplayWrite 4 should be submitted in DCA/RFT format by means of the DisplayWrite "Convert Documents" utility.
[4] Submission of the text files in ASCII format is strongly recommended.

Glossary of Geology Third edition

by **R.L. Bates** *and* **J.A. Jackson**

About 37,000 terms

"A huge book... If what you want to know in terms of definitions or even short explanations is not here, then it is probably of such miniscule importance that it really doesn't matter anyway... highly recommended. "

Geophysics

"This is an indispensible work that testifies to the thoroughness or persistence of the editors and their 150 collaborators."

The Institute of Mining & Metallurgy

THIS THIRD EDITION of the Glossary of Geology contains approximately 37,000 terms, or 1,000 more than the second edition, as well as 650 emendations and corrections. In addition, it includes for the first time the division of cited terms in syllables, with accents to aid in pronunciation. Approximately 150 references have been added to the 2,000 in the second edition. Literature cited ranges from the early 1790s to 1986. New entries are especially numerous in the fields of carbonate sedimentology, hydrogeology, marine geology, mineralogy, ore deposits, plate tectonics, snow and ice, and stratigraphic nomenclature.

Many of the definitions provide background information. Thus the reader will learn the difference between sylvanite and sylvinite, and many other look-alike pairs; the origin of such terms as charnockite and lottal; the meaning of BHP, LVL, MORB, and more than 100 other abbreviations now common in the geoscience vocabulary; and the dates when many terms were first used, the meaning of certain common prefixes, and the preferred term of two or more synonyms.

The authority of this new edition - like that of its predecessors - rests on the expertise of geoscientists from many specialties, who have reviewed definitions, added new terms, and cited references. Their contributions make the Glossary an essential reference work for all in the geoscience community.

Printed on recycled, acid-free paper.

1987 reprinted 1990 754 pages
Price: US $ 97.50 / Dfl. 190.00
ISBN 0-913312-89-4
Published and distributed in the USA & Canada by the American Geological Institute

Elsevier Science Publishers
P.O. Box 1930, 1000 BX Amsterdam,
The Netherlands
P.O. Box 882, Madison Square Station,
New York, NY 10159, USA
The Dutch Guilder price is definitive, US $ prices are given for convenience only and are subject to exchange rate fluctuations.

GLOBAL PALAEOCLIMATE OF THE LATE CENOZOIC

edited by **V.A. Zubakov** *and* **I.I. Borzenkova,** *State Hydrological Institute, Leningrad, U.S.S.R.*

(Developments in Palaeontology and Stratigraphy, 12)

Based on the unified periodization of climatic events, this book describes the history of the global climate during the last 50 million years, with special attention being given to the last 1 million years.

The main content of the book consists of essays on climatostratigraphic sequences in 12 regions of the Northern Hemisphere. Most elaborately treated are the regions in the USSR territory, which are covered by the authors' personal information.

Shortened contents: Preface to the Russian edition of *Palaeoclimates of the Late Cenozoic* by V.A. Zubakov and I.I. Borzenkova (Gidrometeoizdat, 1983). Preface to the Russian edition of *The Global Climatic Events of the Pleistocene*, by V.A. Zubakov (Gidrometeoizdat, 1986).

PART I. THE GLOBAL CLIMATIC EVENTS OF THE PLEISTOCENE. Section I. Methodological problems of palaeclimatology. 1. The time structure of climate. On the definitions of climate, palaeoclimate and palaeoclimatography.On the methods of high-resolution climatostratigraphic correlation and chronological scale of global climatic events. Main features of the glacial climatic regime. Main features of the greenhouse climatic regime. 2. Deep-sea standard for global climatic events. The significance of the oxygen-isotope scale for climatostratigraphic reconstructions. Systematic aspects of "ocean-continent" climatochronological correlation. The significance of geomagnetic data. **Section II. Evidence for climatic changes in the Pleistocene - regional review.** 3. Effects of global climatic events in the Mediterranean - Caspian system. The Mediterranean as a new climatoparastratotype region. The Caspian basin as a major record of changes in humidification in interior Eurasia. 4. The loess assemblage of Eurasia as an indicator of climatic changes in the arid zone. The Loess zone of Europe. Loess in Asia. 5. Middle and high latitudes of the Northern Hemisphere as a major record of continental glaciation in Pleistocene time. Russian plain. Glaciated area in western and central Europe. West Siberia. North-eastern Asia and Beringia. North America. The Arctic and sub-Arctic. **Section III. The history of climate through the Pleistocene.** 6. On the timing of palaeoclimates in the Pleistocene. Debatable problems of inter-regional climatostratigraphic correlation. On correspondence between the numbrs of climathems on land and in the sea. The role of the 400 ka cycle for chronological classification of the Pleistocene. 7. Climatic changes in the Early and Middle Pleistocene. 8. Climatic changes in the Late Pleistocene. 9. Climatic changes through Late Glacial and Post-glacial, 16-0 ka BP. Principles of the time classification of the last 16 ka. On the global temperature trend over the last 16 ka.. On possible causes of climate change in the late glacial-holocene. Moisture conditions in different latitude zones over the late glacial-holocene: a review of empirical data. Empirical data on moisture conditions in tropical and subtropical regions between 0 and 25°N and S. Global climatic events - an empirical basis of high-resolution stratification. On the causes of climatic changes in the Pleistocene. References.

PART II. PRE-PLEISTOCENE CLIMATES: MAIN STEPS OF THE LATE CENOZOIC GLACIAL-PSYCHROSPHERIC REGIME STANDING. Introduction. 10. Palaeoclimates of the pre-Pliocene Cenozoic.
11. Palaeoclimates of the Pliocene. Summary. Subject Index.

1990 472 pages
ISBN 0-444-87309-0
Price: US$ 148.75 / Dfl. 290.00

ELSEVIER SCIENCE PUBLISHERS
P.O. Box 211, 1000 AE Amsterdam, The Netherlands
P.O. Box 882, Madison Square Station, New York, NY 10159, USA

(continued from inside front cover)

Note to contributors
A detailed *Guide for Authors* is available upon your request, and will also be printed in the first volume to appear each year. You are kindly asked to consult this guide. Please pay special attention to the following notes:

Language
The official language of the journal is English, but occasional articles in French and German will be considered for publication. Such articles should start with an abstract in English, headed by an English translation of the title. An abstract in the language of the paper should follow the English abstract. English translations of the figure captions should also be given.

Preparation of the text
a) The manuscript should be typewritten with double spacing and wide margins and include at the beginning of the paper an abstract of not more than 500 words. Words to be printed in italics should be underlined. The metric system should be used throughout.
b) The title page should include, the name(s) of the author(s) and their affiliations.

Abstract
The abstract must be an informative statement of the content of the paper, explaining what the problem is, the methods used (when appropriate), a statement of the results, and the main conclusions. Constructions using phrases such as "this paper discusses", "are described" and "is reported" have no place in an abstract: by reading the abstract, the reader should be able to understand the essential qualities of the paper without referring to the paper itself. See K.K. Landes (Bull. Am. Assoc. Pet. Geol., 1951, Vol. 35, p. 1660) for a concise statement on how to write a good abstract.

References
a) References in the text start with the name of the author(s), followed by the publication date in parentheses.
b) The reference list should be in alphabetical order and on sheets separate from the text.

Tables
Tables should be compiled on separate sheets. A title should be provided for each table and they should be referred to in the text.

Illustrations
a) All illustrations should be numbered consecutively and referred to in the text.
b) Drawings should be completely lettered, the size of the lettering being appropriate to that of the drawings, but taking into account the possible need for reduction in size (preferably not more than 50%). The page format of *Marine Geology* should be considered in designing the drawings.
c) Photographs must be of good quality, printed on glossy paper.
d) Figure captions should be supplied on a separate sheet.
e) If contributors wish to have their original figures returned this should be requested in proof stage at the latest.
f) **Colour figures** cannot normally be accepted unless the reproduction costs are to be met by the author. As a rough guide, the reproduction costs for a one-page figure are ca. Dfl. 2150 (inc. tax). Please consult the publisher for further information.

Proofs
One set of proofs will be sent to the author, to be checked for printer's errors. In case of two or more authors please indicate to whom the proofs should be sent.

Reprints
Fifty reprints of each article published are supplied free of charge. Additional reprints can be ordered on a reprint order form, which is included with the proofs.

Submission of manuscripts
a) Manuscripts originating in the Americas and Far East should be submitted in triplicate to Dr. D.A. McManus, Department of Oceanography, University of Washington, Seattle, Washington 98105, U.S.A. All other manuscripts should be sent in triplicate to the Editorial Office *Marine Geology*, P.O. Box 1930, 1000 BX Amsterdam, The Netherlands.
b) Illustrations should also be submitted in triplicate. One set should be in a form ready for reproduction: the other two may be of lower quality.
c) Authors are requested to submit the names and addresses of four potential referees with their manuscripts.
d) Letter-type contributions should be submitted in triplicate to the Editorial Office *Marine Geology, Letter Section*, P.O. Box 1930, 1000 BX Amsterdam, The Netherlands. Contributions for this section should not exceed 8 printed pages and should be complete in themselves. No foldout illustrations can be accepted. The manuscripts received will be published ca. *three months* after acceptance. In order to achieve rapid publication, no proofs will be sent to the authors. Manuscripts should therefore be prepared with the greatest possible care.
e) **The indication of a FAX number on submission of the manuscript could assist in speeding communications. The FAX number for the Amsterdam office is: 020-5862696.**
f) In order to enable publication as quickly as possible after acceptance, authors are encouraged to submit the final text also on a 3.5″ or 5.25″ diskette. Both double density (DD) and high density (HD) diskettes are acceptable. Make sure, however, that the diskettes are formatted according to their capacity (HD or DD) before copying the files onto them. As with the requirements for manuscript submission, the main text, list of references, tables and figure captions should be stored in separate text files with clearly identifiable file names. The format of these files depends on the wordprocessor used. Texts written with DisplayWrite, MultiMate, Microsoft Word, Samna Word, Sprint, Volkswriter, Wang PC, WordMARC, WordPerfect and Wordstar or supplied in DCA/RFT or DEC/DX format can be readily processed. In all other cases the preferred format is DOS text or ASCII. Essential is that the name and version of the wordprocessing program, the type of computer on which the text was prepared, and the format of the text files are clearly indicated. **Authors are requested to ensure that the contents of the diskette correspond exactly to the contents of the hardcopy manuscript. Discrepancies can lead to proofs of the wrong version being made.**

Submission of an article is understood to imply that the article is original and unpublished and is not being considered for publication elsewhere.
Upon acceptance of an article by the journal the author(s) will be asked to transfer the copyright of the article to the publishers. This transfer will ensure the widest possible dissemination of information under the U.S. Copyright Law.

MARINE GEOLOGY
International Journal of Marine Geology, Geochemistry and Geophysics

(Abstracted/Indexed in: Geoscience Contents, Geo Abstracts, Current Contents, Bulletin Signalétique, Chemical Abstracts, Marine Science Contents Tables, A.G.I.'s Bibliography and Index of Geology, Aquatic Science and Fisheries Abstracts, PASCAL/CNRS and Oceanic Abstracts)

VOL. 106 No. 1/2 CONTENTS APRIL 1992

Research Papers

Book Reviews

Announcement

Authors may now accompany their manuscripts with floppy disks

Please see the notes on the inside back cover and the guide at the back of this issue. Authors are requested to submit a completed checklist with each diskette. Additional copies of the guide and the checklist are available from the publisher.